BULGARIAN CHEMICAL COMMUNICATIONS

2014 Volume 46 / Number 3

Spectrophotometric determination of copper (II) in industrial effluent samples using sulfanilic acid as a ligand system

K.T. Vadiraj *, S.L. Belagali

DOS in Environmental Science, University of Mysore, Karnataka, India

A new UV-visible spectrophotometric method was developed for the determination of copper (II) in industrial wastewater samples. The method is based on complex formation of copper (II) with sulfanilic acid in acidic medium at room temperature. The complex showed maximum absorption at a wavelength of 380 nm with a molar absorptivity value of 6.7×10^{-2} mol^{-1} cm^{-1}. Beer's law is obeyed in the concentration range of 0.3 to 2.1 ppm. Interferences due to zinc (II), cadmium (II), nickel (II), cobalt (II), chromium (III) and several anions were investigated. The proposed method was successfully applied to the determination of copper (II) in industrial effluent samples.

Keywords: Copper (II), Sulfanilic acid (SA), Acidic medium, Beer's Law, Industrial effluent

INTRODUCTION

The entire world is environmental scientist's laboratory. Environmental science deals with the study of atmosphere, water, soil, the release and uptake of materials by plants and animals. It includes various studies on the exchange of chemical species, elements and compounds between the atmosphere, hydrosphere, geosphere and biosphere. This branch has developed, because of the increase in human activities and their effects, frequently not beneficial to the natural environment [1]. Metals, as indispensable components of the nature, constitute about 6 % of the earth. Metals are not biodegradable and have virtually an unlimited lifespan and potential for unlimited recycling. Thus, metals can be considered as renewable materials [2-10]. There are 111 known elements; of these 80 are metals. The important toxic metals and metalloids are: beryllium (Be), osmium (Os), platinum (Pt), mercury (Hg), titanium (Ti), vanadium (V), selenium (Se), chromium (Cr), tellurium (Te), cobalt (Co), copper (Cu), uranium (U), cerium (Ce), silver (Ag), cadmium (Cd), lead (Pb), arsenic (As), antimony (Sb), nickel (Ni), zinc (Zn) and manganese (Mn). Their toxicity varies with threshold limit values (TLV) of 2 µg/m^3 to 5000 µg/m^3, which are the maximum tolerable limits for human beings. The different metals have different degrees of toxicity. A limited number of these metals are carcinogenic. They lead to cancer of lungs, liver, pleura and thyroid. Some of these pollutants are encountered in water and air, effluents, solid wastes and sewages [11-13].

Copper is a reddish metal with a face-centered cubic crystalline structure. It has low chemical reactivity [14]. It is an essential metal for plants, microorganisms, animals and human beings to perform specific biological functions [15, 16]. Copper is often added to fertilizers to serve as a supplement to plants. The failure to supply adequate amounts of copper leads to a variety of biochemical and physiological disorders in plants. In humans, it not only facilitates the conversion of iron to haemoglobin but also stimulates the growth of red blood cells. Copper is an integral part of certain digestive enzymes. Copper has received considerable attention owing to its technological and biological significance. It is an essential constituent of about thirty enzymes and glycoproteins. It is required for the synthesis of haemoglobin and for some biological processes. The concentration of copper is crucial for determining its toxicity to many biological systems. It has been reported that the toxic copper species are $[Cu(OH)]^{+}$, $[Cu_2(OH)_2]^{2+}$ and $CuCO_3$. Therefore, copper ions present in various aqueous systems are considered to be the most toxic of dissolved copper species. Excess concentration of copper in water systems is harmful to human beings; it affects the self-purification of bulk water and disturbs the microbiological treatment of waste water. Thus, the determination of trace amounts of Cu (II) is becoming increasingly important, because of the increased interest in environmental pollution [17-20]. Copper is an essential element for human

* To whom all correspondence should be sent:
E-mail: vadi.raj89@gmail.com

life, but in high doses it can cause anemia, liver damage, stomach and intestinal irritation. Copper normally occurs in drinking water from copper pipes and additives to control algal growth [21]. Long term exposure to copper can cause irritation of nose, mouth, eyes, leading to headache, dizziness, vomiting and diarrhea [14]. Intentional uptake of copper may cause liver and kidney damage and even death. Industrial exposure to copper fumes, dusts and mists may result in metal fume fever, with atrophic changes in nasal mucous membranes. Chronic poisoning with copper results in Wilson's disease, characterized by hepatic cirrhosis, brain damage, renal failure and copper deposition in the cornea [22].

Many analytical techniques are currently available to determine copper concentration in samples with different matrices, such as flame atomic absorption spectroscopy, electrothermal atomic absorption spectroscopy, inductively coupled plasma–atomic emission spectroscopy, inductively coupled plasma–mass spectrometry or differential pulse anodic stripping voltammetry. Besides the well-known advantages of these instrumental techniques (precision, accuracy, sensitivity, selectivity, etc.), all of them present a series of disadvantages, such as high investment costs, complexity and difficult *in situ* application. Many spectrophotometric methods have been developed for the determination of Cu(II) based on reactions with reagents such as S,S'-bis(2-aminophenyl) oxalate [23], chloro(phenyl) glyoxime [24], salicylaldehyde acetoacetic acid hydrazone [25], sodium diethyldithiocarbamate [26], neocuproine (2,9-dimethyl-1,10-phenanthroline) [27], etc. Most of the reported spectrophotometric methods are time consuming, employing many reagents to develop the color and to extract the copper complex into organic solvents.

In the present work, a sensitive and simple method of determination of trace copper in industrial wastewater samples by UV-visible spectrophotometry is described, based on the formation of a copper (II) - sulfanilic acid complex. The influence of some analytical parameters including pH, amount of sulfanilic acid and effect of diverse ions, etc., on the complex formation was investigated.

MATERIALS AND METHODS

Spectrophotometry is often used for determining metals in alloys, minerals and complexes, owing to its selectivity. In comparison with atomic emission spectroscopy, atomic absorption spectroscopy and similar techniques, it offers the advantage of

calibration graphs that are linear over a wider range. A very extensive range of concentrations of substances (10^{-2}–10^{-8} M) may be covered. Color-based identification of materials was probably one of the earliest examples of qualitative molecular absorption spectrophotometry. The recognition that color intensity can be an indicator of concentration was probably the earliest application of molecular absorption spectroscopy for quantitative estimation. This quantitative estimation was done using the human eye as the detector and undispersed sunlight or artificial light as the light source. Later it was found that the accuracy and the precision could be improved by isolating specific frequencies of light using optical filters.

A Systronics UV-visible spectrophotometer 118 with a wavelength range of 200-1000 nm was used for the measurements. It is a single-beam, manual instrument for both qualitative and quantitative absorption spectrometric studies.

All solutions were prepared with analytical reagent-grade chemicals in deionized water. Copper solution was prepared from 2.496 g of analytical reagent-grade copper sulfate crystals dissolved in 100 ml of distilled water. Sulfanilic acid reagent was prepared by solubilizing 1 g of sulfanilic acid in 100 ml of water, slowly by shaking. The pH buffer was prepared from 0.1 g of sodium acetate dissolved in 100 ml of water. Other solutions used for interference studies were prepared by dissolving the required amounts of salts in distilled water.

The procedure followed for the standardization and analysis is as follows:

Add from 0.5 to 5 ml of the copper solution in 20 ml standard flasks (0.15 to 15 ppm of copper). Add 5 ml of sodium acetate solution to each of them. Allow them to stand for a few minutes till the solution gets a whitish color. Add 5 ml of sulfanilic acid solution to the standard flasks. Make up the solution to 20 ml using distilled water and shake well. Then measure the absorbance at 380 nm.

Determination of the suitable pH for complex formation:

All ligands require certain conditions and supporting ions to form the colored complex. In this study it was found that the formation of a complex between copper (II) sulfate and sulfanilic acid solution requires a pH buffer (sodium acetate solution). It brings the system near to neutral pH and allows sulfanilic acid to form a green colored complex with copper (II) ions in the solution.

Determination of the wavelength of maximum absorption of the colored species:

An aliquot of 5 ml of the standard solution containing 0.75 mg L^{-1} of copper (II) was taken in a

20 ml standard flask. Then, 5 ml of sodium acetate solution and 5 ml of sulfanilic acid solution were added and the volume was brought to the mark with distilled water. The solution was mixed well and the absorbance of the colored species was measured at different wavelengths in the range 300-400 nm against the reagent blank, prepared under similar conditions. The absorbance of the colored species was plotted against wavelengths as shown in Figure 1.
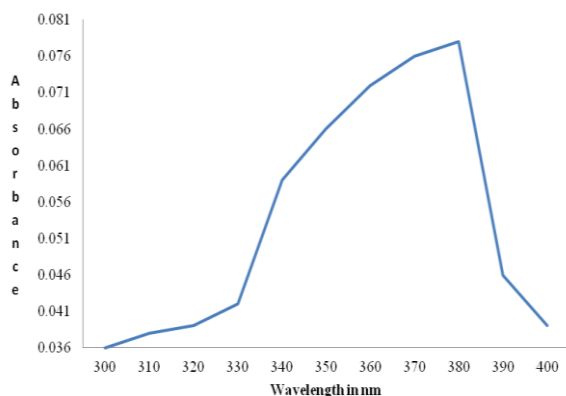

Fig. 1. Absorption spectrum of Cu (II) SA (Cu^{+2}, 0.75 ppm)

Determination of effective sulfanilic acid concentration:

Different aliquots from zero to 10 ml of the standard copper (II) solution were added to 20 ml standard flasks giving solutions of strength 0.3-3 ppm. 5 ml of the 0.1% sodium acetate solution and 5 ml of 1% sulfanilic acid solution were added to each flask. The volume was diluted to the mark with distilled water. The solutions were mixed well and the absorbance of the colored species was measured at 380 nm against the reagent blank, as shown in Figure.2.
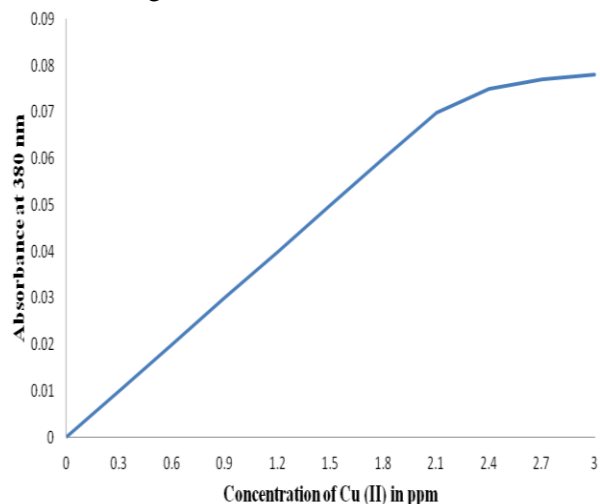

Fig. 2. Effective concentration of Cu (II) with the reagent sulfanilic acid

Preparation of a calibration graph for copper (II):

Different aliquots from zero to 5 ml of the standard solution containing zero to 1.5 ppm of copper (II) were transferred to a series of 20 ml standard flasks. Then, 5 ml of 0.1% sodium acetate and 5 ml of 1% sulfanilic acid solutions were added and the contents were diluted upto the mark with distilled water and mixed well. The absorbance of the colored species was measured at 380 nm against the reagent blank. A calibration graph of absorbance against the concentration of copper (II) was plotted (Figure 3). The calibration graph was used for the determination of copper (II) in various matrices of unknown concentrations.
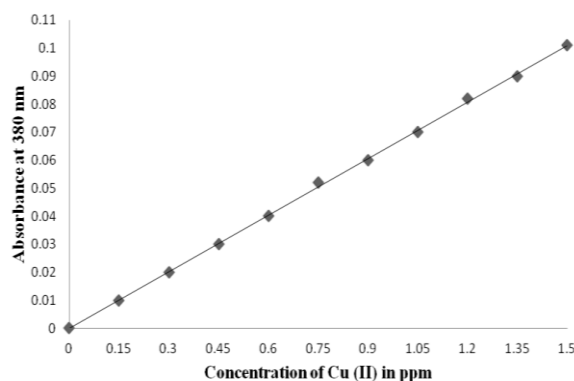

Fig. 3. Beer's law plot of the Cu (II) - sulfanilic acid system

Analysis of industrial effluent:

Copper-containing electro-plating industrial effluent was collected. Suitable aliquots of the sample solutions were analyzed according to the procedure for determining copper (II).

Discussion:

The detailed investigation of the reaction between sulfanilic acid and copper (II) showed that the latter oxidizes sulfanilic acid in sodium acetate medium to a green colored species with an absorbance maximum at 380 nm.

Optimization of experimental variables:

In order to establish the optimum conditions for the formation of copper-sulfanilic acid species, the effect of several experimental variables was studied and is discussed in the following paragraphs.

Absorption spectrum:

The absorption spectrum of the copper-sulfanilic acid colored species in 0.1% sodium acetate solution is shown in Fig.1. Sulfanilic acid with the amino group in para position has an absorbance maximum at 356-380 nm. Therefore, the absorbance measurements were made at 380 nm. Under similar conditions, the reagent blank does not absorb at this wavelength.

Effect of medium and its concentration:

To develop a quantitative method based on this reaction, a study was conducted to determine the most effective acid species and optimum acid concentration to be employed. The green-colored species was unstable in either sodium oxalate or ammonium acetate medium and does not give maximum color intensity in other media. Sodium acetate medium was found to be the most effective buffer compared to the other two. In sodium acetate medium the green color was stable for 25 min and subjected to less interferences from foreign ions.

Effect of the metal ion concentration:

The effect of concentration of copper (II) ions was studied by measuring the absorbance at 380 nm for a solution containing a fixed amount of sulfanilic acid and varying amounts (0.3 to 3 ppm) of copper (II). Below the concentration of 0.09 ppm, copper (II) does not give maximum intensity and above 2.4 ppm, the concentration had no effect on the absorbance values. Hence, a working concentration range up to 1.5 ppm of copper (II) can be estimated. The results of these studies are presented in Figure.2.

Reaction rate and effect of time:

The time required for obtaining the green colored species of copper and sulfanilic acid was examined. Under the optimum conditions, full color development occurred instantaneously and the developed color was found to be stable for a period of 25 minutes.

Effect of diverse ions:

In order to assess the possible analytical applications of the method, the effect of some ions which often accompany copper, was studied. Different amounts of the diverse ions were added to a 0.75 ppm copper (II) solution. An error of less than 2 % in the absorbance values was considered

to be tolerable. The tolerance limits of the foreign ions tested are given in Table 1.

The major advantage of this method was that sulfanilic acid can be used as a selective reagent for the determination of copper in the presence of large amounts of cations like Ni (II), Zn (II), Be (II), and Cd (II) and anions like chlorides (Cl^-), nitrates (NO_3^-), sulfates (SO_4^{2-}) and phosphates (PO_4^{3-}) which are associated with copper in electro-plating industries.

The results also indicate that Cr (IV) and sulfate ions interfere seriously. However, the interference of these ions can be avoided using appropriate masking agents.

APPLICATIONS:

The developed method was applied for the determination of copper in an industrial effluent by the procedure described above. The results are presented in Table 2

CONCLUSIONS:

The proposed method for determination of copper (II) offers the advantage of simplicity, rapidity and sensitivity without the need for heating or extraction. The developed color is stable for 25 min.

This procedure permits a clear determination of color in presence of copper and hence the proposed method can be successfully applied to the determination of trace amounts of copper in industrial effluents.

Table 1: Effect of different ions on the determination of 0.75 ppm of copper (II)

Cations	Tolerance limit in ppm	Anions added	Tolerance limit in ppm
Zn(II)	6	Cl⁻	25
Cd(II)	20	SO_4^{2-}	15
Ni(II)	25	PO_4^{3-}	20
Co(II)	30	NO_3^-	25
Cr(IV)	4	EDTA	0.40

Table 2 Copper (II) concentrations found in the industrial effluent samples

Sample of industrial effluent	Copper certified (ppm)	Copper found (ppm)
Sample 1	0.3	0.27
Sample 2	0.45	0.45

REFERENCES:

1. B. Barbara, Kebbekus Somenath Mitra *Environmental Chemical Analysis* CRC Press, New York, 1997.
2. World Commission on Environment and Development, *Our Common Future*, New York, Oxford University press (1987).
3. C. Baird, *Environmental Chemistry*, W.H Freeman and Company, New York (1995).
4. Gore, *Earth in the Balance: Ecology and the Human Spirit*, New York, Houghton Mifflin (l992).
5. A.K. De, *Environmental Chemistry*, New Age International (P) Limited, New Delhi (1998).
6. G.S. Fell, *Metals in the Environment 2*, Chem. Britain, 167, (1980) 323.
7. K Schwartz, *Clinical Chemistry and Chemical Toxicology of Metals*, Elsevier, (1977).
8. S.D. Lee, *Biochemical Effects of Environmental Pollutants*, Ann Arbor Science Publishers. Inc., Ann Arbor, Mich. (1977).
9. J.L. Casarett and John Doult, *Toxicology: The Basic Science of Poisons*, Macmillan Publishing Co., New York (1975).
10. Ei-Ichiro Ochiai, *Bioinorganic Chemistry*, Allyn and Bacon Inc., Boston Mass (1977).
11. Dayananda B P Ph.D Thesis University of Mysore, Mysore, 2007.
12. S M Khopakar, *Envirnmental Pollution Analysis*, New Age International(P) Ltd., New Delhi, (2001).
13. Kiran Kumar T N Ph.D Thesis University of Mysore, Mysore, 2009.
14. Shanthalakshmi K Ph.D thesis University of Mysore, Mysore, 2009

15. Hashem E Y, Seleim M M, Ahmed M. El-Zohry, *Gre. Chem Let. Revi*., **4**, 241, (2011),.
16. Prafullachandra Tekale, Smruti Tekale, Sudheer Lingayat and P N Pabrekar, J. *Sci Res Rep.,* **1,** 83, (2011).
17. Lutfullah, Saurabh Sharma, Nafisur Rahman, Syed Najmul Hejaz Azmi, Bashir Iqbal, Maisa Ismail Bilal Bait Amburk, Zuweina Masoud Hilal Al Barwani, *J. Chin Chem Soc.*, **57,** 622, (2010).
18. Freemantle, M. H. *Chemistry in Action*, Macmillan Educa Education Ltd.: London, 1989.
19. Sorensen, E. B. M. *Metal Poisoning in Fish*, CRC Press: Boston, MA, (1991).
20. Scheinberg, I. H, Morell, A. G. *In Inorganic Biochemistry*, Eichhorn G.L Eds, Elsevier, New York, **1,** 306, (1973).
21. Orhan Turkoglu and Mustafa Soylak, *J. Chin Chem Soc*., **5**, 575 (2005).
22. Rekha D, Suvardhan K, Suresh Kumar K, Prasad P. Reddy, Jayaraj B, Chiranjeevi P,   *J. Serb. Chem. Soc.,* **72**, 299, (2007).
23. Sinan Nohut, Serdar Karabocek, Saadettin Guner, Yasar Gok, *J. Pharm Biomed Ana.*, **20,** 309, (1999).
24. Srilalitha Vinnakota, Raghavendra Guru Prasad Aluru, Ramana Kumar Kakarla, Seshagiri Vahi Ravindranath Lakshmana Rao, Krishna Rao, *Ovid Uni Ann. Chem*, **22**, 5, (2011).
25. Jankiewicz B, Ptaszyński B, Turek, *Poli J. Envi Studies*, **8**, 35, (1999).
26. Central Pollution Control Board, *Guide Manual: Water and WastewaterAnalysis,* New Delhi, India, 2012.

СПЕКТРОФОТОМЕТРИЧНО ОПРЕДЕЛЯНЕ НА МЕД (II) В ПРОБИ ОТ ПРОМИШЛЕНИ ОТПАДЪЦИ С ПОМОЩТА НА СУЛФАНИЛОВА КИСЕЛИНА КАТО ЛИГАНД

К.Т. Вадирадж*, С.Л. Белагали

Департамент по опазване на околната среда, Университет в Майсор, Карнатака, Индия

(Резюме)

Разработен е нов UV-Vis спектрофотометричен метод за определяне на мед (II) проби от промишлени отпадъчни води. Методът се основава на комплексообразуване на медни йони (II) със сулфанилова киселина в кисела среда при стайна температура. Комплексите показват максимална абсорбция при дължина на вълната 380 nm с моларна абсорбция 6.7×10^{-2} mol^{-1} cm^{-1}. Законът на Beer се спазва в обхват от концентрации 0.3 до 2.1 ppm. Изследвано е пречещото влияние на цинк (II), кадмий (II), никел (II), кобалт (II), хром (III) и няколко аниона. Предложеният метод е приложен успешно за определянето на мед (II) в проби от промишлени отпадъчни води.

Density, viscosity and electrical conductivity of three choline chloride based ionic liquids

A.-M. Popescu, C. Donath, V. Constantin*

"Ilie Murgulescu" Institute of Physical Chemistry of the Romanian Academy, Laboratory of Molten Salts Splaiul Independentei 202, Bucharest-006021, Romania

Three ionic liquids which are binary mixtures of 2-hydroxy-N,N,N-trimethyl-ethyl-ammonium chloride (named also choline chloride, ChCl) with oxalic acid, ethylene glycol and triethanolamine were prepared. Using a composition with 1:1 molar ratio between the components, clear and colorless liquids at room temperature were obtained. The density, viscosity and electrical conductivity were measured over the 30 to 90ºC temperature range. The temperature dependences of the measured properties were established and discussed.

Keywords: Ionic liquids; deep eutectic solvents; density; viscosity; electrical conductivity; quaternary ammonium salt; choline chloride; oxalic acid; ethylene glycol; triethanolamine

INTRODUCTION

Ionic liquids (ILs) are defined as liquids which consist solely of cations and anions and which by definition must have a melting point of 100ºC or below. Ionic liquids have properties that make them ideal for metal electrowinning: wide potential windows, high dissolving capacity for metal salts, avoidance of water and metal/water chemistry and high conductivity compared to non-aqueous solvents. The synthesis of ionic liquids based upon quaternary ammonium salts is already demonstrated [1]. In recent years, ambient temperature ionic liquids have been studied extensively for catalytic and electrochemical purposes [2-4].

It is well known that eutectic mixtures of salts have been utilized to decrease the temperature for molten salts applications. At ambient temperature, melts consisting of organic compounds named *deep eutectic solvents* (DES) can be formed between varieties of quaternary ammonium salts with a hydrogen bond donor as amide, amine, carboxylic acid or alcohol moiety [4, 5].

These DES are low melting, conductive mixtures, in their properties similar to room temperature ionic liquids. Unlike traditional ionic liquids, these eutectic mixtures are easy to prepare in a pure state. Deep eutectic solvents are cheaper to make, much less toxic and sometimes biodegradable. It was proved that both DES and usual ionic liquids are capable of dissolving many metals and metal salts. For this reason they are used for metal electrodeposition.

The principle of obtaining these mixtures can also be applied to other hydrogen donors such as amines and alcohols, in this way some deep eutectic based ionic liquids being formed.

In the present work, we focus only on 1:1 molar ratio mixtures of choline chloride with oxalic acid, ethylene glycol and triethanolamine, respectively, in an attempt to characterize their density, viscosity and conductivity as functions of temperature.

It is already known that viscosity is of key importance to the design of molten salts and ionic liquids, which tend to be more viscous than molecular liquids. The fact that ionic liquids are fundamentally different from molecular liquids means that their physical properties are also qualitatively and quantitatively different from those of molecular liquids. Therefore, the necessity of measuring their densities and transport properties is obvious. We have chosen this composition (1:1) of ionic liquids in order to establish which of them has better physico-chemical properties for being used as electrolyte in metal electrodeposition from ionic liquids. It is worth mentioning that eutectic-based ionic liquids (DES) are actually mixtures of choline chloride with oxalic acid or triethanolamine only; the studied choline chloride-ethylene glycol (1:1) ionic liquid is not a deep eutectic solvent because the corresponding eutectic composition has a molar ratio of 1:2 [4].

---

* To whom all correspondence should be sent:
E-mail: virgilconstantin@yahoo.com

EXPERIMENTAL PART

Choline chloride (ChCl) or 2-hydroxy-N,N,N-trimethylethylammonium chloride is a quaternary ammonium salt (see scheme in Fig. 1) and has a melting point (mp) of 302ºC. Choline chloride is also a complex vitamin that is added as an important nutrient in poultry, pig and other animal foods. Being a hygroscopic compound, ChCl (produced by chemical companies with 99% purity, for instance) is recrystallized from absolute ethanol, filtered and dried under vacuum prior to be used.

Oxalic acid is a relatively strong organic acid and has the appearance of white crystals with a mp of 101.5ºC.

Ethylene glycol (monoethylene glycol, MEG or 1,2-ethanediol) has a mp of -12.9ºC, thus being an alcohol widely used as an automotive engine antifreeze. In its pure form, it is an odorless, colorless, syrupy, sweet tasting and toxic liquid.

Triethanolamine, is a tertiary amine with a mp of 0.5ºC. Like other amines, triethanolamine acts as a weak base due to the lone pair of electrons at the nitrogen atom. Triethanolamine can be abbreviated as TEOA, which can help to distinguish it from triethylamine.
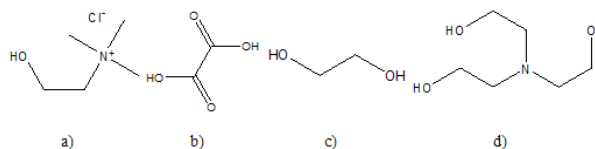

Fig. 1. Skeletal formula of DEP; a-choline chloride; b-oxalic acid; c-ethylene glycol; d-triethanolamine.

Oxalic acid anhydrous (Fluka, >97%), ethylene glycol (Fluka, >97%) and triethanolamine (Aldrich, >98%) were used as purchased. The 1:1 molar mixtures of the above substances were chosen for this study. The ionic liquids were prepared by stirring the two components at a temperature from 80 to 100ºC until a homogenous colorless liquid was formed. For all three mixtures the melting point was lower than the melting point of the components of the mixture.

The density (d), viscosity (η) and specific electrical conductivity (k), were measured by increasing and decreasing the temperature over the 30 to 80ºC temperature range in 10ºC increments for each investigated mixture and they were fitted to linear or polynomial equations.

The densities (d) were measured by the classical platinum sunker method using home-made equipment which was calibrated and tested in molten salt measurements for many years in our laboratory. The Pt sphere volume dependence on temperature was calculated according to the dependence of Pt density on temperature. Details on the employed experimental technique providing a precision of 0.2-0.3% are presented elsewhere [6-9]. This equipment was modified for ionic liquids measurements by coupling it to a temperature controller which maintained the temperature to 0.05ºC precision [10].

The viscosities (η) were measured according to [11-13] with a Cannon-Ubbelohde viscometer having a constant of 1.026. The standard deviation for ten measurements on double distilled water at 20°C, was 0.1 s. In an Ubbelohde viscometer the time that the liquid level takes to flow between two ring marks indicates the viscosity of the test fluid [11-12]. The relative standard deviation for ten measurements on double distilled water at 20°C, was $<\pm3\%$. Measurements of flow times of the liquids were performed for at least two replicates at each temperature and the results were averaged.

The electrical conductivity (κ) measurements were carried out on a multichannel WTW multi 340i conductometer and pH-meter (WTW GmbH Germany) [14] provided with a WMB 340i drill and a platinized platinum electrode. The ionic liquid was put into a glass tube (introduced in a thermostated bath) with a ground joint and the measuring cell was well sealed to prevent moisture diffusion. The precision of the conductivity measurements was ±0.5%.

RESULTS AND DISCUSSION

Density

Density is an important characteristic property of any liquid. Very limited information is known about the densities of ionic liquids and DES based on choline chloride. Density values of ChCl-urea (1:2 molar ratio), ChCl-malonic acid (1:1) and ChCl-ethylene glycol (1:2) mixtures within the temperature range from 25 to 75°C were reported recently [15]. In a previous study we presented density data of ChCl-urea (1:2), ChCl-malonic acid (1:1) and ChCl- citric acid (1:1) ionic liquids [16]. We report here the density data of the binary mixtures (1:1 molar ratio) of choline chloride with oxalic acid, ethylene glycol and triethanolamine; the values obtained for these systems are presented in Fig. 2.

As can be seen from this figure, the density d (g cm^{-3}) follows a linear dependence with temperature t (ºC) according to a first-order equation:

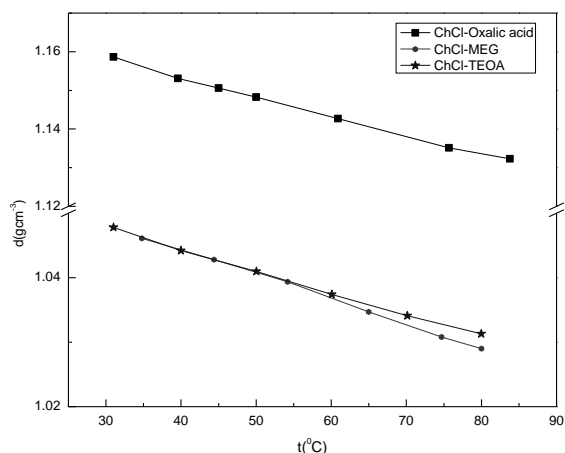$$d = a - bt \qquad (1)$$

Fig. 2. Density evolution with temperature for 1:1 m ChCl-A [A=oxalic acid, etylene glycol (MEG), triethanolamine (TEOA)] ionic liquids.

where: a and b are coefficients of the straight lines presented in Table 1.The decrease of density with increasing temperature is in a good accordance with the general evolution of both molten salts (which may be considered as high temperature ionic liquids) and ionic liquids in general [9, 14-19]. As we could not find in the literature any density data reported for these ionic liquids, we could not compare our results with those of other authors.

Viscosity

The viscosity is a parameter influencing the hydrodynamic processes in all applications of ionic liquids, for instance in electrolysis cells. Some aspects of transport phenomena in pure molten salts and ionic liquids are simpler than similar phenomena in aqueous solutions [20]. Unfortunately, there are very few data on the viscosity of ionic liquids in general and of choline chloride based ionic liquids in particular [5, 14-16, 21].

Although it was already established that the presence of water reduced the viscosity of ionic liquids [22] we did not pay attention to the quantity of water in our mixtures, as we were interested in obtaining data for a direct technological process using common available substances.

It is known that viscosity at 20-30ºC ranged between 66-1110 cP for a variety of ionic liquids

[23]. As shown in Fig. 3, the viscosities of the studied 1:1 ionic liquids, reported earlier [10], change significantly as a function of temperature. Thus, the viscosity values were found to cover the range 15-130 cP, which is in good agreement with those found for ionic liquids in general [23]. This evolution with temperature is similar to that for most of the ionic liquids reported in the literature and also with that of molten salts [5, 7, 14-17, 21].
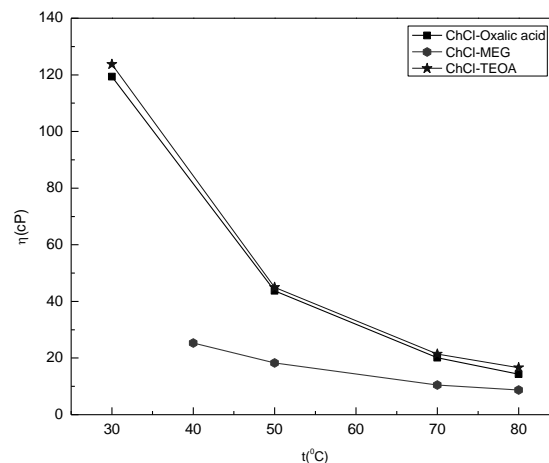

Fig. 3 Viscosity evolution with temperature for 1:1 m ChCl-A (A=oxalic acid, ethylene glycol, triethanolamine) ionic liquids.

It can be noticed that the ChCl-oxalic acid system is a low viscosity room temperature ionic liquid, whereas ChCl-ethylene glycol and ChCl-triethanolamine can be considered as high viscosity ionic liquids.

The van der Waals and hydrogen bonding interactions are believed to govern the viscosity of room-temperature ionic liquids [24]. The increase of viscosity for various ionic liquids compared to molecular solvents was attributed to enhanced van der Waals forces relative to the hydrogen bonding [25]. Regarding the influence of temperature on viscosity, the viscosity η (cP) of the studied ionic liquids is given as a polynomial temperature t (ºC) function:

$$\eta = a + bt + ct^2 \qquad (2)$$

where a, b and c are coefficients presented in Table 2.

Table 1. Constants of the equation for temperature dependence of density (g cm^{-3}) together with correlation coefficients and temperature ranges. Ionic liquids: 1:1 molar ratio choline chloride - A (oxalic acid, ethylene glycol, triethanolamine) mixtures.

System	Coefficients of Eq. (1)		Correlation Coefficient (R)	Temperature range t (ºC)
	a	b·10^4		
ChCl-oxalic acid	1.1733	4.9573	0.9986	30-90
ChCl-ethylene glycol	1.0593	3.7831	0.9991	30-80
ChCl-triethanolamine	1.0572	3.2694	0.9994	30-80

Table 2. Constants of the equation for temperature dependence of viscosity (cP), together with the correlation coefficients and the temperature ranges. Ionic liquids: 1:1 molar ratio choline chloride - A (oxalic acid, ethylene glycol, triethanolamine) mixtures.

System	Coefficients of Eq. (2)			Correlation coefficient (R)	Temperature range t (^{o}C)
	a	b	c		
ChCl-oxalic acid	305.050	7.781	0.052	0.9995	30-80
ChCl-ethylene glycol	69.281	-1.449	0.009	0.9995	40-80
ChCl-triethanolamine	319.502	-8.229	0.009	0.9995	30-80

We can describe the change in viscosity with temperature by an expression derived from an Arrhenius dependence [8]:

$$ln\eta = ln\eta_0 + E_\eta/RT \qquad (3)$$

where η_0 is a constant and E_η is the activation energy of the viscous flow.

Fig.4 shows that all data for viscosity obey well Eq. 3 (with correlation coefficients R>0.99), which points to the validity of an Arrhenius temperature dependence for all studied ionic liquids, in accordance with other literature data on deep eutectic solvents or ionic liquids [5, 14-17]. It is clear that an increase in temperature diminishes the strength of interactions between the cation and the anion and should result in lower viscosity values [25, 26]. These results suggest that slow mass-transfer processes occurring at room temperatures, due to high viscosity of ionic liquids, will be accelerated at elevated temperatures. For choline chloride-oxalic acid (1:1) mixture, the data obtained in this study are similar to the literature data [5].
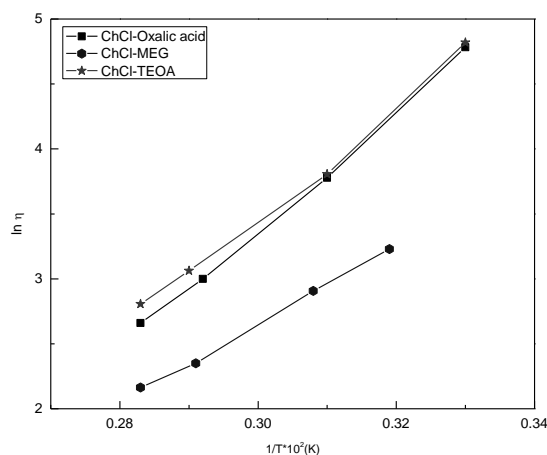

Fig. 4 Arrhenius plots of viscosity for ChCl-A (A=oxalic acid, ethylene glycol, triethanolamine) ionic liquids.

Specific electrical conductivity

The literature [3-5] indicates values of electrical conductivities for DES and common ionic liquids in the range of 0.1-14 mS cm^{-1}; of course, they should change with composition and temperature. Fig. 5 shows the plots of conductivity for the three ionic liquids studied by us in the temperature range from 30 to 80°C. It is obvious that the choline chloride-ethylene glycol mixture has the highest electrical conductivity in the studied series, whereas the choline chloride-triethanolamine system has the lowest electrical conductivity.
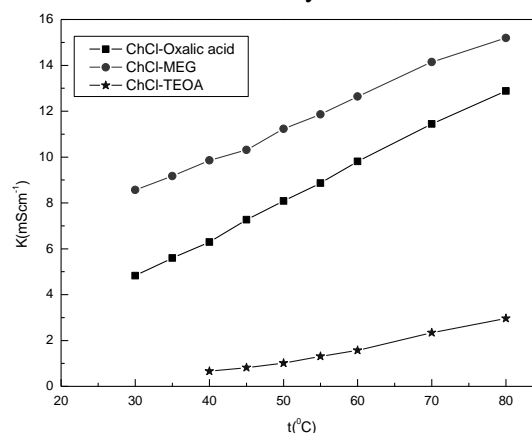

Fig. 5 Conductivity evolution with temperature for 1:1 ChCl-A (A=oxalic acid, ethylene glycol, triethanolamine) ionic liquids.

We can propose in this case a linear dependence of the specific conductivity (κ) on temperature (t ^{o}C) which is given by eq. 4:

$$\kappa = a + bt \qquad (4)$$

where a and b are the coefficients presented in Table 3 together with temperature ranges and corresponding correlation factors (R).

Table 3. Constants of the equation for temperature dependence of specific conductivity, together with correlation factors and temperature ranges for 1:1 choline chloride-A (oxalic acid, ethylene glycol, triethanolamine) mixtures.

System	Coefficients of Eq.4		Correlation factor (R)	Temperature range t (^{o}C)
	a	b		
ChCl-Oxalic Acid	-0.0334	0.1624	0.9995	30-80
ChCl-Ethylene Glycol	4.2715	0.1390	0.9992	30-80
ChCl-Triethanolamine	-1.9698	0.0611	0.9980	40-80

We can observe that the conductivity values obtained for the studied ionic liquids (ChCl-A) are similar to those for other ionic liquids reported previously [3, 5, 15, 16, 21, 27].

Analogous to the viscosity data, the electric conductivity data of ionic liquids at various temperatures were fitted according to an Arrhenius equation [26]:

$$\ln\kappa = \ln\kappa_0 - E_K/RT \qquad (5)$$

where E_K is the activation energy for electrical conduction.

Fig. 6 shows that the graphical representations for all studied ionic liquids fit Eq.5 accurately, which is in a good agreement with other conductivity data for ionic liquids [5, 15-17, 21].
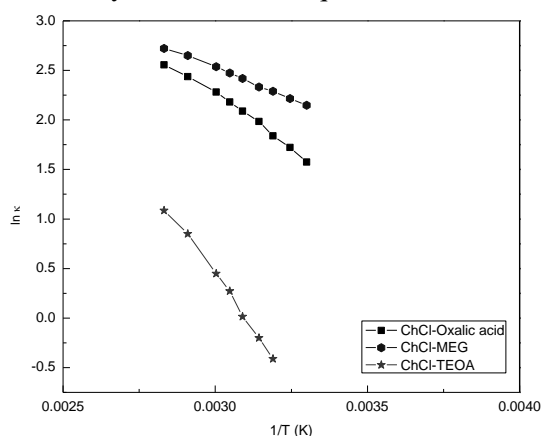

Fig. 6 Plot of log conductivity *vs.* reciprocal of absolute temperature for the DES studied.

CONCLUSIONS

The values of physical properties (density, viscosity and electrical conductivity) of three 1:1 molar mixtures of choline chloride with oxalic acid (OA), ethylene glycol (EG) and triethanolamine (TEOA), respectively, were found to be of the same order of magnitude as those of other ionic liquids and DES and are also dependent on temperature.

Both the density and viscosity of these mixtures decrease with increasing temperature, while electrical conductivity increases with temperature.

A comparison of the properties of the three studied ionic liquids leads to the following series:

$$d_{TEOA} < d_{EG} < d_{OA} \qquad (6)$$
$$\eta_{EG} < \eta_{OA} < \eta_{TA} \qquad (7)$$
$$\kappa_{TEOA} < \kappa_{OA} < \kappa_{EG} \qquad (8)$$

Obviously, the choline chloride-ethylene glycol system is the most suitable one for electrochemical purposes. It seems, however, not to be proper as an electrolyte because of its high viscosity and low electrical conductivity. The system choline chloride-oxalic acid is an intermediate electrolyte

proposed for electrodeposition and may be advantageous, despite its relatively high density and viscosity.

We mention once again that some of these data are obtained for the first time experimentally as they have not yet been reported in any of the literature consulted.

REFERENCES

1. A. P. Abbott, G. Capper, D. L. Davies, R. Rasheed, *Inorg. Chem.,* **43**, 3447 (2004).
2. J. Dupont, R. F. de Souza, P. A. Z. Suarez, *Chem. Rev.,* **102**, 3667 (2002).
3. P. Wasserscheid and P. Welton eds., Ionic Liquids in Synthesis, Wiley-VCH Verlag, Weinheim, 2003.
4. F. Endres, A. P. Abbott, D. R Mac Farlane eds., Electrodeposition from Ionic Liquids, Wiley-VCH Verlag, Weinheim, 2008.
5. A. P. Abbott, D. Boothby, G. Capper, D. L. Davies, R. Rasheed, *J. Am. Chem. Soc.,* **126**, 9142 (2004).
6. I. Murgulescu, S. Zuca, *Rev. Roum. Chim.,* **4**, 227 (1959).
7. A. M. Popescu, BS chemistry thesis-Viscosity of molten alkaly fluoride, Bucharest, Romania, 1977.
8. S. Zuca, R. Borcan, *Rev. Roum. Chim.,* **15**, 1681 (1970).
9. A. M. Popescu, *Rev. Roum. Chim.,* **44**, 765 (1999).
10. A. M. Popescu, V. Constantin, M. Olteanu, A. Baran, A. Iovescu, M. Dutu, R. Dumitrache, in: *International Conference of Physical Chemistry-ROMPHYSCHEM 13, 3-5 Sept. 2008, Bucharest, Romania, S5, Book of abstracts, p.101.*
11. A. M. James, Practical Physical Chemistry, 2nd ed., J. & A. Churchill Ltd, London, Chap. 5.2, 1967, p. 79.
12. Determination of kinematic viscosity using the Ubbelohde viscometer, DIN 51562-1, 1999.
13. Glass Capillary Kinematic Viscometers-Specifications and Operating Instructions, ISO 3105, 1994.
14. A. M. Popescu, V. Constantin, *Chem. Res. Chinese U.,* **30**, 119 (2014).
15. O. Ciocirlan, O. Iulian, O. Croitoru, *Rev. Chim. (Bucharest),* **61**, 721 (2010).
16. A. M. Popescu, V. Constantin, A. Florea, A. Baran, *Rev. Chim. (Bucharest),* **62**, 531 (2011).
17. Y. Geng, S. Chen, W. Tengfang, Y. Dahong, P. Changjun, L. Honglai, H. Ying, *J. Molec. Liq.,* **143**, 100 (2008).
18. M. Olteanu, R. Borcan, M. Constantinescu, S. Zuca, *Rev. Roum. Chim.,* **39**, 673 (1994).

19. J. Jacquemin, P. Husson, A. A. H. Padua, V. Majer, *Green Chem.*, **8**, 172 (2006).
20. J. O'M Bockris, A. R. Reddy, Modern Electrochemistry, 1st ed., Plenum Press, NY, 1970, 1, Chapter 6.
21. A. P. Abbott, G. Capper, D. L. Davies, R. Rasheed, V. Tambyrajah, *Chem. Commun.,* **1**, 70 (2003).
22. K. R. Seddon, S. Annegret, M. J. Tores, *Pure Appl .Chem.*, **72**, 2275 (2000).
23. W. M. Reichert, *Green Chemistry,* **3**, 156 (2001).

24. P. Bonhote, A. P. Dias, N. Papageorgiou, K. Kalyanasundaram, M. Gratzel, *Inorg. Chem.,* **35**, 1168 (1996).
25. J. G. Huddleston, A. E. Visser, W. M. Reichert, H. D. Willauer, G. A. Broker, R. D. Rogers, *Green Chem.*, **3**, 156 (2001).
26. A. G. Fadeev, M. M. Meager, *Chem. Commun.,* **3**, 295 (2001).
27. P. Wasserscheid, T. Welton, *Angew. Chem. Int. Ed.,* **39**, 3272 (2000).
28. J. O'M Bockris, E. H. Crook, H. Bloom, N. E. Richards, *Proc. R. Soc.,* A255, 558 (1960).

ПЛЪТНОСТ, ВИСКОЗИТЕТ И ЕЛЕКТРОПРОВОДНОСТ НА ТРИ ЙОННИ ТЕЧНОСТИ НА ОСНОВАТА НА ХОЛИН-ХЛОРИД

А.-М. Попеску, К. Донат, В. Константин*

Лаборатория по солеви стопилки, Институт по физикохимич „Илие Мургулеску", Румънска академия, Букурещ, Румъния

(Резюме)

Получени са три йонни течности, представляващи бинарни смеси от 2-хидрокси-N,N,N-триметил-етил-амониев хлорид (наричан още холин-хлорид, ChCl) с оксалова киселина, етиленгликол и триетаноламин. Приготвени са смеси в моларно отношение 1:1 между компонените, представляващи бистри и безцветни течности при стайна температура. Техните плътности, вискозитет и електропроводност са измерени при температури в интервала 30 до 90ºC. Обсъдени са температурните зависимости на измерените характеристики.

Poly (4-vinylpyridinium tribromide): an efficient catalyst for the synthesis of 1,1-diacetates from aldehydes

M. Hajjami*, A. Ghorbani-Choghamarani, M. Norouzi

Department of Chemistry, Faculty of Science, Ilam University, P.O. Box 69315516, Ilam, Iran

Poly(4-vinylpyridinium tribromide) is an excellent catalyst for the protection of aldehydes as 1,1-diacetate derivatives, by using acetic anhydride under solvent-free conditions. This method has some advantages such as mild reaction conditions, good to excellent yields and use of non metallic catalyst.

Keywords: 1,1-Diacetate; Poly(4-vinylpyridinium tribromide); Acetic anhydride; Aldehyde; Acylal.

INTRODUCTION

1,1-diacetates are some of the essential carbonyl protecting groups because of their stability in neutral and basic media [1]. Diacetates of α,β-unsaturated aldehydes are important starting materials for synthesis of dienes in Diels–Alder reactions [2,3]; they are also useful intermediates in various transformations [4]. Moreover, acylals can be converted into other functional groups by reaction with suitable nucleophiles [5,6].

In the literature, many methods are reported for the preparation of 1,1-diacetates from aldehydes using acetic anhydride and various catalysts [7-8]. The catalysts have been used for these protection reactions to improve yields, reaction times and temperature. Some of the reported catalysts for the preparation of 1,1-diacetates from aldehydes and acetic anhydride include FeF_3 [9], 1,3-dibromo-5,5-dimethylhydantoin [10], $FeCl_3$-SiO_2 [11], PVC-$FeCl_3$ [12], $SnCl_4$-SiO_2 [13], amberlyst-15 [14], $Zr(SO_4)_2.4H_2O$-SiO_2 [15], P_2O_5-SiO_2 [16], $H_3PW_{12}O_{40}$ [17], N-bromosuccinimide [18], $Zr(HSO_4)_4$ [19], etc. Some of these reported methods suffer from at least one of the following drawbacks: reactions under oxidizing conditions, use of halogenated solvents, long reaction times, and high toxicity.

Polymer supported reagents used as catalysts have acquired wide interest in recent years [20-24] because of the ease of work-up and product purification and minimized environmental damages. Herein we report poly(4-vinylpyridinium tribromide) catalyzed rapid and mild synthesis of 1,1-diacetates from aldehydes under solvent free conditions.

RESULTS AND DISCUSSION

In continuation of our studies on the application of poly(4-vinylpyridinium tribromide) in organic reactions [25-27], we have found that the combination of acetic anhydride as acylating agent and catalytic amount of poly(4-vinylpyridinium tribromide) could be an efficient protocol for conversion of aldehydes into their corresponding 1,1-diacetates.

Initially, to find out an appropriate solvent, the reaction of 4-chlorobenzaldehyde was performed in different solvents, the results of which are summarized in Table 1. It was observed that solvent-free conditions are best for the synthesis of acylals. Therefore, we report a convenient method for the effective conversion of aldehydes to their corresponding 1,1-diacetates by using Ac_2O and catalytic amount of PVP-Br_3 under solvent-free conditions, as depicted in Scheme 1.
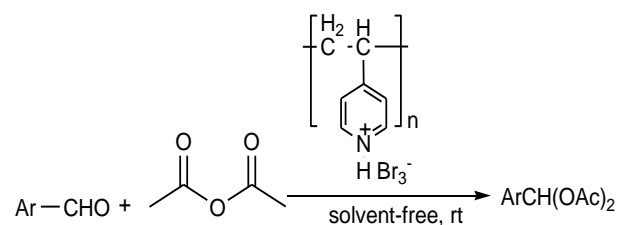
Scheme 1. Conversion of aldehydes to 1,1-diacetates

---

* To whom all correspondence should be sent:
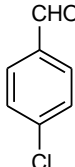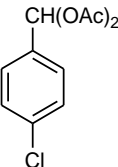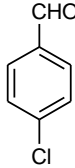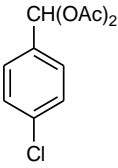E-mail: mHajjami@yahoo.com
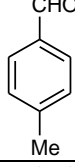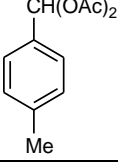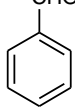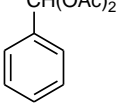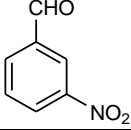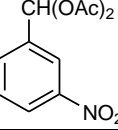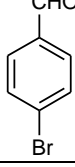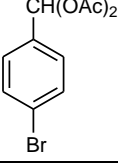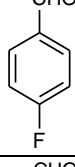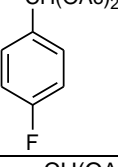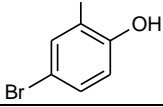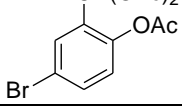
Table 1: Optimization of solvent for the synthesis of 4-chlorobenzene aldehyde 1,1-diacetate by acetic anhydride and catalytic amount of poly(4-vinylpyridinium tribromide) at room temprature.[a]

Entry	Solvent	Time (h)	Yield (%)[b]
1	Ethylacetate	24	35
2	Chloroform	24	51
3	Dichloromethane	24	32
4	Acetonitrile	24	27
5	n-Hexane	24	30
6	Solvent-free	105 min	93[c]

[a] reaction condition; substrate: acetic anhydride: poly(4-vinylpyridinium tribromide): solvent (1mmol: 2mmol: 0.035g: 3mL).
[b] yield isolated by short column chromatography . [c] isolated yield.

Table 2: PVP-Br$_3$-catalysed conversion of aldehydes to 1,1-diacetates with Ac$_2$O under solvent-free conditions.

Entry	Substrate	Product	Acetic anhydride (mmol)/ Catalyst (g)		Time (min)	Yield (%)[a]
1	CHO / Cl	CH(OAc)$_2$ / Cl	2	0.035	105	93
2	CHO / Cl	CH(OAc)$_2$ / Cl	2	--[b]	24 h	--[c]
3	CHO / Me	CH(OAc)$_2$ / Me	2	0.035	90	94
4	CHO	CH(OAc)$_2$	2	0.035	60	89
5	CHO / NO$_2$	CH(OAc)$_2$ / NO$_2$	2	0.035	75	70
6	CHO / Br	CH(OAc)$_2$ / Br	2	0.035	50	94
7	CHO / F	CH(OAc)$_2$ / F	2	0.035	46	91
8	CHO / OH / Br	CH(OAc)$_2$ / OAc / Br	2	0.035	47	98

[a] Isolated yield. [b] Reaction in the absence of catalyst. [c] No reaction.

The results of this study are summarized in Table 2. As shown in Table 2, various aromatic aldehydes were converted to corresponding acylals in high yields with short reaction times under solvent-free conditions. It should be noted that these acylation reactions did not proceed with the use of acetic anhydride alone even after 24 hours, and the presence of poly(4-vinylpyridinium tribromide) as catalyst is necessary. The result is presented in entry 2, Table 2.

A possible mechanism suggested for this reaction is shown in Scheme 2.
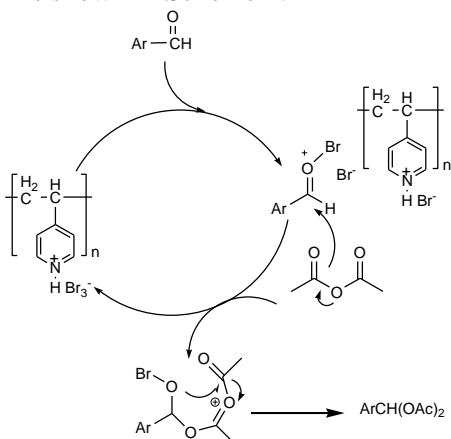
Scheme 2. Mechanism of the protection of aldehydes as 1,1-diacetates

In conclusion, herein we report a mild and efficient polymeric catalyst for the preparation of 1,1-diacetates from aldehydes in the presence of acetic anhydride under solvent-free conditions at room temperature. This method has some advantages such as rapid and inexpensive synthesis having a low environmental impact.

EXPERIMENTAL

General

Chemicals were purchased from Fluka, Merck and Aldrich chemical companies. The products were characterized by comparison of their spectral (^{1}H NMR, and ^{13}C NMR) and physical data with those of authentic samples.

Preparation of poly(4-vinylpyridinium tribromide)

In a 50 mL round-bottomed flask, 1 mL of HBr (47%) and 1.85 g of poly(4-vinylpyridine) were stirred for 1 h, then kept at 50 ºC for 24 h to obtain dry poly(4-vinylpyridinium bromide). In the next step 1.2 mL of Br_2 was added to the resulting powder; this mixture was stirred for 2 h and an orange crystalline solid, poly(4-vinylpyridinium tribromide), was quantitatively obtained (Scheme 3) [18].

General procedure for the protection of aldehydes

A mixture of aldehyde (1 mmol), acetic anhydride (2 mL) and poly(4-vinylpyridinium tribromide) (0.035 g) was stirred under solvent-free conditions at room temperature (the progress of the reaction was monitored by TLC). After reaction completion, the reaction was quenched with water (5 mL) and then washed with 5% $NaHCO_3$ (5 mL). The product was extracted with CH_2Cl_2 (4×5 mL). After separation of the organic layer, anhydrous Na_2SO_4 (1.5 g) was added to the solution and was filtered off after 20 min. Finally, dichloromethane was evaporated and pure acylals were obtained in good yields.

Selected ^{1}H NMR and ^{13}C NMR data

4-chlorobenzene aldehyde 1,1-diacetate: ^{1}H-NMR(CDCl$_3$, 400MHz)= δ_H (ppm): 2.15 (s, 6H), 7.39 (d, J=7.6 Hz, 2H), 7.48 (d, J=8.2 Hz, 2H), 7.662 (s, 1H). ^{13}C-NMR(CDCl$_3$, 100MHz)= δ_C (ppm): 20.8, 89.1, 128.2, 128.9, 134, 135.1, 168.7.

5-bromo-2-oxyacetatebenzaldehyde 1,1-diacetate: ^{1}H-NMR(CDCl$_3$, 400MHz)= δ_H (ppm): 2.143 (s, 6H), 2.365 (s, 3H), 7.047 (d, J=8.8 Hz, 1H), 7.568 (d, J=8.8 Hz, 1H), 7.788 (d, J=2.4 Hz, 1H), 7.876 (s, 1H). ^{13}C-NMR(CDCl$_3$, 100MHz)= δ_C (ppm): 20.7, 20.8, 84.4, 119.3, 124.9, 129.8, 130.9, 133.7, 147.2, 168.3, 169.1.
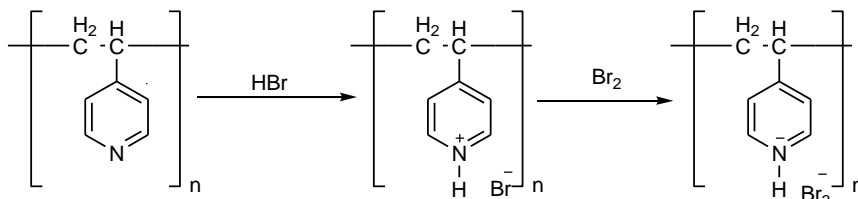
Scheme 3. Preparation of poly(4-vinylpyridinium tribromide)

REFERENCES

1. K.S. Kochhar, B.S. Bal, R.P. Deshpande, S.N. Rajadyaksha, H.W. Pinnick, *J. Org. Chem.*, **48,** 1765 (1983).
2. B.B. Snider, S.G. Amin, *Synth. Commun.*, **8**, 117 (1978).
3. G. Saucy, R. Marbet, H. Lindlar, O. Isler, *Helv. Chim. Acta.*, **42**, 1945 (1959).
4. H. Tani, K. Masumoto, T. Inamasu, H. Suzuki, *Tetrahedron Lett.*, **32**, 2039 (1991).
5. J.S. Yadav, V.B. Subba Reddy, P. Shrihari, *Synlett*, 673 (2001).
6. M. Sandberg, L.K. Sydness, *Tetrahedron Lett.*, **39**, 6361 (1998).
7. F. Shirini, M. Mamaghani, T. Mostashari, M. Abedini, *Bull. Korean Chem. Soc.*, **31**, 2399 (2010).
8. F. Shirini, S. Akbari-Dadamahaleh, A. Mohammad-Khah, *J. Catal. Chem.*, **363**, 10 (2012).
9. V.T. Kamble, R.A. Tayade, B.S. Davane, K.R. Kadam, *Aust. J. Chem.*, **60,** 590 (2007).
10. D. Azarifar, H. Ghasemnejad, F. Ramezanianlehmali, *Mendeleev Commun.*, **15**, 209 (2005).
11. C. Wang, M. Li, *Synth. Commun.*, **32,** 3469 (2002).
12. Y.Q. Li, *Synth. Commun.*, **30**, 3913 (2000).
13. Y.Q. Li, L.H. Cheng, *Chin. Chem. Lett.*, 12, 565 (2001).
14. A. Vijender Reddy, K. Ravinder, V.L. Niranjan Reddy, V. Ravikanth, Y. Venkateswarlu, *Synth. Commun.*, **33**, 1531 (2003).
15. T. Jin, G. Feng, M. Yang, T. Li, *Synth. Commun.*, **34**, 1645 (2004).
16. B.F. Mirjalili, M.A. Zolfigol, A. Bamoniri, *Phosphorus, Sulfur, and Silicon*, **179**, 19 (2004).
17. J.R. Satam, R.V. Jayaram, *Synth. Commun.*, **38**, 595 (2008).
18. B. Karimi, H. Seradj, G.R. Ebrahimian, *Synlett*, 623 (2000).
19. B.F. Mirjalili, M.A. Zolfigol, A. Bamoniri, N. Sheikhan, *J. Chin. Chem. Soc.*, **53**, 955 (2006).
20. N.G. Khaligh, F. Shirini, *J. Catal. Chem.*, **348**, 20 (2011).
21. F. Shirini, O.G. Jolodar, *J. Catal. Chem.*, **356**, 69 (2012).
22. H. Firouzabadi, N. Iranpoor, H.R. Shaterian, *Bull. Korean Chem. Soc.*, **75**, 2195 (2002).
23. H. Firouzabadi, N. Iranpoor, F. Nowrouzi, K. Amani, *Tetrahedron Lett.*, **44**, 3951 (2003).
24. H. Firouzabadi, N. Iranpoor, S. Farahi, *Scientia Iranica*, **15**, 413 (2008).
25. A. Ghorbani-Choghamarani, M.A. Zolfigol, M. Hajjami, K. Darvishi, L. Gholamnia, *Collect. Czech. Chem. Commun.*, **75**, 607 (2010).
26. A. Ghorbani-Choghamarani, M. Norouzi, *Bull. Korean Chem. Soc.*, **32**, 1399 (2011).
27. A. Ghorbani-Choghamarani, M. Nikoorazm, H. Goudarziafshar, M. Abbasi, Bull. Korean Chem. Soc., 32, 693 (2011).

ПОЛИ (4-ВИНИЛПИРИДИН ТРИБРОМИД): ЕФЕКТИВЕН КАТАЛИЗАТОР ЗА СИНТЕЗАТА НА 1,1-ДИАЦЕТАТИ ОТ АЛДЕХИДИ

М. Хаджами, А. Горбани-Чогамарани, М. Норузи

Департамент по химия. Научен факултет, Университет Илам, Иран

(Резюме)

Поли (4-винилпиридин трибромид)-ът е отличен катализатор за защита на алдехиди като 1,1-диацетат'ови производни с помощта на оцетен анхидрид в отсъствие на разтворител. Методът има предимства: меки реакционни условия, добри до отлични добиви и използване на неметален катализатор.

The edge version of MEC index of one-pentagonal carbon nanocones

A. Nejati, M. Alaeiyan[*]

Department of Mathematics, College of Basic Sciences, Karaj Branch, Islamic Azad University, Alborz, Iran

Let G be a molecular graph, the edge modified eccentric connectivity index of G is defined as $\Lambda_e(G) = \sum_{f \in E(G)} S_f \cdot ecc(f)$, where S_f is the sum of the degrees of neighborhoods of an edge f and ecc(f) is its eccentricity. In this paper an exact formula for the edge modified eccentric connectivity index of one-pentagonal carbon nanocones was computed.

Keywords: edge modified eccentric connectivity index, carbon nanocones, eccentricity

INTRODUCTION

Molecular descriptors are playing significant role in chemistry, pharmacology, etc. Among them, topological indices have a prominent place [15]. There are numerous topological descriptors that have found some applications in theoretical chemistry, especially in QSPR/QSAR research.

More recently, a new topological index, *eccentric connectivity index*, has been investigated. This topological model has been shown to give a high degree of predictability of pharmaceutical properties, and may provide leads for the development of safe and potent anti-HIV compounds. We encourage the reader to consult papers [1–9] for some applications and papers [10–14] for the mathematical properties of this topological index.

One-pentagonal carbon nanocones, Fig. 1, were originally discovered by Ge and Sattler in 1994 [17]. These are constructed from a graphene sheet by removing a 60° wedge and joining the edges thus producing a cone with a single pentagonal defect at the apex. One-pentagonal carbon nanocones consist of one pentagone, its core surrounded by layers of hexagons. If there are *n* layers, then the graph of this molecule is denoted by $G = \mathrm{CNC}_5[n]$.

Now, we introduce some notation and terminology. Let G be a graph with vertex set $V(G)$ and edge set $E(G)$. Let $deg(v)$ denote the degree of the vertex *v* in *G*. If $deg(v) = 1$, then *v* is said to be a *pendent vertex*. An edge incident to a pendent vertex is said to be a *pendent edge*. For two vertices *u* and *v* in $V(G)$, we denote by $d(u,v)$ the distance between *u* and *v*, i.e., the length of the shortest path connecting *u* and *v*. The *eccentricity* of a vertex *v* in $V(G)$, denoted by $ecc(v)$, is defined as

$$ecc(v) = \max\{d(u,v) \mid u \in V(G)\}$$

The *diameter* of a graph G is then defined to be $\max\{ecc(v) \mid v \in V(G)\}$. The *eccentric connectivity index*, $\xi^c(G)$, of a graph G is defined as

$$\xi^c(G) = \sum_{v \in V(G)} \deg(v) \cdot ecc(v)$$

The *modified eccentric connectivity index* of G is defined as $\Lambda(G) = \sum_{v \in V(G)} S_v \cdot ecc(v)$, where S_v is the sum of the degrees of neighborhoods of an edge *f* and $ecc(f)$ is its eccentricity.

Let $f = uv$ be an edge in $E(G)$. Then the degree of the edge *f* is defined as $\deg(u) + \deg(v) - 2$. For two edges $f_1 = u_1 v_1$, $f_1 = u_2 v_2$ in $E(G)$, the distance between f_1 and f_2, denoted by $d(f_1, f_2)$, is defined to be

$$d(f_1, f_2) = \min\{d(u_1, u_2), d(u_1, v_2), d(v_1, u_2), d(v_1, v_2)\}$$

The *eccentricity* of an edge *f*, denoted by $ecc(f)$, is defined as

$$ecc(f) = \max\{d(f,e) \mid e \in E(G)\}$$

The *edge eccentric connectivity index* of G [16], denoted by $\xi_e^c(G)$, is defined as

$$\xi_e^c(G) = \sum_{f \in E(G)} \deg(f) \cdot ecc(f)$$

Also the *edge modified eccentric connectivity index* of G is defined as $\Lambda_e(G) = \sum_{f \in E(G)} S_f \cdot ecc(f)$, where S_f is the sum of the degrees of neighborhoods of an edge *f* and

* To whom all correspondence should be sent:
E-mail: alaeiyan@iust.ac.ir

$ecc(f)$ is its eccentricity.

In this paper an exact formula for the edge modified eccentric connectivity index of one-pentagonal carbon nanocones was computed.

RESULTS AND DISCUSSION

Let $C[n] = CNC_5[n]$. In the following lemma, the maximum and minimum edge eccentric connectivity of C[n] is computed.
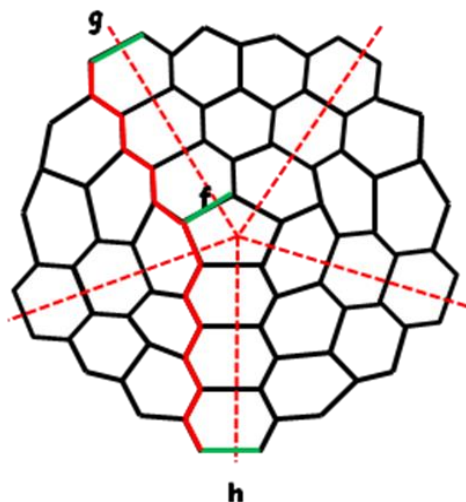

Fig. 1 A maximum and minimum path for computing eccentricity in CNC5[3]
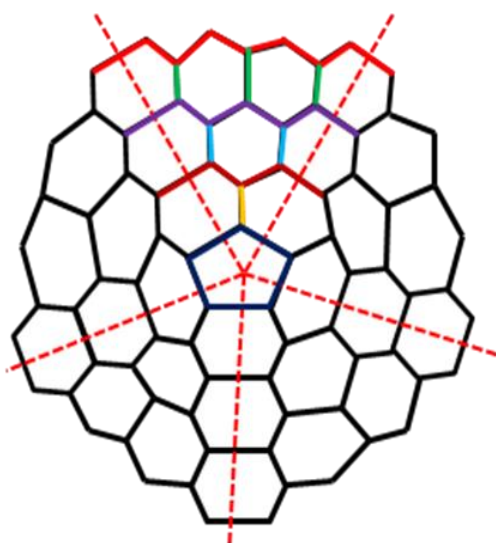

Fig. 2 The edges set with same eccentric connectivity for one section in CNC5[3]

Lemma 1. For any edge f in $E(C[n])$, we have
$$Max(ecc(f)) = 4n+1 ,$$
$$Min(ecc(f)) = 2n+1 .$$

Proof. Suppose f is an edge of the central pentagon of $C[n]$. Then from Fig. 1, one can see that there exists an edge g of degree 2 such that $d(f, g) = 2n$ and there exists another edge h of

degree 2 such that $d(f, h) = 2n+1$. Therefore, the shortest path with maximum length is connecting two edges of degree 2 in C[n] and thus the proof is completed.

In the following theorem we compute the edge eccentric connectivity index of C[n].

Theorem 1. The edge modified eccentric connectivity index of C[n] is computed as
$$\Lambda_e(C[n]) = 400n^3 + 520n^2 + 180n + 20 .$$

Proof. Considering Figs. 1 and 2, it can be seen that we have 10n+5 numbers of edges with maximum eccentric connectivity, such as 5 numbers of edges type 1, 10 numbers of edges type 2 and 10n-10 numbers of edges type 3. Also 5n numbers of edges type 4 with eccentric connectivity of 4n, 10n-5 numbers of edges type 5 with eccentric connectivity of 4n-1, and so it continues until we have five edges of type 2n+2 with eccentric connectivity of 2n+2 and five edges of type 2n+3 with minimum eccentric connectivity of 2n+1. It is easy to check that the sum of the degrees of neighborhoods of five edges of maximum eccentric connectivity is 6. The sum of the degrees of neighborhoods of 10 edges of maximum eccentric connectivity is 9 and the sum of the degrees of neighborhoods of 10n-10 edges of maximum eccentric connectivity is 10. Also the sum of the degrees of neighborhoods of 5n edges of type 4 is 14. On the other hand, the sum of the degrees of neighborhoods of other types of edges is 16. (See Table 1).

Table 1. Types of edges for C[n]

Types of edges	Num	Ecc	S_f
1	5	4n+1	6
2	10	4n+1	9
3	10n-10	4n+1	10
4	5n	4n	14
5	10n-5	4n-1	16
6	5n-5	4n-2	16
7	10n-15	4n-3	16
8	5n-10	4n-4	16
9	10n-25	4n-5	16
...	...	...	...
2n	10	2n+4	16
2n+1	15	2n+3	16
2n+2	5	2n+2	16
2n+3	5	2n+1	16

This implies that
$$\Lambda_e(C[n]) = \sum_{f \in E(C[n])} S_f \cdot ecc(f)$$

463

$$= 5 \times 6 \times (4n+1) + 10 \times 9 \times (4n+1)$$
$$+ (10n-10) \times 10 \times (4n+1) + 5n \times 14 \times 4n$$
$$+ 16 \sum_{k=1}^{n} (10n-10k+5)(4n-2k+1)$$
$$+ 16 \sum_{k=1}^{n-1} (5n-5k)(4n-2k).$$

Therefore,

$$\Lambda_e(C[n]) = 400n^3 + 520n^2 + 180n + 20.$$

Thus, this proof is completed.

REFERENCES

1. H. Dureja, A.K. Madan, *J. Mol. Model.*, **11,** 525 (2005).
2. H. Dureja, A.K. Madan, *Int. J. Pharm.*, **323,** 27 (2006).
3. H. Dureja, A.K. Madan, *Chem. Biol. Drug Des.*, **73,** 258 (2009).
4. V. Kumar, A.K. Madan, *J. Math. Chem.*, **39,** 511 (2006).
5. V. Kumar, A.K. Madan, *J. Math. Chem.*, **42,** 925 (2007).
6. V. Lather, A.K. Madan, *Croat. Chem. Acta*, **78,** 55 (2005).
7. S. Sardana, A.K. Madan, *MATCH Commun. Math. Comput. Chem.*, **43,** 85 (2001).
8. S. Sardana, A.K. Madan, *MATCH Commun. Math. Comput. Chem.*, **45,** 35 (2002).
9. V. Sharma, R. Goswami, A.K. Madan, *J. Chem. Inf. Model.*, **37,** 273 (1997).
10. M.J. Morgan, S. Mukwembi, H.C. Swart, *Disc. Math.*, (2010); doi:10.1016/j.disc.2009.12.013.
11. A. Ilic, I. Gutman, *MATCH Commun. Math. Comput. Chem.*, **65,** 731 (2011).
12. X. Xu, The eccentric connectivity index of trees of given order and matching number (Submitted for publication).
13. B. Zhou, *MATCH Commun. Math. Comput. Chem.*, **63,** 181 (2010).
14. A.R. Ashrafi, T. Doslic, M. Saheli, *MATCH Commun. Math. Comput. Chem.*, **65,** 221 (2011).
15. R. Todeschini, V. Consonni, Handbook of Molecular Descriptors (Wiley-VCH, Weinheim, 2000)
16. X. Xu, Y. Guo, *Int. Math. Forum*, **7**, 273 (2012).
17. M. Ge, K. Sattler, *Chem. Phys. Lett.,* **220**, 192 (1994).

РЕБРЕНО МОДИФИЦИРАН ИНДЕКС НА ЕКСЦЕНТРИЧНА СВЪРЗАНОСТ НА ЕДНО-ПЕНТАГОНАЛЕН НАНОКОНУС

А. Неджати, М. Алаеян*

Департамент по математика, Колеж по основни науки, клон Карадж, Ислямски университет „Азад", Алборз, Иран

(Резюме)

Нека G е молекулярен граф. Ребрено модифицираният индекс на ексцентрична свързаност на G се дефинира с $\Lambda_e(G) = \sum_{f \in E(G)} S_f \cdot ecc(f)$, където S_f е сумата от степените на съседство на реброто f и ecc(f) е неговата ексцентричност. В тази статия е намерена точна формула за ребрено модифициран индекс на ексцентрична свързаност на едно-пентагонален въглероден наноконус.

Lipid composition of flaxseeds

O. T. Teneva[1], M. D. Zlatanov[1*], G. A. Antova[1], M. Y. Angelova-Romova[1], M. P. Marcheva[2]

[1]*Department of Chemical Technology, Plovdiv University "Paisii Hilendarski", Plovdiv, Bulgaria;*

[2]*Agricultural University, Plovdiv, Bulgaria*

The content and composition of glyceride oil of four genotypes of flaxseeds (A900013, A900015, A900017 and A900018) were investigated with a view to their application as food or as a source of oil for technical and pharmaceutical purposes. The flaxseeds contain 34.2 %, 39.1 %, 37.2 % and 44.4 % glyceride oil, respectively. The content of phospholipids, mainly phosphatidylcholine, phosphatidylinositol and phosphatidylethanolamine of the four varieties was 0.9 %, 0.8 %, 1.0 % and 0.6 %, respectively. The total amounts of sterols were found to be 0.2 - 0.3 % in all oils. β-Sitosterol predominated (more than 55.0 %), followed by campesterol (13.1 - 26.1 %) and stigmasterol (3.4 - 15.0 %). In the tocopherol fraction analyzed by high performance liquid chromatography γ-tocopherol predominated (766 mg/kg, 770 mg/kg, 775 mg/kg and 602 mg/kg, respectively), followed by γ-tocotrienol. In the triacylglycerols linolenic acid predominated (37.6 %, 33.5 %, 42.9 % and 45.8 %, respectively), followed by oleic and linoleic acids. Higher quantities of palmitic and oleic acids were established in the phospholipids and the sterol esters than in the triacylglycerols.

Keywords: flaxseed glyceride oil, fatty acids, phospholipids, sterols, tocopherols.

INTRODUCTION

The plant linen (flax) *Linum usitatissimum* L., fam. Linaceae has been cultivated as a source of fibers and glyceride oil since antiquity in West Asia and the Mediterranean. The flaxseeds are the richest ones in glyceride oil which has been used as food, for medicinal purposes to treat inflammatory and vascular problems, for manufacturing of paints, linoleum, varnishes, etc. [1 - 3]. The oil contains polyunsaturated fatty acids, as linolenic (ω - 3) and linoleic (ω - 6) acid. The beneficial effect of flaxseed oil on coronary heart disease, tumours, hormonal diseases and the usage of the oil as a food supplement is due to linolenic acid [1, 4 – 8, 11].

The content of oil in the seeds is about 40.0 % according to several reports [2, 9, 10, 12]. The fatty acid profile varies depending on the conditions of growth. In the triacylglycerol fraction, predominant is the α-linolenic acid (50.0 - 60.0 % according to [2, 3, 8, 11, 13 – 19, 21], 30.0 - 50.0 % according to El-Beltagi *et al.* [1], Herchi *et al.* [20]). Other major components are the oleic acid (about 30.0 %) and the linoleic acid (10.0 - 20.0 %). The oil contains relatively low quantities of saturated palmitic acid (5.0 - 7.0 %) and stearic acid (3.0 - 6.0%) [1 - 3, 13, 15, 17 - 21].

Besides triacylglycerols, other micro components, such as phospholipids, sterols and tocopherols, are of great significance for estimating the food value of the flaxseed oil.

Sterols are present in the oil in a relatively lower amount (about 0.2 - 0.4%) [19, 22]. β-Sitosterol is the main component (more than 50.0 %), followed by campesterol, stigmasterol and Δ^5- avenasterol [3, 12].

The total content of phospholipids, mainly phosphatidylcholine, phosphatidylinositol and phosphatidylethanolamine was found to be 1.0 - 1.5 % [19].

According to Przybylski [3], Bozan and Temelli [16], and Gunstone [22], the total amount of tocopherols in the oil was found to be 300 - 700 mg/kg. γ-Tocopherol predominates in the tocopherol fraction (more than 70.0 %), α-tocopherol and γ-tocotrienol are also detected.

In the present investigation we have attempted to characterize the composition of seeds, the fatty acid composition of triacylglycerols; the main individual phospholipids and sterol esters; the content and composition of sterols, phospholipids, tocopherols, free and esterified sterols of glyceride oils recovered from seeds of four Bulgarian flax genotypes with a view to their implementation in breeding programs focused on the usage of flax seeds as a source of food oil, as well as for technical and pharmaceutical purposes.

---

* To whom all correspondence should be sent:
E-mail: magzlat@uni-plovdiv.bg

MATERIALS AND METHODS

All solvents and reagents were of analytical grade and were used without additional purification. Reference phospholipids and fatty acid methyl esters were purchased from Fluka (Chemie Gmbh, Switzerland). Reference tocopherol isomers and individual sterols were purchased from Merck (Darmstadt, Germany). Thin-layer chromatography (TLC) plates were prepared in the laboratory using silica gel 60 G (Merck, Darmstadt, Germany).

Samples. Four genotypes of *Linum usitatissimum* L. - *A900013* - var. *elatum-multicaule*, *A900015* and *A900017* - var. *usitatissimum* and *A900018* - var. *caesium* were cultivated in a trial field of the IPGR Sadovo - Southern Bulgaria in 2011. The accessions are local landraces and were obtained by expeditions in Bulgaria. Characterization, evaluation and conservation were executed at the National genebank in IPGR Sadovo. They are representative for the various purposes of the plant: *A900013* may be used as primary technical crop for fibre production, *A900018* is an oil crop, *A900015* and *A900017* are intermediate species for both usages. Standard crop production system was applied.

Isolation of glyceride oil and determination of the oil content. The seeds (20 g sample) were air-dried (10 % humidity). The humidity was determined by drying at 105^0C to constant weight. Flaxseed oil was extracted from finely ground seeds with hexane in a Soxhlet apparatus for 8 h [23]. After extraction the solvent was removed in a rotary vacuum evaporator and the oil was determined by weight.

Fatty acids. Fatty acid composition of triacylglycerols and sterol esters was determined by gas chromatography (GC) of fatty acid methyl esters (FAME) [24]. FAME were prepared by pre-esterification with sulfuric acid in methanol as catalyst [25] and were purified by TLC on silica gel 60 G with mobile phase hexane : acetone = 100 : 8 (by volume). The operating conditions were as follows: GC HP 5890 gas chromatograph (Hewlett Packard GmbH, Austria) equipped with 60 m × 0.25 mm × 0.25 µm DB – 23 column (Agilent Technologies, Santa Clara CA, USA) and flame ionization detector. The temperature gradient was: 130^0C for 1 min, 130 - 170^0C at 6.5^0C/min, 170 - 215 ^{0}C at 30^0C/min, 215^0C for 9 min, 215 - 230^0C at 40^0C/min to 230^0C for 1 min. Hydrogen was the carrier gas, split 100 : 1. The temperature of detector and injector was kept at 270^0C. Identification of fatty acids was performed by comparison with a standard mixture of FAME.

Phospholipids. The phospholipid composition was determined following a previously reported procedure [26]. The air-dried seeds were subjected to Folch extraction [25]. Polar lipids were isolated from the total lipids by column chromatography. Briefly, the sample (100 mg) was applied on a 40 cm × 2 cm glass column packed with silica gel Unisil 100 - 200 mesh (Clarkson Chemicals Co., USA) and was eluted in sequence with chloroform (for neutral lipids, sterols and sterol esters), and methanol (for phospholipids). The phospholipid classes were isolated by two-dimensional thin-layer chromatography on 20 cm × 20 cm glass plates with 0.2 mm Silica gel 60 G layer impregnated with aqueous $(NH_4)_2SO_4$ (1.0 %). In the first direction the plate was developed with chloroform : methanol : ammonia, 65 : 25 : 5 and in the second – with chloroform : acetone : methanol : acetic acid : water, 50 : 20 : 10 : 10 : 5 (by volume) [27]. The individual phospholipids were detected and identified by spraying with specific reagents [25]: Dragendorff test (detection of choline-containing phospholipids); ninhydrin spray (for phospholipids with free amino groups), and Shiff's reagent (for inositol containing phospholipids). Additional identification was performed by comparing the respective R_f values with those of authentic commercial standards subjected to silica gel TLC under identical experimental conditions. The quantification was carried out spectrophotometrically against a calibration curve by measuring the phosphorus content at 700 nm after scrapping the respective phospholipid spot and mineralization of the substance with a mixture of perchloric acid and sulphuric acid, 1:1 (by volume). The calibration curve was constructed by using a standard solution of KH_2PO_4 (1 - 130 µg/ml, as phosphorus).

Sterols. The glyceride oil (sample size of 100 mg) was applied on 20 cm × 20 cm glass plates (1 mm thick silica gel G layer) and was developed with n-hexane : acetone, 100 : 8 (by volume). Free (R_f = 0.4) and esterified sterols (R_f = 0.8) were detected under UV light by spraying the edges of each plate with 2′,7′- dichlorofluorescein, they were then scraped, transferred to small glass columns and eluted with diethyl ether. The solvent was evaporated under a stream of nitrogen and the residue was weighed in a small glass container to a constant weight. Free sterols were then subjected to GC without derivatization. Sterol esters were hydrolyzed with ethanolic KOH, sterols were extracted with n-hexane and purified by TLC under the above conditions prior to GC analysis [28]. The sterol composition was determined on a HP 5890

gas chromatograph (Hewlett Packard GmbH, Austria) equipped with a 30 m × 0.25 mm DB – 5 capillary column (Agilent Technologies, Santa Clara CA, USA) and flame ionization detector. The temperature gradient varied from 90ºC (hold 2 min) up to 290ºC at a rate of 15ºC/min and then up to 310ºC at a rate of 4ºC/min (hold 10 min); the injector temperature was 300ºC and the detector temperature was 320ºC. Hydrogen was the carrier gas at a flow rate of 0.8 ml/min; split 100:1. Identification was confirmed by comparison of retention times with those of a standard mixture of sterols.

Tocopherols. High performance liquid chromatography (HPLC) on a Merck-Hitachi (Merck, Darmstadt, Germany) instrument equipped with 250 mm × 4 mm Nucleosil Si 50-5 column (Merck, Darmstadt, Germany) and fluorescent detector Merck-Hitachi F 1000 was used directly in the oil for determination of the total content and the individual composition of tocopherols [29]. The operating conditions were as follows: mobile phase of n - hexane : dioxane, 96 : 4 (by volume), flow rate 1 ml/min, excitation 295 nm, emission 330 nm. A 20 µl solution of crude oil (2.0 %) was injected. Tocopherols were identified by comparing the retention times with those of authentic individual pure tocopherols. The tocopherol content was calculated based on the tocopherol peak areas in the sample *vs.* tocopherol peak area of a standard tocopherol solution.

Statistical analysis. All analyses were made in triplicate. Statistical differences between samples were tested using ANOVA. Data were expressed as mean ± SD. The level of significance was set at $p < 0.05$.

RESULTS AND DISCUSSION

General characteristics of the seeds and oils

The content of oil in the seeds and the main lipid components are shown in Table 1.

The highest oil content (44.4 %) was found to be in the *A900018* flaxseed variety. The other studied species contain quantities close to the data reported earlier [2, 10]. The phospholipid content (0.6 - 1.0 %) and the sterol value are lower than the data reported by Piłat and Zadernowski [19] and Gunstone [22]. Tocopherol content is higher than results found in other varieties of flax seed oils excluding *A900018* where the content is the same as reported earlier [19, 22].

Fatty acid composition of triacylglycerols

Fatty acid composition of triacylglycerols is presented in Table 2.

The qualitative and quantitative composition of all investigated oils is different. The main components are linolenic, oleic and linoleic acids. The content of linolenic acid in the A900018 flaxseed oil (45.8%) is higher than that of other species at the expense of a lower level of oleic acid. This quantity is lower than the values reported by Bera et al. [15] – 50.0 - 60.0 %, but very close to the data announced earlier by El-Beltagi et al. [1], and Herchi et al. [20] – 30.0 - 50.0 %. In addition, flax oil contains 15.2 - 17.8 % of the important omega-6 linoleic acid (all cis-9,12 – C18:2), which

Table 1 Oil content in the seeds and content of biologically active compounds in glyceride oils

№	Compounds		Varieties			
			A900013	*A900015*	*A900017*	*A900018*
1	Oil content, % wt		34.2 ± 0.7	39.1 ± 0.8	37.2 ± 1.5	44.4 ± 1.3
2	Phospholipids, % wt		0.9 ± 0.01	0.8 ± 0.01	1.0 ± 0.04	0.6 ± 0.01
3	Sterols, % wt	Free Sterols	0.26 ± 0.01	0.20 ± 0.01	0.26 ± 0.01	0.14 ± 0.01
		Est. Sterols	0.07 ± 0.002	0.03 ± 0.006	0.04 ± 0.008	0.04 ± 0.008
4	Tocopherols, mg/kg		766 ± 22	770 ± 31	775 ± 31	602 ± 25
5	Triacylglycerols, % wt		98.8±1.3	99.0±1.3	98.7±1.1	99.2±1.1

Table 2. Fatty acid composition of triacylglycerols*, % wt

Fatty acids, % wt	Varieties			
	A900013	*A900015*	*A900017*	*A900018*
$C_{8:0}$	n.d.	0.1 ± 0.03	n.d.	n.d.
$C_{10:0}$	n.d.	0.1 ± 0.03	n.d.	n.d.
$C_{12:0}$	n.d.	0.1 ± 0.02	n.d.	0.1 ± 0.03
$C_{14:0}$	0.2 ± 0.04	0.1 ± 0.02	0.1 ± 0.02	0.1 ± 0.05
$C_{14:1}$	0.1 ± 0.03	n.d.	n.d.	n.d.
$C_{15:0}$	n.d.	n.d.	n.d.	n.d.
$C_{16:0}$	9.0 ± 0.3	10.4 ± 0.2	8.4 ± 0.2	7.7 ± 0.2
$C_{16:1}$	0.1 ± 0.02	0.2 ± 0.06	0.1 ± 0.04	0.1 ± 0.02
$C_{17:0}$	0.1 ± 0.04	0.1 ± 0.03	0.1 ± 0.04	0.1 ± 0.02
$C_{18:0}$	4.8 ± 0.2	5.7 ± 0.3	4.0 ± 0.1	5.5 ± 0.2
$C_{18:1}$	30.6 ± 0.6	31.6 ± 0.6	28.8 ± 0.9	24.6 ± 0.7
$C_{18:2}$	17.5 ± 0.7	17.8 ± 0.7	15.2 ± 0.6	15.6 ± 0.6
$C_{18:3}$	37.6 ± 1.1	33.5 ± 1.1	42.9 ± 0.9	45.8 ± 1.4
$C_{20:0}$	n.d.	n.d.	0.1 ± 0.03	0.2 ± 0.04
$C_{20:1}$	n.d.	n.d.	0.3 ± 0.06	0.2 ± 0.04
$C_{20:2}$	n.d.	n.d.	n.d.	n.d.
$C_{22:0}$	n.d.	0.3 ±0.02	n.d.	n.d.
SFA	14.1	16.9	12.7	13.7
MUFA	30.8	31.8	29.2	24.9
PUFA	55.1	51.3	58.1	61.4

*Average of three determinations, n.d. – not detected, SFA – saturated fatty acids, MUFA – monounsaturated fatty acids, PUFA – polyunsaturated fatty acids

increases the content of essential fatty acids to over 50.0 %. The amount of oleic acid varies in the interval 24.6 - 31.6 %. The total content of saturated fatty acids is 12.7-16.9%, mainly palmitic and stearic acids, while $C_{12:0}$, $C_{14:0}$, $C_{16:1}$, $C_{20:0}$, $C_{20:1}$, and $C_{22:0}$ were found around 0.1 - 0.3 %. The total quantity of the saturated fatty acids is also close to the literature data [1, 15]. Some differences in the triacylglycerol composition between obtained and reported data can be explained by different agricultural, mainly temperature conditions, for the cultivation of the plants.

Phospholipids

The phospholipid composition of flaxseeds is presented on Figure 1.

Phospholipids comprise the main classes typical for plant oils, with phosphatidylcholine (PC) (26.1 %, 42.8 %, 36.8 % and 35.7 %, respectively) and phosphatidylinositol (PI) (38.8 %, 35.5 %, 40.1 % and 37.5 %, respectively) as main components followed by phosphatidylethanolamine (PEA), phosphatidic acids (PA), diphosphatidylglycerol
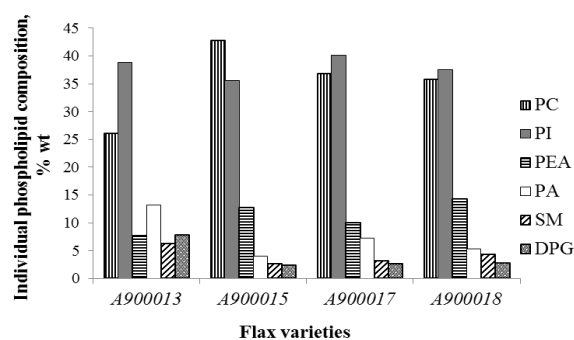

Fig.1 Phospholipid composition of flax seed oils, % wt
PC – Phosphatidylcholine; PI – Phosphatidylinositol; PEA – Phosphatidylethanolamine*;* PA – Phosphatidic acids*;* SM – Sphingomyelin*;* DPG – Diphosphatidylglycerol

and sphingomyelin. These percentages are different from the data reported earlier by Herchi *et al.* [20] where the content of phosphatidylcholine was 7.0 - 18.0 %; of phosphatidylinositol – 29.0 - 32.0 % and of phosphatidylethanolamine – 27.0 - 40.0 %.

Figure 2 presents the fatty acid composition of the individual phospholipid classes.
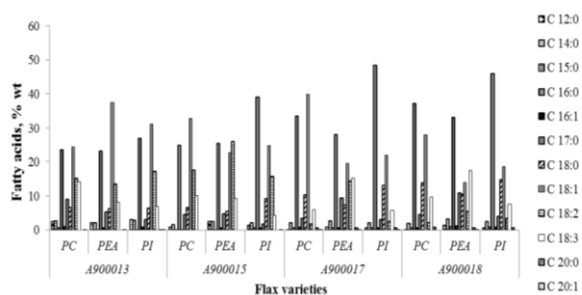
Fig. 2 Fatty acid composition of individual phospholipid classes:
PC – Phosphatidylcholine; PI – Phosphatidylinositol;
PEA – Phosphatidylethanolamine

The qualitative fatty acid profile of the separate individual phospholipids is similar, but the quantitative composition is different. Palmitic acid was found to be the main component in all phospholipid classes (23.3 - 48.5 %), followed by oleic acid (14.0 - 39.8 %). Linoleic and linolenic acids are found in relatively low contents. Highest content of saturated fatty acids, mainly palmitic and stearic was observed in phosphatidylinositol (43.5 - 69.7 %), while their values in phosphatidylcholine and phosphatidylethanolamine are relatively lower (39.1 - 59.6 % and 39.7 - 61.1 %, respectively) at the expense of a higher level of linolenic acid. Significant quantities of monounsaturated fatty acids were established in phosphatidylcholine (25.6 - 41.0 %) and of polyunsaturated fatty acids in phosphatidylethanolamine (21.7 - 35.3 %).

Sterols

Free sterols comprise more than 75.0 % of the total sterols as β-sitosterol (54.8 - 72.9 %) being the main component in all four varieties and in both free and esterified sterol fractions. Campesterol (13.1 – 26.1 %) and stigmasterol (3.4 – 15.0 %) are next main components in free sterols and sterol esters (Figure 3).
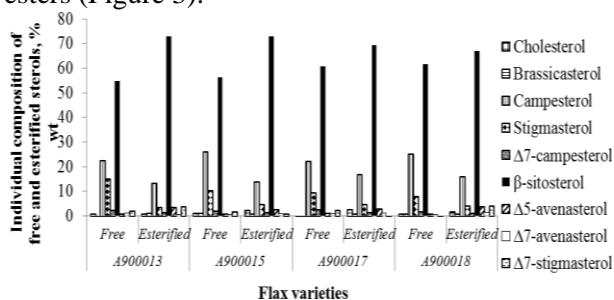

Fig. 3 Individual composition of free and esterified sterols

Free sterols and sterol esters have the same individual composition but quantitative differences between the components. Thus, the content of campesterol is higher in free sterols (22.1 - 26.1 % *vs*. 13.1 - 16.8 %) than in sterol esters. Stigmasterol also substantially predominates in free sterols (8.0 - 15.0 %) than in sterol esters (3.4 - 4.7 %). On the other hand the quantity of β-sitosterol is significantly higher in sterol esters than in the free sterol fraction (72.9 % *vs*. 54.8 %, 72.8 % *vs*. 56.3 %, 69.2 % *vs*. 60.6 % and 67.0 % *vs*. 61.5 %, respectively). In agreement with recent data for other plant oils (Herchi *et al.* [32]; Phillips *et al.* [30]; Alasalvar *et al.* [31]), minor amounts of cholesterol are detected in free and esterified sterols of all four samples and in each analyzed variety. The content of cholesterol in sterol esters is higher than in free sterols (0.8 - 2.5 % *vs*. 0.6 - 1.1 %). The presence of cholesterol is believed to be a result of the same biosynthetic pathway as that of plant sterols, i.e. *via* cycloartenol as a key intermediate.

Twelve fatty acids were identified in sterol esters (Table 3), oleic acid being the major component (43.5 %, 39.8 %, 42.7 % and 38.0 %, respectively), followed by palmitic acid (32.9 %, 34.6 %, 29.2 % and 31.3 %, respectively) and stearic acid (8.2 %, 14.9 %, 16.0 % and 20.5 %, respectively). Linolenic and linoleic acids vary between 0.3 - 1.3 % and 0.3 -1.5 %, respectively.

Tocopherols

The tocopherol composition is given in Table 4 and results show that these are represented mainly by γ-tocopherol (over 65.0 %), followed by γ-tocotrienol (~ 30.0 %) and minor amounts of α-tocopherol. These results about qualitative composition are similar to data reported earlier [3, 16], but the content of γ-tocotrienol is significantly higher than in other investigated flax seed oils.

Fatty acid composition and distribution of fatty acids between the lipid classes

Figure 4 presents the ratio of unsaturated *vs*. saturated fatty acids in each lipid class (phospholipids are presented with an average value) outlining the respective relative unsaturation (saturation) of triacylglycerols, sterol esters and phospholipids.

The picture clearly shows that among the lipid classes studied, triacylglycerols are the most highly unsaturated where the content of polyunsaturated acids was found to be more than 50.0 %, followed by monounsaturated acids – about 30.0 %.

Table 3 Fatty acid composition of esterified sterols, wt %

Fatty acids, % wt	Varieties			
	A900013	*A900015*	*A900017*	*A900018*
$C_{14:0}$	9.1 ± 0.3	3.1 ± 0.1	2.8 ± 0.2	2.2 ± 0.3
$C_{14:1}$	0.4 ± 0.01	0.4 ± 0.01	2.9 ± 0.1	1.3 ± 0.1
$C_{15:0}$	1.0 ± 0.2	0.6 ± 0.01	0.6 ± 0.01	0.6 ± 0.01
$C_{16:0}$	32.9 ± 1.3	34.6 ± 1.4	29.2 ± 0.9	31.3 ± 1.1
$C_{16:1}$	0.8 ± 0.02	0.9 ± 0.02	0.8 ± 0.02	0.5 ± 0.01
$C_{17:0}$	0.3 ± 0.01	0.5 ± 0.01	0.6 ± 0.02	0.8 ± 0.03
$C_{18:0}$	8.2 ± 0.3	14.9 ± 0.5	16.0 ± 0.5	20.5 ± 0.6
$C_{18:1}$	43.5 ± 0.9	39.8 ± 1.2	42.7 ± 1.3	38.0 ± 0.8
$C_{18:2}$	0.3 ± 0.01	1.5 ± 0.1	1.4 ± 0.4	0.5 ± 0.01
$C_{18:3}$	0.6 ± 0.01	1.3 ± 0.1	0.3 ± 0.01	0.5 ± 0.01
$C_{20:0}$	2.0 ± 0.1	1.4 ± 0.2	2.1 ± 0.2	3.1 ± 0.1
$C_{20:2}$	0.8 ± 0.02	1.0 ± 0.03	0.6 ± 0.01	0.7 ± 0.02
SFA	53.5	55.1	51.3	58.5
MUFA	45.5	41.1	46.4	39.8
PUFA	1.0	3.8	2.3	1.7

SFA – saturated fatty acids, MUFA – monounsaturated fatty acids, PUFA – polyunsaturated fatty acids

Table 4 Individual tocopherol composition of flax seed oils, % wt

Tocopherols, % wt	Varieties			
	A900013	*A900015*	*A900017*	*A900018*
α-Tocopherol	1.2 ± 0.1	1.8 ± 0.1	0.6 ± 0.1	4.8 ± 0.1
γ-Tocopherol	69.6 ± 2.1	67.6 ± 2.7	67.3 ± 1.3	68.8 ± 2.7
γ-Tocotrienol	29.2 ± 1.2	30.6 ± 0.7	32.1 ± 0.8	26.4 ± 0.6
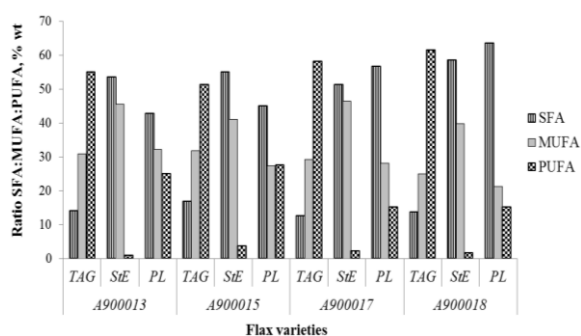
Fig. 4 Distribution of fatty acid classes in triacyglycerols, sterol esters and phospholipids
SFA – saturated fatty acids; MUFA – monounsaturated fatty acids; PUFA – polyunsaturated fatty acids; TAG – triacylglycerols; StE – sterol esters; PL – phospholipids

Monounsaturated and saturated acids predominate in the sterol ester fraction while polyunsaturated acids were detected in small quantities. The saturated fatty acids were found in high amounts (42.8 – 63.5 %) in phospholipids. The same trend was found for other oils – sunflower oil [33], walnut, hazelnut, almond oils [34], tomato seed oil [35] displaying the lipid features outlined above.

Finally, some rare or uncommon fatty acids (at amounts of approximately 1.0 %) were identified and quantified in the sterol esters and phospholipids (purified by TLC and preconcentrated prior to analysis): $C_{12:0}$, $C_{14:1}$, $C_{15:0}$ and $C_{17:0}$. Evidently, these could not be detected in the total fatty acid composition because the quantities were below the detection limits of the GC-FID system in use (note the low content of these fatty acids and the low content of sterol esters and phospholipids in the oil). These fatty acids, especially with odd chain, are considered not typical for plants and are rarely

and only recently detected when a detailed analysis of individual lipid classes has been performed. In conclusion, the quantitative fatty acid composition is specific for each phospholipid and sterol ester species in a given variety and differs between the same phospholipid species.

CONCLUSION

The lipid composition of the investigated flax seeds (oil content in the seeds, triacylglycerols, phospholipids, sterols, tocopherols in the oils) has some quantitative differences as a result of the genotype, climatic, agrometeorologic conditions, but these differences are not significant between the separate varieties and data from earlier investigations. The fatty acid composition of the separate lipid classes: triacylglycerols, phospholipids and sterols is various which is due to different stages of the biosynthesis of fatty acid and respective substances. The obtained information can be useful for estimation of the food value of the flaxseed oils with a view to future flax breeding programs.

REFERENCES

1. H. S. El-Beltagi, Z. A. Salama, D. M. El-Hariri: Evaluation of fatty acids profile and the content of some secondary metabolites in seeds of different flax cultivars (Linum Usitatissimum L.). *General and Applied Plant Physiology*, 33: 187-202 (2007).
2. W.-S. Choo, J. Birch, J.-P.Dufour: Physicochemical and quality characteristics of cold-pressed flaxseed oils. *Journal of Food Composition and Analysis*, 20: 202-211 (2007).
3. R. Przybylski: Flax Oil and High Linolenic Oils. Bailey's Industrial Oil and Fat Products, Sixth Edition, Six Volume Set. Edited by Fereidoon Shahidi. Copyright 2005 John Wiley & Sons, Inc., 281-292 (2005).
4. S. Cunnane, S. Ganguli, C. Menard, A. Liede, M. Hamadeh, Z. Chen, T. Wolever, D. Jenkins: High α-linolenic acid flaxseed (Linum usitatissimum L.): some nutritional properties in humans. *British Journal of Nutrition*, 69: 443-453 (1993).
5. S. Huang, D. Milles: Gamma-linolenic acid: Metabolism and its roles in nutrition and medicine. Champaign, IL, AOCS Press (1996).
6. S. Huang, A. Ziboh: Gamma-linolenic acid: Recent advances in biotechnology and clinical applications. Champaign, IL, AOCS Press (2001).
7. A. P. Simopoulos: The importance of the ratio of omega-6/omega-3 essential fatty acids. *Biomedicine and Pharmacotherapy*, 56: 365-379 (2002).
8. D. H. Morris: Flax – A Health and Nutrition Primer, Chapter Description and composition of flax. Flax Council of Canada (2007).
9. Y. Coskuner, E. Karababa: Some physical properties of flaxseed (Linum usitatissimum L.). *Journal of Food Engineering*, 78: 1067-1073 (2007).
10. H. S. El-Beltagi, Z. A. Salama, D. M. El-Hariri: Variations in oil and some phytochemical contents in flaxseed cultivars (Linum usitatissimum L.). *Electronic Journal of Environmental, Agricultural and Food Chemistry*, 10: 2711-2721 (2011).
11. A. N. Martinchik, A. K. Baturin, V. V. Zubtsovz., V. Y. Molofeev: Nutritional value and functional properties of flaxseed. *Voprosy Pitaniia*, 81: 4-10 (2012).
12. D. M. Kasote, Y. S. Badhe, M. V. Hegde: Effect of mechanical press oil extraction processing on quality of linseed oil. *Industrial Crops and Products*, 42: 10-13 (2013).
13. A. G. Vereshchagin, G.V. Novitskaya: The triglyceride composition of linseed oil. *Journal of the American Oil Chemists' Society*, 42: 970-974 (1965).
14. A. Overeem, G.J.H. Buisman, J.T.P. Derksen, F.P. Cuperus, L. Molhoek, W. Grisnich, C. Goemans: Seed oils rich in linolenic acid as renewable feedstock for environment - friendly crosslinkers in powder coatings. *Industrial Crops and Products*, 10: 157-165 (1999).
15. D. Bera, D. Lahiri, A. Nag: Studies on a natural antioxidant for stabilization of edible oil and comparison with synthetic antioxidants. *Journal of Food Engineering*, 74: 542-545 (2006).
16. B. Bozan, F. Temelli: Chemical composition and oxidative stability of flax, safflower and poppy seed and seed oils. *Bioresource Technology*, 99: 6354-6359 (2008).
17. F. D. Gunstone, J. L. Harwood, F. B. Padley: The lipid handbook. Chapman and Haal, London (2003).
18. K. Vijaimohan, M. Jainu, K. E. Sabitha, S. Subramaniyam, C. Anandhan, C. S. Shyamala Devi: Beneficial effects of alpha linolenic acid rich flaxseed oil on growth performance and hepatic cholesterol metabolism in high fat diet in fed rats. *Life Sciences*, 79: 448-454 (2006).
19. B. Piłat, R. Zadernowski: Physicochemical characteristics of linseed oil and flour. Polish Journal of Natural Sciences, 25: 106-113 (2010).
20. W. Herchi, F. Sakouhi, S. Boukhchina, H. Kallel, C. Pepe: Changes in fatty acids, tocochromanols, carotenoids and chlorophylls content during flaxseed development. *Journal of the American Oil Chemists' Society*, 88: 1011-1017 (2011).
21. O. N. Ciftci, R. Przybylski, M. Rudzińska: Lipid components of flax, perilla and chia seeds. *European Journal of Lipid Science and Technology,* 114: 794-800 (2012).

22. F. Gunstone: Vegetable oils in food technology: Composition, Properties and Uses. The lipid handbook, (3rd Edition): 318-320 (2002).
23. Oilseeds – Determination of oil content (Reference method). ISO 659 (2009).
24. Animal and vegetable fat and oils – Analysis by gas chromatography of methyl esters of fatty acids. ISO 5508 (1990).
25. W.-W. Christie, Lipid Analysis. The Oily Press: Bridgwater (3rd Edition), England (2003).
26. M. Zlatanov, G. Antova, M. Angelova-Romova, S. Momchilova, S. Taneva, B. Nikolova-Damyanova: Lipid Structure of Lallemantia Seed Oil: A Potential Source of Omega-3 and Omega-6 Fatty Acids for Nutritional Supplements. *Journal of the American Oil Chemists' Society*, 89: 1393-1401 (2012).
27. R. Schneiter, G. Daum: Analysis of yeast lipids, In: Yeast Protocol: Second Edition, Methods in Molecular Biology, 313, Edited by: Xiao W., Humana Press Inc., Totowa N.J. (2006).
28. Animal and vegetable fat and oils – Determination of individual and total sterols contents (Gas chromatographic method). ISO 12228 (1999).
29. Animal and vegetable fat and oils – Determination of tocopherol and tocotrienol contents by High-Performance Liquid Chromatography. ISO 9936 (2006).
30. K. M. Phillips, D. M. Ruggio, J. I. Toivo, M. A. Swank, A. H. Simpkins: Free and esterified sterol composition of edible oils and fats. *Journal of Food Composition and Analysis*, 15: 123-142 (2002).
31. C. Alasalvar, J.S. Amaral, G. Satir, F. Shahidi: Lipid characteristics and essential minerals of native Turkish hazelnut varieties (Corylus avellana L.). *Food Chemistry*, 113: 919-925 (2009).
32. W. Herchi, S. Harrabi, K. Sebei, S. Rochut, S. Boukhchina, C. Pepe, H. Kallel: Phytosterols accumulation in the seeds of Linum usitatissimum L. *Plant Physiology and Biochemistry*, 47: 880-885 (2009).
33. M. Zlatanov, M. Angelova-Romova, G. Antova, R. Dimitrova, S. Momchilova, B. Nikolova-Damyanova: Variations in fatty acids, phospholipids and sterols during the seed development of a high oleic sunflower variety. *Journal of the American Oil Chemists' Society*, 86: 867-875 (2009).
34. S. Momchilova, B. Nikolova-Damyanova: Quantitative TLC and gas chromatography determination of the lipid composition of raw and microwaved roasted walnuts, hazelnuts, and almonds. *Journal of Liquid Chromatography and Related Technologies*, 30: 2267-2285 (2007).
35. V. Kiosseoglou, D. Boskou: The composition of free and esterified sterols in tomato seed oil. *Oleagin*, 44: 113-115 (1989).

ЛИПИДЕН СЪСТАВ НА ЛЕНЕНИ СЕМЕНА

О. Тенева[1], М. Златанов[1], Г. Антова[1], М. Ангелова – Ромова[1], М. Марчева[2]

[1]Катедра Химична технология, ПУ „Паисий Хилендарски", Пловдив, България
[2]Аграрен университет, Пловдив, България

(Резюме)

Изследвани са съдържанието и съставът на глицеридно масло, изолирано от четири генотипа ленени семена (A900013, A900015, A900017 и A900018) с оглед тяхното приложение като храна и като източник на масло за технически и фармацевтични цели. Лененитe масла съдържат 34,2%, 39,1%, 37,2% и 44,4% глицеридно масло. Съдържанието на фосфолипиди, основно на фосфатидилхолин, фосфатидилинозитол и фосфатидилетаноламин на четирите сорта е съответно 0,9%, 0,8%,1,0% и 0,6%. Във всички масла общото съдържание на стероли е 0,2 – 0,3%, като бета-ситостерол преобладава (повече от 55,0%), следвано от кампестерол (13,1 – 26,1%) и стигмастерол (3,4 – 15,0%). Във фракцията токофероли (общо съдържание 766 мг/кг, 770 мг/кг, 775 мг/кг и 602 мг/кг), анализирана с високоефективна течно-течна хроматография, гама-токоферолът преобладава, следвано от гама-токотриенол. В триацилглицеролите основен компонент е линоленовата киселина (37,6%, 33,5%, 42,9% и 45,8%), следвана от олеинова и линолова киселина. В сравнение с триацилглицеролите, по-високи количества палмитинова и олеинова киселина, са установени във фосфолипидната фракция и в стероловите естери.

Physico-chemical properties of sunflower oil enriched with ω-3 fatty acids

K. Nikolova[1*], M. Perifanova-Nemska[1], G. Uzunova[1], T. Eftimov[2], G. Antova[2], A. Aladjadjiyan[3], V. Plachkova[2], W. Bock[4]

[1]University of Food Technologies, Plovdiv, Bulgaria,
[2]Faculty of Physics and Faculty of Chemistry, Plovdiv University, Plovdiv, Bulgaria
[3]Agricultural University, Plovdiv
[4]Université du Québec en Outaouais, Gatineau, Québec, Canada.

The physico-chemical properties (fatty acid composition, content of tocopherols, oxidation stability, color parameters etc) of linolic type sunflower oil enriched with ω-3 fatty acids by the addition of flaxseed oil have been investigated. It has been found that for sunflower oil enriched with flaxseed oil the linolic acid content increases from 0.1 % to 8. 11%. Due to the low oxidation stability of linolic oil, the overall oxidation stability decreases for the sample with addition of 20 % flaxseed oil, but this decrease is not essential and the obtained enriched sunflower oil has a good ratio of the ω-3/ω-6 fatty acids. It has been established that the enrichment of sunflower oil with 20% flaxseed oil leads to rise of linolic acid content to 8.11 %. Obtained enriched sunflower oil has good ratio of ω-3/ω-6 fatty acids. Oxidation stability of sunflower oil with a 20% addition of flaxseed oil declined from 10 h to 6h. The addition of flaxseed to sunflower oil does not enrich it essentially with chlorophyll, but causes a significant increase of β-carotene, which is an important component for the human health. Linear regression models between the intensity of fluorescence spectra in the UV range and the general content of tocopherols and β-carotene has been found.

Keywords: sunflower oil, flax oil, ω-3 fatty acids, fluorescence, fatty acid content

INTRODUCTION

Vegetable oils are an indispensable food component. They are a source of substances needed for humans and indispensable fatty acids, phospholipids, fatty soluble vitamins, sterols etc [1]. From the point of view of biological activity, the value of vegetable oils is determined from the presence of indispensable fatty acids, linolic (ω-6) and linoleic (ω-3) as well as from the quantity and quality of the tocopherol contents and other biologically active components.

The nutrition of a healthy human being as well as in the case of different chronic diseases not only the presence of poly non-saturated fatty acids, but also the ratio ω-6/ω-3 of fatty acids is of essential significance. According to certain authors [2, 3], for healthy people the ratio ω-6/ω-3 is recommended to be 10:1, while in the case of a diet it is recommended 3:1 to 5:1.

Sunflower oil is traditionally used in Bulgarian households. Flaxseed oil is characterized by high contents of α-linolic acid and is the only source of ω-3 fatty acids of vegetable origin. The mixtures of vegetable oils, enriched with ω-3 fatty acids can be used for the production of different type of mayonnaises, sauces and other emulsion products [4].

The objective of the present work is to study the dependence between the biological value of the sunflower oil enriched with ω- 3 fatty acids as well as their physico-chemical indicators.

MATERIALS AND METHODS

Samples for investigation have been prepared by mixing popular Bulgarian sunflower oil „Biser" with cold pressed flaxseed oil of Turkish origin in volumic concentrations 10% and 20%. The products for samples were commercially available and purchased from the food stores and were stored in dark place and at room temperature. The samples were analyzed immediately after being prepared.

Fatty acid content of the vegetable oils has been determined using gas chromatography (GC) method used previously [4-5]. Fatty acid methyl esters (FAME) were purified by silica gel TLC on 20x20 cm plates covered with 0.2 mm Silica gel 60 G layer (Merck, Darmstadt, Germany) with mobile phase n-hexane:acetone 100:8 (by volume). GC was performed on a HP 5890 (Hewlett Packard GmbH, Austria) gas chromatograph equipped with a 30 m x 0.25 mm (inner diameter) capillary InnoWax column (cross-linked to polyethylene

---

glycol, Hewlett Packard GmbH, Austria) and a fire ionization detector.

The column temperature was programmed to rise from 165ºC to 240ºC by step 4ºC/min and held at this temperature for 10 min; injector and detector temperatures were 260ºC. Carrier gas was nitrogen at a flow rate 0.8 cm^3/min; split was 100:1. Identification was performed by comparison of retention times with those of a standard mixture of fatty acids subjected to GC under identical experimental conditions [6].

Tocopherols in the vegetable oils were determined directly by high performance liquid chromatography (HPLC) [7] on a "Merck-Hitachi" (Merck, Darmstadt, Germany) equipment with 250 mm x 4 mm Nucleosil Si 50-5 column (Merck, Darmstadt, Germany) and fluorescent detector "Merck-Hitachi" F 1000. The operating conditions were as follows: mobile phase of *n*-hexane: dioxan 96:4 (by volume), flow rate 1 cm^3/min, excitation 295 nm, emission 330 nm. 20 μl 1% solution of oil in hexane were injected. Tocopherols were identified by comparing the retention times with those of authentic individual tocopherols.

The oxidation stability has been determined using the Rancimat 679 equipment at temperature of 100 °C with a volume rate of air flow of 20 dm^3/h [8].

The degree of oxidation of vegetable oils has been determined by ultraviolet (UV) spectroscopy that provides information about the primary products of the oxidation. The absorption of a 0.2% solution of isooctane at $\lambda = 232$ nm and $\lambda = 268$ nm has been measured using a Spectrophotometer S − 26, Boeco, Germany.

The optical properties of samples were studied using the following equipment:

- The color parameters were directly taken with Lovibond PFX 880 (Tintometer Limited, UK) in both colorimetric systems XYZ and CIE Lab. Transmission spectra in the visible range have been recorded using a 10 cm long cuvette (recommended for the study of refined vegetable oils). A software program developed specially for the equipment allowed determination of chlorophyll and *β*-carotene.

- The fluorescence spectra in UV and visible regions were measured on Fiber optic spectrometer (AvaSpec-2038, Avantes). Its sensitivity is in the range 200 – 1100 nm and it has resolution of about 5 nm. The oil samples were placed in 10mm cuvette and irradiated by light emitting diodes (LEDs) having emission wavelength 305 nm, 370 nm, 395 nm, 425 nm and 450 nm. Fluorescence

spectra in visible region have been taken from a direction orthogonal to the line of transmission, as shown in the Figure 1.
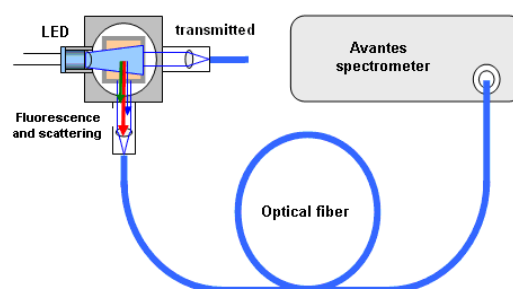

Fig. 1. Experimental set-up for the observation of fluorescence spectra.

UV spectra were obtained on micro layer of the studied samples formed between two quartz plates with detecting optical fiber placed directly in contact with the oil sample as shown in Fig.2.
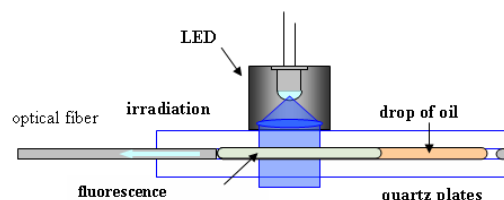

Fig. 2. Representation of the scheme of UV fluorescence using glass plates.

Statistical analysis of results:

Three samples per treatment were measured. Differences were considered significant for $p < 0.05$. One way analysis of variance (ANOVA) was performed. The average results are presented in the corresponding tables.

RESULTS AND DISCUSSIONS

Fatty acid composition is the most important characteristic of vegetable oils as related to its nutrition value, as well as to its oxidation stability. The results for fatty-acid contents of the tested samples are presented in Table 1.

The sunflower oil sample under study is of the linolic type. In this type the linoleic acid dominates over the oleic fatty acid. From nutrition point of view chosen oil is a suitable sample for enrichment because linolic acid belongs to the essential fatty acids that are indispensable for the human organism. Flax oil is rich in linoleic acid (ω-3). Its addition to sunflower oil in proportions of 10% and

Table 1. Fatty acid composition of sunflower oil, flaxseed oil and their mixture

Fatty acids, %	Sunflower oil	Flax oil	Sunflower oil + 10 % flax oil	Sunflower oil + 20 % flax oil
$C_{8:0}$	-	-	0.93 ± 0.02	-
$C_{14:0}$	-	-	-	0.1 ± 0.01
$C_{16:0}$	7.35 ± 0.12	6.28 ± 0.14	7.35 ± 0.17	6.5 ± 0.14
$C_{16:1}$	1.04 ± 0.04	-	0.17 ± 0.01	0.10 ± 0.01
$C_{18:0}$	3.39 ± 0.08	4.15 ± 0.05	3.15 ± 0.10	2.91 ± 0.12
$C_{18:1}$	32.16 ± 1.14	20.85 ± 1.05	33.51 ± 1.04	29.94 ± 1.24
$C_{18:2}$	56.06 ± 1.74	28.39 ± 1.28	50.50 ± 1.72	51.73 ± 1.71
$C_{18:3}$	traces	40.33 ± 1.62	3.75 ± 0.20	8.11 ± 0.17
$C_{22:0}$	-	-	0.64 ± 0.02	0.61 ± 0.02

* $C_{8:0}$- caprylic acid; $C_{14:0}$- myristic acid; $C_{16:0}$ – palmitic acid; $C_{16:1}$ - palmitoleic acid; $C_{18:0}$ – stearic acid; $C_{18:1}$ – oleic acid; $C_{18:2}$ – linoleic acid; $C_{18:3}$ – linolenic acid; $C_{22:0}$– behenic acid

Table 2. Content of tocopherols and tocopherol composition of sunflower oil, flax oil and their binary mixtures

| Tocopherols (T) and Tocotrienols (T-3), %	Sunflower oil	Flax oil	10 % flax oil in sunflower oil	20 % flax oil in sunflower oil
α - T	100 ± 2.7	19.5 ± 0.23	90.9 ± 1.96	79.7 ± 3.2
γ-T	-	59.1 ± 1.12	4.5 ± 0.11	13.5 ± 0.44
γ- T-3	-	21.4 ± 1.07	4.6 ± 0.16	6.8 ± 0.23
Total, mg/kg	588.6	447.7	555.1	514.1

20% leads to an increase of linoleic acid content in sunflower oil with 3.75% and 8.11 % respectively, while in the non-enriched sunflower oil it reaches 0.1% at most (See Table 1). The content of the oleic acid in the enriched with flax oil is not significantly lower than that of pure sunflower oil sample. The latter allows expecting that the oxidation stability of the enriched oils under study will be essentially altered. Due to the low oxidation stability of flax oil, the oxidation stability of mixed sunflower oils decreases smoothly with raising the addition of flaxseed oil (See Fig. 3)

The sample of sunflower oil with 20% flax oil provides good ω-6/ω-3 ratios of fatty acids. This combination provides also better oxidation stability.

In addition to the fatty acid composition of the studied samples the tocopherol content has been studied as well. The tocopherol content and composition of oil is directly defined by high-performance liquid chromatography with fluorescence detection. The results are presented in Table 2.

As seen from Table 2 the general quantity of tocopherols in the studied oil samples changes linearly with the addition of flaxseed oil.

As seen from both figures 3 and 4 linear regression model shows a dependence of the tocopherol content (y) on the induction period (x) expressed as $y = 20.63\,x + 393.7$ with a correlation coefficient $R^2 = 0.99$.
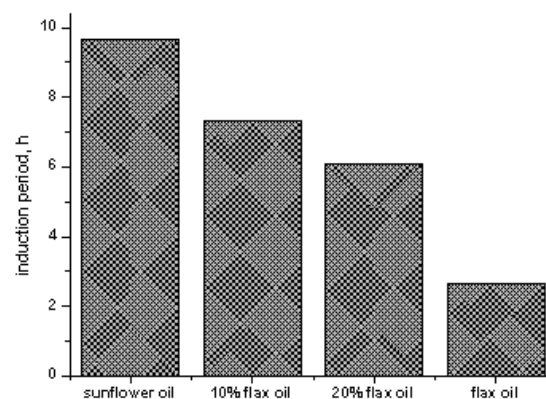
Fig. 3. Oxidation stability of sunflower oil and its binary mixtures.
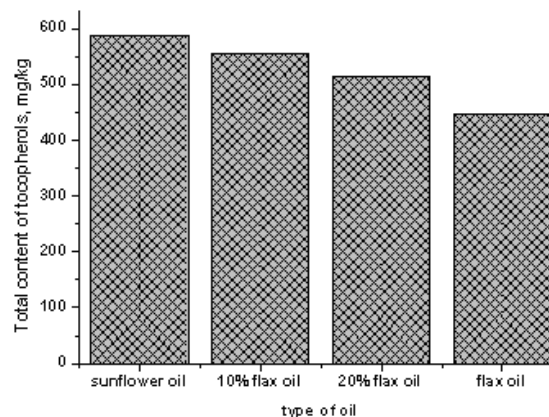
Fig. 4. Total content of tocopherols of sunflower oil and its binary mixtures

Observed comparatively good oxidation stability of the sample with 20% addition of flax oil can be explained with the presence of γ-tocopherol and trienol in the mixture.

In addition to improved nutrition value (high content of fatty solvent vitamins A, D, E and K, indispensable fatty acids) and oxidation stability, the enriched oils must have acceptable color indicators for the customer. The data for the color parameters of the samples in the two colorimetric systems are shown in Fig. 5.
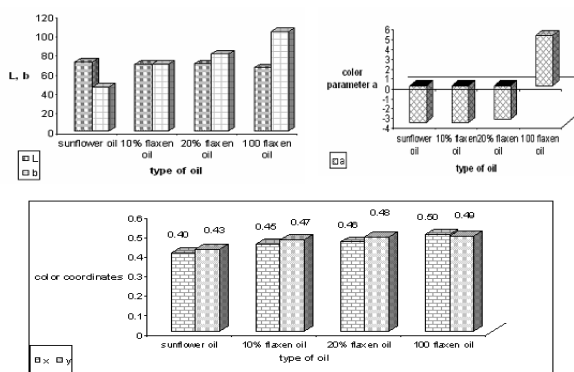

Fig. 5. Color parameters of enriched, non-enriched sunflower and flaxseed oil

The data for the color parameters show that the red component ($a^* > 0$) is predominant only in flax oil, while in all of the rest the green one dominates. The addition of flaxseed oil in greater quantities (20 %) causes the increase of red component. Although flaxseed oil is characterized by a lower brightness compared to sunflower oil this does not lead to an essential change in outer appearance of trade products. The enriched samples have a clearly expressed yellow color. '

With the increase of the content of flax oil the b* component rises essentially, which is proved by the red-yellow-blue (RYB) system, used especially to determine the colour of vegetable oils. From the obtained experimental data it is clear that the yellow component is 19 and 27 relative unit (r.u.), respectively for the 10% and 20% flax oil samples, while for sunflower oil it is 7.7 r. u.

The degree of oxidation of studied samples is estimated through indirect determination of primary oxidation products (peroxides) of absorption of conjugated diene structures which are formed from linoleate units using UV spectroscopy at 232 nm and from the absorption of conjugate triene structures at 268 nm. "Fresh" oils of linoleic type are characterized with absorption of conjugate dienes lower than 5.8 [9].

The results of measurements are presented in Table 3, where A_{232nm} and A_{268nm} are absorption maxima in relative units at 232 nm and 268 nm, respectively.

Table 3. Absorption of conjugate dienes of carbonyl compounds.

Type	A_{232nm}	A_{268nm}
Sunflower oil	1.57	0.45
Flax oil	1.94	0.83
10 % flax oil + sunflower oil	1.61	0.51
20 % flax oil + sunflower oil	1.55	0.55

According to the conjugated dienes, the vegetable oils can be defined as "fresh". The highest absorption value is obtained for pure flaxseed oil, but it lies in the limits for fresh oils. Similar value (around 2.11) for its absorption is reported in [10]. The undesirable oxidation during technological processes is low - absorption for pure sunflower and enriched oils lies in a narrow range between 0.45 and 0.55. The value of the dienes in flaxseed oil is higher.

Fluorescence spectra of investigated oils in the visible diapason have been recorded at four irradiation wavelength - 370 nm, 395 nm, 425 nm and 450 nm. On figure 6 only the spectra at λ=425 nm have been presented, because at this wavelength the differences in the fluorescence maximum intensities and the wavelength at which it is observed are most clearly expressed.
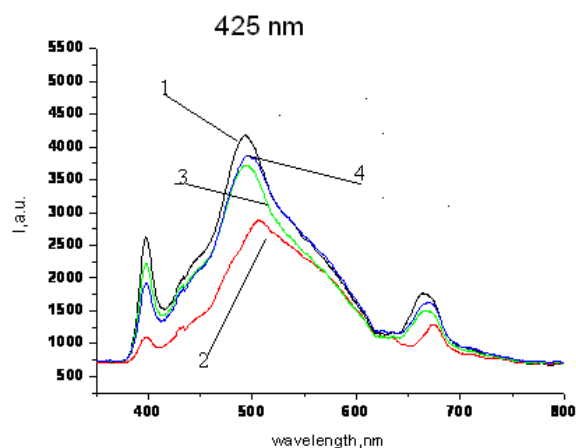

Fig. 6. Fluorescence spectra at λ=425 nm for flaxseed oil, sunflower oil and its mixtures. *1-sunflower oil; 2-flax oil; 3- 10%flax oil in sunflower oil; 4-20% flax oil in sunflower oil*

Two clearly expressed maxima have been observed for all investigated samples. One maximum is broad with high intensity belongs to the range $\lambda \in (490 \div 510)$ nm, the other one with rather lower intensity - to the range $\lambda \in (660 \div 675)$

nm. Latter one is due to the chlorophyll content in studied oils, while the first can be attributed to product of oil oxidation, as well as to the content of oleic acid. The comparison with data in Table 1 shows that the lowest fluorescence intensity is accounted for flaxseed oil – at 509 nm. In flaxseed oil the content of oleic acid is lowest (20.87 %), compared with samples with sunflower oil. A relation between the intensity of the fluorescence peak at 500 nm for excitation with λ=425 nm and absorption in UV diapason at λ=270 nm has been observed. The following correlation was found $I_{500} = -3151.x + 5458.9$ with correlation coefficient $R^2 = 0.949$ (x is absorption of the sample at λ=270 nm).

The addition of flaxseed oil to sunflower oil does not enriches it essentially with chlorophyll, but leads to expressive rise of β – carotene, that is important component for human health. β – Carotene and chlorophyll content in studied samples are presented in figure 7.
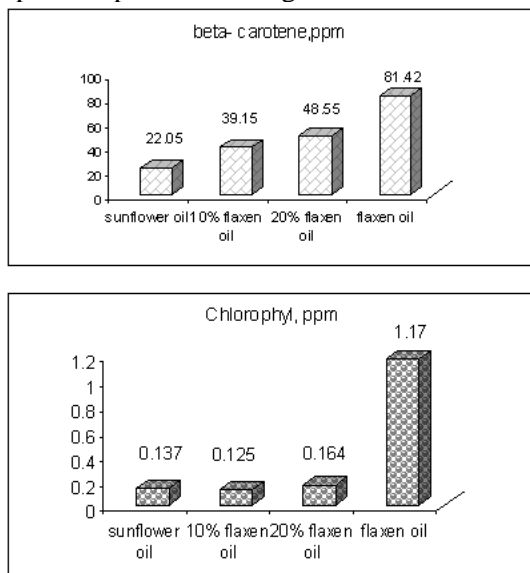

Fig. 7 β – carotene and chlorophyll content in flaxseed oil, sunflower oil and binary mixtures

Fluorescence spectroscopy in UV diapason is related mostly to the existence of pigments and tocopherols in studied samples. The fluorescence spectra for excitation with 305 nm are shown at figure 8.

Three maxima have been observed – one in the region 332-342 nm, the second at 430 nm and the third in the range 485-490 nm. Both first and second are related to the tocopherol content, the last is attributed to the presence of β – carotene in the samples.

The tocopherol content decreases in the samples of pure sunflower oil and those in enriched with

flaxseed oil. The ratio of intensity of excitation wavelength λ = 305 nm and that of fluorescence at λ =340 nm (first fluorescence maximum) is related to the tocopherol content of studied samples can be described by following equation $I_{305} / I_{340} = 0.002.x - 0.4772$, where x is the total tocopherol content. The correlation coefficient is $R^2 = 0.916$
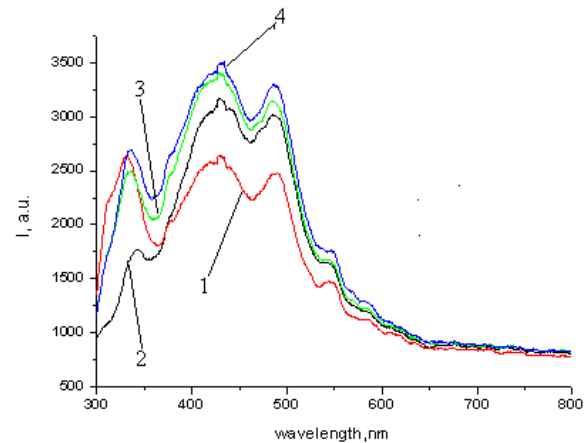

Fig. 8 The fluorescence spectra at 305 nm for sunflower oil, flaxseed oil and binary mixtures. *1-sunflower oil; 2-flax oil; 3- 10%flax oil in sunflower oil; 4-20% flax oil in sunflower oil*

The third fluorescence maximum observed at excitation wavelength λ = 305 nm suggests good correlation with □-carotene content. The linear regression models for the fluorescence maxima at λ = 485 nm can be presented respectively with $I_{485} = 32.001.x + 1805.4$, and $R^2 = 0.97$, where x represents β-carotene content in studied samples

CONCLUSSIONS

The addition of flaxseed oil with volume concentration 10% and 20% to sunflower one leads to enrichment of mixed sunflower oil with linolic acid (*ω*-3) with concentration respectively 3.75% and 8.11%. The pure sunflower oil does not content linolic acid.

The addition of flaxseed oil with volume concentration 20% to sunflower one provides for high ratio *ω*-3 /*ω*-6 of fatty acids, but brings to decrease of oxidation stability.

Enriched sunflower oil mixtures do not change essentially its chlorophyll content, while the content of β-carotene significantly rises. Their brightness slightly decreases compared with pure sunflower oil, but addition of flaxseed oil does not lead to significant change in trade appearance of the products.

Relation between fluorescence intensity in the visible region at 500 nm and oxidation products, defined through UV spectroscopy, is established to be: $I_{500} = -3151.x + 5458.9$ (x is absorption of the sample at λ=270 nm) with correlation coefficient $R^2 = 0.949$.

The following correlation dependences have been established:

-Between total content of tocopherols (y) and the induction period (x) of oxidation y = 20.63 x + 393.7 with correlation coefficient R2 = 0.99.

-Between the fluorescence maxima at λ = 485 nm at excitation wavelength λ = 305 nm and β-carotene content: $I_{485} = 32.001.x + 1805.4$, R2 = 0.97

-Between the ratio of intensity at excitation wavelength λ = 305 nm and that of fluorescence at λ =340 nm (first fluorescence maximum) and the tocopherol content of studied samples described by following equation: $I_{305} / I_{340} = 0.002.x - 0.4772$ with correlation coefficient R^2 = 0.916.

REFERENCES

1. Tabakaeva, T.K. Kalenik, *Oil Industry*, 2, 34-35, (2007).
2. A Guseva, *Oil Industry*, 6, 31-34, (2010).
3. I.Okara, K. G. Zamlyak, T. K. Kalenik, *Oil and fat production*, 2, 8-10, (2009).
4. L.V.Golubeeva, O. I Dolmatova,. L. I Vasilenko, R.I. Igdisamova, A. A.Gubanova, *Fat and oil industry*, 6, 18-19, (2012)
5. ISO 5509:2000. Animal and vegetable fats and oils. Preparation of methyl esters of fatty acids. 2000. p. 30.
6. ISO 5508:2004. Animal and vegetable fats and oils. Analysis by gas chromatography of methyl esters of fatty acids. 2004. p. 9.
7. ISO 9936:2006. Animal and vegetable fats and oils. Determination of tocopherols and tocotrienols contents. Method using high-performance liquid chromatography. 2006. p. 17
8. ISO 6886:2006. Animal and vegetable fats and oils, Determination of oxidation stability (accelerated oxidation test). 2006. p.13
9. M. P. Yanishlieva-Maslarova, Auto-oxidation and oxidative stability of lipid components and complex lipid components. Dissertation for the award of DSc. in Chemistry, BAS, BULGARIA ,1985.
10. I. V Kuzmanova, I. Totseva, Sv. Panaiotova, E.Marinova, St. Momchilova, Food and Flavour *Industry,* **8**, 52-56, 2010.

ФИЗИКО-ХИМИЧНИ СВОЙСТВА НА СЛЪНЧОГЛЕДОВО МАСЛО, ОБОГАТЕНО С ω-3 МАСТНИ КИСЕЛИНИ

К. Николова[1], М. Перифанова-Немска[1], Г. Узунова[1], Т. Евтимов[2], Г. Антова[2], А. Аладжаджиян[3], В. Бок[4]

[1]*Университет по хранителни технологии, Пловдив,*
[2]*Пловдивдски Университет „Паисий Хилендарски", Пловдив*
[3]*Аграрен университет, Пловдив*
[4]*Университет на Квебек в Отава, Гатино, Квебек, Канада*

(Резюме)

Изследвани са физико-химичните свойства (мастнокиселинен състав, токофероли, оксидантна стабилност, цветови параметри и др.) на слънчогледово масло от линолов тип при обогатяването му с мастни киселини чрез добавяне на ленено масло. Снети са флуоресцентните спектри във видимата и УВ област на спектъра, изследвано е поглъщането на пробите в УВ диапазона. Установено е, че при обогатяване на слънчогледово масло с 20% ленено масло количеството на линоленовата киселина нараства от 0.1% до 8.11%. Полученото обогатено слънчогледово масло има добро съотношение на ω-3/ω-6 мастни киселини. Оксидантната стабилност на слънчогледово масло с 20% добавка на ленено масло намалява от 10h на 6h. Добавянето на ленено масло към слънчогледовото масло не го обогатява съществено с хлорофил, но води до значително увеличаване на съдържанието на β-каротен, който е много важен компонент за човешкия организъм. Установени са линейно-регресионни модели между интензитетите на флуоресцентните спектри в УВ диапазона и общото съдържание на токофероли и β-каротен.

Catalytic synthesis of 1,3-diaryl-2-propene-1-ones by using heteropolyacids as heterogeneous recyclable green catalysts

A. Gharib [1,2]*, N. Noroozi Pesyan [3], L. Vojdanifard [4], M. Jahangir[1], M. Roshani[1], S. Moghadasi[2], H. R. Akhavan[2]

[1]*Department of Chemistry, Islamic Azad University, Mashhad, IRAN*
[2]*Agricultural Researches and Services Center, Mashhad, IRAN*
[3]*Department of Chemistry, Faculty of Science, Urmia University, 57159, Urmia, IRAN*
[4]*Education Organization of Razavi Khorasan, Education Ministry, Mashhad, IRAN*

New convenient conditions for the synthesis of 1,3-diaryl-2-propene-1-ones are described. 1,3-diaryl-2-propene-1-ones were readily prepared in the presence of heteropolyacids as heterogeneous recyclable catalysts in good yields and short times.

Key words: Heteropolyacids, Aromatic aldehyde, Acetophenone, 1,3-diaryl-2-propene-1-ones, Heterogeneous, Catalyst.

INTRODUCTION

(1,3-diaryl-2-propene-1-ones), chalcones are natural substances found in a number of plants or are synthetically prepared. They display many biological activities, *viz.*, antiviral, anti-inflammatory, antimicrobial, antimitotic, antitumor, analgesic, and antipyretic properties [1]. In addition, these compounds are of a high interest due to their use as starting materials in the synthesis of a series of heterocyclic compounds [2] like, isoxazoles, quinolinones, thiadiazines, benzofuranones, benzodiazepine, tetrahydro-2-chromens [3], flavones, etc. Moreover, these are important intermediates in many addition reactions of nucleophiles due to the inductive polarization of carbonyl group at the *β*-position. The main method for the synthesis of chalcones is the classical Claisen-Schmidt condensation in the presence of aqueous alkaline bases [4], $Ba(OH)_2$ [5], LiOH, microwave irradiation, ultrasound irradiation [6]. They are also obtained *via* the Suzuki reaction [7], Wittig reaction, Friedel-Crafts acylation with cinnamoyl chloride, or photo-fries rearrangement of phenyl cinnamates. In aldol condensation, the preparation of chalcones requires at least two-steps of aldol formation and dehydration. Jhala *et al*. synthesized chalcone using basic alumina under microwave irradiation [8]. There are numerous acid-catalyzed organic reactions and the use of solid acid catalysts is very important in several industrial and environmental processes [9]. In recent times, inorganic solid-catalyzed organic transformations are gaining much importance due to the proven advantage of heterogeneous catalysts, such as simplified product isolation, mild reaction conditions, high selectivity, easy recovery and catalyst reuse, and reduced generation of waste byproducts [10]. The reactions catalyzed by both heterogeneous and homogeneous systems have been reviewed by many researchers [11]. The reactions in which they can be used, from dehydration, cyclization or esterification up to amine oxidation or olefin epoxidation, may find wide applications in fine chemical production, such as fragrances, pharmaceutical and food [12]. Although there are many structural types of HPAs, the majority of the catalytic applications use the most common Keggin-type HPAs [13], especially for acid catalysts, owing to their availability and chemical stability. Other catalysts such as Wells-Dawson and Preyssler heteropolyacids are already being used [14].

EXPERIMENTAL SECTION

All chemicals were obtained from Merck and were used as received. $H_4[PMo_{11}VO_{40}]$, $H_6[PMo9V_3O_{40}]$ and $H_5[PMo_{10}V_2O_{40}]$ were prepared according to the literature [15-17]. The Wells-Dawson species $H_6[P_2W_{18}O_{62}]$ was prepared as described elsewhere [16], from an aqueous solution of α/β $K_6P_2W_{18}O_{62}×10H_2O$ salt, which was treated with ether and concentrated (37%) HCl solution. IR spectra were obtained with a Buck Scientific 500 spectrometer. ^{1}H-NMR spectra were

* To whom all correspondence should be sent:
E-mail: aligharib5@yahoo.com

recorded on a Bruker 200 MHz FT-NMR. All products are known compounds and were characterized by mp, IR and ^{1}H NMR. Melting points were measured by the capillary tube method with an Electrothermal 9200 apparatus.

Typical procedure for preparation of 1,3-diphenyl prop-2-en-1-ones (3a-j):

A mixture of 4-hydroxy acetophenone **1a** (3 mmol,), benzaldehyde **2a** (3 mmol) and $H_6[P_2W_{18}O_{62}]$ (0.03 g) was stirred at different temperatures using water as a green solvent (10 mL) for the appropriate time (Table 1). After completion of the reaction, as indicated by TLC, the catalyst was filtered off using a Buechner funnel (Ø = 6.0 cm) and washed with 20 mL dichloromethane. The filtrate was concentrated on a rotary evaporator. The reaction mixture was extracted with diethyl ether (3 × 10 mL). The combined organic layers were dried over anhydrous $MgSO_4$ and the solvent was evaporated to afford 1,3-diphenyl prop-2-en-1-ones, which were purified by column chromatography to afford 1,3-diphenyl prop-2-en-1-ones.

Spectral data of selected compounds:

1,3-Diphenyl prop-2-en-1-one (**3a**):
^{1}H NMR (CDCl₃, 200 MHz): δ 7.82 (1H, d, β-H, J = 7.50 Hz), 7.06 (1H, d, α-H, J =7.50 Hz), 8.02 (dd, 2H), 7.45-7.72 (m, 8H, Ar-H, J = 6.94 Hz,); ^{13}CNMR (CDCl₃, 100 MHz): δ 120.91, 127. 95, 128.43, 128.75, 129.48, 134.69, 135.66, 137.96, 145.37, 188.90. Anal. calcd for $C_{15}H_{12}O$: C 86.51, H 5.81; found: C 86.41, H 5.72.

1-(4-hydroxyphenyl)-3-phenylprop-2-en-1-one (**3b**):
^{1}H NMR (CDCl₃, 200 MHz): δ 7.88 (1H, d, β-H, J = 15.06 Hz), 6.86 (1H, d, α-H, J = 15.18 Hz), 6.95-7.72 (9H, m, Ar-H), 10.75 (1H, s, Ar-OH); ^{13}CNMR (CDCl₃, 100 MHz): δ 116.65, 121.46, 127.96, 128.76, 130.87, 131.44, 135.70, 146.10, 165.20, 189.90. Anal. calcd for $C_{15}H_{12}O_2$: C 80.34, H 5.39; found: C 80.24, H 5.47.

(E)-3-(4-hydroxyphenyl)-1-phenylprop-2-en-1-one (**3c**):
^{1}H NMR (CDCl₃, 200 MHz): δ 7.79 (1H, d, β-H, J = 8.50 Hz), 6.56 (1H, d, α-H, J = 8.50 Hz),6.65-7.89 (9H, m, Ar-H), 9.67 (1H, s, Ar-OH); ^{13}CNMR (CDCl₃, 100 MHz): δ 115.90, 121.47, 127.88, 128.90, 129.67, 130.78, 134.65, 145.70, 158.23, 190.35. Anal. calcd for $C_{15}H_{12}O_2$: C 80.34, H 5.39; found: C 80.26, H 5.30.

3-(4-chlorophenyl)-1-(4-hydroxyphenyl) prop-2-en-1-one (**3d**):
^{1}H NMR (CDCl₃, 200 MHz): δ 7.88(1H, d, β-H, J= 17.52 Hz), 6.86 (1H, d, α-H, J = 17.62

Hz), 7.28-7.64 (8H, m, Ar-H, J = 8.50 Hz), 10.05 (1H, s, Ar-OH). ^{13}CNMR (CDCl₃, 100 MHz): δ 115.90, 121.50, 129.47, 130.41, 130.67, 136.34, 140.87, 145.23, 158.21, 190.15. Anal. calcd for $C_{15}H_{11}ClO_2$: C 69.64, H 4.29; found: C 69.57, H 4.19.

3-(4-chlorophenyl)-1-phenylprop-2-en-1-one (**3e**):
^{1}H NMR (CDCl₃, 200 MHz): δ 7.80(1H, d, β-H, J= 15.20 Hz), 7.16 (1H, d, α-H, J= 15.12 Hz), 7.4-7.74 (9H, m, Ar-H, J= 8.60 Hz), 10.05 (1H, s, Ar-OH). ^{13}CNMR (CDCl₃, 100 MHz): δ 122.10, 128.60, 128.65, 128.89, 129.34, 133.45, 133.68, 134.68, 138.25,145.67. Anal. calcd for $C_{15}H_{11}ClO$: C 74.23, H 6.59; found: C 74.10, H 6.45.

3-(4-(dimethylamino)phenyl)-1-(4-hydroxyphenyl)prop-2-en-1-one (**3f**):
^{1}H NMR (CDCl₃, 200 MHz): δ 7.90 (1H, d, β-H, J = 15.80 Hz), 6.85(1H, d, α-H, J = 15.56 Hz), 9.25(1H, s, Ar-OH), 3.05(6H, s, -N(CH₃)₂), 7.05-7.80(8H, m, Ar-H). ^{13}CNMR (CDCl₃, 100 MHz): δ 45.65, 111.80, 116.65, 121.80, 125.23, 129.80, 131.60, 145.35, 150.78, 165.00. Anal. calcd for $C_{17}H_{17}NO_2$: C 76.38, H 6.41, N 5.24; found: C 76.24, H 6.33, N 5.16.

3-(4-(dimethylamino)phenyl)-1-(2-hydroxy-3,5-dimethylphenyl)prop-2-en-1-one (**3g**):
^{1}H NMR (CDCl₃, 200 MHz): δ 7.85 (1H, d, β-H, J = 14.71 Hz), 7.05(1H, d, α-H, J = 14.67 Hz), 13.03(1H, s, Ar-OH), 3.08 (6H, s, -N(CH₃)2), 2.35 (6H, s, Ar-CH₃), 6.85-7.80 (6H, m, Ar-H). ^{13}CNMR (CDCl₃, 100 MHz): δ 28.60, 44.57, 11.80, 118.75, 122.45, 124.88, 126.70, 129.75, 132.00, 134.45, 145.60, 150.35, 158.90, 193.10. Anal. calcd for $C_{19}H_{21}NO_2$: C 77.26, H 7.17, N 4.74; found: C 77.12, H 7.08, N 4.69.

1-(4-hydroxyphenyl)-3-(3,4,5-trimethoxyphenyl)prop-2-en-1-one (**3h**):
^{1}H NMR (CDCl₃, 200 MHz): δ 8.20 (2H, d, Ar-H, J =8.92Hz), 7.40 (2H, d, Ar-H, J =8.70 Hz),7.05 (2H, s, Ar-H), 6.92 (1H, d, β-H, J = 15.83 Hz), 6.75 (1H, d, α-H, J = 15.83 Hz), 3.80-3.90 (9H, s, 3x OCH₃), 11.05(1H,s, Ar-OH). ^{13}CNMR (CDCl₃, 100 MHz): δ 57.70, 61.25, 104.25, 116.69, 122.20, 126.60, 131.70, 139.34, 145.56,153.00, 164.50, 190.15. Anal. calcd for $C_{18}H_{18}O_5$: C 68.78, H 7.17; found: C 68.56, H 7.18.

3-(2-hydroxyphenyl)-3-oxoprop-1-enyl)-4H-chromen-4-one (**3i**):
^{1}H NMR (CDCl₃, 200 MHz): δ 7.65 (1H, d, β-H, J =11.43 Hz), 7.15 (1H, d, α-H, J =12.00 Hz), 12.45(1H, s, Ar-OH), 8.65 (s, 1H,), 7.10-8.05(8H, m, Ar-H). ^{13}CNMR (CDCl₃, 100 MHz): δ 109.30, 119.68, 120.45, 123.46, 123.95, 126.34, 129.20, 134.76, 135.55, 136.87, 137.80, 157.57, 163.45,

189.90. Anal. calcd for $C_{18}H_{12}O_3$: C 78.25, H 4.38; found: C 78.18, H 4.29.

3-(5-chloro-2-hydroxyphenyl)-3-oxoprop-1-enyl)-4H-chromen-4-one (3j) :

^{1}H NMR (CDCl3, 200 MHz): δ 7.85(1H, d, β-H, J =11.40 Hz), 7.15(1H, d, α-H, J =11.32 Hz), 12.75(1H, Ar-OH), 8.55(s, 1H), 6.85-7.95(7H, m, Ar-H). ^{13}CNMR (CDCl3, 100 MHz): δ 109.25, 119.48, 123.56, 125.98, 129.90, 130.97, 134.68, 135.47, 135.40, 137.89, 158.24, 163.56, 198.57. Anal. calcd for $C_{19}H_{13}ClO_3$: C 70.27, H 4.03; found: C 72.47, H 3.93.
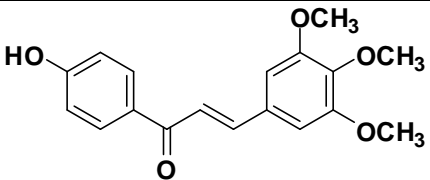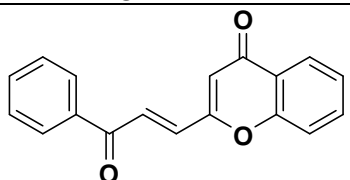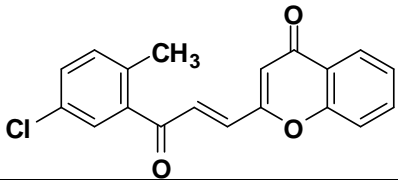
RESULTS AND DISCUSSION

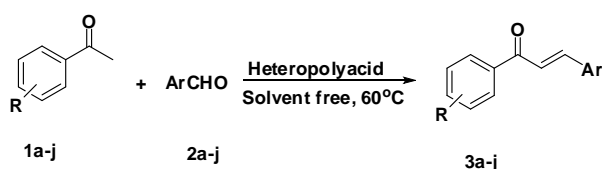In a systematic study in the presence of all catalysts, the reaction was examined with different solvents and then in the solvent of choice. The effect of the reaction temperature was also studied. Next, using the best solvent and temperature, the effect of the reaction time was studied. In a typical example we have carried out a reaction of 4-hydroxy acetophenone **1a** with benzaldehyde **2a** in the presence of Wells–Dawson type of heteropolyacids $H_6[P_2W_{18}O_{62}]$, $H_4[PMo_{11}VO_{40}]$, $H_5[PMo_{10}V_2O_{40}]$ and $H_6[PMo_9V_3O_{40}]$ at 60°C using water as a green solvent to afford the corresponding 1,3-diaryl-2-propene-1-one (**3a**) (Table 1) without any side products and in excellent yields with short reaction time (Scheme 1). The progress of the reaction was monitored by TLC. After completion of the reaction, the usual work-up afforded pure chalcones in excellent yields (82-96%), Table 1.

Table 1. Synthesis of 1,3-diaryl-2-propene-1-ones in the presence of a Wells–Dawson, $H_6[P_2W_{18}O_{62}]$ heteropolyacid catalyst at different temperatures using water as a green solvent

Entry	Products (3a-i)	Time (min)	Mp (°C)		[a]Yield (%)		
			Found	Reported	25 °C	50 °C	60 °C
1		48	57-59	54-56	57	71	90
2		64	173-175	172-174	64	83	96
3		68	184-186	180-181	61	74	82
4		79	175-177	173-174	65	72	87
5		55	111-113	113-114	68	84	92
6		72	119-122	120-122	61	77	95
7		77	135-137	-	57	73	86

Entry	Structure					
8	HO-C6H4-C(O)-CH=CH-C6H2(OCH3)3	75	162-165	-	59	71	91
9	(chromone / flavone-type structure with phenyl prop-2-en-1-one)	84	147-149	-	61	75	93
10	(2-methyl-5-chlorophenyl chromone prop-2-en-1-one)	85	112-115	-	59	70	84

[a] Isolated yields.

Scheme 1. Synthesis of 1,3-diaryl-2-propene-1-ones using heteropolyacid catalysts at 60°C and water as a green solvent

R-C6H4-C(O)-CH3 (1a-j) + ArCHO (2a-j) →(Heteropolyacid, Solvent free, 60°C)→ R-C6H4-C(O)-CH=CH-Ar (3a-j)

Effect of the catalyst type

Initially, we compared the catalytic performance of Keggin, $H_5[PMo_{10}V_2O_{40}]$, $H_4[PMo_{11}VO_{40}]$, $H_6[PMo_9V_3O_{40}]$ with Wells–Dawson, $H_6[P_2W_{18}O_{62}]$ in the synthesis of 1,3-diaryl-2-propene-1-one derivatives. The results are shown in Table 2. The yield of product decreases in the following order: $H_6[P_2W_{18}O_{62}]>H_6[PMo9V_3O_{40}]>H_5[PMo_{10}V_2O_{40}]>H_4[PMo_{11}VO_{40}]>H_2SO_4>Yb(OTf)_3>Hf[N(SO_2C_8F_{17})_2]_4>Bi(OTf)_3$

Table 2. Synthesis of (E)-chalcone 3a using various heteropolyacid catalysts at 60°C and water as a green solvent

Entry	Catalyst	Time (min)	[a]Yield (%)
1	$H_6[P_2W_{18}O_{62}]$	48	90
2	$H_6[PMo_9V_3O_{40}]$	48	85
3	$H_5[PMo_{10}V_2O_{40}]$	48	81
4	$H_4[PMo_{11}VO_{40}]$	48	74
5	Free	600	-
6	$Hf[N(SO_2C_8F_{17})_2]_4$	59	64
7	$Yb(OTf)_3$	66	66
8	$Bi(OTf)_3$	74	62
9	H_2SO_4	78	70

[a]Isolated yields.

As can be seen, Wells–Dawson type of heteropolyacid $H_6[P_2W_{18}O_{62}]$, is more effective than the other heteropoly anions and in the presence of this catalyst the highest yields of products are obtained. The interesting feature of this polyanion compared to the other heteropolyacids is its hydrolytic stability (pH 0-12), which is very important in catalytic processes.

Comparison of $H_5[PMo_{10}V_2O_{40}]$, $H_4[PMo_{11}VO_{40}]$, $H_6[PMo_9V_3O_{40}]$ with Wells–Dawson, $H_6[P_2W_{18}O_{62}]$, showed that the activity was always higher for Wells–Dawson, $H_6[P_2W_{18}O_{62}]$. In other words, Wells–Dawson, $H_6[P_2W_{18}O_{62}]$ is a better catalyst for the synthesis of 1,3-diaryl-2-propene-1-ones, and the acid strength of this solid acid catalyst is higher than that of H_2SO_4 (with serious environmental and operational problems). Heteropolyacid with a tungsten atom shows higher acidity than its molybdenum analogue [18, 19]. It seems clear that the acid strength of the protons on Wells–Dawson, $H_6[P_2W_{18}O_{62}]$ (tungsten atom shows higher acidity than molybdenum) is sufficient to catalyze the synthesis of 1,3-diaryl-2-propene-1-ones, and potentially all protons are active sites.

Table 3. Synthesis of 1-(4-hydroxyphenyl)-3-phenylprop-2-en-1-one 3b using various heteropolyacid catalysts and water as a green solvent at 60°C

Entry	Catalyst	Time (min)	[a]Yield (%)
1	$H_6[P_2W_{18}O_{62}]$	64	96
2	$H_6[PMo_9V_3O_{40}]$	64	91
3	$H_5[PMo_{10}V_2O_{40}]$	64	84
4	$H_4[PMo_{11}VO_{40}]$	64	80
5	Free	600	-
6	$Hf[N(SO_2C_8F_{17})_2]_4$	61	58
7	$Yb(OTf)_3$	69	63
8	$Bi(OTf)_3$	79	60
9	H_2SO_4	77	68

[a]Isolated yields.

Effect of the solvent

The synthesis of 1,3-diaryl-2-propene-1-one derivatives at 60ºC was carried out using various common solvents such as ethanol, methanol, THF, $CHCl_3$ and acetonitrile. The results are shown in Table 4. With all catalysts, the highest yields of the products were obtained under solvent-free conditions (water as a green solvent). In addition, the time required for completion of the reaction was found to be shorter under solvent-free conditions (water as a green solvent).

The results (Table 4) show that the $H_6[P_2W_{18}O_{62}]$ catalyst is better with respect to yield and reaction conditions. In all cases, the $H_6[P_2W_{18}O_{62}]$ heteropolyacids show higher activity compared to the Keggin-type heteropolyacids, $Hf[N(SO_2C_8F_{17})_2]_4$, $Bi(OTf)_3$, $Yb(OTf)_3$ and H_2SO_4 (Table 4, entries 27-29).

The reaction proceeds cleanly at 60ºC, however at room temperature using a solvent it required longer reaction time (Table 2). In the absence of catalyst, the reaction did not yield any product even after long reaction time (10 h). This method not only affords the products in good yields but also avoids the problems associated with catalyst cost, handling, safety and pollution. These catalysts are non-volatile, easy to handle and thermally robust and can be considered as ecofriendly for a variety of organic transformations. The results are presented in Table **1**. In all cases, the reactions proceeded rapidly and with high efficiency at 60ºC and water as a green solvent. IR spectra of the chalcones showed a characteristic band in the region near 1625 cm^{-1} due to >C=O stretching vibrations. All chalcones showed absorption in the region 1575-1610 cm^{-1} due to (-CH=CH-) ethylenic double bond. ^1H NMR spectra showed characteristic doublet signals near δ 6.84 and δ 7.96 due to olefinic a,b-protons. These findings are in agreement with the confirmed product.

Effect of temperature

The effect of temperature was studied by carrying out the reactions at different temperatures [25 ºC, 50 ºC and 60 ºC)]. As is shown in Table 1**,** by raising the reaction temperature from ambient temperature 25 ºC to 60 ºC, the yield of the

Table 4. Synthesis of 3a in the presence of different solvents and various heteropolyacid (HPAs) catalysts at different temperatures

Entry	Solvent	Catalyst	Temperature (ºC)	Time (min)	^{a}Yield (%)
1	Water	$H_6[P_2W_{18}O_{62}]$	60	48	90
2	Water	$H_6[PMo_9V_3O_{40}]$	60	54	85
3	Water	$H_5[PMo_{10}V_2O_{40}]$	60	44	81
4	Water	$H_4[PMo_{11}VO_{40}]$	60	54	74
5	Ethanol	$H_6[P_2W_{18}O_{62}]$	60	50	88
6	Ethanol	$H_6[PMo_9V_3O_{40}]$	60	58	83
7	Ethanol	$H_5[PMo_{10}V_2O_{40}]$	60	58	78
8	Ethanol	$H_4[PMo_{11}VO_{40}]$	60	58	76
9	Methanol	$H_6[P_2W_{18}O_{62}]$	60	60	86
10	Methanol	$H_6[PMo_9V_3O_{40}]$	60	65	83
11	Methanol	$H_5[PMo_{10}V_2O_{40}]$	60	65	77
12	Methanol	$H_4[PMo_{11}VO_{40}]$	60	65	74
13	THF	$H_6[P_2W_{18}O_{62}]$	60	89	81
14	THF	$H_6[PMo_9V_3O_{40}]$	60	94	77
15	THF	$H_5[PMo_{10}V_2O_{40}]$	60	94	72
16	THF	$H_4[PMo_{11}VO_{40}]$	60	94	68
17	$CHCl_3$	$H_6[P_2W_{18}O_{62}]$	60	78	83
18	$CHCl_3$	$H_6[PMo_9V_3O_{40}]$	60	72	80
19	$CHCl_3$	$H_5[PMo_{10}V_2O_{40}]$	60	72	75
20	$CHCl_3$	$H_4[PMo_{11}VO_{40}]$	60	72	71
21	Acetonitrile	$H_6[P_2W_{18}O_{62}]$	60	88	80
22	Acetonitrile	$H_6[PMo_9V_3O_{40}]$	60	83	77
23	Acetonitrile	$H_5[PMo_{10}V_2O_{40}]$	60	83	71
24	Acetonitrile	$H_4[PMo_{11}VO_{40}]$	60	83	66
25	FREE	FREE	60	600	-
26	Water	$Hf[N(SO_2C_8F_{17})_2]_4$	60	59	64
27	Water	$Yb(OTf)_3$	60	66	66
28	Water	$Bi(OTf)_3$	60	74	62
29	Water	H_2SO_4	60	78	70

^{a}Isolated yields.

reactions increased. From these results, it was concluded that 60 ºC would be the optimum temperature for all reactions. The reaction proceeds very cleanly and free of side products in water as a green solvent.

Reusability of the catalyst

The catalyst was recovered after the reaction and was reused in the synthesis of 1,3-diaryl-2-propene-1-ones. Several recoveries have only slightly decreased the catalytic activity, pointing to the stability and retention capability of this useful polyanion. At the end of the reaction, the catalyst was filtered, washed with diethyl ether, dried at 130 ºC for 1 h, and reused in another reaction. The recycled catalyst was used for three reactions without any appreciable lost in its catalytic activities being observed. In Table **5**, the efficiency of $H_6[P_2W_{18}O_{62}]$ in the synthesis of **3a** after five recoveries is reported. As it is shown in Table **5,** the first, second, third, fourth and fifth reaction using recovered $H_6[P_2W_{18}O_{62}]$ afforded similar yields.

Table 5. Reuse of the $H_6[P_2W_{18}O_{62}]$ catalyst for the synthesis of 3a.

Entry	Run	[a]Yield (%)	Time (min)
1	1	89	48
2	2	88	48
3	3	88	48
4	4	86	48
5	5	84	48

[a]Isolated yields.

CONCLUSION

We have demonstrated an alternative simple procedure for the synthesis of 1,3-diaryl-2-propene-1-one derivatives using Wells–Dawson, $H_6[P_2W_{18}O_{62}]$ heteropolyacid catalyst as an ecofriendly, reusable, inexpensive and efficient catalyst. The method has advantages in terms of yield, heterogeneous nature, expenses, availability of reagents and reusability of the green catalyst, short reaction times and easy work-up procedure.

REFERENCES

1. R. Kalirajan, S. U. Sivakumar S. Jubie, B. Gowramma B. Suresh, *Int. J. Chem. Tech. Res..* **1,** 27 (2009).
2. S. Wang, G. Yu, J. Lu, K. XiaO, Y. Hu, H. Hu, *Synthesis,* 487 (2003).
3. S. R. Sarda, V. A. Puri, A. B. Rode, T. N. Dalawe, W. N. Jadhav, R. P. Pawar, *Arkivoc.* **16,** 242 (2007).
4. Y. Rajendra Prasad, A. Lakshmana Rao, R. Rambabu, P. Ravi Kumar, *Oriental J. Chem.* **23**, 927 (2007).
5. M. Srinivasa Rao, J. Kotesh, R. Narukulla, H. Duddeck, *Arkivoc,* **14,** 96 (2004).
6. V. Calvino, M. Picallo, A. J. López-Peinado, R .M. Martín-Aranda, C. J. Durán-Valle, *Appl. Surface Sci.,* **252**, 6071 (2006).
7. N. Eddarir, S. Catelle, Y. Bakkour, C. Ronlando, *Tetrahedron Lett.*, **44**, 5359 (2003).
8. G. Thirunarayanan G. Vanangamudi, *Arkivoc.* **12,** 58 (2004).
9. A. Corma, H. García, *Chem. Rev.* **103,** 4307 (2003).
10. B.M. Reddy, P. M. Sreekanth, P. Lakshmanan, *J. Mol. Catal. A. Chem.* **237,** 93 (2005).
11. L. Wilson, J. H. Clark, *J Pure Appl. Chem.* **72,** 1313 (2000).
12. G. Sartori, R. Ballini, F. Bigi, G. Bosica, R. Maggi, P. Righi, *Chem. Rev.* **104,** 199 (2004).
13. M. Misono, N. Nojiri*, Appl. Catal. A. Gen.* **64,** 1 (1990).
14. T. Okuhara, *Catal. Today.* **73,** 167 (2002).
15. I. V. Kozhevnikov, Catalysts for fine chemical synthesis Catalysis by polyoxometalates*,* Wiley, England, **2** (2000).
16. G. Romanelli, J. C. Autino, G. Baronetti, *Molecules,* **6,** 1006 (2001).
17. M. M. Heravi, T. Benmord. K. Bakhtiari, F. F. Bamoharram, H. A. Oskooie, *J. Mol. Catal. A: Chem.* **264,** 318 (2006).
18. I. V. Kozhevnikov, *Russ. Chem. Rev.* **56**, 811 (1987).
19. F.F. Bamoharram, M. M. Heravi, M. Roshani, A. Gharib, M. Jahangir, *J. Mol. Catal.* **252**, 90 (2006).

КАТАЛИТИЧНА СИНТЕЗА НА 1,3-ДИАРИЛ-2-ПРОПЕН-1-ОНИ ИЗПОЛЗВАЙКИ ХЕТЕРОПОЛИКИСЕЛИНИ КАТО РЕЦИКЛИРУЕМ ЗЕЛЕН КАТАЛИЗАТОР

А. Гариб [1,2], Н. Норузи Песян [3], Л. Вожданифард [4], М. Джахангир[1], М. Рошани[1], С. Могадаси[2], Х. Р. Акхаван[2]

[1]*Департамент по химия, Ислямски университет „Азад“, Машхад, Иран*
[2]*Център по земеделски изследвания и услуги, Машхад, Иран*
[3] *Департамент по химия, Научен факултет, Университет Урмиа, 57159, Урмиа, Иран*
[4]*Образователна организация на Разави Кхорасан, Министерство на образованието, Машхад, Иран*

(Резюме)

Описани са нови подходящи условия за синтезата на 1,3-диарил-2-пропен-1-они. Тези съединения лесно се получават в присъствие на хетерополикиселини като хетерогенни рециклируеми катализатори с добри добиви и за кратко време.

Synthesis of β–amino carbonyl compounds using ZnO nanoparticles as a green, effective and reusable catalyst

A.Gharib[1,2*], N. Noroozi Pesyan [3], L. Vojdanifard [4], M.Jahangir[1], M.Roshani[1], S. Moghadasi[2]

[1]*Department of Chemistry, Islamic Azad University, Mashhad, IRAN*
[2]*Agricultural Researches and Services Center, Mashhad, IRAN*
[3]*Department of Chemistry, Faculty of Science, Urmia University, 57159, Urmia, IRAN*
[4]*Education Organization of Razavi Khorasan, Education Ministry, Mashhad, IRAN*

A new efficient one-pot three-component condensation of aromatic aldehydes, aromatic ketones, and aromatic amines in the presence of ZnO nanoparticles as an inexpensive and effective catalyst for the synthesis of β-amino carbonyl compounds by Mannich reaction is described. The reaction was carried out at room temperature under solvent-free conditions. Mild reaction temperature, cost-effective catalyst, simple product separation and catalyst recycling were notable achievements in the reaction. Simple experimental conditions and product isolation procedure make this protocol potentially applicable for the development of a clean and environment-friendly strategy for the synthesis of β-amino ketones. The present methodology offers several advantages such as good yields, short reaction times and a recyclable catalyst with a very easy work-up.

Keywords: Nanoparticles, ZnO, β-Amino carbonyl; β1,β2-Diamino diketone; solvent-free; Isophthalic aldehyde.

INTRODUCTION

Cysteine proteases are ubiquitous in nature and have been implicated in the etiology of a number of disease states [1]. Over the past two decades, selective and reversible inhibitors for this class of enzymes have been an area of intense research [2]. These investigations have led to a number of reversible inhibitors such as peptidyl aldehydes, α-ketoamides and α-keto heterocycles [3]. Recently, researchers from SmithKline Beecham have reported the design and synthesis of a novel class of cysteine protease inhibitors based on a 1,3-diamino ketone scaffold (Figure 1) [4].
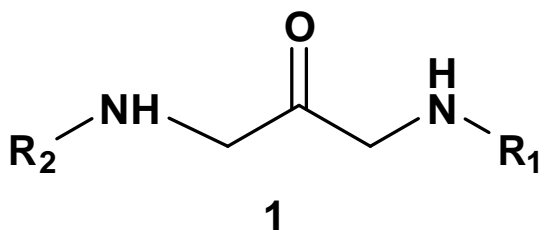

Fig.1. Diamino ketone

In recent years, the use of multicomponent reactions has gained considerable attention in organic synthesis. In particular, the Mannich reaction has been widely used for the synthesis of β-amino carbonyl compounds. Owing to their importance as valuable building blocks for the preparation of 1,3-amino alcohols [5, 6], β-amino acids [7], as well as for the synthesis of various bioactive molecules such as the antibiotics nikkomycins and neopolyoxines [8, 9], several methods have been reported in the literature for the synthesis of β-amino carbonyl compounds using catalysts such as $HClO_4$-SiO_2 [10], silica supported sulfuric acid [11], bromodimethylsulfonium bromide (BDMS) [12], TMSCl [13], p-TSA [14], Sml3[15], Amberlyst-15 [16], and $AuCl_3$-PPh_3[17]. These methods have, however, certain drawbacks such as moisture sensitivity of the catalyst [7, 18], longer reaction time [4–6], and use of an expensive metal salt as catalyst [19–21]. There is still scope, therefore, for an improved method for the synthesis of β-amino carbonyl compounds which can avoid the use of expensive and sensitive catalysts. Furthermore, the use of inorganic solid supported reagents provides an attractive procedure due to their characteristic properties such as enhanced reactivity and selectivity, simple work-up procedure, and milder reaction conditions [22–25]. Among these inorganic supported reagents, iodine

---

* To whom all correspondence should be sent:
E-mail aligharib5@yahoo.com

supported on dehydrated neutral alumina has found wide application because of its property to form an activated iodonium ion [24]. Therefore, activated iodonium ion produced from iodine adsorbed on neutral alumina has been used for the coupling reactions of aldehydes, enolizable ketones or 1,3-dicarbonyls with methyl carbamate or aromatic amines using microwaves as an energy source superior to conventional methods [26–28] in terms of shorter reaction time and minimized reaction by-products. Recently, a method using molecular iodine as the catalyst has been reported for the synthesis of β-amino carbonyl compounds *via* a three-component reaction involving aldehydes, ketones, and benzyl carbamates with good yields. However, this method has the disadvantage of a longer reaction time [29].

EXPERIMENTAL SECTION

Thin-layer chromatography was performed using commercially prepared 60-mesh silica gel plates and visualization was effected with short-wavelength UV light (254 nm). The IR spectra were recorded on a Shimadzu model impact 400D FT-IR spectrophotometer using KBr pellets. ^{1}H NMR were recorded on a Bruker AC-300F 400 MHz spectrometer in CDCl$_3$ using TMS as an internal standard with 1H resonance frequency of 400 MHz. Zn dust (Qualigens Fine Chemicals, AR grade, 325 mesh, 99.90% purity), *o*-hydroxy benzaldehydes and 1,3-dicarbonyl compounds were commercial, procured from Hi Media Laboratories Pvt. Ltd., and were used without further purification. The melting points were determined by open capillaries and were used uncorrected.

Synthesis of 1,3-diphenyl-3-(phenylamino) propan-1-one derivatives

In a typical experiment, amine (0.20 mmol), ketone (0.20 mmol), ZnO nanoparticles catalyst (10 mol%) and aldehyde (0.20 mmol) were successively added to ethanol (2 mL) (or better solvent-free). The resultant mixture was stirred at room temperature for 4 h and then quenched with saturated NaHCO$_3$.aq (5 mL) and brine (5 mL). The mixture was extracted with ethyl acetate, washed with brine, dried over Na$_2$SO$_4$, concentrated, distilled with solvents and crystallized in hot ethanol to give the desired product. After the required reaction time, ether was added to extract ZnO nanoparticles, the latter were separated by filtration and could be reused for the next run after a simple treatment including washing with ether (2×5 mL) and drying in air at 100 °C for 6 h.

Spectral data:

1,3-Diphenyl-3-(phenylamino)propan-1-one (4a)

IR (KBr, cm^{-1}): 3395, 3024, 2975, 1673, 1599, 1515, 1297, 1220, 1080, 1027, 1001, 860, 694, 515; ^{1}H-NMR (400 MHz, CDCl$_3$, δ/ppm): 7.90 (m, 2H), 7.50 (m, 10H), 6.63 (m, 3H), 5.00 (dd, *J* = 5.2 and 7.5 Hz, 1H), 4.56 (br, 1H), 3.50 (dd, *J* = 5.2 and 16.1 Hz, 1H), 3.40 (dd, *J*= 7.5 and 16.1 Hz, 1H); ^{13}C-NMR (400 MHz, CDCl$_3$, δ/ppm): 198.2, 147.0, 142.8, 136.7, 133.4, 129.2, 128.7, 128.6, 128.2, 127.6, 126.3, 117.7, 113.6, 54.7, 46.2; HRMS calcd for C$_{21}$H$_{19}$NO 301.1467, found 301.1471. Calcd for C$_{21}$H$_{19}$NO: C 83.66, H 6.37, N 4.64. Found: C 83.61, H 6.40, N 4.69%. HRMS (EI) Calcd. for C$_{21}$H$_{19}$NO [M]$^+$, 301.1003, Found 301.1006.

3-[(4-Chlorophenyl)amino]-1,3-diphenylpropan-1-one (4b)

IR (KBr, cm^{-1}): 3393, 3034, 1672, 1595, 1515, 1377, 1292, 1224, 1080, 1005, 929, 860, 749, 690, 620, 518; ^{1}H-NMR (400 MHz, CDCl$_3$, δ/ppm): 7.85 (m, 2H), 7.43 (m, 8H), 7.01 (m, 2H), 6.46 (m, 2H), 4.95 (dd, *J* = 5.0 and 7.7 Hz, 1H), 3.47 (dd, *J* = 5.0 and 16.2 Hz, 1H), 3.40 (dd, *J* = 7.6 and 16.1 Hz, 1H); ^{13}C-NMR (400 MHz, CDCl$_3$, δ/ppm): 198.2, 145.7, 142.1, 136.5, 133.2, 128.9, 128.7, 128.4, 128.2, 127.4, 126.2, 122.5, 114.8, 54.6, 46.2; Anal Calcd for C$_{21}$H$_{18}$NClO: C 75.12, N 4.16, H 5.37. Found: C 75.10, N 4.22, H 5.41%. HRMS (EI) Calcd. for C$_{21}$H$_{18}$NClO [M]$^+$, 335.1004, Found 335.1007.

3-(N-Phenylamino)-3-(3-chlorophenyl)-1-phenylacetone (4c)

IR (KBr, cm^{-1}): 3397, 3025, 2974, 1673, 1597, 1516, 1296, 1220, 1083, 1027, 1002, 860, 694, 515. ^{1}H-NMR (400 MHz, CDCl$_3$, δ/ppm): 3.40 (2H, m), 4.91 (1H, m), 6.50 (2H, d, J=7.95Hz),7.36 (3H, d, J=7.95Hz), 7.47 (21H, m), 7.84 (2H, d, J=7.8Hz); ^{13}C-NMR (400 MHz, CDCl$_3$, δ/ppm): 211.6, 147.7, 140.6, 129.8, 129.5, 128.5, 125.9, 120.9, 1133.3, 57.9, 55.8, 41.1, 27.5. Anal Calcd for C$_{21}$H$_{18}$ClNO: C 75.09, N 4.15, H 5.40. Found: C 75.00, N 4.07, H 5.56%. HRMS (EI) Calcd. for C$_{21}$H$_{18}$ClNO [M]$^+$, 335.1002, Found 335.1006.

3-(N-Phenylamino)-3-(3-bromophenyl)-1-phenylacetone (4d)

IR (KBr, cm^{-1}): 3392, 3020, 2931, 1675, 1506, 1489, 1361, 1307, 1270, 1110, 1072, 865, 752, 680, 510. ^{1}H-NMR (400 MHz, CDCl$_3$, δ/ppm): 3.40 (2H,m), 4.95 (1H,m), 6.52 (2H,d,J=7.95Hz),7.37 (3H, d,J=7.95Hz), 7.47 (21H,m), 7.84 (2H,d,J=7.8Hz); IR (KBr, cm^{-1}): 3397, 3025, 2974, 1674, 1596, 1515, 1296, 1220, 1080, 1027, 1004, 860, 695, 514. ^{13}C-NMR (400

MHz, CDCl$_3$, δ/ppm): 200.1, 147.5, 145.8, 145.5, 136.6, 133.1, 131.2, 129.8, 129.5, 129.2, 128.9, 128.7, 125.8, 120.6, 113.8, 113.6, 113.1, 72.5, 53.6. Anal Calcd for C$_{21}$H$_{18}$BrNO: C 66.31, N 3.66, H 4.76. Found: C 66.29, N 3.60, H 4.70%. HRMS (EI) Calcd. for C$_{21}$H$_{18}$BrNO [M]$^+$, 379.1000, Found 379.1005.

3-(N-p-Bromophenylamino)-1,3-diphenyl-1-acetone (4e)

IR (KBr, cm^{-1}): 3398, 3023, 2935, 1675, 1509, 1485, 1366, 1307, 1275, 1119, 1073, 860, 755, 683, 518. ^{1}H-NMR (400 MHz, CDCl$_3$, δ/ppm): 3.40 (2H,m), 4.86 (1H,m), 6.36 (2H,d,J=7.9Hz), 7.08 (2H,d, J=8.26Hz), 7.19 (3H,m), 7.34 (2H, d, J=9Hz),7.39 (2H,m), 7.49 (1H,m), 7.84 (2H, d, J=7.95Hz); ^{13}C-NMR (400 MHz, CDCl$_3$, δ/ppm): 200.1, 146.5, 145.8, 140.5, 136.6, 133.1, 132.4, 131.2, 129.8, 129.5, 129.2, 128.9, 128.7, 128.3, 126.8, 120.6, 115.2, 114.6, 114.1, 72.5, 54.3. Anal Calcd for C$_{21}$H$_{18}$BrNO: C 66.31, N 3.66, H 4.76. Found: C 66.29, N 3.60, H 4.70%. HRMS (EI) Calcd. for C$_{21}$H$_{18}$BrNO [M]$^+$, 379.1000, Found 379.1005.

3-(N-Methyl-N-phenylamino)-1,3-diphenyl-1-acetone (4f)

IR (KBr, cm^{-1}): 3386, 3027, 2935, 1677, 1503, 1485, 1369, 1309, 1271, 1120, 1075, 862, 754, 687, 519. ^{1}H-NMR (400 MHz, CDCl$_3$, δ/ppm): 3.42 (2H, d), 4.94 (1H, m), 6.49 (2H, d),6.57 (1H,m), 7.03 (2H, m), 4.18(3H, s), 7.25 (2H, m), 7.35 (5H, m), 7.88 (2H, d); ^{13}C-NMR (400 MHz, CDCl$_3$, δ/ppm): 200.2, 149.5, 136.6, 133.2, 129.5, 128.7, 128.5, 128.3, 127.9, 121.8, 114.4, 58.8. IR (KBr, cm^{-1}): 3397, 3025, 2976, 1670, 1598, 1515, 1296, 1220, 1080, 1025, 1001, 865, 694, 511. Anal Calcd for C$_{22}$H$_{21}$NO: C 83.77, N 4.41, H 6.70. Found: C 83.71, N 4.37, H 6.79%. HRMS (EI) Calcd. for C$_{22}$H$_{21}$NO [M]$^+$, 315.2002, Found 315.1004.

2-[1-(N-Methyl-N-phenylamino)-1-phenyl] methylcyclohexanone (4g)

IR (KBr, cm^{-1}): 3398, 3010, 2925, 2810, 1673, 1597, 1505, 1312, 1115, 1047, 864, 695, 522. ^{1}H-NMR (400 MHz, CDCl$_3$, δ/ppm): 1.66 (2H, m), 1.89 (4H, m), 2.45 (2H, d), 2.76 (1H, t), 4.65 (3H, s), 6.54 (2H, d, J=7.90Hz), 6.64 (1H, m),7.06 (2H, m), 7.25 (1H, m), 7.32 (2H, m), 7.38 (2H, m), 7.42 (2H, d, J=7.9Hz); ^{13}C-NMR (400 MHz, CDCl$_3$, δ/ppm): 211.6, 149.7, 142.6, 129.6, 128.5, 128.1, 125.9, 114.4, 60.3, 41.1, 27.4. Anal Calcd for C$_{20}$H$_{23}$NO: C 81.88, N 4.77, H 7.90. Found: C 81.80, N 4.69, H 7.69%. HRMS (EI) Calcd. for C$_{20}$H$_{23}$NO [M]$^+$, 293.2004, Found 293.2007.

3-(N-*p*-Bromophenylamino)-1-phenyl] methylcyclohexanone (4h)

IR (KBr, cm^{-1}): 3398, 3010, 2925, 2812, 1675, 1599, 1505,1312, 1117, 1047, 863, 693,523. ^{1}H-NMR (400 MHz, CDCl$_3$, δ/ppm): 1.66 (2H, m), 1.89 (4H, m), 2.40 (2H, m), 2.75 (1H, m), 4.63 (1H, d, J=7.09Hz), 6.54 (2H, d, J=7.90Hz), 6.63 (1H, m),7.05 (2H, m), 7.23 (1H, m), 7.32 (2H, m), 7.39 (2H, m), 7.41 (2H, d, J=7.9Hz); ^{13}C-NMR (400 MHz, CDCl$_3$, δ/ppm): 211.6, 147.7, 139.5, 131.4, 129.5, 128.4, 120.8, 120.4, 113.5, 57.7, 55.8, 27.5. Anal Calcd for C$_{19}$H$_{20}$BrNO: C 63.71, N 3.90, H 5.62. Found: C 63.65, N 3.77, H 5.69%. HRMS (EI) Calcd. for C$_{19}$H$_{20}$BrNO [M]$^+$, 357.1002, Found 357.1006.

2-[1-(N-Phenylamino)-1-(3-chlorophenyl] methylcyclohexanone (4i)

IR (KBr, cm^{-1}): 3397, 3010, 2925, 2810, 1673, 1599, 1505, 1312, 1115, 1047, 863, 693,525. ^{1}H-NMR (400 MHz, CDCl$_3$, δ/ppm): 1.65 (2H, m), 1.90 (4H, m), 2.39 (2H, m), 2.76 (1H, m), 4.64 (1H, d, J=7.09Hz), 6.54 (2H, d, J=7.90Hz), 6.64 (1H, m),7.05 (2H, m), 7.25 (1H, m), 7.33 (2H, m), 7.39 (2H, m), 7.43 (2H, d, J=7.9Hz); ^{13}C-NMR (400 MHz, CDCl$_3$, δ/ppm): 211.6, 147.7, 141.8, 134.2, 129.5, 127.8, 126.3, 126.1, 126.0, 120.7, 113.6, 57.7, 55.4, 55.3, 41.1, 27.4. Anal Calcd for C$_{19}$H$_{20}$ClNO: C 72.70, N 4.45, H 6.40. Found: C 72.63, N 4.38, H 6.56%. HRMS (EI) Calcd. for C$_{19}$H$_{20}$ClNO [M]$^+$, 313.1001, Found 313.1008.

2-[1-(N-Phenylamino)-1-(3-bromophenyl] methylcyclohexanone (4j)

IR (KBr, cm^{-1}): 3397, 3011, 2925, 2810, 1675, 1598, 1506, 1310, 1117, 1046, 860, 695,523. ^{1}H-NMR (400 MHz, CDCl$_3$, δ/ppm): 1.66 (2H, m), 1.90 (4H, m), 2.39 (2H, m), 2.75 (1H, m), 4.64 (1H, d, J=7.09Hz), 6.54 (2H, d, J=7.90Hz), 6.63 (1H, m),7.05 (2H, m), 7.25 (1H, m), 7.32 (2H, m), 7.39 (2H, m), 7.42 (2H, d, J=7.9Hz); ^{13}C-NMR (400 MHz, CDCl$_3$, δ/ppm): 211.6, 147.7, 142.8, 132.6, 129.6, 129.3, 127.2, 120.8, 113.6, 57.9, 55.1, 24.4. Anal Calcd for C$_{19}$H$_{20}$BrNO: C 63.70, N 3.90, H 5.61. Found: C 63.62, N 3.73, H 5.79%. HRMS (EI) Calcd. for C$_{19}$H$_{20}$BrNO [M]$^+$, 357.1003, Found 357.1007.

2-[1-(N-Phenylamino)-1-phenyl] methylcyclohexanone (4k)

IR (KBr, cm^{-1}): 3396, 3010, 2925, 2810, 1675, 1598, 1507, 1312, 1115, 1045, 860, 694, 524. ^{1}H-NMR (400 MHz, CDCl$_3$, δ/ppm): 1.67 (2H, m), 1.90 (4H,m), 2.41 (2H, m), 2.75 (1H, m), 4.62 (1H, d, J=7.09Hz), 6.54 (2H, d, J=7.90Hz), 6.635 (1H, m),7.05 (2H, m), 7.25 (1H, m), 7.32 (2H, m), 7.39 (2H, m), 7.43 (2H, d, J=7.9Hz); ^{13}C-NMR (400 MHz, CDCl$_3$, δ/ppm): 211.7, 147.1, 142.5, 132.1, 129.5, 129.0, 127.6, 120.1, 113.5, 57.4, 55.0, 24.7. Anal Calcd for C$_{19}$H$_{21}$NO: C 81.66, N 5.00, H

7.55. Found: C 81.60, N 5.23, H 7.64%. HRMS (EI) Calcd. for $C_{19}H_{21}NO$ [M]$^+$, 279.2001, Found 279.2009.

1,3-Bis[1-(phenylamino)-3-oxo-3-phenylpropyl]-benzene (4l)

IR (KBr, cm^{-1}): 3340, 3077, 2955, 1676, 1594, 1528, 1380, 1312, 1281, 1214, 1187, 1168, 1076, 1113, 1077, 1016, 812, 738, 515; ^{1}H-NMR (400 MHz, CDCl$_3$, δ/ppm): 7.91 (m, 10H), 7.76 (m, 10H), 7.48 (s, 1H), 6.63 (m, 3H), 5.00 (m, 2H), 4.37 (m, 4H), 3.50 (m, 1H), 3.40 (m, 1H); ^{13}C-NMR (400 MHz, CDCl$_3$, δ/ppm): 207.05, 163.84, 148.50, 141.85, 131.17, 129.88, 128.53, 126.18, 122.51, 119.58, 117.23, 115.12, 114.28, 110.47, 50.88, 40.80; Anal Calcd for $C_{36}H_{33}N_2O_2$: C 82.28, H 6.29. Found: C 82.35, H 6.19. HRMS (EI) Calcd. for $C_{36}H_{33}N_2O_2$ [M]$^+$, 524.2004, Found 524.2008.

1,3-Bis[1-(methylphenylamino)-3-oxo-3-phenylpropyl]-benzene (4m)

IR (KBr, cm^{-1}): 3337, 3010, 2922, 2812, 1675, 1592, 1508, 1485, 1366, 1308, 1274, 1119, 1072, 863, 697, 520; ^{1}H-NMR (400 MHz, CDCl$_3$, δ/ppm): 7.96 (m, 10H), 7.53 (m, 10H), 6.67 (m, 3H), 5.05 (m, 2H), 4.38 (m, 4H), 3.51 (m, 1H), 3.46 (m, 1H), 2.04 (s, 6H); ^{13}C-NMR (400 MHz, CDCl$_3$, δ/ppm): 206.95, 165.84, 149.20, 142.05, 131.47, 129.19, 129.13, 127.01, 122.61, 119.58, 118.11, 115.42, 113.98, 111.23, 50.78, 40.76, 25.12; Anal Calcd for $C_{38}H_{36}N_2O_2$: C 82.46, H 6.69. Found: C 82.55, H 6.61. HRMS (EI) Calcd. for $C_{38}H_{36}N_2O_2$ [M]$^+$, 552.3001, Found 552.3005.

1,3-Bis[1-(4-methylphenylamino)-3-oxo-3-phenylpropyl]-benzene (4n)

IR (KBr, cm^{-1}): 3337, 3012, 2925, 2810, 1675, 1594, 1508, 1486, 1367, 1309, 1273, 1119, 1070, 864, 699, 522; ^{1}H-NMR (400 MHz, CDCl$_3$, δ/ppm): 7.89 (m, 10H), 7.39 (m, 10H), 6.61 (m, 3H), 4.92 (m, 2H), 4.27 (m, 4H), 3.52 (m, 1H), 3.28 (m, 1H), 1.30 (S, 6H); ^{13}C-NMR (400 MHz, CDCl$_3$, δ/ppm): 206.93, 165.84, 149.24, 142.13, 131.27, 129.21, 129.83, 127.11, 122.64, 119.61, 118.21, 115.32, 113.98, 111.23, 50.77, 40.77, 25.13; Anal Calcd for $C_{38}H_{36}N_2O_2$: C 82.46, H 6.69. Found: C 82.52, H 6.63. HRMS (EI) Calcd. for $C_{38}H_{36}N_2O_2$ [M]$^+$, 552.3001, Found 552.3005.

1,3-Bis[1-(3-bromatedphenylamino)-3-oxo-3-phenylpropyl]-benzene (4o)

IR (KBr, cm^{-1}): 3338, 3020, 2936, 1677, 1508, 1485, 1369, 1305, 1274, 1119, 1073, 859, 755, 684, 517; ^{1}H-NMR (400 MHz, CDCl$_3$, δ/ppm): 8.11 (m, 4H), 8.01 (m, 4H), 7.84 (m, 10H), 7.51 (m, 4H), 7.47 (s, 2H), 4.42 (m, 4H), 3.56 (m, 1H), 3.52 (m, 1H); ^{13}C-NMR (400 MHz, CDCl$_3$, δ/ppm): 206.93, 165.85, 149.33, 142.15, 131.57, 129.61, 129.93, 127.16, 122.69, 119.51, 118.32, 115.42, 113.95,

111.41, 50.69, 40.87; Anal Calcd for $C_{36}H_{30}N_2O_2Br_2$: C 63.34, H 4.40. Found: C 63.39, H 4.39. HRMS (EI) Calcd. for $C_{36}H_{30}N_2O_2Br_2$ [M]$^+$, 680.1005, Found 680.1008.

Catalyst preparation

Zinc oxide nanoparticles used in the experiments were produced according to the procedure [30] modified as follows. Zinc powder 0.019 g (0.3 mmol) in dust form was sonicated for 2 h with 4 mL of *n*-butanol. To the above solution, 1.2 mL of triethanolamine (TEA) was added slowly. It was then sonicated for ten more minutes. Finally, the mixture was irradiated in a closed vessel mono-mode microwave reactor at 140°C and 10.9 bar for 6 min. The obtained white solid suspension was centrifuged, washed several times with distilled water and vacuum dried. After calcination at 900°C for 1 h the product could be stored for an extended period of time. It was characterized using scanning electron microscopy (SEM), and X-ray powder diffraction (XRD) techniques.

RESULTS AND DISCUSSION

In general, nanoparticles are considered to be more reactive because they offer higher surface area and more coordination sites. The surface area of the catalyst increases tremendously when the size decreases to nano levels which are responsible for the higher catalytic activity. Studies on the interaction of alcohols with Zn metal have revealed that the C–O bond of the alcohol is readily cleaved on the zinc metal surface giving hydrocarbons and oxide species on the metal surface [31]. The structure directing additive is a common approach to control morphology, as shown by the effect of ethylene diamine in hydrothermal ZnO nanorod synthesis. Di- and tri-organic amines, as well as long-chain glycols are reported to promote rod-like morphologies by increasing the base content during synthesis [32]. Thus, triethanol amine was used as size stabilizer and was found effective in directing the morphology of ZnO nanoparticles. The obtained particles were characterized by X-ray powder diffraction (XRD) (Figure 2). The XRD pattern of the newly prepared zinc oxide nanoparticles showed the presence of peaks corresponding to hexagonal wurtzite structure [33]. The size of the particles was computed from the width of the first peak using the Debye-Scherrer formula D = K λ/β COS θ, where K is a constant, λ is the wavelength of X-ray radiation (1.54056 Å), β is the corrected full width at half maximum and θ is Bragg angle. The 2θ value is 19.0104.
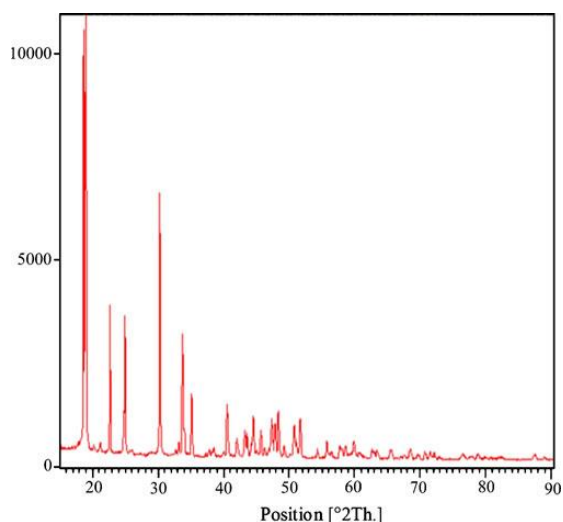
Fig. 2. XRD pattern of the ZnO nanoparticles.

Surface structure of all samples was characterized on a Nicolet Avatar 360 Fourier transform infrared (FT-IR) spectroscope. Measurements were performed with pressed pellets using KBr powder as a diluent. The FT-IR spectrum was recorded in the range between 400 and 4000 cm^{-1}. The crystallite size of the powder particles was calculated as about 30 nm. The morphology of the sample was investigated with scanning electron microscopy (SEM) (see Figure 3) which showed ZnO to be nanostructured. This may be the result of the presence of a small amount of

triethanolamine, which acts as a stabilizer. These nanoparticles are generally not uniform, very similar to those described in the literature [32].

In order to evaluate the catalytic efficiency of ZnO nanoparticles, a model reaction was carried out on the synthesis of Mannich base **4a** by condensation of acetophenone, benzaldehyde and aniline (Scheme 1). The results of the synthesis of (1,3-diphenyl-3-(phenylamino)propan-1-one (**4a**) using various catalysts are shown in Table 1. As Table 1 indicates, the reaction proceeded efficiently in the presence of ZnO nanoparticles catalyst and the desired product (**4a**) was obtained in good to excellent yield, 94% (Table 1, entry 1). In the absence of catalyst, the reaction did not procee (Table 1, entry 9).

With the optimized of amount of catalyst, we found that 10 mol% of ZnO nanoparticles could effectively catalyze the reaction for synthesis of the desired product. Using 5 mol% of ZnO nanoparticles, the reaction took place for a longer time. Using more than 20 mol% ZnO nanoparticles had a weaker effect on the yield and time of the reaction. It is remarkable that the reaction carried out by changing the size of the particles from nanoparticles to bulk resulted in a drop in the catalytic activity. It is interesting to note that the ZnO nanoparticle catalyst catalyses the reaction in excellent yield within a shorter reaction time than the bulk (Table 2).

Fig. 3. Scanning electron microscopy (SEM) image of the synthesized ZnO nanoparticles.
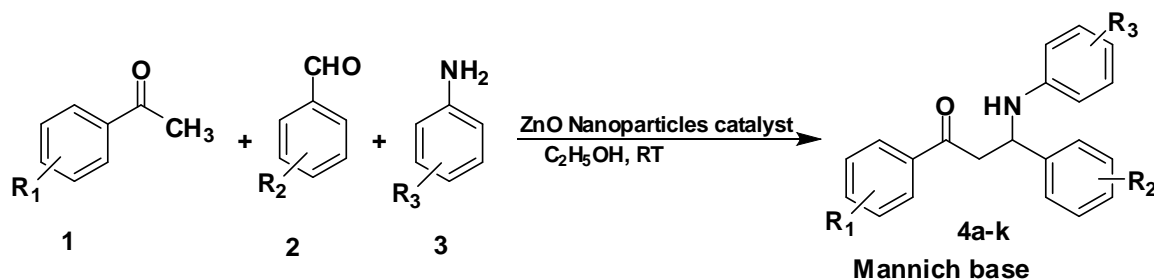
Scheme 1. Synthesis of β-amino carbonyl compounds from amines, acetophenone and aldehydes catalyzed by ZnO nanoparticles catalyst

490

Table 1. Mannich reaction in the synthesis of (1,3-diphenyl-3-(phenylamino)propan-1-one (**4a**) with various catalysts

Entry	Catalyst	Time (h)	[a]Yield (%)
1	ZnO nanoparticles	1	94
2	$SnCl_2.2H_2O$	12	71
3	$Fe_2(SO_4)_3.6H_2O$	12	0
4	$Al_2(SO_4)_3.18H_2O$	14	0
5	$AlCl_3.6H_2O$	4	85
6	$CeCl_3.7H_2O$	15	57
7	$Zn(OAc)_2.2H_2O$	14	0
8	CH_3COOH	27	0
9	Free	24	0

[a]Isolated yield.

Table 2. Optimization of the ZnO nanoparticles catalysed model reaction for the synthesis of 1,3-diphenyl-3-(phenylamino)propan-1-one (4a).

Entry	Catalyst (mol %)	Time (h)	[a]Yields(%)
1	Free (No catalyst)	19	0
2	ZnO nano (5%)	4	60[b]
3	ZnO nano (10%)	1	94[b]
4	ZnO nano (20%)	2.5	74[c]
5	ZnO bulk (10%)	6.5	36.5[b]
6	ZnO nano (20%)	3.5	71[d]
7	ZnO nano (30%)	4	68.5[c]
8	ZnO nano (30%)	5	57.5[d]
9	ZnO nano (40%)	6	52[c]
10	ZnO nano (40%)	7.5	46[d]

[a]Isolated yield; [b]Reaction was carried out at room temperature; [c]Reaction was carried out at 70°C; [d]Reaction was carried out at 80°C

Effect of catalyst

When the experiment was conducted at room temperature, the corresponding product was generated with a good yield (Table 2, entries 2, 3, 5). The effect of temperature was studied by carrying out the reactions at different temperatures [room temperature (25 ºC), 70 and 80 ºC] and various moles (10, 20, 30 and 40 mol%). As Table **2** shows, by raising the reaction temperature from ambient temperature (25 ºC) to 70 and 80 ºC, the yield decreased. From these results, it was concluded that 25 ºC would be the best temperature for all reactions. In other words, any further increase in the amount of the catalyst and temperature would have a negative effect on the reaction yield. From these experiments we found that the optimum reaction conditions are: 10 mol% catalyst and room temperature. Different types of amines with either electron pumping or electron withdrawing groups were subjected to Mannich condensation reactions with various ketones (aromatic and alicyclic) and various aldehydes (aromatic and alicyclic) with either electron pumping or electron withdrawing substituents, in the presence of ZnO nanoparticles under solvent-free conditions at room temperature. To compare the efficiency of solvent-free *vs.* solution conditions, the reaction was examined in several solvents. Thus, a mixture of benzaldehyde, acetophenone, aniline and ZnO nanoparticles catalyst at room temperature in different solvents was used. The results are depicted in Table 3. As it is seen, lower yields and longer reaction times are observed in solution conditions. Therefore, the solvent-free method is more efficient. To investigate the versatility and capacity of the present method, the reactions of amines were examined with ketones and aldehydes at room temperature (Table 4). As Table 4 indicates, the reactions proceeded efficiently and the desired products were obtained in good to excellent yields (compound **4a**).
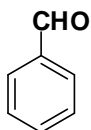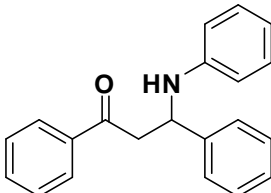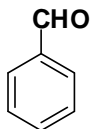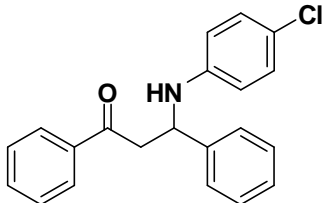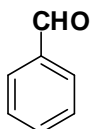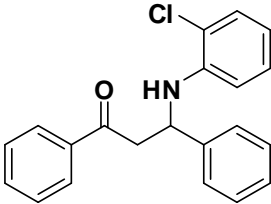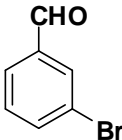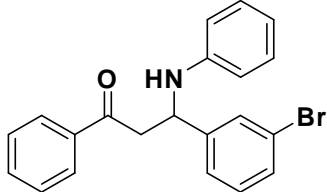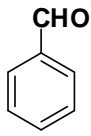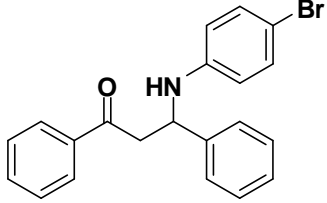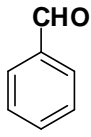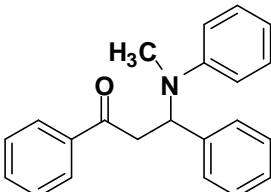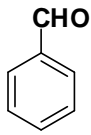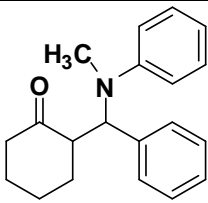
Table 3. Effect of solvents on the condensation between benzaldehyde, acetophenone and aniline in the presence of ZnO nanoparticles at room temperature, (4a).
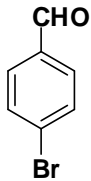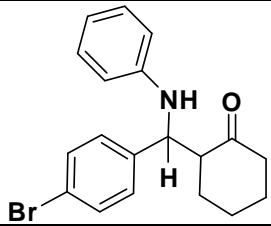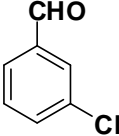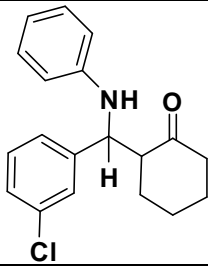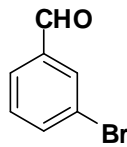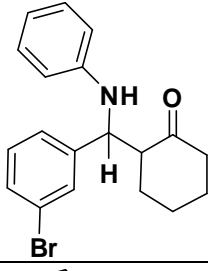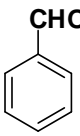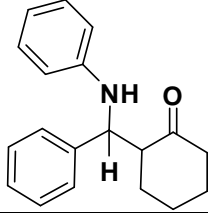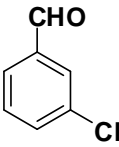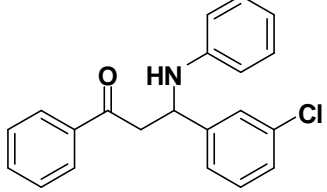
Entry	Solvents	Time (h)	[a,b]Yield (%)
1	Free	1	94
2	CH_3CN	5	84
3	CH_3OH	3	81
4	$C_6H_5CH_3$	3	29
5	C_2H_5OH	3	88
6	H_2O	9	41
7	DMF	5	27
8	Dioxane	5	32
9	THF	6	30
10	DMSO	4.5	31

[a]Reaction conditions: aniline (0.2 mmol), acetophenone (0.2 mmol) and aldehyde (2 mmol); catalyst: ZnO nanoparticles (10 mol%); reaction temperature: 25 ºC;
[b]Isolated yield of 1,3-diphenyl-3-(phenylamino)propan-1-one.

A wide variety of aromatic ketones, aromatic aldehydes and aromatic amines were tested to establish the scope of this catalytic transformation (Table 4). In all cases it was observed that the reactions proceed smoothly at room temperature. Besides ortho-substituted aromatic amine, the aromatic ketones, aromatic aldehydes and aromatic amines bearing both electron donating and electron withdrawing groups underwent this one-pot three components condensation to furnish the corresponding Mannich base in high yields. Particularly, substituents having weak electron-donating groups such as –Cl are favorable for the transformation. Meta-substituted and para-substituted aromatic amines all gave good results, but ortho-substituted aromatic amine afforded the corresponding Mannich base in a moderate yield after long reaction time because of a large steric hindrance effect (Table 4, entry 3).

Table 4. Synthesis of β-amino carbonyl compounds from amines, ketones, and aldehydes at room temperature over ZnO nanoparticles catalyst

Entry	Aldehyde	Product	Time (h)	[a,b]Yield (%)	m.p.°C (lit)
1	CHO		1	94(94, 93,91, 90.5)[c]	168-170(119)[33]
2	CHO		1	90	169-71 (170-71) [32,33]
3	CHO		17	59	115-116
4	CHO		11	96(96, 95, 94, 93.5)[c]	165-168
5	CHO			92.5	178-180(178)[32]
6	CHO		1	97(96, 95, 94, 92.5)[c]	135-137
7	CHO		1	96	149-151

8	CHO / Br (benzaldehyde)	NH, O, H, Br structure	1	94	141-143
9	CHO / Cl	NH, O, H, Cl structure	1	92	130-132
10	CHO / Br	NH, O, H, Br structure	1	97	134-135
11	CHO	NH, O, H structure	1	91	128-129(129)[33]
12	CHO / Cl	O, HN, Cl structure	2.5	96	119-120(119)[33]

[a]Reaction conditions: amines (0.2 mmol), ketones (0.2 mmol) and aldehydes (0.2 mmol)
[b]Isolated yield. [c]Yield of catalyst recycled four times

Based on such a good result, we tested isophthalic aldehyde and aniline under the same conditions and found that they also possessed good activity in the reaction. However, so far, attention has been paid mainly to the synthesis of mono-functional β-amino carbonyl compounds derivatives, and *β1,β2*-diamino diketone compounds were seldom investigated. Therefore, we firstly synthesized *β1,β2*-diamino diketone compounds and their derivatives with good yields (Scheme 2).
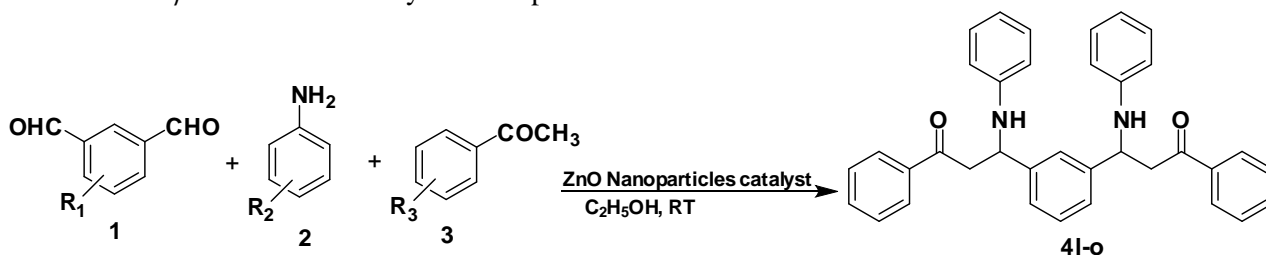
Scheme 2. Synthesis of β1,β2-diamino diketone compounds from amines, acetophenone and isophthalic aldehyde catalyzed by ZnO nanoparticles catalyst

With the best catalyst in hand, further experiments were carried out to test the different parameters affecting the reaction system. So the effect of reaction temperature, time, and solvents was tested. Additionally, aromatic aldehydes with different structures were tested, and their activities in this system were compared, too. These results showed that solvent-free conditions were the best (Table 3, entry 1). Various aldehydes, amines and ketones catalyzed by ZnO nanoparticles at ambient temperature (Table 4) were found to be efficient. The following features were excellent in these reactions: (1) A 1:1:1 mixture of benzaldehyde, aniline, and acetophenone with 10 mmol% of ZnO nanoparticles gave the Mannich adduct in 94% yield (Table 4, entry 1). All examined amines could readily react with acetophenone and aldehyde to give the corresponding β-amino carbonyl compounds with good yields. Using 4-methyl aniline as a substrate, the yields of β-amino carbonyl compounds were nearly the same as using aniline as a substrate, which indicated the good activity of ZnO nanoparticles for β-amino carbonyl compounds synthesis (Table 4, entry 4). An important feature was that all products listed in Table 4 could be simply separated. Monoaldehydes, as well as dialdehydes reacted well with amines and ketones, and dialdehydes behaved similarly to monoaldehydes. When isophthalic aldehyde reacted with lower steric hindrance amines, good yields were obtained. However, when it reacted with N-methylaniline, the yields of *β1,β2*-diamino diketone compounds were relatively low, which showed the importance of the electronic effect upon these reactions (Table 5, Entries 1-4).

Table 5. Synthesis of β1,β2-diamino diketone compounds from aniline, acetophenone, and aldehyde at room temperature over ZnO nanoparticles catalyst

Entry	Aldehyde	Product	Time (h)	[a]Yield (%)	m.p.$^{\circ}$C
1			4.5	87.5	164-166
2			12.5	64	172-175
3			5	92	184-186
4			5.5	95.5	198-200

[a]Reaction conditions: aniline (0.2 mmol), acetophenone (0.2 mmol) and isophthalic aldehyde (0.2 mmol); catalyst: ZnO nanoparticles (10 mol%); reaction temperature: room temperature; reaction solvent: EtOH.
[b]Isolated yield

3. 1. Regeneration of catalyst

To examine the reusability, the catalyst recovered by filtration from the reaction mixture after dilution with ethyl acetate was reused in subsequent experiments (up to four cycles) under similar reaction conditions. The product yields remained comparable in these experiments (Figure 4), which points to the recyclability and reusability of the catalyst without significant loss of activity.
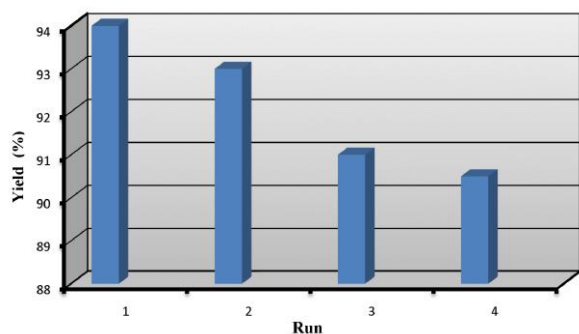

Fig. 4. Recyclability of ZnO nanoparticles catalyst for the synthesis of 1,3-diphenyl-3-(phenylamino)propan-1-one (**4a**).

CONCLUSION

Three-component reactions of aldehydes, ketones and various amines were efficiently catalyzed by ZnO nanoparticles in organic solvents. Aromatic and aliphatic aldehydes all reacted with good yields. ZnO nanoparticles played an important role in acceleration of the reactions. So, ZnO nanoparticles behaved as a green catalyst in Mannich reactions. The ZnO nanoparticles were used to catalyze Mannich reactions under solvent-free conditions to afford the corresponding β-amino carbonyl compound (Mannich base) in excellent yields in a shorter time. The ZnO nanoparticles were easily separated from the reaction mixture by extraction with ether. The ZnO nanoparticles are reusable several times without any significant loss in potentiality. We have demonstrated an efficient and environmentally friendly approach for the synthesis of β-amino carbonyl compounds *via* one-pot three-component condensation of aromatic ketones, aromatic aldehydes and aromatic amines using ZnO nanoparticles as a recyclable catalyst. High yields, reduced reaction time, mild reaction condition, easy work-up procedure, inexpensive and commercially available catalyst make this approach an interesting alternative to the existing methods. The present method is a very efficient and selective protocol for Mannich condensation reactions of various aldehydes, amines and ketones in the presence of a reusable and environmentally benign catalyst. We have developed an efficient, facile and environmentally acceptable methodology for the synthesis of coumarin derivatives using ZnO nanoparticles catalyst under solvent-free conditions. The advantages of this environmentally benign and safe protocol include a simple reaction setup, very mild reaction conditions, high product yields, short reaction times, possibility for reusing the catalyst, selectivity and solvent-free conditions.

REFERENCES

1. T. Aoyagi, H. Umezawa, In Proteases and Biological Control; E. Reich, D. B. Rifkin, E. Shaw, Eds.; Cold Spring Harbor Press: Cold Spring Harbor, 1975; pp. 429-454.
2. D. Rasnick, *Perspect. Drug Discovery Des,* 647 (1996).
3. S. Mehdi, *Bioorg. Chem,* 21, 249 (1993).
4. D. S. Yamashita, *J. Am. Chem. Soc*, 119, 11351 (1997).
5. J. Barluenga, A. L. Viado, E. Aguilar, S. Fustero, B. Olano, *Journal of Organic Chemistry*, **58**, 5972 (1993).
6. D. Enders, M. Moser, G. Geibel, M. C. Laufer, *Synthesis*, **12**, 2040 (2004).
7. M. Mukhopadhyay, B. Bhatia, J. Iqbal, *Tetrahedron Letters*, **38**, 1083, (1997).
8. K. Kobinata, M. Uramoto, M. Nishii, H. Kusakabe, G. Nakamura, K. Isono, *Agricultural and Biological Chemistry*, **44**, 1709 (1980).
9. U. Daehn, H. Hagenmaier, H. Hoehne, W. A. Koenig, G. Wolf, H. Zaehner, *Archives of Microbiology*, **107**, 143 (1976).
10. H. R. Shaterian, A. Hosseinian, M. Ghashang, *Synthetic Communications*, **38**, 3766 (2008).
11. M. M. Khodaei, A. R.Khosropour, P. Fattahpour, *Tetrahedron Letters*, **46**, 2105 (2005).
12. A. T. Khan, T. Parvin, L. H. Choudhury, *Journal of Organic Chemistry*, **73**, 8398 (2008).
13. M. M. Heravi, L. Ranjbar, F. Derikvand, F. F. Bamoharram, *Journal of Molecular Catalysis A*, **271**, 28 (2007).
14. B. Das, K. R. Reddy, Y. Srinivas, R. A. Kumar, *Canadian Journal of Chemistry*, **85**, 479 (2007).
15. X. Wang, H. Mao, Y. Yu, X. Zhu, C. Zhu, *Synthetic Communications*, **37**, 3751 (2007).
16. B. Das, K. R. Reddy, *Helvetica Chimica Acta*, **89**, 3109 (2006).
17. L.W. Xu, C. G. Xia, L. Li, *Journal of Organic Chemistry*, **69**, 8482 (2004).
18. B. A. Bunin, *The Combinatorial Index*, Academic Press, New York, NY, USA, 1998.
19. A. W. Czarnik, S. H. DeWitt, Eds., *A Practical Guide to Combinatorial Chemistry*, American Chemical Society, Washington, DC, USA, 1997.
20. K. C. Nicolaou, R. Hanko, W. Hartwig, *Handbook of Combinatorial Chemistry*, Wiley-VCH, Weinheim, Germany, 2002.
21. I. Saxena, D. C. Borah, J. C. Sarma, *Tetrahedron Letters*, **46**, 1159 (2005).
22. S. Caddick, *Tetrahedron*, 51, 10403 (1995).

23. D. M. P. Mingos, Microwaves in chemical synthesis, *Chemistry and Industry*, **596** (1994).
24. M. Larhed, C. Moberg, A. Hallberg, **35**, 717 (2002).
25. P. Phukan, D. Kataki, P. Chakraborty, *Tetrahedron Letters*, **47**, 5523 (2006).
26. K. R. Harikumar, C. N. R. Rao, *Phys. J. Chem. B.* **103**, 2445 (1999).
27. M. A. Shah, *African Phys. Rev.*, **2,** 0011 (2008).
28. B. Liu, H. C. Zeng, *JACS Commun.*, **125,** 4430 (2003).

29. C-H. Lu, C-H.Yeh, *Ceram. Int.* **26,** 35 (2000).
30. E. Rafiee, S. Eavani, F. Khajooei Nejad, M. Joshaghani, *Tetrahedron*, **66**, 6858 (2010).
31. Z. Li, X. L. Ma, J. Liu, X. Feng, G. Q. Tian, A. G. Zhu, *J. Mol. Catal. A: Chem,* 272 (2007.)
32. H. Wu, X.M. Chen, Y. Wan, L. Ye, H.Q. Xin, H.H. Xu, C.H. Yue, L.I. Pang, R. Ma, D. Shi, *Tetrahedron Lett.,* **50**, 1062 (2009).

СИНТЕЗА НА β–АМИНО-КАРБОНИЛНИ СЪЕДИНЕНИЯ ИЗПОЛЗВАЙКИ НАНОЧАСТИЦИ ОТ ZNO КАТО ЗЕЛЕН, ЕФЕКТИВЕН И МНОГОКРАТНО УПОТРЕБЯВАН КАТАЛИЗАТОР

А. Гариб [1,2], Н. Норузи Песян [3], Л. Вожданифард [4], М. Джахангир[1], М. Рошани[1], С. Могадаси[2],

[1]*Департамент по химия, Ислямски университет „Азад“, Машхад, Иран*
[2]*Център по земеделски изследвания и услуги, Машхад, Иран*
[3] *Департамент по химия, Научен факултет, Университет Урмиа, 57159, Урмиа, Иран*
[4]*Образователна организация на Разави Кхорасан, Министерство на образованието, Машхад, Иран*

(Резюме)

Описана е нова едноетапна и ефективна трикомпонентна кондензация на ароматни алдехиди, ароматни кетони и ароматни амини в присъствие на наночастици от ZnO като евтин и ефективен катализатор за синтезата на β-амино-карбонилни съединения по реакцията на Mannich. Реакцията протича при стайна температура без разтворител. Умерената температура, евтиният катализатор, лесното отделяне на продуктите и рециклирането на катализатора са главните постижения при тази реакция. Простите експериментални условия и процедурата по изолирането на продуктите прави този метод приложим за разработването на чиста и екологически съвместима стратегия за синтезата на β-кетони. Настоящата методология предлага няколко предимства: добър добив, кратко реакционно време и рециклируем катализатор.

Development and validation of a potentiometric titration method for the determination of montelukast sodium in a pharmaceutical preparation and its protonation constant

N. Aslan, P. E. Erden, E. Canel, E. Kilic

Department of Chemistry, Faculty of Science, Ankara University, Ankara, TURKEY

In this study, a potentiometric titration method for the determination of montelukast sodium in pharmaceutical dosage forms was developed and validated. For this purpose, the potentiometric titration of the standard montelukast sodium was carried out using hydrochloric acid as titrant. The method was found to be highly accurate and precise, having a relative standard deviation of less than 1.0%. From the titration data the stoichiometric protonation constant was calculated in 40% ethanol−60% water and 60% ethanol−40% water (v/v) mixtures at constant temperature of 25.0 ± 0.1 °C and ionic strength of 1.0×10^{-1} M NaCl. The protonation constant was found to be 6.25 in 40% ethanol−60% (v/v) water mixture and 5.95 in 60% ethanol-40% (v/v) water mixture. Furthermore, it was shown that the method could be successfully applied to the assay of commercial pharmaceuticals containing 10.0 mg montelukast sodium. The validity of the method was tested by recovery studies of standard additions to a tablet solution and the results were found to be highly satisfactory. This titration method is simple, rapid, accurate, precise and low cost for quality controls of commercial pharmaceutical dosage forms.

Keywords: Montelukast sodium; potentiometric titration; pharmaceutical dosage, ethanol-water mixture.

INTRODUCTION

Montelukast is an oral selective leukotriene receptor antagonist [1,2] which is being used in the treatment of asthma. It belongs to a styryl-quinolines series with the chemical name {sodium salt of 2-[1-[[(1R)-1-[3-[2-(7-chloroquinolin-2-yl)ethenyl]phenyl]-3-[2-(2-hydroxypropan-2-yl) phenyl] propyl] sulfanylmethyl] cyclopropyl] acetic acid} (Fig.1). It was developed by Merck as a therapeutic agent for the treatment of bronchial asthma [3] by means of once daily oral administration.
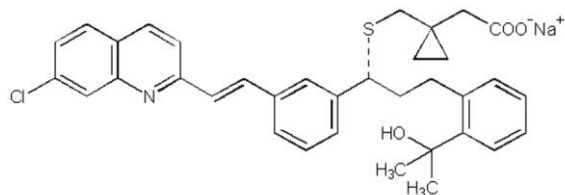

Fig.1. Chemical structure of montelukast sodium

The main objective of this paper is to propose a selective and validated potentiometric method for determining montelukast sodium and applying it to pharmaceutical dosage forms. A variety of analytical methods dedicated to the analysis of montelukast sodium have been previously reported.

Most of them involve spectrophotometry [4], capillary electrophoresis [3], high performance liquid chromatography (HPLC) [5], high performance thin layer chromatography (HPTLC) [6], voltammetry [7]. Literature survey reveals that there are no potentiometric titration methods for the determination of montelukast sodium in ethanol-water mixture in pharmaceutical dosage forms. The analytical method reported here was validated considering linearity, accuracy and precision.

In this study, the stoichiometric protonation constants of montelukast sodium in 40% ethanol−%60 water (v/v) and 60% ethanol−%40 water (v/v) mixtures were determined. In pharmacology, ionization of a compound alters its physical behaviour and macro properties such as solubility and lipophilicity. For example, ionization of any compound will increase the solubility in water and decrease the lipophilicity. This is exploited in drug development to increase the concentration of a compound in the blood by adjusting the pK_a of an ionizable group [8]. The determination of the stoichiometric protonation constants of montelukast sodium is very important also from the point of absorption, distribution and elimination of the drug which is orally administered. The effective use of this compound depends greatly upon our knowledge of its ionization constants. There is only one study on the potentiometric determination of pKa constants of

---

* To whom all correspondence should be sent:
E-mail: naslan70@gmail.com

montelukast sodium, which was performed in the 40% dioxane − 60% water (v/v) solvent mixture [1]. This study is therefore expected to provide an important addition to the data that already exist in the literature. It is thought that the data obtained in 1.0×10^{-1} M NaCl, which simulates the ionic strength of biological media, will be very useful for determining the effective mechanism of this compound which has significant pharmaceutical potential. The data related to protonation constants in different organic-solvent mixtures will be valuable in the further understanding of biological systems.

There are various techniques such as potentiometry, conductometry and spectrophotometry used in the determination of protonation constants. In this study potentiometric technique was employed since it has the widest area of application and reliability [9-12].

EXPERIMENTAL

Chemicals and standard solutions

Montelukast sodium was purchased from Merck and it was used as a standard. Ethanol, hydrochloric acid, sodium hydroxide, potassium hydrogen phthalate and sodium chloride were of analytical grade (Merck) and were used without further purification.

Onceair: Tablet formulation containing montelukast sodium equivalent to montelukast 10 mg per tablet (Abdi İbrahim, Turkey) was procured from the local pharmacy.

Standard sodium hydroxide solution: Solution of standard base containing 1.0×10^{-1} M NaCl was prepared in the ethanol-water mixtures examined (v/v) and was standardized potentiometrically against potassium hydrogen phthalate (Merck) using Gran's plot techniques [13-14].

Standard hydrochloric acid solution: Acid solution prepared in redistilled low-conductivity water was standardized by titration against standardized sodium hydroxide solution.

Standard montelukast sodium solution: Standard stock solution of montelukast sodium was prepared at a concentration of 1.0×10^{-2} M in ethanol. The montelukast sodium solution used in potentiometric titration was prepared by dilution of the stock solution with ethanol. Montelukast sodium is a light-sensitive compound; therefore the stock solution was prepared daily and kept in amber glass volumetric flask to protect from light [3].

Tablet solution: Twenty eight Onceair tablets were weighed and their average weight was calculated. All tablets were finely powdered in a mortar and homogenized. The required amount of this powder was transferred to a 100.0 mL volumetric flask. 80.0 mL of ethanol was added to the same flask, sonicated for at least thirty minutes to ensure complete dissolution and diluted to 100.0 mL with ethanol.

Equipment

All potentiometric measurements were performed in an 80-mL jacketed titration cell thermostated at 25.0 ± 0.1°C. An Orion 940A Model pH-ion meter (Beverly, MA, USA) fitted with a combined pH electrode (Ingold) containing a filling solution of 1.0×10^{-1} M NaCl was used for measuring the cell emf values. The titrant, hydrochloric acid, was added by using Orion 960 Autochemistry system. The potentiometric cell was calibrated before each experiment so that the hydrogen ion concentration rather than the activity was measured [15-16]. For the ethanol-water solvent mixtures studied, reproducible values of autoprotolysis constants (K_{ap}) were calculated from several series of [H^+] and [OH^-] measurements at a constant ionic strength of 1.0×10^{-1} M NaCl [17-19].

The following solutions prepared in water and each of the solvent mixtures studied (total volume = 50.0 mL) were titrated potentiometrically with standard 5.0×10^{-2} M HCl dissolved in the corresponding solvents: (i) 5.0×10^{-2} M NaOH (for cell calibration); (ii) 1.0×10^{-3} M montelukast sodium. During each titration the ionic strength was maintained at 1.0×10^{-1} M NaCl and a potential reading was taken after a suitable time (normally 2-3 min) for equilibration.

The protonation constants of the montelukast sodium were determined by a method described by Irving and Rossotti [20]. The average of protons associated with the ligand (n_A) at different pH values was calculated by analyzing the titration data for 40% ethanol−%60 water and 60% ethanol−%40 water mixtures. The pKa values were calculated from the curve obtained by plotting n_A versus pH.

The content of montelukast sodium in the pharmaceutical preparations was estimated via potentiometric titration with standardized hydrochloric acid solution under the same conditions described for the standard montelukast sodium.

RESULTS AND DISCUSSION

Potentiometry

Method development

For potentiometric analysis, different organic solvents and organic solvent-water mixtures were

tried to obtain the best potentiometric titration curve. 40% ethanol−60% water (v/v) mixture was found to be an appropriate medium for the potentiometric titration of montelukast sodium.

In this study assay of tablets, recovery and precision studies were performed using the experimental conditions described. Protonation constant of montelukast sodium was determined in 40% and 60% ethanol−water (v/v) mixtures and the effect of solvent upon the protonation constant was investigated.

Protonation constants of montelukast sodium

The stoichiometric protonation constants were determined with an electrochemical cell calibrated in each medium to measure the hydrogen ion concentration. For this purpose, firstly, the hydrochloric acid solutions were titrated with the sodium hydroxide solutions prepared in each medium and the potential values were plotted against the logarithm of the hydrogen ion concentration to determine the calibration constants (E' and k). The calibration constants obtained from these curves are tabulated in Table 1, which shows that the glass electrode used in ethanol-water mixtures gave a Nernstian response with a slope of (59.1 ± 0.1) mV. Therefore, it was concluded that the electrode could be used to determine the stoichiometric protonation constant for all media.

Table 1. Calibration constants obtained in 40% ethanol–60% water (v/v) and 60% ethanol–40% water (v/v) mixtures with a combined glass pH electrode.

Medium	Calibration constant (n=3)	
	$E'_{(mean)}$ (mV)	k (mV-pH^{-1})
40% ethanol – 60% water	340.3 ± 1.9	59.1 ± 0.1
60% ethanol – 40% water	333.9 ± 1.2	59.0 ± 0.1

n, is number of analyses

The autoprotolysis constants (K_{ap}) for each medium were determined using the same acid-base titration data and are tabulated in Table 2. It was observed that the value obtained was found to be in good agreement with those reported in the literature [21-22].

Table 2. Autoprotolysis constants obtained in 40% ethanol–60% water (v/v) and 60% ethanol–40% water (v/v) mixtures.

Medium	pK_{ap}	pK_{ap} (in literature)
40% ethanol – 60% water	14.15 ± 0.01	14.24 [21]
60% ethanol – 40% water	14.32 ± 0.01	14.39 [21]

As there are a very limited number of studies related to the protonation constants of montelukast sodium, [1], the data obtained in this study will make an important contribution to the literature. Especially the protonation constants obtained in 1.0×10^{-1} M NaCl medium, which simulates biological systems, will shed light on the reaction mechanisms in biological reactions of montelukast sodium.

In the literature, two protonation constants of montelukast sodium are given [1]. However, in our study, we found one protonation constant for montelukast sodium. As can be seen from Fig. 4, the formation curve (n_A-pH) was found between 0 and 1. This indicates that the $\log_{10}K$ value of only one of the two protons could be determined for the ethanol-water mixtures studied.
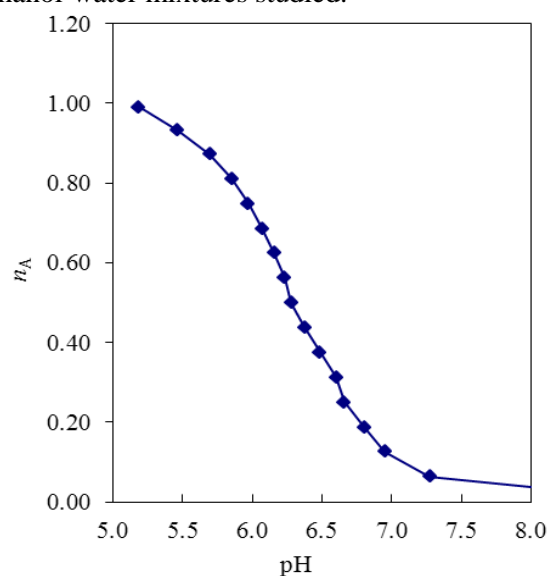

Fig. 4 nA-pH curves from the potentiometric titration of montelukast sodium standard in 40% ethanol-60% water (v/v) mixture. (I = 1.0×10^{-1} M NaCl; t = 25.0 ± 0.1 °C)

The numerical values of the protonation constant of montelukast sodium determined potentiometrically in 1.0×10^{-1} M NaCl at 25 °C are listed in Table 3.

Table 3. The stoichiometric protonation constants of montelukast sodium at 25.0 (± 0.1) °C for different ethanol-water (v/v) mixtures (I = 1.0×10^{-1} M NaCl).

40% ethanol-60% water	60% ethanol-40% water
$\log_{10}K_1 \pm$ S.D.	$\log_{10}K_1 \pm$ S.D.
6.25 ± 0.03	5.95 ± 0.02

S.D. is standard deviation

The determinations were carried out in 40% and 60% ethanol−water (v/v) mixtures. The resulting stoichiometric protonation constants were calculated by the Irving-Rossotti method [20]. An example of the n_A − pH curve of montelukast

sodium obtained from the experimental data is given in Figure 4.

The protonation constants given in Table 3 are defined by Equation 1 where B^- represents the montelukast anion:

$$B^- + H^+ \rightleftharpoons HB \quad K_1 = [HB]/[B^-][H^+] \tag{1}$$

where $\log_{10}K_1$ values refer to the equilibria related to the attachment of H^+ to the oxygen atom in the acetate group.

As seen from Table 3, the $\log_{10}K_1$ values of montelukast sodium decrease with increasing ethanol percentage. The increase in the ethanol concentration decreases the dielectric constant of the medium. HB is better solvated than the B^- species in ethanol-rich media.

Potentiometric determination of standard montelukast sodium

In this study, montelukast sodium was titrated potentiometrically with hydrochloric acid as a titrant in 30%, 40%, 50%, 60%, 70% and 80% ethanol–water (v/v) mixtures at constant temperature of 25°C and ionic strength of 1.0×10^{-1} M NaCl. Since montelukast sodium behaves as a weak base in ethanol–water mixtures, its titration curve does not display a perceivable inflection for the second point of equivalence for all media studied. The best titration curve was obtained in 40% ethanol–60% water (v/v) mixture. Therefore, recovery, repeatability and assay studies were done in this medium. A typical potentiometric titration curve with only one inflection point is given in Figure 2. As seen from the figure, the changes at the titration end point were satisfactory enough for accurate and reproducible end point detection. The determination of equivalence points from the potentiometric data was carried using the Gran's method [13-14].

In order to assess the repeatability (precision) of the method, known amounts of chemically pure laboratory working standard solution were analyzed in three replicates. As seen from the data in Table 4, the values found by the proposed method are in good agreement with the taken value and furthermore the mean relative standard deviation is less than ± 3%. This indicates that the accuracy and precision of this method is quite satisfactory

Table 4. Titrimetric determination of chemically pure laboratory working standard of montelukast sodium.

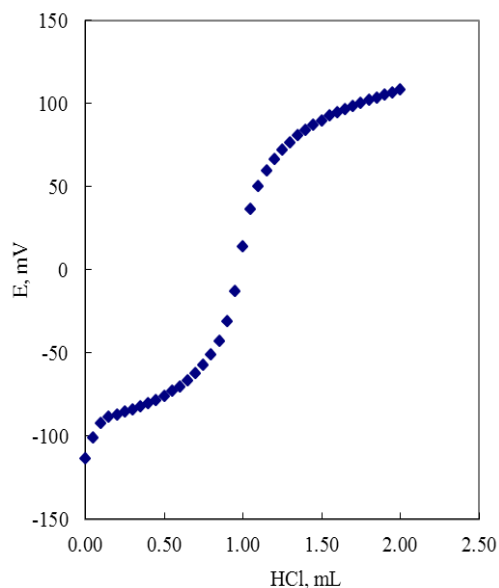| 40% ethanol – 60% water (v/v)				
Taken,mg	Found, mg (n = 3)	Bias, %	S.D.	RSD,%
30.0	31.2	4.0	0.26	0.83
50.0	52.8	4.2	0.47	0.90
75.0	73.6	1.5	0.20	0.27

S.D, is standard deviation and

Fig.2. Potentiometric titration curve for montelukast sodium standard titrated with 5.0×10^{-2} M hydrochloric acid in 40% ethanol – 60% water (v/v) mixture.

Determination of the active component in pharmaceuticals

In order to evaluate the adequacy of the proposed method to be used for the analysis of pharmaceutical preparations, montelukast sodium was determined in 40% ethanol – 60% water (v/v) mixture in tablet formulations under the same conditions as for the pure montelukast sodium. The similarity of the shapes of potentiometric titration curve of pure montelukast sodium and its corresponding pharmaceutical proves that the excipients which might be present in the pharmaceutical preparations do not affect the titration curve (Fig. 3).
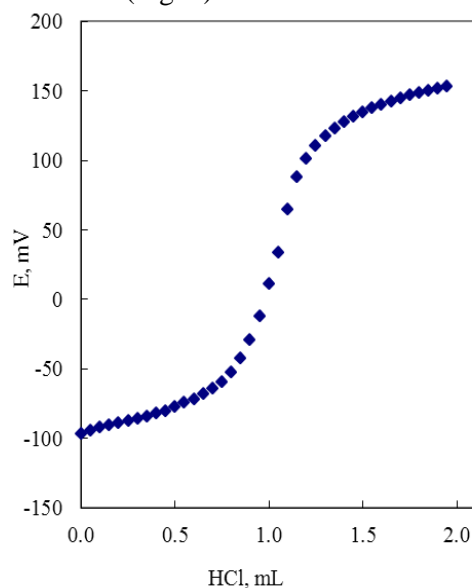

Fig.3 Potentiometric titration curve for pharmaceutical dosage form of montelukast sodium titrated with 5.0×10^{-2} M hydrochloric acid in a 40% ethanol – 60% water (v/v) mixture.

Table 5 summarizes the results obtained for the montelukast sodium in the corresponding pharmaceutical, expressed as labeled contents. The data given in Table 5 clearly indicate that the content of montelukast sodium in the pharmaceuticals can be safely determined using this method without interference from other substances in the preparations.

Table 5. Determination of montelukast sodium in pharmaceutical preparation.

Tablet (Batch Number)	Labeled (mg)	Found (mg)	Label % ± S.D (n = 3)
I	10.0	10.3	102.6 ± 0.43
II	10.0	9.8	98.3 ± 0.27

S.D, is standard deviation and n, is number of analysis

Recovery studies of standard additions to the commercial pharmaceuticals were carried out in order to provide further evidence of the validity of the proposed method. For this purpose, standard montelukast sodium solution was added to pharmaceutical formulation solutions at three different concentration levels. The results are tabulated in Table 6. It can be seen from this table that the mean recoveries and standard deviation values are in the range of 97.6–101.8% and 0.5–0.9, respectively, which is a good evidence of the validity of the method.

Comparing the obtained results with those of many of the already existing procedures for the determination of montelukast sodium, which require special instrumentation, reagents, precautions and experience, it is seen that the proposed potentiometric method exhibits the advantages of simple operation, reasonable selectivity, fast response, low-cost and sufficient accuracy in pharmaceutical formulations. Therefore this method can be used for routine analysis of montelukast sodium in combined tablet dosage forms without prior separation.

REFERENCES

1. I. Narin, S. Sarioglan, B. Anilanmert and H. Sari, *J. Sol. Chem.* **39**, 1582 (2010).
2. V. Choudhari, A. Kale, S. Abnawe, B. Kuchekar, V. Gawli and N. Patil, *Int. J Pharm. Tech. Res*. **2,** 4 (2010).
3. Y. Shakalisava and F. Regan, *J Sep. Sci.,* **3,** 1137 (2008) .
4. S.A. Patel, D.J. Patel and J.N. Patel, *Int. Res. J Pharm.*, **2,** 154 (2011).
5. I.A. Alsarra, *Saudi Pharm.*, **12,** 136 (2004).
6. A.S. Rathore, L. Sathiyanarayanan and K.R. Mahadik, *Pharm. Anal. Acta*, **1,** 1 (2010).
7. I.A. Alsarra, M. Al-Omar, E.A. Gadkariem and F. Belal, *Il Farmaco*, **60,** 563 (2005).
8. A. Avdeef, John Wiley and Sons, New Jersey, 2003.
9. A.E. Martell and M. Calvin, Chemistry of the Methal Chelate Compounds. Prentice-Hall, New York, 613, 1952.
10. F.C. Rossotti and H. Rossotti, The Determination of Stability Constants. McGraw-Hill, New York, 1961.
11. R.G. Bates, Determination of pH, Theory and Practice. 2nd Ed., John Wiley and Sons, New York, ISBN-13: 9780471056478, 479 (1973).
12. G. Gran, H. Dahlenborg, S. Laurell and M. Rottenberg, *Acta Chem. Scand*., **4,** 559 (1950).
13. G. Gran, *Analyst*, **77**, 661 (1952).
14. M. Meloun , J. Havel and Hogfeldt H. Computation of Solution Equilibria. Wiley, New York. (1988).
15. A.E. Martell and R.J. Motekaitis, The determination and use of stability constants. VCH Publishers, Weinheim, New York, ISBN-13: 9780895737410, 216 (1988).
16. E. Canel, A. Gultepe, A. Dogan and E. Kilic,. *J Sol. Chem.*, **35,** 5 (2006).
17. E.P. Serjeant, Potentiometry and Potentiometric Titrations. Wiley, New York, ISBN-**13**: 9780471077459, 725 (1984).
18. L.G. Hepler, E.M. Woolley and D.G. Hukot, *J Phys. Chem.*, **74,** 3908 (1970).
19. H.M. Irving and H.S. Rossotti, *J Chem. Soc*., **165,** 2904 (1954).
20. E. Kilic and N. Aslan, *Microchim. Acta*, **151,** 89, (2005).
21. M. Faraji, A. Farajtabar and F. Gharib, *J. Appl. Chem. Res*., **9**, 7 (2009).

Table 6. Recovery studies of standard additions to the pharmaceutical preparation.

Pharmaceutical	Active component	Taken, mg	Added, mg	Found, mg	% Mean recovery ± S.D. (n=3)
OnceAir	Montelukast sodium	25.0	25.0	48.8	97.6 ± 0.5
		25.0	30.0	54.9	99.9 ± 0.5
		25.0	35.0	61.1	101.8 ± 0.9

S.D, is standard deviation and n, is number of analyses

МЕТОД ЗА ПОТЕНЦИОМЕТРИЧНО ТИТРУВАНЕ ЗА ОПРЕДЕЛЯНЕ НА НАТРИЕВА СОЛ НА МОНТЕЛУКАСТ ВЪВ ФАРМАЦЕВТИЧНИ ПРЕПАРАТИ И НА КОНСТАНТАТА МУ НА ПРОТОНИРАНЕ

Н. Аслан, П.Е. Ерден, Е. Джанел, Е. Килич

Департамент по химия, Научен факултет, Университет в Анкара, Турция

(Резюме)

Разработен е и е проверен метод за потенциометрично титруване и определяне на натриевата сол на монтелукаст във фармацевтични препарати. За тази цел са титрувани стандартни проби със солна киселина. Методът е много точен и надежден със стандартно отклонение под 1.0%. От тези данни е изчислена стехиометричната константа на протониране в среди от етанол/вода (40:60) и (60:40) обемни части при 25.0 $\pm$ 0.1ºC и йонна сила на 1.0×10^{-1} M NaCl. Константите на протониране са съответно 6.25 за средата етанол/вода (40:60) и 5.95 в среда (60:40). Показано е, че методът може да се използва успешно при анализа на търговски препарати, съдържащи 10,0 mg натриева сол на монтелукаст. Валидността на метода е изпитан чрез определяне на добива по метода на стандартната добавка към разтвори на таблетки, като резултатите са задоволителни. Методът е прост, бърз и евтин за качествен контрол на търговски фармацевтични форми.

Synthesis, characterization and biological evaluation of new benzimidazoles

A. Ahmadi

Department of Chemistry, Faculty of Science, Karaj Branch, Islamic Azad University, Karaj, Iran

The benzimidazoles moieties play an important role in medical field with so many pharmacological activities such as antifungal activities. In the present study, we have reported the synthesis, spectral studies and antifungal evaluation of some novel benzimidazoles. The structures of all the synthesized compounds were deduced by elemental analysis and different spectroscopic techniques (IR, ^{1}H- and ^{13}C-NMR and Mass Spectroscopy) and in vitro antifungal activities of these compounds tested against Candida albicans, Candida glabrata, and Candida krusei. The tested compounds displayed in vitro antifungal activity and Minimum Inhibitory Concentration (MIC) was determined for all compounds. The derivatives have shown moderate to good activity when compared with commercially available fungicides.

Keywords: benzimidazole, spectroscopic techniques, antifungal activity, fungicides..

INTRODUCTION

Benzimidazole is the heterocyclic compound formed from benzene and imidazole ring containing nitrogen, oxygen, sulphor and its derivatives are of wide interest because of their diverse biological activity and clinical applications, they are remarkably effective compounds both with respect to their inhibitory activity and their favorable selectivity ratio. In fact the benzimidazoles moieties play an important role in medical field with so many pharmacological activities. The potency of these clinically useful drugs in treatment of microbial infections and other activities encouraged the development of some more potent and significant compounds. Benzimidazole nucleus is an important heterocyclic ring, a wide variety of Benzimidazole derivatives are known for their chemotherapeutic importance and antimicrobial activities [1-6], especially antifungal activity [7-9] anti-inflammatory [10], and antioxidant [11-15]. In this context, It has been found that Benzimidazole derivatives to retard especial type of fungus that attack certain class of patients such as cancer chemotherapy and HIV patients. In particular, Candidiasis is the fungal infection most that is frequently associated with HIV-positive patients [16-17]. Benzimidazole derivatives were found to retard Cryptococcosis growth, which is the main cause of morbidity in AIDS patients [18,19].

Due to great potential of the moiety, synthesis of benzimidazole derivatives was carried out to evaluate their antifungal. In generally benzimidazoles are readily formed by heating *o*-phenylenediamines with carboxylic acids or aldehydes. For example, benzimidazole itself is produced by heating *o*-phenylenedamine with 90% formic acid or formaldehyde [20]. In this work, is reported a study on synthesis of some novel brom derivatives of 2-bromomethyl-benzimidazole (Structures of **5-10** in Figure 1). These derivatives were screened for antifungal activity against against *Candida albicans*, *Candida glabrata*, and *Candida krusei*.
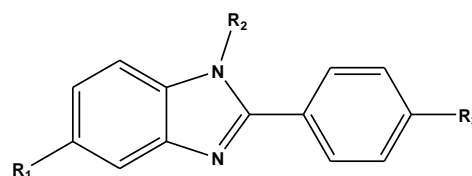

5)	$R_1 = NO_2$	$R_2 = i\text{-}C_3H_7$	$R_3 = H$
6)	$R_1 = NO_2$	$R_2 = i\text{-}C_3H_7$	$R_3 = Br$
7)	$R_1 = NO_2$	$R_2 = \hexagon$	$R_3 = Br$
8)	$R_1 = NH_2$	$R_2 = i\text{-}C_3H_7$	$R_3 = H$
9)	$R_1 = NH_2$	$R_2 = i\text{-}C_3H_7$	$R_3 = Br$
10)	$R_1 = NH_2$	$R_2 = \hexagon$	$R_3 = Br$

Fig.1. Chemical structures of chemical compound synthesized

The structures of the obtained compounds were characterized and the target compounds (**1c-9c**) were screened for their antibacterial activity against various strains of *Escherichia coli* and *Staphylococcus aureus* and antifungal activity against *Candida albicans*.

---

* To whom all correspondence should be sent:
E-mail: ahmadikiau@yahoo.com

EXPERIMENTAL

Material and Equipment

All chemicals and solvents were obtained from E-Merck and Sigma-Aldrich and used without further purification. All melting points are uncorrected and taken with an Electrothermal melting point apparatus (Electrothermal Eng. Ltd, Essex, UK). IR spectra were determinate in KBr on a Shimadzu Dr-8031 instrument. The ^{1}H and ^{13}C-NMR spectrums of the synthesized compounds were measured in DMSO-d_6 or CDCl$_3$ solution and TMS as the internal standard using a Varian Mercury 400, 400MHz instrument. All Chemical shifts were reported as δ (ppm) values. The Mass Spectra were recorded on a LCQ ion trap mass spectrometer (Thermo Fisher. San Jose.CA, USA), equipped with an EI source. Elemental analyses were carried out using a Perkin-Elmer, CHN elemental analyzer.

Synthesis of Compounds
General procedure for the preparation of the compounds (5-7)

1-Bromo-2,4-dinitrobenzene (2 mmol, 0.5 gr) is mixed with DMF (5 ml) and isopropyl/cyclohexylamine (2.2 mmol). The mixture is heated at reflux for 12 hrs then cooled and concentrated under vacuum (Intermediates **2a** and **2b**). The 2-nitro group of compounds **2a** and **2b** was reduced to 2-amino (**3a** and **3b**) by using Na$_2$S/NaHCO$_3$ in methanol according to Willitzer et al. method [21]. To a mixture of the appropriate benzaldehyde derivative (**4a** and **4b**) (1.5 mmol) in 5 mL of EtOH, then was added a solution of 0.01 mole of Na$_2$S$_2$O$_5$ in 5 ml of water in portions to the cooled ethanolic solution. The precipitate formed was filtered off and dried. A total of 1.2 mmol of this precipitate and 1.2 mmol of compound **3a** or **3b** in 5 ml of DMF were heated under reflux for 8 hr, and then it was concentrated. At the end of this period the reaction mixture was cooled and poured into water and the resulting solid was collected, washed with water. The precipitate re-crystallized from ethanol-water mixture (Scheme 1) [22, 23].

5-Nitro-2-phenyl -1-isopropyl benzimidazol (5)

Cream powder; Yield 71%; m.p. 131-133 °C; IR (KBr, cm^{-1}): 2971 (CH), 1650 (N=C), 1302 (C-N stretching), 895 (C-C bonding aromatic). ^{1}H-NMR (δ/ppm): 1.33 (t, 6H, CH$_3$), 3.73 (m, 1H, CH), 7.21-7.59 (5H, m, Ar-benzimidazole), 8.01 (d, 1H, Jo= 8.8 Hz, H-7), 8.25 (dd, 1H, Jo =8.8 Hz, Jm= 2 Hz, H-6), 8.59 (d, 1H, Jm= 2 Hz, H-4). ^{13}C-NMR (δ / ppm): 22.6, 45.3, 112.1, 117, 119, 125.5, 128.5, 129.5, 130.0, 133.5, 137.1, 143.4, 146.7. Anal. Calcd. for C$_{16}$H$_{15}$N$_3$O$_2$: C, 68.32; H, 5.33; N, 14.95 %. Found: C, 67.91; H, 5.30; N, 15.08 %. MS (m/z, *regulatory intensity*, %): 281 (*100*), 282 (*18*).

2-(p-Bromophenyl)-1-isopropyl-5-nitro benzimidazol (6)

Light yellow powder; Yield 69%, m.p. 155-157 °C; IR (KBr, cm^{-1}): 2983 (CH), 1663 (N=C), 1288 (C-N stretching), 879 (C-C bonding aromatic), 673 (C-Br); ^{1}H-NMR (δ/ppm): 1.41 (t, 6H, CH$_3$), 3.85 (m, 1H, CH), 7.30-7.50 (4H, m, Ar-benzimidazole), 7.80 (d, 1H, Jo= 8.8 Hz, H-7), 8.12 (dd, 1H, Jo =8.8 Hz, Jm= 2 Hz, H-6), 8.60 (d, 1H, Jm= 2 Hz, H-4); ^{13}C-NMR (δ/ppm): 19.7, 40.3, 114.5, 118, 121, 127.5, 130.5, 133.5, 134.0, 136.5, 139.2, 146.1, 149.2. Anal. Calcd. for C$_{16}$H$_{14}$BrN$_3$O$_2$: C, 53.30; H, 3.88; N, 11.66 %. Found: C, 53.35; H, 3.83; N, 11.61 %. MS (m/z, *regulatory intensity*, %): 359 (100), 361(98), 360 (20).

2-(p-Bromophenyl)-1-cyclohexyl-5-nitro benzimidazol (7)

Yellow powder; Yield 88%; m.p. 181-183 °C; IR (KBr, cm^{-1}): 2936 (CH), 1664 (N=C), 1285 (C-N stretching), 910 (C-C bonding aromatic), 675 (C-Br); ^{1}H-NMR (δ/ppm): 1.54-2.86 (m, 10H, CH$_2$), 3.25 (1H,s,CH, Cyclohexyl), 7.21-7.44 (4H, m, Ar-benzimidazole), 7.70 (d, 1H, Jo= 8.8 Hz, H-7), 8.23
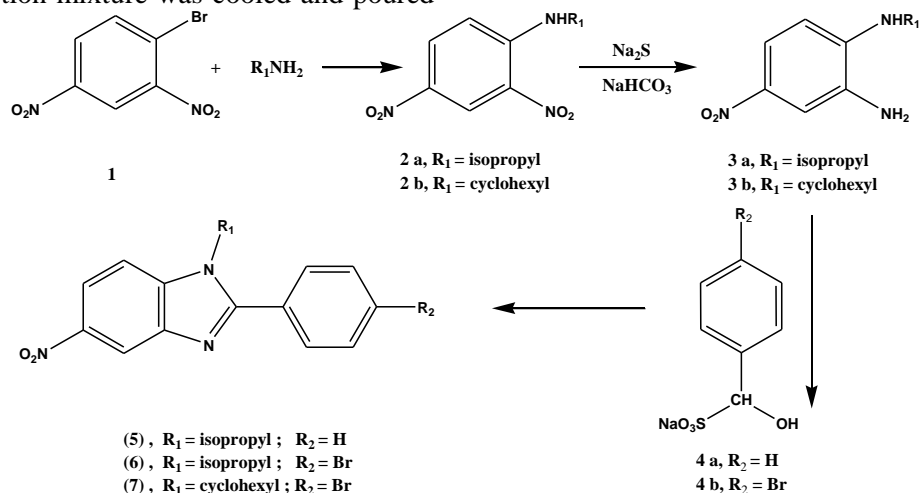
Scheme 1. Schematic synthesis of intermediates and new compounds (**5-7**).

(dd, 1H, Jo =8.8 Hz, Jm= 2 Hz, H-6), 8.59 (d, 1H, Jm= 2 Hz, H-4); ^{13}C-NMR (δ/ppm): 26.5, 29.5, 65.5, 113.5, 118.0, 121.5, 122, 124, 126.5, 132.5, 136.5, 141.3, 148.0. Anal. Calcd. For $C_{19}H_{18}BrN_3O_2$: C, 56.96; H, 4.50; N, 10.50 %, Found: C, 56.90; H, 4.46; N, 10.41 %. MS (m/z, *regulatory intensity*, %): 401 (100), 399 (100), 400 (25).

General procedure for the preparation of the compounds (8-10)

Mixture of 5-Nitrobenzimidazole derivatives **5-7** (1 mmol) in 10 mL of hot EtOH and 10 mL of 6N HCl were heated under reflux and then $SnCl_2.2H_2O$ was added in portions until the starting material was completely exhausted. The ethanol was decanted; the residue was made alkaline with KOH, then, extracted with EtOAc, and washed with water. EtOAc was evaporated slowly and the precipitate re-crystallized from ethanol (Scheme 2) [21-23].

1- Isopropyl-2-pjenyl-1H-benzimidazole-5-ylamine (8)

Cream powder; Yield 75%; m. p. 191-193 ºC; IR (KBr, cm^{-1}):3155 (NH), 2981 (CH), 1628 (N=C), 1285 (C-N stretching), 887 (C-C bonding aromatic); ^{1}H-NMR (δ/ppm): 1.43 (t, 6H, CH$_3$), 3.95 (m, 1H, CH), 4.8 (s, 2H, NH$_2$), 6.95-7.69 (3H, m, Ar-Bbenzimidazole), 7.60 (d, 1H, Jo= 8.8 Hz, H-7), 8.11 (dd, 1H, Jo =8.8 Hz, Jm= 2 Hz, H-6), 8.44 (d, 1H, Jm= 2 Hz, H-4); ^{13}C-NMR (δ/ppm): 24.2, 48.1,112.5, 115, 117, 119, 129.7 ,130.8, 131.0,134.5, 137, 139.8 , 145.2 . Anal. Calcd. for $C_{16}H_{17}N_3$: C, 76.46; H, 6.82; N, 16.72 %. Found: C, 76.85; H, 6.79; N, 16.62 %. MS (m/z, *regulatory intensity*, %): 251 (100), 252 (18).

2-(4-Bromo-phenyl)-1-isopropyl-1H-benzimidazole-5-ylamine (9)

Light Yellow powder; Yield 78%, m. p. 137-139ºC; Anal.Calcd. for $C_{16}H_{16}BrN_3$: C, 58.19; H, 4.88; N, 12.72 %. Found: C, 58.05; H, 4.90; N, 12.76 %. IR (KBr, cm^{-1}): 3330 (NH), 2945 (CH), 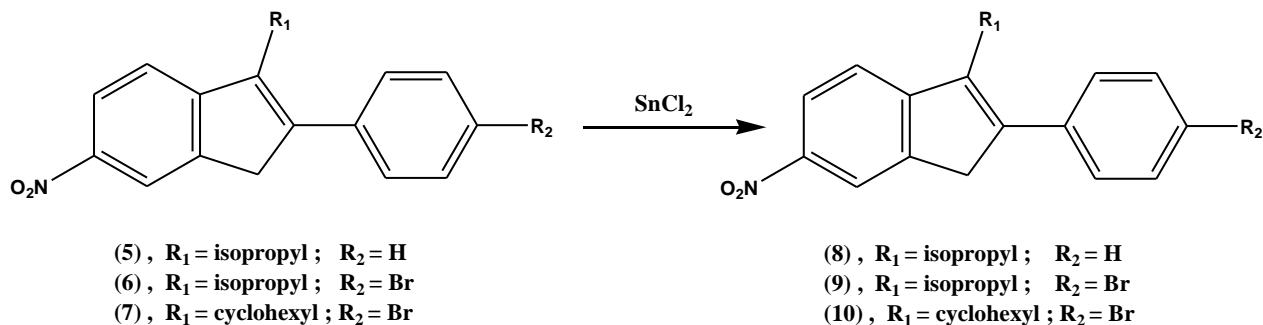1632 (N=C), 1288 (C-N stretching), 912 (C-C bonding aromatic), 691 (C-Br); ^{1}H-NMR (δ/ppm): 1.56 (t, 6H, CH$_3$), 4.22 (m, 1H, CH), 5.1 (s, 2H, NH$_2$), 6.95-7.69 (3H, m, Ar-Bbenzimidazole), 7.75 (d, 1H, Jo= 8.8 Hz, H-7), 8.25 (dd, 1H, Jo =8.8 Hz, Jm= 2 Hz, H-6), 8.56 (d, 1H, Jm= 2 Hz, H-4). ^{13}C-NMR (δ/ppm): 21.2, 42.1, 109.5, 114, 118, 120, 127.5, 131.8, 132.3, 135.2, 138.2, 139.8, 147.3. Anal.Calcd. for $C_{16}H_{16}BrN_3$: C, 58.19; H, 4.88; N, 12.72 %. Found: C, 58.05; H, 4.90; N, 12.76 %. MS (m/z, *regulatory intensity*, %): 329 (100), 331 (97), 332 (20).

2-(4-Bromo-phenyl)-1-cyclohexyl-1H-benzimidazole-5-ylamine (10)

Yellow powder; Yield 85%, m. p. 189-191 ºC; IR (KBr, cm^{-1}): 3155 (NH), 2991 (CH), 1661 (N=C), 1296 (C-N stretching), 905 (C-C bonding aromatic), 699 (C-Br);^{1}H-NMR (δ/ppm): 1.69-2.20 (m, 10H, CH$_2$), 4.65-4.75 (m, 1H, CH), 4.85 (s, 2H, NH$_2$), 6.91-7.64 (3H, m, Ar-Bbenzimidazole), 7.71 (d, 1H, Jo= 8.8 Hz, H-7), 8.42 (dd, 1H, Jo =8.8 Hz, Jm= 2 Hz, H-6), 8.62 (d, 1H, Jm= 2 Hz, H-4). ^{13}C-NMR (δ/ppm): 29.7, 30.9, 61.5, 113.5, 114.0,116, 117.5, 125.6, 127.8, 132.5, 138.5, 140.5, 143.1. Anal. Calcd. For $C_{19}H_{20}BrN_3$: C, 61.63; H, 5.44; N, 11.35 %. Found: C, 61.66; H, 5.39; N, 11.46 %. MS (m/z, *regulatory intensity*, %): 369 (100), 371 (95), 370 (21).

Antifungal activity assay

The yeasts Candida albicans, patient isolate Candida glabrata and Candida krusei were grown on Sabouraud Dextrose Broth (Difco); the yeasts were incubated for 48 h at 25.91°C. The antifungal activity tests were carried out at pH 7.4 in Sabouraud Dextrose Broth and the 2-fold dilution was applied. A set of tubes containing only inoculated broth was kept as controls. After incubation for 48 h at 25.91°C, the last tube with no yeast growth was recorded to represent minimum inhibitory concentration (MIC), expressed in µg/mL.

(**5**) , R$_1$ = isopropyl ;   R$_2$ = H
(**6**) , R$_1$ = isopropyl ;   R$_2$ = Br
(**7**) , R$_1$ = cyclohexyl ; R$_2$ = Br

(**8**) , R$_1$ = isopropyl ;   R$_2$ = H
(**9**) , R$_1$ = isopropyl ;   R$_2$ = Br
(**10**) , R$_1$ = cyclohexyl ; R$_2$ = Br

Scheme 2. Schematic synthesis of new compounds (**8 - 10**).

RESULTS AND DISCUSSION

Chemistry

In continuation of our interest to investigate of new pharmaceutical potential compounds, the syntheses of biologically active benzimidazole derivatives were carried out in this study. To materialize the proposed project, initially, intermediates were synthesized from 1-Bromo-2,4-dinitrobenzene by reaction with isopropyl/cyclo-hexylamine in DMF according to the literature [21]. The 2-nitro group of compounds was reduced to 2-amino by using $Na_2S/NaHCO_3$ in methanol [21]. Condensation of o-phenylenediamines with the $Na_2S_2O_5$ adduct of appropriate benzaldehydes in DMF [24] gave **5-7**. Reduction of compounds **5-7** with $SnCl_2.2H_2O$ produced **8-10**. The structures of **5-10** were deduced from their elemental analysis, mass spectrometric data, ^1H- and ^{13}C-NMR, and IR spectral data, given in Experimental section.

Antifungal activity

The in vitro antifungal activity of the compounds was tested by the tube dilution technique [25]. Each of the test compounds and standards Miconazole, Fluconazole and Cotrimoxazole were dissolved in 10% DMSO, at concentrations of 100 μg/mL. Further dilutions of the compounds and standards in the test medium were prepared at the required quantities of 50, 25, 12.5, 6.25, 3.125, 1.5 and 0.75 μg/mL concentrations. The final inoculums size was 10^5 CFU/mL. The MICs were defined as the lowest concentrations of the compounds that prevented visible growth. It was determined that the solvent had no antifungal activity against any of the test microorganisms. All the compounds were tested for their in vitro growth inhibitory activity against C. albicans, patient isolate C. glabrata and C. krusei (Table 1). Compounds **5, 7, 8** and **10** possessed comparable activity to fluconazole and cotrimoxazole against C. albicans with a MIC of 12.5 μg/mL. However none of the compounds was superior to the standards used against any fungi.

CONCLUSION

A series of some novel Benzimidazole derivatives were successfully synthesized and characterized using IR, ^1H- and ^{13}C-NMR, mass spectroscopy and elemental analysis. Our studies clearly demonstrate that novel Benzimidazole derivatives had significant antifungal activity against different fungi species. As a consequence, we can conclude that newly synthesized Benzimidazole derivatives can be used for the development of new fungicide.

REFERENCES

1. S. Utku, M. Gokce, B. Ozcelik , E. Bercin, *Turk J. Pharm. Sci*. **5(2)**, 107(2008).
2. L. L. Kruse, D. L. Ladd, R. B. Harrsch, F. L. McCabe, S. M. Mong, L. Faucette, R. Johnson, *J. Med. Chem*. **32,** 409 (1989)**.**
3. I. Islam, E. S. Skibo, R. T. Dorr , D. S. Alberts, *J. Med. Chem*. **34,** 2954 (1991).
4. V. J. Habernickel, *Drugs made in Germany* **35,** 97 (1992)**.**
5. T. Fukuda, T. Saito, S. Tajima, K. Shimohara, K. Ito, *Arzneim.-Forsch./DrugRes*. **34,** 805 (1984)**.**
6. H. Nakano, T. Inoue, N. Kawasaki, H. Miyataka, H. Matsumoto, T. Taguchi, N. Inagaki, H. Nagai, T. Satoh, *Chem. Pharm. Bull*. **47,** 1573 (1999).
7. B. Can-Eke, M.O. Puskullu, E. Buyukbingol, M. Ican, *Chemico-Biological Interactions* **113,** 65 (1998).
8. C. Kus, G. Ayhan-Kilcigil, B. Can-Eke, M. Iscan, *Arch. Pharm. Res*. **27,** 156 (2004).
9. G. Ayhan-Kilcigil, C. Ku, T. Coban, B. Can-Eke, M. Lcan, *J. Enz. Inhibit. Med. Chem.*, **19,** 129 (2004)**.**
10. H. Göker, G. Ayhan-Kilcigil, M. Tunçbilek, C. Kus, R. Ertan, E. Kendi, S. Ozbey, M. Fort, C. Garcia, A. J. Farre, *Heterocycles,* **51,** 2561(1999).
11. A.E. Abdel-Rahman, A.M. Mahmoud, G.M. El-Naggar, H.A. El-Sherief, *Pharmazie* **38,** 589 (1983).
12. F.S.G. Soliman, S.M. Rida, E.A.M Badawey, T. Kappe, *Arch.Pharm*. **317,** 951(1984).
13. R.A. Coburn, M.T. Clark, R.T. Evans, R,J, Genco, *J. Med. Chem*. **30,** 205 (1987).
14. N.S. Habib, S. Abdel-Hamid, M. El-Hawash, *Farmaco*, **44,** 1225 (1989).
15. H. Göker, C. Ku, D.W. Boykin, S. Yildiz, N. Altanlar, *Bioorg.Med.Chem*. **10,** 2589 (2002).
16. S. Ozden, H. Karata, S. Yildiz, H. Goker, *Arch. Pharm. Pharm. Med. Chem*. **337,** 556 (2004).
17. S. Ozden, D. Atabey, S. Yildiz, H. Göker, *Bioorg. Med. Chem*. **13,** 1587 (2005).
18. L. Küçflkgflzel, G. Küçflkgflzel, S. Rollas, M. Kiraz, *Bioorg.Med.Chem.Letters*, **11,** 1703 (2001).
19. M.S. El-Gaby, J.A. Micky, N.M. Taha, M.A.M. El-Sharief**,** *J.Chin.Chem.Soc*. **49,** 407 (2002).
20. Finar I.L. Organic Chemistry: Stereochemistry and the Chemistry of Natural Products, John Wiley and Sons, Inc., New York, 5 th Ed., , 2: 631 (1975).
21. H. Willitzer, D. Brauniger, D. Engelmann, D. Krebs, W. Ozegowski, M. Tonew, *Pharmazie***, 33,** 30 (1978).
22. A. Ahmadi, B. Nahri-Niknafs, *E-Journal of Chemistry*, **8 (S1)**, S85-S90 (2011).
23. G. Ayhan Kilcigil, N. Altanlar, *Turk. J. Chem.* **30,** 223 (2006).
24. H.F. Ridley, R.G.W. Spickett, G.M.J. Timmis, *Heterocyclic Chem*. **2,** 453 (1965).

25. D.F. Sahm, J.A. Washington, *Antibacterial Susceptibility Tests: Dilution Methods,* in Manual of Clinical Microbiology, 5th ed., eds. A. Balowes, W.J. Hausler, K.L. Hermann, H.D. Shadomy, American Society for Microbiology, Washington DC USA, ,p.1105(1991).

Синтеза, охарактеризиране и биологична оценка на нови бензимидазоли

А. Ахмади

Департамент по химия, Научен факултет, клон Карадж, Ислямски университет „Азад“, Карадж, Иран

(Резюме)

Бензимидазолевото ядро е от голямо значение в медицинската химия и много бензимидазол-съдържащи съединения проявяват значителна биологична активност. В настоящата работа са изследвани синтезите, спектралните характеристики и биологичните свойства на девет нови производни на бензимидазола. Структурите на синтезираните съединения са охарактеризирани чрез IR, 1H-NMR, 13C-NMR, мас-спектроскопия and CHN-елементен анализ. Антибактериалната активност на съединенията е оценена спрямо щамовете *Candida albicans, Candida glabrata, and Candida krusei.* Изследваните съединения показват ин витро противогъбично действие и минималната инхибираща концентрация (MIC) е определена за всички съединения. Производните показват от умерена до добра активност в сравнение с наличните в търговската мрежа фунгициди.

Effect of porosity on the flow with heat transfer of a non-Newtonian power law fluid due to a rotating disk with uniform suction and injection

H.A. Attia, I.H. Abdelmaksoud, W.A. Ahmed*, M.M. Elbarawy

Department of Engineering Mathematics and Physics, Faculty of Engineering, Fayoum University, El-Fayoum-63514, Egypt

The steady flow through a porous medium of an incompressible non-Newtonian power law fluid due to the uniform rotation of a rotating disk of infinite extent is studied with heat transfer. The disk is immersed in a porous medium that is assumed to obey Darcy's model while a uniform injection or suction is applied through its porous surface. A numerical solution for the governing nonlinear differential equations is obtained. The effect of characteristics of the non-Newtonian fluid, the porosity of the medium and the suction or injection velocity on the velocity and temperature distributions is analyzed.

NOMENCLATURE

D_{ij} : rate of strain tensor,

Ec: Eckert number,

(F, G, H): non-dimensional velocity components,

k: thermal conductivity,

K: consistency coefficient,

$K1$: Darcy permeability,

m: porosity parameter,

n: power-law index,

Nu: Nusselt number,

p: pressure gradient,

P: non-dimensional pressure,

p_∞ : pressure of the ambient fluid,

Pr: Prandtl number,

Q: rate of heat transfer,

T: temperature of the fluid,

T_w: temperature of the disk,

T_∞ : temperature of the ambient fluid,

S: suction parameter,

w_o: vertical velocity at the disk,

$\vec{V}$: velocity vector,

(u, v, w): velocity components,

(r, φ, z): cylindrical coordinates,

θ : non-dimensional temperature,

μ: viscosity of the fluid,

ν : kinematic viscosity of the fluid,

ρ: density of the fluid,

ω : angular velocity of the disk,

τ : stress tensor,

ζ : non-dimensional distance.

INTRODUCTION

The mathematical formulation of the steady fluid flow due to the rotation of a disk with infinite extension was obtained by von Karman in 1921 [1]. A similarity transformation was introduced which reduced the governing partial differential equations to ordinary differential equations. Later, Cochran [2] obtained an asymptotic solution for the resulting system of ordinary differential equations. The extension of the steady state problem to the transient state was carried out by Benton [3]. The heat transfer from a rotating disk maintained at a constant temperature was studied by many authors under different assumptions [4,5]. Attia [6] extended the problem discussed in [4,5] to the transient state considering an electrically conducting fluid and in the presence of an applied uniform magnetic field. The practical importance of non-Newtonian fluids attracted the attention of many authors to study their rule in rotating disk flow. The steady flow of a non-Newtonian fluid due to a rotating disk with uniform suction was considered by Mithal [7]. Mitschka [8] and Mitschka and Ulbrecht [9] extended the von Karman analysis to non-Newtonian of the power-law type fluids. Motion of power-law fluids in the presence of a magnetic field has been studied earlier by several authors [10-12]. Examples of non-Newtonian fluids which might be conductors of electricity were given by Sarpkaya [13], flow of nuclear slurries and of mercury amalgams, and lubrication with heavy oils and greases. The problem studied by Mitschka [8] and Mitschka and Ulbrecht [9] was reconsidered in [14] with a

* To whom all correspondence should be sent:
E-mail: waleed.abdelmagied@invensys.com

particular view to address the reliability of their numerical solutions of the extremely non-linear ordinary differential equations arising in the presence of a non-linear rheological equation of state. The magnetohydrodynamic flow of a power-law fluid over a rotating disk is of particular interest since the magnetic force field in this case vanishes outside the viscous boundary layer and therefore affects the fluid motion only within the boundary layer. The effect of an externally applied magnetic field on the flow of a power-law fluid due to a rotating disk, and in particular how effectively a uniform magnetic field can be utilized as a means of flow control, was studied [15-17]. Batista [18] obtained an analytical solution of the Navier–Stokes equations for the case of the steady flow of an incompressible fluid between two uniformly co-rotating disks. Turkyilmazoglu [19] obtained an exact solution for the flow of a viscous hydromagnetic fluid due to the rotation of an infinite disk in the presence of an axial uniform steady magnetic field with the inclusion of Hall current effect. Nazir and Mahmood [20] studied the effects of disks contracting, rotation and heat transfer on the viscous fluid between heated contracting rotating disks. Bachok et al. [21] studied the steady flow of an incompressible viscous fluid due to a rotating disk in a nano fluid. Devi and Devi [22] studied the thermal radiation effect over an electrically conducting, Newtonian fluid in a steady laminar magnetohydrodynamic convective flow over a porous rotating infinite disk with consideration of heat and mass transfer. Ming et al. [23] studied the steady flow and heat transfer of a viscous incompressible power-law fluid over a rotating infinite disk. Assuming that the thermal conductivity follows the same function as the viscosity, the governing equations in the boundary layer are transformed into a set of ordinary differential equations by a generalized Karman similarity transformation. The corresponding nonlinear two-point boundary value problem was solved by the multi-shooting method. Attia [24], Sahoo [25] and Osalusi [26] provided some researches about the Reiner–Rivlin model. Urkyilmazoglu [27] obtained exact solutions to the steady Navier–Stokes equations for the incompressible Newtonian viscous electrically conducting fluid flow motion due to a disk rotating with a constant angular speed. The rotating disk flow through a porous medium that obeys Darcy's model was carried out by Attia [28,29].

In the present paper, the steady laminar flow through a porous medium of an incompressible viscous non-Newtonian power-law fluid due to the uniform rotation of a disk of infinite extent in the presence of uniform suction and injection is studied with heat transfer. A uniform injection or suction is applied perpendicularly through the surface of the disk which is maintained at a constant temperature. The flow in the porous medium deals with the analysis in which the differential equation governing the fluid motion is based on the Darcy's law which accounts for the drag exerted by the porous medium [30,31]. The governing nonlinear differential equations for the flow and temperature distributions are solved numerically using the method of finite differences. The effect of the porosity of the medium, the characteristics of the non-Newtonian power-law fluid and the suction or injection velocity on the steady flow and temperature fields is presented and discussed.

BASIC EQUATIONS

Let the disk lies in the plane $z=0$ and the space $z>0$ is occupied by an incompressible viscous non-Newtonian power law fluid as shown in Fig.1.
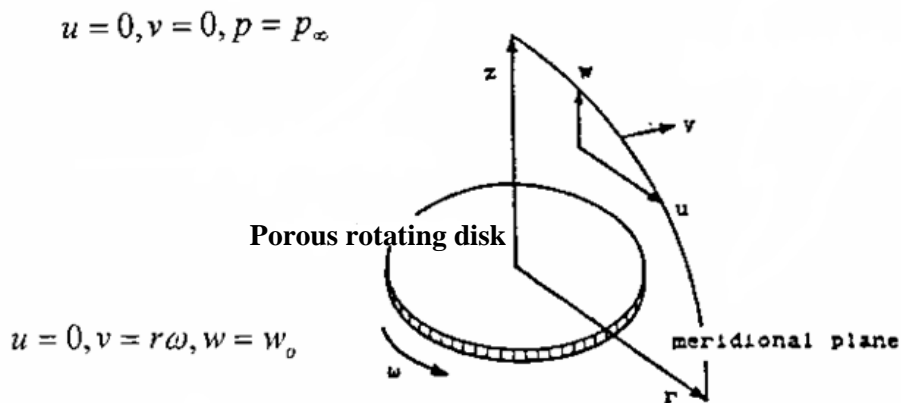
$$u = 0, v = 0, p = p_\infty$$

$$u = 0, v = r\omega, w = w_0$$

Porous rotating disk

Fig. 1: Flow Configuration

Fig.1. Flow configuration

The motion is due to rotation of an insulated disk of an infinite extent about an axis perpendicular to its plane with constant angular speed ω. Otherwise the fluid is at rest under pressure p_∞. The disk is maintained at a constant temperature T_w. A uniform injection or suction is applied at the surface of the disk for the entire range from large injection velocities to large suction velocities. The steady flow induced by a rotating disk immersed in a porous medium where the Darcy's model is assumed [30,31]. u, v and w the velocity components in the radial, azimuthal and vertical directions, respectively.

The non-Newtonian fluid considered in the present work is the power law model, where, the stress τ is related to the rate of strain tensor D_{ij} as [7].

$$\tau = 2\mu D = 2K(2D_{ij} D_{ji})^{(n-1)/2} D \qquad (1)$$

where, D denotes the deformation or rate of strain, tensor and K and n are the consistency coefficient and the power law index, respectively.

The equations of steady motion are given by the continuity equation

$$\frac{\partial u}{\partial r} + \frac{u}{r} + \frac{\partial w}{\partial z} = 0 \qquad (2)$$

and the momentum transfer equations

$$\rho(u\frac{\partial u}{\partial r} + w\frac{\partial u}{\partial z} - \frac{v^2}{r}) = \frac{\partial \tau_r^r}{\partial r} + \frac{\partial \tau_r^z}{\partial z} + \frac{\tau_r^r - \tau_\varphi^\varphi}{r} - \frac{\mu}{K1}u \qquad (3)$$

$$\rho(u\frac{\partial v}{\partial r} + w\frac{\partial v}{\partial z} + \frac{uv}{r}) = \frac{\partial \tau_\varphi^r}{\partial r} + \frac{\partial \tau_\varphi^z}{\partial z} + \frac{2\tau_\varphi^r}{r} - \frac{\mu}{K1}v \qquad (4)$$

$$\rho(u\frac{\partial w}{\partial r} + w\frac{\partial w}{\partial z}) = \frac{\partial \tau_z^r}{\partial r} + \frac{\partial \tau_z^z}{\partial z} + \frac{\tau_z^r}{r} - \frac{\mu}{K1}w \qquad (5)$$

where, ρ is the density of the fluid. The boundary conditions are given as

$$u = 0, \quad v = r\omega, \quad w = w_o \quad \text{at } z = 0 \qquad (6a)$$

$$u \to 0, \quad v \to 0, \quad p \to p_\infty \quad \text{as } z \to \infty \qquad (6b)$$

where $K1$ is the Darcy permeability [30-31]. Eq. (6a) indicates the no-slip conditions of viscous flow applied at the surface of the disk and ensures that the convective velocity normal to the surface of the disk specifies the mass injection or withdrawal. Due to the uniform suction or injection, the vertical velocity component takes a constant non-zero value w_o at $z=0$. Far from the surface of the disk, all fluid velocities must vanish aside the induced axial component as indicated in Eq. (6b).

Due to the difference in temperature between the wall and the ambient fluid, heat transfer takes place. The energy equation takes the form [5];

$$\rho c_p (u\frac{\partial T}{\partial r} + w\frac{\partial T}{\partial z}) = k\frac{\partial^2 T}{\partial z^2} + \mu((\frac{\partial u}{\partial z})^2 + (\frac{\partial v}{\partial z})^2) + \frac{k}{r}\frac{\partial}{\partial r}(\frac{1}{r}\frac{\partial T}{\partial r}) \qquad (7)$$

where, T is the temperature of the fluid, c_p is the specific heat at constant pressure of the fluid, and k is the thermal conductivity of the fluid. The boundary conditions for the energy problem are that, by continuity considerations, the temperature equals T_w at the surface of the disk. At large distances from the disk, T tends to T_∞ where T_∞ is the temperature of the ambient fluid.

We introduce von Karman transformations adapted for power-law fluid flow [1,15],

$$u = r\omega F(\zeta), \quad v = r\omega G(\zeta),$$

$$w = \left(\frac{\omega^{1-2n}}{K/\rho}\right)^{-1/(1+n)} r^{(n-1)/(n+1)} H(\zeta),$$

$$\zeta = z\left(\frac{\omega^{2-n}}{K/\rho}\right)^{1/(1+n)} r^{(1-n)/(n+1)},$$

$$\theta = (T-T_\infty)/(T_w-T_\infty)$$

where, ζ is a non-dimensional distance measured along the axis of rotation, F, G, H and θ are non-dimensional functions of ζ, and ν is the kinematic viscosity of the fluid, $\nu = \mu/\rho$. With these definitions, Eqs. (2)-(7) take the form

$$H' + 2F - \left(\frac{1-n}{1+n}\right)\zeta F' = 0 \qquad (8)$$

$$F^2 + G^2 + \left(H + \left(\frac{1-n}{1+n}\right)\zeta F\right)F' + mF = \left(((F')^2 + (G')^2)^{(n-1)/2} F'\right)' \qquad (9)$$

$$2FG + \left(H + \left(\frac{1-n}{1+n}\right)\zeta F\right)G' + mG = \left(((F')^2 + (G')^2)^{(n-1)/2} G'\right)' \qquad (10)$$

$$F = 0, \quad G = 1, \quad H = S \quad \text{at } \zeta = 0 \qquad (11a)$$

$$F \to 0, G \to 0 \quad \text{as } \zeta \to \infty \qquad (11b)$$

$$\frac{1}{Pr}\theta'' - H\theta' + Ec((F')^2 + (G')^2)^{(n+1)/2} = 0 \qquad (12)$$

where, prime denotes differentiation with respect to ζ, $Pr = \mu_0^{2/(n+1)} c_p(\omega^3 r^2)^{\frac{n-1}{n+1}}/k$ is the Prandtl number, $Ec = \omega^2 r^2/c_p(T_w - T_\infty)$ is the Eckert number and $m = \nu/K\omega$ is the porosity parameter. The boundary conditions for the velocity problem are given by eqs 11-12 where, $S = w_o/\sqrt{\omega\nu}$ is the uniform suction or injection parameter which takes constant negative values for suction and constant positive values for injection. The boundary conditions in terms of θ are expressed as

$$\theta(0) = 1, \quad \theta \to 0 \quad \text{as } \zeta \to \infty \qquad (13)$$

The above system of Eqs. (8)-(13) is sufficient to solve for the three components of the flow velocity.

The heat transfer from the disk surface to the fluid is computed by application of Fourier's law

$$Q = -k(\frac{dT}{dz})_w$$

Introducing the transformed variables, the expression for Q becomes

$$Q = -k(T_w - T_\infty)\sqrt{\frac{\omega}{\nu}}\theta'(0)$$

By rephrasing the heat transfer results in terms of a Nusselt number defined as,

$Nu = Q\sqrt{\omega/\nu}/k(T_w - T_\infty)$ the latter equation becomes

$$Nu = -\theta'(0) \qquad (14)$$

The system of non-linear ordinary differential equations (8)-(13) is solved for the three components of the flow velocity and temperature, using the Crank-Nicolson implicit method [32]. The resulting system of difference equations has to be solved in the infinite domain $0<\zeta<\infty$. A finite domain in the ζ-direction can be used instead with ζ chosen large enough to ensure that the solutions are not affected by imposing the asymptotic conditions at a finite distance. The independence of the results from the length of the finite domain and the grid density was ensured and successfully checked by various trial and error numerical experimentations. Computations are carried out for $30\leq\zeta_\infty\leq40$ for $n \leq 1$, $8\leq\zeta_\infty\leq12$ for $n > 1$ and step size $\Delta\zeta=0.001$ which are found adequate for the ranges of the parameters studied here.

RESULTS AND DISCUSSION

Figs 2(a,b,c,d) present the steady state velocity components and temperature, G, F, H, and θ, respectively, for various values of the power-law index $n=0.5$, 1, 1.5 and the porosity parameter $m=0$, 1.

In these figures, $S=0$, $Ec=0.2$ and $Pr=0.72$. For the Newtonian case, the azimuthal velocity component G decays rapidly with the vertical distance from the disk as shown in Fig. 2a. Consequently, the centrifugal force produces an outward flow in the radial direction with velocity F which is compensated by an axial inflow towards the rotating disk with velocity H as depicted in Figs. 2b and 2c. Also Fig. 1a shows that the rate of decaying decreases for the case of shear-thinning fluids ($n<1$) whereas it increases for the case of shear-thickening fluids ($n>1$).
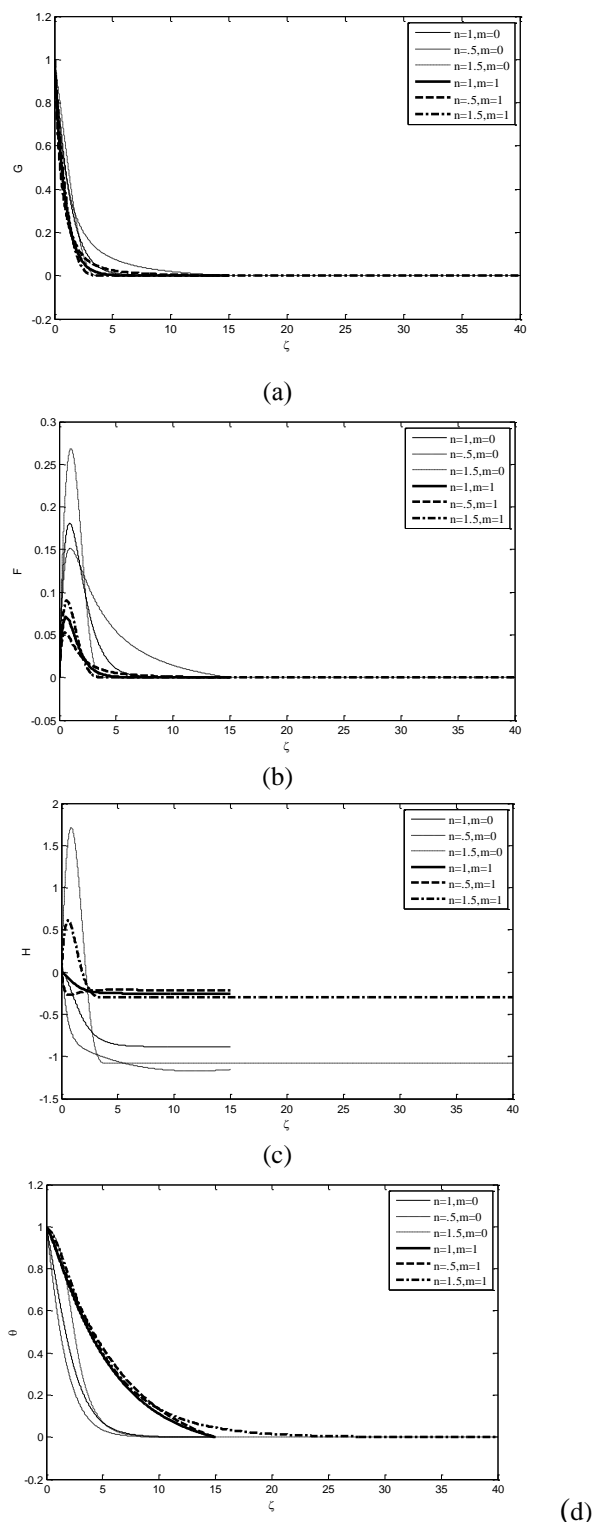

(a)

(b)

(c)

(d)

Fig. 2 Variation of G, F, H, and θ for various of n and m and for $S=0$, $Ec=0.2$ and $Pr=0.72$

Figure 2b indicates an interesting effect on the velocity component F for the case of shear-thinning fluids ($n<1$) is that, although the location of the peak in the radial velocity component F remains the same as in the Newtonian case, the shear-driven fluid motion in the plane parallel to the disk tends to penetrate further into the otherwise stagnant fluid

511

than for the case of Newtonian fluid. Consequently, this leads to the thickening of the boundary layer which gives rise to a significantly enhanced inflow in the axial direction. Another interesting result presented in Fig. 2c which is the appearance of peaks in the axial velocity components for the non-Newtonian case near the surface of the disk with the presence of cross-over points in the profiles of H for the case of shear-thickening fluids ($n>1$) which becomes more apparent for the non-porous case. We conclude that the effect of non-Newtonian fluid characteristics on the axial flow towards the disk depends on the porosity parameter. Figs. 2(a,b,c) show that only for the case of shear-thinning fluids ($n<1$), the velocity components F and G in the plane parallel to the disk reach their asymptotic zero values closer to the disk than the axial velocity component H reaches its asymptotic infinite value. It is clear from Figs. 2(a,b,c) that the porosity of the medium has a damping effect on the three velocity components G, F, and H which is expected.

Figure 2d indicates that increasing the porosity parameter m increases θ due to the effect of the porosity in damping the axial flow towards the disk and, consequently, prevents bringing the fluid at a near-ambient temperature towards the surface of the disk in addition to the effect of Joule dissipation.

It is indicated in all Figs. 2(a,b,c,d) that the effect of the porosity of the medium on the velocity components and temperature is more pronounced for the case of shear-thinning fluids ($n<1$) than the case of shear-thickening fluids ($n>1$). Figure 2d depicts the effect of increasing the power-law index n in increasing θ in the non-porous case due to its effect in decreasing the axial flow towards the disk. On the other hand, in the porous case, increasing the power-law index n decreases θ due to its effect in increasing the axial flow towards the disk which helps bringing the fluid at a near-ambient temperature towards the surface of the disk. We conclude that, the effect of non-Newtonian fluid characteristics on the temperature distribution depends on the porosity parameter.

Figs. 3(a,b,c,d) and 4(a,b,c,d) present the influence of the axial flow at the surface of the disk for injection ($S=1$) and suction ($S=-1$) respectively, on the steady state velocity components and temperature, F, G, H, and θ, respectively, for various values of the power-law index $n=0.5$, 1, 1.5 and the porosity parameter $m=0$, 1.
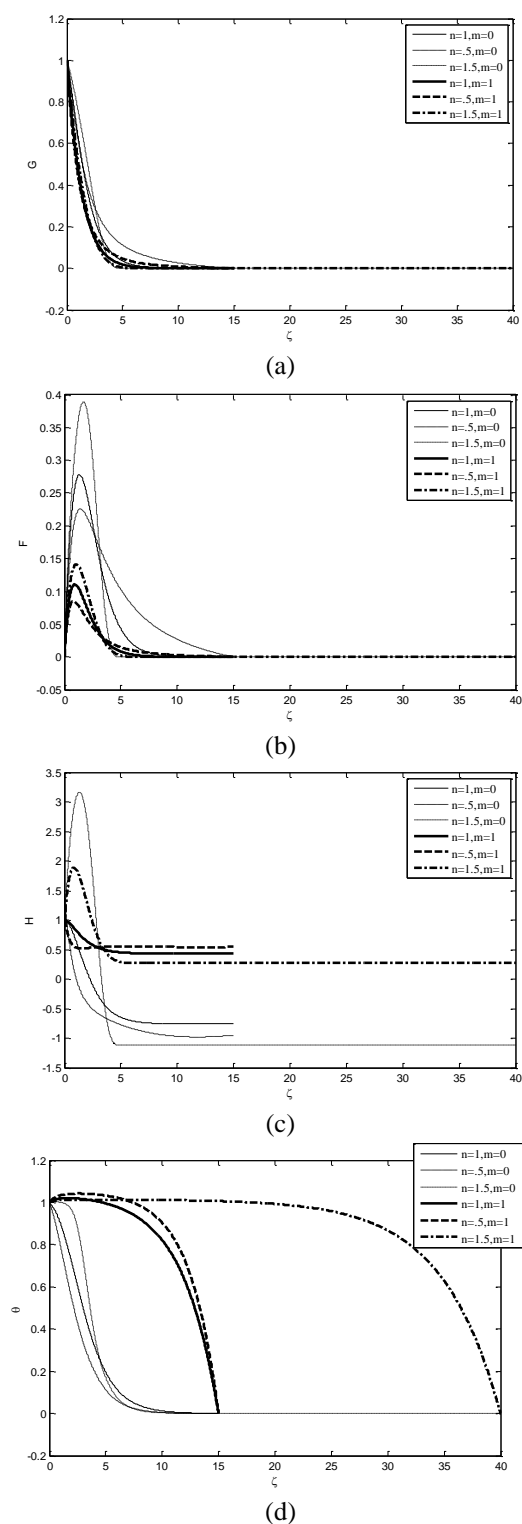

(a)

(b)

(c)

(d)

Fig. 3. Variation of F, G, H and θ for various n and m and for $S=1$, $Ec=0.2$, and $Pr=0.72$.
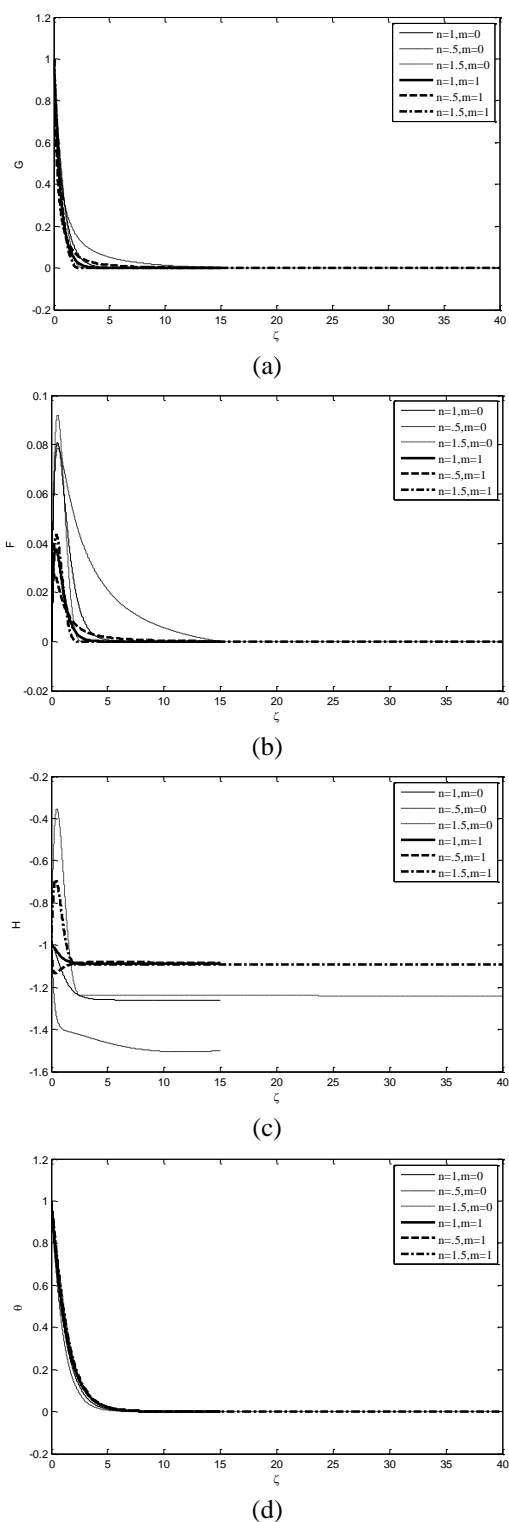
(a)

(b)

(c)

(d)

Fig. 4 Variation of G, F, H and θ for various of n and m and for $S=-1$, $Ec=0.2$ and $Pr=0.72$.

In these figures, $Ec=0.2$, $Pr=0.72$. It is clear from Figs. 3b and 4b that increasing the suction velocity leads to a rapid decrease in F while increasing the injection velocity increases F. The effect of the porosity of the medium and the non-Newtonian fluid characteristics on the radial and azimuthal flows is more pronounced in the case of

injection than that in the case of suction as shown in Figs. 3(b,c) and 4(b,c).

Figure 3c indicates that increasing the injection velocity reduces the axial flow towards the disk while with increasing injection velocity, the outflow penetrates to greater distances from the disk surface. Figure 4c shows that increasing the suction velocity increases the axial flow towards the disk while the magnitude of the axial velocity at infinity is larger than that at the disk. Figs. 3d and 4d indicate the effect of the fluid injection in decreasing the temperature significantly by blanketing the surface with fluid whose temperature is close to the wall temperature. Suction has an opposite effect on the temperature, since fluid at near-ambient temperature is brought to the neighborhood of the surface of the disk. The influence of the porosity and the flow index on the temperature distribution is more apparent in the case of injection than in the case of suction.

Table 1 presents the variation of the radial wall shear $F'(0)$, azimuthal wall shear $G'(0)$, the axial inflow at infinity $H(\infty)$ and the Nusselt number at the surface of the disk $\theta'(0)$ for various values of the parameter n, m and respectively, for $S=0$, $Ec=0.2$, $Pr=0.72$.

It is clear that increasing n increases the radial wall shear while decreases the azimuthal wall shear and its effect is more apparent for the non-porous case. On the other hand, the influence of the parameter n on the axial inflow at infinity depends on the porosity parameter. Increasing n decreases the axial inflow towards the disk in the non-porous case, while slightly increases it in the porous case. It is clear from the results presented in Table 1 that increasing the parameter n decreases the heat transfer at the surface of the disk and consequently decreases the Nusselt number Nu. Increasing the porosity parameter m decreases the radial wall shear, the axial inflow at infinity, the heat transfer at the surface of the disk, but increases the azimuthal wall shear. Tables 2 and 3 present the variation of the radial wall shear, azimuthal wall shear, the axial inflow at infinity, the Nusselt number at the surface of the disk for various values of the parameter n, m and, respectively, for $S=1$ and $S=-1$ and for $Ec=0.2$, $Pr=0.72$.

It is interesting to see the reversal of the sign of the axial inflow at infinity and the heat transfer coefficient in the injection case. Also, it is depicted that the influence of the porosity on both the radial and the azimuthal wall shears becomes more apparent for the case of injection ($S=1$) then the case of suction ($S=-1$).

Table 1 Variation of F'(0), G'(0), H (∞), θ'(0) for various values of *n* and *m* and for S=0, Pr=0.72 and Ec=0.20.

Power Law Index(*n*)	F'(0)		-G'(0)		-H(∞)		-θ'(0)	
	m=1	m=0	m=1	m=0	m=1	m=0	m=1	m=0
1.5	0.5458	0.3166	0.563	0.9606	0.7349	0.2556	0.2135	0.0404
1.3	0.5313	0.3131	0.5804	0.992	0.7704	0.2553	0.2339	0.0407
1.1	0.517	0.3103	0.6024	1.0378	0.8334	0.2543	0.261	0.0409
1	0.5102	0.3093	0.6159	1.0691	0.8845	0.2533	0.2761	0.0089
0.9	0.4938	0.3062	0.6696	1.127	0.9134	0.244	0.368	0.0187
0.8	0.4794	0.3041	0.7294	1.2005	0.989	0.2344	0.4732	0.030
0.6	0.4583	0.3041	0.879	1.4300	1.2694	0.2125	0.6842	0.0526
0.5	0.4523	0.3074	0.9813	1.6228	1.4087	0.1977	0.7719	0.058

Table 2 Variation of F'(0), G'(0), H(∞), θ'(0) for various values of *n* and *m* and for S=1, Pr=0.72 and Ec=0.20.

Power Law Index(*n*)	F'(0)		-G'(0)		-H(∞)		-θ'(0)	
	m=0	m=1	m=0	m=1	m=0	m=1	m=0	m=1
1.5	0.5393	0.3466	0.2605	0.6541	0.5968	-0.3897	0.0327	-0.0886
1.3	0.5214	0.3368	0.277	0.6652	0.6296	-0.4048	0.0397	-0.0928
1.1	0.5008	0.3267	0.2939	0.6806	0.6694	-0.422	0.0497	-0.0976
1	0.4895	0.3217	0.3022	0.6907	0.7607	-0.4317	0.0546	-0.1077
0.9	0.4748	0.3152	0.337	0.7175	0.7824	-0.4621	0.1135	-0.1146
0.8	0.4574	0.3088	0.3714	0.749	0.8637	-0.4923	01973	-0.1224
0.6	0.4156	0.2963	0.4333	0.8327	1.1377	-0.5545	0.3905	-0.1409
0.5	0.3903	0.2902	0.4575	0.8904	1.2558	-0.590	0.4711	-0.1513

Table 3 Variation of F'(0), G'(0), H (∞), θ'(0) for various values of n and m and for S=-1, Pr=0.72 and Ec=0.20.

Power Law Index(*n*)	F'(0)		-G'(0)		-H(∞)		-θ'(0)	
	m=0	m=1	m=0	m=1	m=0	m=1	m=0	m=1
1.5	0.3613	0.2345	1.0519	1.3672	1.1903	1.0868	0.6655	0.5779
1.3	0.3691	0.2396	1.0854	1.4492	1.2072	1.0878	0.681	0.5835
1.1	0.3811	0.2465	1.1374	1.5712	1.2365	1.0891	0.7022	0.5900
1	0.3896	0.251	1.1752	1.6571	1.2606	1.0898	0.7156	0.5933
0.9	0.3941	0.255	1.2544	1.7894	1.2864	1.0889	0.772	0.6165
0.8	0.4026	0.2604	1.3622	1.9584	1.3346	1.0878	0.8375	0.6408
0.6	0.4395	0.2795	1.7426	2.5783	1.5402	1.0842	0.9842	0.6869
0.5	0.479	0.2971	2.1089	3.1979	1.6635	1.0802	1.0522	0.7026

CONCLUSIONS

In this paper the steady flow through a porous medium of a non-Newtonian fluid induced by a rotating disk with heat transfer was studied in the presence of a uniform suction and injection. The effect of the porosity parameter, the non-Newtonian fluid characteristics and the uniform suction or injection velocity on the velocity and temperature distributions was considered.

It is interesting to find the appearance of peaks in the axial velocity components for the non-Newtonian case near the surface of the disk with the presence of cross-over points in the profiles of *H* in the porous case. It is depicted that the effect of the non-Newtonian fluid characteristics on the axial flow towards the disk and temperature distribution depends on the porosity parameter. It is depicted that the influence of the porosity on both the radial and azimuthal wall shears becomes more apparent for the cases of suction or injection. It is concluded that the influence of the porosity and the flow index on the temperature distribution is more apparent in the case of injection than the case of suction. It is interesting to see the reversal of the sign of the axial inflow at infinity and the heat transfer coefficient in the injection case.

REFERENCES

1. von Karman, T., , *ZAMM*, **1**, 233, (1921)
2. Cochran, W.G., *Proc. Cambridge Philos. Soc.* **30,** 365, (1934)
3. Benton, E.R., *Fluid Mechanics*, **24**, 781, (1966)
4. Millsaps, K. and Pohlhausen, K., *J. of the Aeronautical Sciences*, **19**, 120, (1952)
5. Sparrow, E.M. and Gregg, J.L., *ASME J. of Heat Transfer*, 294, (1960)

6. Attia, H.A., *Fluid Dynamics Research* **23**, 283, (1998)

7. Mithal, K.G., *Quart. J. Mech. Appl. Math.*, XIV, 401, (1961)

8. Mitschka, P., *Coll. Czech. Chem. Comm.*, **29**, 2892, (1964)

9. Mitschka, P., and Ulbreche, J., *Coll. Czech. Chem. Comm.,* **30**, 2511, (1965)

10. Andersson, H,I., Bech, K.H., Dandapat, B.S., *Int. J. Non-Linear Mech.*, **27**, 929, (1992)

11. Djukic, D.S, ", *AIChE J.*, **19**, 1159, (1973)

12. Djukic, D.S, *Trans. ASME J. Appl. Mech.*, **41**,. 822, (1974)

13. Sarpkaya, T., *AIChE J.*, **7**, 324,(1961)

14. Andersson, H.I., Korte de, E., and Meland, R., *Fluid Dynamics Research*, **28**, 75, (2001)

15. Andersson, H.I. and Korte de, E., *Eur. J. of Mech. B/Fluids*, 21, 317, (2002)

16. Attia, H.A., Ewis, K.M., Abd-maksoud, I.H., and Abdeen, M.A.M., *Russian Journal of Physical Chemistry* A, **86**, 2063, (2012)

17. Attia, H.A., Ewis, K.M., Abd-elmaksoud, I.H., and AwadAllah, N.A., *KSIAM Journal*, **16**, 169, (2012)

18. M. Batista, *Applied Mathematical Modelling*, **35**, 5225, (2011)

19. Turkyilmazoglu, M., *International Journal of Non-Linear Mechanics*, **46** , 1042, (2011)

20. A.Nazir, T. Mahmood, *Applied Mathematical Modelling,* **35**, 3154, (2011)

21. N. Bachok , A. Ishak,, I. Pop , *Physica B*, **406** 1767, (2011)

22. Anjali Devi, S.P., Uma Devi, R., , *Commun. Nonlinear Sci. Numer. Simulat.*, **16**, 1917, (2011)

23. Ch. Ming, L. Zheng, X. Zhang, *International Communications in Heat and Mass Transfer,* **38**, 280, (2011)

24. Attia, H.A., *Communications in Nonlinear Science and Numerical Simulation*, **13**, 1571, (2008)

25. Sahoo, B., *Communications in Nonlinear Science and Numerical Simulation,* **14**, 2982, (2009)

26. Osalusi, E. , Side, J. , Harris, R. , Johnston, B. , *International Communications in Heat and Mass Transfer*, **34**, 1030, (2007)

27. Turkyilmazoglu, M., *International Journal of Non Linear Mechanics,* 46, 306, (2011)

28. Attia, H.A., *Journal of Porous Medium* (JPM), **9**, 789, (2006)

29. Attia, H.A., *CNSNS*, **13**(8), 1571, (2008)

30. Ingham, D.B. and Pop, I., "Transport phenomena in porous media", Pergamon, Oxford, 2002

31. Khaled, A.R.A. and Vafai, K., *Int. J. Heat Mass Transf.*, **46**, 4989, (2003)

32. Ames, W.F., Numerical methods in partial differential equations, 2nd ed., Academic Press, New York, 1977

ЕФЕКТ НА ПОРЬОЗНОСТТА ВЪРХУ ПОТОК С ПРЕНОС НА ТОПЛИНА НА НЕНЮТОНОВ ФЛУИД, ДЪЛЖАЩ СЕ НА ВЪРТЯЩ СЕ ДИСК С ПОСТОЯННО ВСМУКВАНЕ И ИНЖЕКТИРАНЕ

Х. А. Атиа, И.Х. Абделмаксуд, В.А. Ахмед*, М. М. Елбарави

Департамент по инженерство, математика и физика, Инженерен факултет, Университет Файум, Ел-Файум-63514, Египет

(Резюме)

Беше изследван устойчивият поток, дължащ се постоянното въртене на въртящ се диск с безкрайна големина с пренос на топлина, на несвиваем ненютонов флуид през пореста среда. Дискът е потопен в порьозна среда, която се предполага, че се подчинява на модела на Дарси докато постоянното инжектиране или всмукване се прилага чрез порестата му повърхност. Получено е числено решение за ръководните нелинейни диференциални уравнения. Ефектът на характеристиките на не-Нютоновия флуид, порьозността на средата и скоростта на засмукване или инжектиране върху разпределенията на скоростта и температурата са анализирани.

Study of the interference effect of propranolol and amlodipine drugs on their interaction with human serum albumin based on molecular dynamics simulation method

M. R. Bozorgmehr[1*], M. R. Housaindokht[2,3]

[1] Department of Chemistry, Mashhad Branch, Islamic Azad University, Mashhad, Iran
[2] Biophysical Chemistry Laboratory, Department of Chemistry, Faculty of Science, Ferdowsi University of Mashhad, Mashhad, Iran
[3]Institute of Biotechnology, Ferdowsi University of Mashhad., Mashhad, Iran

The interference effect of two drugs, namely propranolol and amlodipine on their interaction with human serum albumin (HSA) was investigated. For this purpose, HSA-bilirubin and HSA-warfarin simulation systems were used as a model for comparison with experimental evidences. Four simulations, i.e. "HSA only", "HSA-propranolol", "HSA-amlodipine" and "HSA-propranolol-amlodipine" were designed with equal proportions of drugs. A new algorithm was proposed in order to determine the residues of high affinity for binding to each drug. The new pattern is based on counting the times of drug referral to each residue during simulation. Binding sites of bilirubin and warfarin on the human serum albumin were determined in this manner; the residues in IIA and IIIA sub-domains assume high affinity for these drugs. The acquired results are in good agreement with experimental findings. To study the mutual drug effects, the binding sites of propranolol and amlodipine on protein were determined separately and in presence of both drugs. The obtained results indicated that in absence of drug interference, the number of residues having affinity for propranolol is larger than that for amlodipine; the number of residues having affinity to propranolol considerably decreases in amlodipine presence. The protein secondary and tertiary structure changes were compared in presence and absence of drugs for interpreting the obtained results.

Keywords: drug interaction, ligand binding, warfarin, tertiary structure

INTRODUCTION

Human serum albumin is the most abundant protein in blood plasma constituting 60% of the total blood protein. In adults' blood, albumin concentration is approximately 40 mg/ml [1]. It is known that this protein mobilizes different compounds including biliary salts, fatty acids, variety of drugs such as diazepam, warfarin and tamoxifen. The main physiological role of human serum albumin seems to be the transfer of metabolites and other soluble substances to target tissues through blood circulation, and stabilization of pH and osmotic pressure of blood plasma.

HSA is a single chain protein of 585 residues. This protein is composed of 3 homologous domains each of which is divided into 2 sub-domains. Domain I includes residues 1 to 195, domain II – residues 196 to 383 and domain III – residues 384 to 585. Each domain consists of ten helices; the first six helices form the sub-domain A and the latter four helices – the sub-domain B of each domain. 17 disulfide bridges and a free cysteine (CYS34) exist in the structure of the protein. Domains I, II and III have 5, 6 and 6 disulfide bridges, respectively. CYS34 residue is situated on the protein surface while its sulfur atom is located in the protein and is enclosed by the residues PRO35, HIS35, VAL77 and TYR84, preventing sulfhydryl groups from coupling with outer parts.

Analysis of the crystallographic structure of HSA indicated that there exist two major binding sites in the sub-domains IIA and IIIA for different compounds; they are designated as "binding site I" and "binding site II", respectively [2]. In most cases, hydrophobic residues form a hydrophobic hole playing a crucial role in drug mobilization. Furthermore, it is proved that fatty acids having large residues are bound to sub-domains IB and IIIB [3]. Warfarin binds to "site I" with high affinity. Some studies have shown that warfarin shares with drugs like amlodipine, aspirin and indometacin binding to "site I" [4]. Other investigations have indicated that low amounts of fatty acids or an increase in pH would lead to enhancement of warfarin binding affinity for HSA; however, its mechanism has not been well understood [2].

* To whom all correspondence should be sent:
E-mail: mr_bozorgmehr@yahoo.com

Beta blockers are those drugs used for controlling heart beats and heart protection after heart attack [5]. Propranolol is among such blockers. Amlodipine is a long-acting calcium channel blocker (dihydropyridine class) used as an anti-hypertensive agent and in the treatment of angina. The aim of this study is to evaluate the molecular dynamic simulation of the interference effect of these drugs in binding to HSA.

CALCULATION METHOD

All calculations were carried out by Gromacs software version 4.5.4 and the GROMOS 43a1 force field [6, 7]. It is demonstrated that the experimental observations of protein conformations and stability are reproduced by GROMOS force field in aqueous [8, 9] and non-aqueous [10, 11] media in high pressure systems [12] and at the interface of two different media [13]. Moreover, the comparison of GROMOS force field with other biomolecular force fields showed that GROMOS commonly delivers a better representation of the experimentally observed structural behavior of the proteins [14, 15]. Six simulation boxes in $8 \times 8 \times 8 \ nm^3$ dimensions were designed and HSA (PDB ID: 1AO6) was placed in the box centers. 100 molecules of warfarin, bilirubin, propranolol and amlodipine, respectively, were placed in each of the first four simulation boxes; 50 propranolol molecules and 50 amlodipine molecules were put inside the fifth box and no drug was added to the sixth one. Since drug potential parameters are not defined in Gromacs software, Dundee webserver was used to assign these parameters [16]. In order to use this web server optimized structure of the molecule of interest is needed. Optimized structures of propranolol, warfarin, bilirubin, and amlodipine were calculated using B3LYP/6-31G (d,p) *ab initio* methods implemented in Gaussian 03 quantum mechanics packages [17].Then all simulation boxes were filled with SPC water. For having neutral conditions in terms of electrical charge, suitable number of ions is added to each box.

To create a suitable starting point for simulation and eliminating the initial kinetic energy of the system, the energies of all abovementioned simulation boxes were minimized through steepest descent algorithm. Subsequently, all systems were simulated by position restrained algorithm; in this stage, the water molecules surrounding the protein were equilibrated. Then each grid was simulated for 50 nano-seconds with a 2 femto-seconds time-step. LINCS algorithm [18] was employed to fix the chemical bonds between the atoms of the protein and SETTLE algorithm [19] in the case of solvent molecules. All simulations were done at a temperature of 300 Kelvin. As simulation boxes contain molecules of different dimensions, each molecule will have its own specific kinetic energy; i.e. smaller molecules like those of the solvent have higher energy and larger molecules like protein have lower kinetic energy. Accordingly, the solvent will be warmer than the soluble matter during simulation. This is referred to as a "hot solvent-cold solute" phenomenon. In order to prevent this phenomenon and to control the temperature, each of the designed systems is coupled with a thermal bath. All boxes are coupled with a V-rescale bath to control system temperature. To calculate the electrostatic interactions, PME algorithm was used. In this algorithm every atom interacts with all atoms in the simulation box and all of their images in an infinite number of identical copies surrounding the main box, so that satisfactory results are produced for the electrostatic interactions [20, 21].

RESULTS AND DISCUSSION

Binding of drugs to a binding site is a dynamic process during which the drug moves in its binding site and can have different orientations. For determining the binding site of each drug, the following procedures were conducted:

a- The collisions between drugs and each of the protein residues are counted during simulation, n_i . For drug atoms being located at a distance not greater than 4 Å, each of the respective residue atoms is considered as a "collision". This distance is a limit proposed in references [22, 23].

b- Average numbers of collisions to each residue are computed. To calculate the average number, the total number of collisions is divided into a number of protein residues. $\langle n_i \rangle = \sum n_i / n_r$

In this relation, "n_r" is the number of protein residues (here 585).

c- Binding conformational factor is defined as $P_i = n_i / \langle n_i \rangle$. This quantity might assume different values signifying the following conditions:

The residue i with $P_i >1$ is considered to have affinity toward the drug, while with $P_i <1$ it has no affinity.

This simple algorithm was developed by our research group and was successfully utilized for predicting the binding site of thiourea to lysozyme,

the protein binding site of sodium dodecyl sulfate (SDS) to cobra cardio toxin, and the binding site of sodium dodecyl sulfate (SDS) to carbonic anhydrase [24]. The residues having P_i >1 in HSA-warfarin in the performed simulations were determined by this method and the results are listed in Table 1. According to the reported values, it is evident that in addition to residues in IIA and IIIA sub-domains which were reported as binding sites in the experimental reports [2], residues of domain I were also encountered. The results related to bilirubin are also reported in Table 1 and indicate that these residues are located in sub-domains IIA and IIIA, which is in agreement with experimental data. In Table 2, the residues having P_i >1 for HSA in presence of propranolol and amlodipine and equal proportions of each drug are presented.

Table 1 the residues having P_i greater than unit

HSA-Warfarin					HSA- bilirubin			
583	173	363	120	164	583	499	66	356
585	277	62	387	84	584	105	210	275
584	500	300	233	446	585	41	500	325
171	172	574	66	227	277	441	283	312
95	207	289	93	146	386	479	287	308
391	161	11	55	42	118	565	453	213
268	418	286	544	472	281	323	582	123
115	65	310	78	404	564	282	55	364
271	46	142	12	441	322	45	444	383
498	470	501	479		269	56	445	559
228	327	293	119		129	566	115	119
497	113	407	294		13	538	440	575
281	543	394	516		473	318	375	314
411	399	330	471		472	229	372	376
168	521	278	318		465	397	437	501
41	325	275	287		274	126	263	474
269	359	499	406		475	516	116	
145	206	110	582		443	399	373	
229	114	210	480		515	517	172	
398	550	547	303		390	497	305	
47	578	392	16		234	580	37	
157	540	130	283		398	514	449	
326	167	160	317		171	326	138	
270	468	77	61		496	360	468	
496	395	322	124		446	237	369	
267	560	514	517		12	44	206	
337	138	323	538		64	498	365	
112	34	135	230		495	65	396	
545	362	295	388		466	267	266	
117	546	410	74		570	280	324	
226	320	321	333		467	469	180	
282	290	412	118		574	5	230	
542	177	324	466		233	9	307	
469	127	116	51		521	379	168	
141	126	94	408		571	403	161	
541	559	174	575		359	476	387	
515	495	280	302		130	560	581	
319	403	301	69		418	87	270	
123	390	53	581		57	536	480	
64	213	50	360		117	6	58	

Table 2 the residues having P_i greater than unit

HSA- Amlodipine						HSA- Propranolol					HSA- Amlodipine-Propranolol			
85	578	233	92	512	585	375	545	389	496	319	583	479	310	549
584	495	358	439	383	581	318	546	435	571	573	584	399	418	89

580	41	298	317	582	463	322	468	70	467	585	205	369	313
579	225	80	295	583	539	532	520	273	480	398	138	85	500
583	45	52	300	580	362	356	323	241	118	83	238	403	108
581	557	96	575	584	577	359	253	294	296	61	498	81	317
582	244	249	471	579	76	308	81	324	98	322	546	362	94
125	353	373	173	260	94	574	361	306	109	480	302	296	575
277	364	94	48	167	465	78	171	314	124	492	467	177	16
264	360	505	555	559	578	125	56	188	262	497	312	577	271
263	53	552	266	393	392	299	286	169	338	59	319	543	367
393	538	309	246	263	201	570	477	345	115	496	472	135	90
260	462	78	487	562	558	390	326	557	534	268	581	574	517
497	301	90	483	369	226	414	466	320		476	339	364	300
556	553	122	467	576	386	90	209	377		270	60	363	303
394	392	49	62	365	372	295	126	101		320	121	289	15
390	310	55	100	9	379	80	168	316		368	120	209	297
91	539	366	461	560	73	267	82	398		473	324	326	522
558	352	491	89	203	8	493	77	575		550	582	330	494
369	576	315	267	57	206	278	358	490		161	13	468	481
46	559	493	313	264	266	298	563	550		207	469	545	578
501	494	335	414	277	86	475	92	561		82	323	208	37
318	484	469	305	60	497	46	337	426		542	490	397	63
387	506	283	163	83	55	495	127	130		318	62	470	127
230	38	7	241	6	491	376	166	41		580	376	274	579
496	365	8	463	116	469	185	87	489		269	180	58	371
126	504	34	276	476	108	394	311	104		206	64	366	11
468	492	273	226	373	205	131	274	291		299	301	293	372
319	465	76	472	225	321	366	58	222		267	365	134	204
560	54	79	362	5	265	229	492	395		105	391	488	573
265	577	81	279	230	164	13	461	110		495	257	477	493
499	314	278	435	202	567	464	59	285		394	298	547	14
308	73	574	64	382	91	256	544	61		314	519	260	373
561	297	124	51	30	102	360	364	512		84	80	518	420
511	361	510	498	227	79	129	52	297		241	501	359	168
299	44	564	74	237	439	97	508	240		157	327	551	499
167	201	164	480	114	54	184	472	380		321	264	181	395
502	229	391	128	315	566	74	543	53		12	122	86	
97	436	93	234	224	436	252	305	399		491	502	176	
359	562	30	127	442	462	353	335	276		338	277	315	

As indicated in the table, residues with affinity for propranolol drug exceed those affined for amlodipine in absence of drug interference. However, the numerical value of Pi for residues affined for amlodipine is larger than that of residues having affinity for propranolol (data not shown); thus, more alterations are expected in residues with affinity for binding to propranolol in the case of two drugs interference in binding to HSA. This happens because of the fact that amlodipine would primarily occupy the binding sites due to its higher affinity and both drugs will compete for binding to the protein. The residues with $P_i>1$ are illustrated in Table 2 for propranolol and amlodipine affinities in a system with equal proportions of both drugs. According to the table, it is seen that residues with $P_i>1$ remarkably decline in terms of propranolol affinity. Alterations in protein secondary and tertiary structural changes in the simulated systems were investigated for result interpretations. In Figure 1 the secondary structure of HSA along with its sequence is depicted to illustrate the numbers listed in Tables 1 and 2. In this figure red and blue colors show helices and coil secondary structures, respectively.
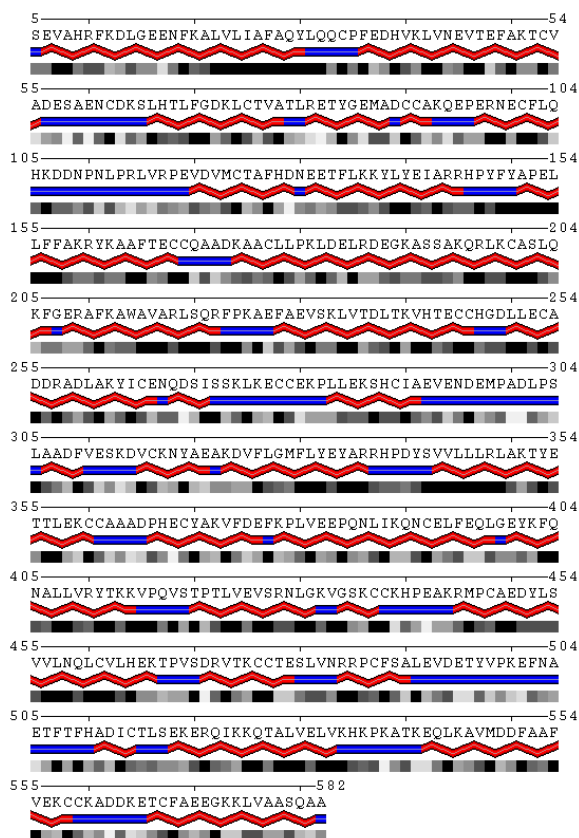
Fig. 1. Secondary structure of HSA along with its sequence depicted to illustrate the numbers listed in Tables 1 and 2.

Secondary Structure

Percentages of all structures including alpha helix, 3_{10} helix, turn and coil were calculated by the Kabsch-Sander method and DSSP program for HSA in the simulations [25]. The results are shown in Figure 2.
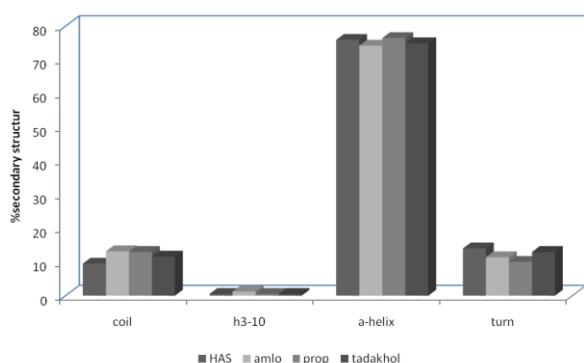

Fig. 2. HSA secondary structures percentage in the studied simulations.

As implied by the figure, amlodipine has a more reduced helix structure than propranolol, whereas the latter resulted in improved alpha helix structure to some extent. Turn structure has also decreased in the presence of propranolol and amlodipine. Turn and 3_{10} helix structures have increased in presence of amlodipine implying that in its presence alpha

520

helix structure is converted into 3_{10} helix and coil structures. In general, the figure suggests that the protein secondary structural change is more considerable in presence of amlodipine compared to propranolol.

Tertiary Structure

Contact map was used to manifest the tertiary structure change of HSA in different conditions in this study. In Figure 3, the contact map of HSA is compared in presence and absence of propranolol.
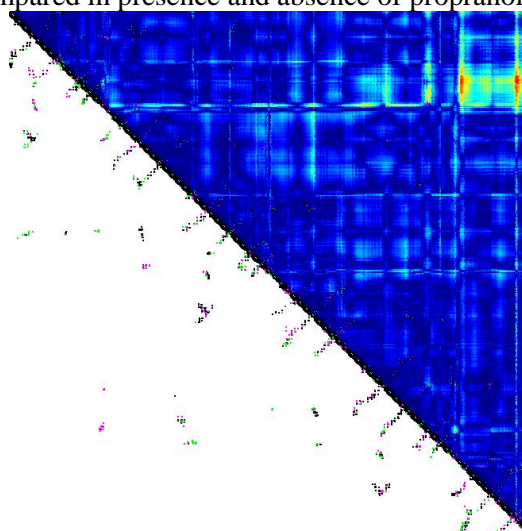
Fig. 3. Contact map of HSA in presence and absence of propranolol.

In the lower triangle of the contact map, pink color denotes the contacts existing in the protein in presence of propranolol but not existing in its absence, while green color represents the contacts existing in drug absence but not existing in its presence. Black color denotes the contacts in the HSA structure, which are common both in presence and absence of the drug. Variation curve of the distance between the ith and j[th] protein residues in presence and absence of drug is shown in the upper triangle of the contact diagram. Red and blue colors are related to the highest and the lowest changes of distance between the residues, respectively. According to the figure, the highest changes belong to the contact area of residues 66 and 495 and the contact region of residues 66 and 578.

In Figure 4, the contact map of HSA is compared in presence and absence of amlodipine. In the lower triangle of the contact diagram, green color specifies contacts existing in the protein in presence of amlodipine but not existing in absence of the drug, while pink color represents contacts existing in the protein in drug absence but not existing in its presence. Variation curve of the distance between the ith and j[th] protein residues in presence and absence of drug is shown in the upper triangle of the contact diagram. Extended variation

range is observed in the contact diagram compared to Figure 4 indicating that the protein tertiary structure is more influenced by amlodipine.
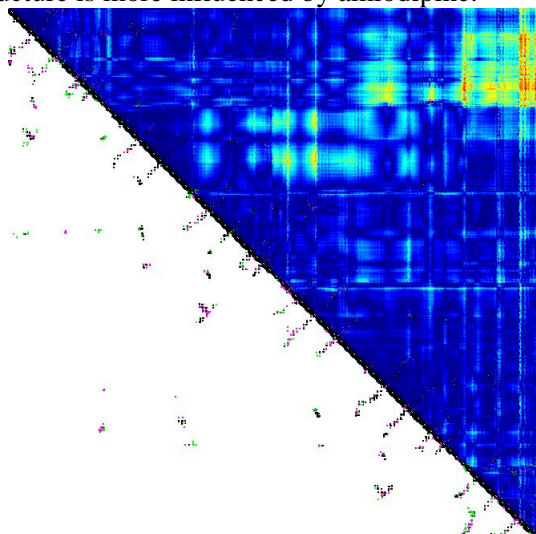
Fig. 4. Contact map of HSA in presence and absence of amlodipine.

In Figure 5, the protein contact map is compared in presence and absence of drug for equal proportions of both drugs.
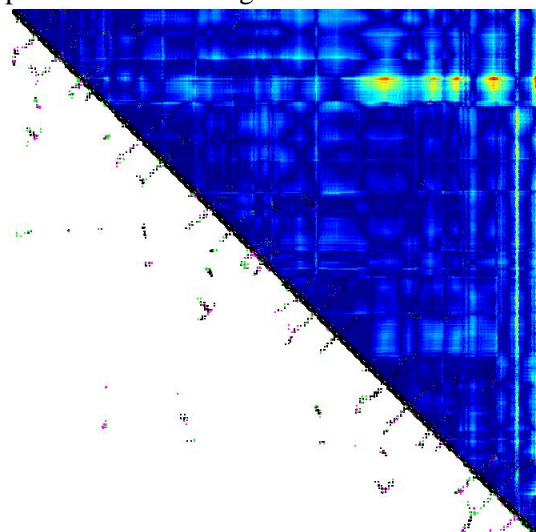
Fig. 5. Protein contact map in presence and absence of drug for equal proportions of both propranolol and amlodipine.

In the lower triangle of the contact diagram, green color signifies contacts existing in the protein in presence of amlodipine and propranolol but not existing in their absence, while pink color represents contacts existing in the protein in drugs absence but not existing in their presence. Needleman algorithm available in contact map view software was applied for generating the contact diagrams [26].

Hence, according to the abovementioned results, the protein structure is more influenced by amlodipine.

REFERENCES

1. Dockal, M., D.C. Carter, and F. Rüker, *Journal of Biological Chemistry,* **274**(41): 29303, (1999)
2. Petitpas, I., et al., I. Journal of Biological Chemistry, **276**(25): 22804, (2001)
3. Fujiwara, S.-i. and T. Amisaki, *Biophysical journal*, **94**(1): 95,(2008)
4. Abdollahpour, N., et al., *Journal of Luminescence,* 131(9), 1885, (2011)
5. Garcia-Domenech, R., et al., *Bioorganic & Medicinal Chemistry Letters*, **7**(5), 567,1997
6. Berendsen, H.J., D. van der Spoel, and R. van Drunen, *Computer Physics Communications*, **91**(1),43, (1995)
7. Van Der Spoel, D., et al., J*ournal of computational chemistry*, **26**(16), 1701, (2005)
8. Melchionna, S., M. Barteri, and G. Ciccotti, *Journal of Physical Chemistry*, **100**, 19241, (1996)
9. Dıaz-Vergara, N. and A. Pineiro, J*ournal of physical Chemistry B*, 112, 3529, (2008)
10. Soares, C.M., V. H.Teixeira, and A.M. Baptista, *Biophysical Journal*, **84**,1628–1641, (2003)
11. Micaelo, N.M. and C.M. Soares*, Journal of Physical Chemistry B*, **112**, 2566, (2008)
12. Trzesniak, D., R.D. Lins, and W.F.v. Gunsteren1, *Protein Under Pressure: PROTEINS: Structure, Function, and Bioinformatics*, **65**,. 136, (2006)
13. Jensen, M.Ø., et al., *Biophysical Journal*, **83**, 98, (2002)
14. Spoel, D.v.d. and E. Lindahl, *Journal of Physical Chemistry B*, **107**, 11178, (2003)
15. Todorova, N., et al., *Journal of Physical Chemistry B*, **112**,11137, (2008)
16. Schuttelkopf, A.W. and D.M. van Aalten, *Acta Crystallographica Section D: Biological Crystallography*, **60**(8), 1355, (2004)
17. Frisch, M.J., et al., *Gaussian 03, Revision C.02*, 2003.
18. Berendsen, H.J., et al., *In: Pullman, B. (Ed.), Intermolecular Forces. Reidel Dordrecht, The Netherlands.* 1981.
19. Darden, T., D. York, and L. Pedersen, *J. Chem. Phys*, **98**,10089, (1993)
20. Darden, T., D. York, and L. Pedersen, *The Journal of chemical physics*, **98**, 10089, (1993)
21. Danciulescu, C., B. Nick, and F.-J. Wortmann, *Biomacromolecules*, **5**(6), 2165, (2004)
22. Psachoulia, E., P.J. Bond, and M.S. Sansom, *Biochemistry*, **45(**30), 9053, (2006)
23. Bond, P.J., et al., J*ournal of the American Chemical Society*, **126**(49), 15948, (2004)
24. Housaindokht, M.R., M. Bozorgmehr, and M. Bahrololoom, *Journal of theoretical biology*, **254**(2), 294, (2008)
25. Kabsch, W. and C. Sander, *Biopolymers*, **22**(12), 2577, (1983)
26. Vehlow, C., et al., *Bioinformatics*, **27**(11), 1573, (2011)

ИЗСЛЕДВАНЕ НА ЕФЕКТА НА ИНТЕРФЕРЕНЦИЯ НА ПРОПАНОЛОЛ И АМЛОДИПИН ВЪРХУ ВЗАИМОДЕЙСТВИЕТО С АЛБУМИН ОТ ЧОВЕШКИ СЕРУМ ЧРЕЗ МЕТОДА НА СИНАМИЧНО СИМУЛИРАНЕ

М.Р. Бозоргмехр[1*], М.Р. Хусаиндокхт[2,3]

[1] Департамент по химия, Ислямски университет „Азад“, клон Машхад, Машхад, Иран
[2] Лаборатория по биофизична химия, Департамент по химия, Научен факултет, Университет „Фердоуси“ в Машхад, Иран
[3]Институт по биотехнология, Университет „Фердоуси“ в Машхад, Иран

Изследването има за цел да проучи ефектът на интерференция на две лекарства: пропанолол и амлодипин, върху взаимодействието с албумин от човешки серум (HSA). За тази цел са използвани системи за симулиране на HSA-билирубин и HSA-варфарин като модели за сравнение с опитни данни. Четири симулации, т.е. “само HSA”, “HSA-пропанолол”, “HSA-амлодипин” и “HSA- пропанолол - амлодипин” са конструирани с еднакви пропорции на лекарствата. Предложен е нов алгоритъм за определяне на остатъчните количества с висок афинитет на свързване за всяко лекарство. Предложен е нов модел на взаимодействие основан на преброяването на свързването на лекарствата към всеки остатък. По този начин са определени центровете за свързване на билирубина и варфарина върху HSA; остатъците в IIA и IIIA суб-домейни предполагат висок афинитет за тези лекарства. Получените резултати са в добро съгласие с опитните наблюдения. За изследването на съвместния ефект на лекарствата центровете на свързване на пропанолола и амлодипина върху протеините в присъствие на двете лекарства. Получените резултати показват, че в отсъствие на интерференция на лекарствата броят на остатъците с афинитет към пропанолола е по-голям от остатъците с афинитет към амлодипин. Броят на остатъците с афинитет към пропанолола намалява значително в присъствие на амлодипин. Измененията на вторичната и третичната структура са сравнени в писъствие и отсъствие на лекарства за интерпретиране на получените резултати.

Synthesis of functionalized piperidines by one-pot multicomponent reaction using nano-crystalline solid acid catalysts

A. Teimouri [1,*], A. N. Chermahini [2], L. Ghorbanian [3]

[1] Chemistry Department, Payame Noor University, Tehran, I. R. of Iran
[2] Department of Chemistry, Isfahan University of Technology, Isfahan, Iran
[3] Materials Engineering Department, Isfahan University of Technology, Isfahan, Iran

A simple and convenient one-pot multicomponent reaction for the synthesis of functionalized piperidines was developed. The procedure involves mixing of 1,3-dicarbonyl compounds, amines and aromatic aldehydes in ethanol at room temperature using nano-sulfated zirconia, nano-structured ZnO, nano-γ-alumina and nano-ZSM-5 zeolites, as the catalyst. The optical properties of the nano-structured organic molecules were studied. The advantages of the methods are short reaction times, mild conditions, and easy work-up. The catalysts can be recovered for the subsequent reactions and reused without any appreciable loss of efficiency.

Keywords: piperidines, nano-sulfated zirconia, nano-structured ZnO, nano-γ-alumina, nano-ZSM-5 zeolites.

INTRODUCTION

Piperidine and its analogues are widely distributed in many natural products, biologically active molecules and organic fine chemicals. [1] Some of them also act as pharmaceutical agents. [2] Compounds containing piperidine structural motif exhibit anti-hypertensive [3], anti-bacterial [4], anti-convulsant, anti-inflammatory [5] and antimalarial activities [6].

Thus, the synthesis of highly substituted piperidines has gained considerable attention [7], and a number of procedures have been developed using several approaches such as imino-Diels-Alder reactions [8], aza-Prins-cyclizations [9], intramolecular Michael reactions [10] and intramolecular Mannich reaction [11]. An alternative strategy for the synthesis of functionalized piperidines is using multicomponent reactions (MCRs).

Nowadays, one-pot multicomponent reactions have received special attention over their multistep variants for reasons of economy, energy efficiency, and general environmental friendliness. [12] The functionalized piperidines have been reported using MCRs strategy by employing catalysts, such as a combination of molecular iodine [13], L-proline [6], bromodimethylsulfonium bromide (BDMS) [14], tetrabutylammonium tribromide (TBATB) [15], InCl$_3$ [16], ZrOCl$_2$.8H$_2$O [17], Bi(NO$_3$)$_3$.5H$_2$O [18], CAN [19], ZrCl$_4$ [20] and NiClO$_4$.6H$_2$O [21]. Therefore, there is a need for a highly efficient, versatile, and eco-friendly synthetic protocol to obtain these valuable compounds in good yields.

In the recent years, the use of nano-structured ZnO [22], nano-sulfated zirconia [23], nano-γ-alumina [24], and nano-ZSM-5 zeolite [25] catalysts has received considerable interest in organic synthesis. This extensive application of heterogeneous catalysts in synthetic organic chemistry can make the synthetic process more efficient from both environmental and economic point of view [26] and the used catalyst can be easily recycled.

As a part of our continuing efforts towards the development of useful synthetic methodologies [27], herein we report an efficient process for synthesis of functionalized piperidines by the reaction of 1,3-dicarbonyl compounds, amines and aromatic aldehydes using nano-structured ZnO, nano-sulfated zirconia, nano-γ-alumina and nano-ZSM-5 zeolites as the catalyst.

EXPERIMENTAL

Materials

All reagents were purchased from Merck and Aldrich and were used without further purification. Melting points reported were determined by an open capillary method using a Galen Kamp melting point apparatus and are uncorrected.

Instruments

Products were characterized by spectroscopy data (IR, FTIR, ^{1}H NMR and ^{13}C NMR spectra), elemental analysis (CHN) and melting points. A JASCO FT/IR-680 PLUS spectrometer was used to record IR spectra using KBr pellets. NMR spectra were recorded on a Bruker 400 Ultrashield NMR

* To whom all correspondence should be sent:
E-mail: a_teimouri@pnu.ac.ir

instrument using DMSO-d6 as a solvent. Mass spectra were recorded on a Shimadzu Gas Chromatograph Mass Spectrometer GCMS-QP5050A/Q P5000.

Catalyst preparation
Synthesis of nano-crystalline sulfated zirconia

Nano-crystalline sulfated zirconia was prepared by one step sol–gel technique [28]. A typical synthesis involves the addition of concentrated sulfuric acid (1.02 ml) to zirconium n-propoxide precursor (30 wt%) followed by hydrolysis with water. After 3 h aging at room temperature, the resulting gel was dried at 110°C for 12 h followed by calcination at 600°C for 2 h.

Synthesis of nano-structured ZnO

Nano-structured ZnO was prepared by one step sol–gel technique [29]. In a typical procedure, mixtures of ethanol, diethanolamine (DEA) and zinc acetate dihydrate, were prepared. The concentration of zinc acetate dihydrate in the solvent was 0.2 M. The molar ratio of zinc acetate dihydrate and diethanolamine was 1.0. pH of the mixture was adjusted to about 9. When the zinc acetate crystals were completely dissolved, sodium hydroxide (NaOH) pellets were added to the solution to increase pH of the mixture to about 11. The resultant solution was then transferred to a Teflon-lined stainless steel autoclave which was sealed and maintained at 130 °C for 24 h.

Synthesis of nano-γ-Al$_2$O$_3$ catalyst

Nano-γ-Al$_2$O$_3$ was prepared by the sol–gel method according to a described procedure [24]. In a typical experiment, aluminum nitrate (15.614 g) was added to 400 ml of deionized water. Similarly a solution of sodium carbonate was prepared by dissolving (7.95 g) in 400 ml of deionized water. 200 ml of the deionized water was taken in a 2 l capacity round-bottom flask and was stirred well using a magnetic stirrer. Then sodium carbonate and aluminum nitrate solutions were added drop wise to 200 ml of deionized water (from separate burettes).

The temperature was maintained at 70 °C during the experiment. pH after precipitation was found to be in the range of 7.5–8.5. The mixture was stirred for 4 h. The digested precipitates were filtered and re-dispersed again in 2 l of hot deionized water, filtered and finally washed with ethanol, followed by acetone to avoid contamination by Na ions; and air dried at room temperature. The dried precipitates were calcined in a furnace at 550 °C for 5 h to produce nano-sized γ-Al$_2$O$_3$ powders.

Synthesis of nano-ZSM-5

For synthesis of nano-ZSM-5, tetrapropyl ammonium hydroxide and tetraethyl orthosilicate were the sources of aluminum and silicon, respectively. Nano-ZSM-5 zeolite was synthesized according to a procedure described earlier [30]. The components were mixed under constant stirring. After adding all ingredients the solution was left to hydrolyze at room temperature for 48 h. The gel thus obtained was heated at 80 °C to evaporate water and ethanol formed during the reaction. The obtained solution was charged to a Teflon-lined stainless steel autoclave under pressure and static conditions at 170 °C for 48 h. The solid phase obtained was filtered, washed with distilled water several times, dried at 120 °C and then calcinated at 550 °C for 12 hours.

Characterization

X-ray diffraction patterns were recorded on a diffractometer (Philips X'pert) using CuKα radiation (λ=1.5405 Å), The angle range was between 0 and 80° (figure 1), Crystallite size of the crystalline phase was determined from the peak of maximum intensity (2θ=30.18) by using the Scherrer formula, [31] with a shape factor (K) of 0.9, as shown below:

Crystallite size = K.λ/W.cosθ, where $W=W_b−W_s$ and W_b is the broadened profile width of the sample and W_s is the standard profile width of the reference silicon sample. FT-IR spectra of the catalysts were recorded on a FT-IR spectrophotometer in the range of 400–4000 cm^{-1} with a resolution of 4 cm^{-1} by mixing the sample with KBr (figure 2).

Specific surface area, pore volume and pore size distribution of sulfated zirconia samples calcined at 600∘C were determined from N$_2$ adsorption–desorption isotherms at 77K (ASAP 2010 Micromeritics). Surface area was calculated by using BET equation; pore volume and pore size distribution were calculated by the BJH method. [32]

The samples were degassed under vacuum at 120 ∘C for 4 h prior to the adsorption measurement to evacuate the physisorbed moisture. The detailed imaging information about the morphology and surface texture of the catalyst was provided by SEM (Philips XL30 ESEM TMP), part of the spectral data has been published in our previous work [27]. The bulk sulfur (wt.%) retained in the sulfated zirconia samples before and after calcination at 600 °C was analyzed by a C H N S/O elemental analyzer.

GENERAL EXPERIMENTAL PROCEDURE

To the reaction mixture of amine (2 mmol) and methyl acetoacetate (1 mmol) in ethanol (5 mL) catalyst was added and the mixture was stirred at room temperature. After 30 min, aromatic aldehyde

(2 mmol) was added to the reaction mixture and stirring was continued for completion. The reaction was monitored by TLC. After the reaction was completed, EtOAc (2×20 mL) was added to the reaction mixture and the catalyst was separated by filtration. The organic solvent was removed under reduced pressure. The obtained products were further purified by chromatography on silica gel (ethyl acetate/n-hexane 30:70) as an eluent. Compounds were characterized by spectral data.

Spectral data for compound (1a) m.p. 180-182 °C, FTIR (KBr, cm^{-1}) v_{max}: 3447, 2918, 1663, 1589, 1504, 1347, 1070; ^{1}H NMR spectrum (DMSO-d6, 400 MHz), δ_H, ppm: 10.20 (1H, s, NH), 7.31-7.25 (8H, m, ArH), 7.14 (2H, d, ArH), 7.15-7.08 (5H, m, ArH), 6.61 (1H, t, ArH), 6.49 (2H, d, ArH), 6.42 (1H, s, H), 6.25 (2H, d, ArH), 5.12 (1H, d, H-6), 3.91 (3H, s, Me), 2.84 (1H, dd, H), 2.73 (1H, dd, H); ^{13}C NMR spectrum (100MHz, CDCl$_3$), δ_C, ppm: 168.5, 156.1, 147.3, 144.2, 142.7, 137.7, 129.1, 128.3, 128.4, 128.0, 127.2, 126.6, 126.3, 125.9, 125.5, 116.1, 113.3, 98.2, 58.1, 55.4, 51.6, 33.6; MS: m/z (M$^+$+1): 462.22; Anal. Calcd for C$_{31}$H$_{28}$N$_2$O$_2$: C, 80.84; H, 6.13; N, 6.08. Found: C, 80.71; H, 6.03; N, 6.01.

Spectral data for compound (1b) m.p. 210-212 °C, FTIR (KBr, cm^{-1}) v_{max}: 3250, 2943, 1660, 1591, 1519, 1436, 1172, 1070; ^{1}H NMR spectrum (DMSO-d6, 400 MHz), δ_H, ppm: 10.26 (1H, s, NH), 7.39-7.25 (5H, m, ArH), 7.12 (2H, d, ArH), 7.07 (2H, t, ArH), 7.05 (2H, d, ArH), 7.01 (2H, d, ArH), 6.62 (1H, t, ArH), 6.43 (2H, d, ArH), 6.38 (2H, d, ArH), 6.32 (1H, s, H-2), 5.05 (1H, d, H), 3.88 (3H, s, OMe), 2.80 (1H, dd, H), 2.71 (1H, dd, H); ^{13}C NMR spectrum (100MHz, CDCl$_3$), δ_C, ppm: 168.2, 156.0, 146.4, 142.5, 141.3, 137.5, 133.1, 132.1, 129.3, 128.7, 128.5, 128.1, 127.7, 126.2, 125.9, 116.9, 113.1, 97.2, 57.6, 54.4, 51.0, 33.6; MS: m/z (M$^+$+1): 530.14; Anal. Calcd for C$_{31}$H$_{26}$N$_2$O$_2$Cl$_2$: C, 70.32; H, 4.95; N, 5.29. Found: C, 70.23; H, 4.81; N, 5.14.

Spectral data for compound (1c) m.p. 242-244 °C, FTIR (KBr, cm^{-1}) v_{max}: 3257, 2953, 1661, 1590, 1517, 1435, 1175, 1070; ^{1}H NMR spectrum (DMSO-d6, 400 MHz), δ_H, ppm: 10.22 (1H, s, NH), 7.43 (2H, d, ArH), 7.41 (2H, d, ArH), 7.16 (2H, d, ArH), 7.14 (2H, d, ArH), 7.13 (1H, t, ArH), 7.06 (2H, t, ArH), 7.00 (2H, d, ArH), 6.67 (1H, t, ArH), 6.43 (2H, d, ArH), 6.38 (2H, d, ArH), 6.32 (1H, s, H-2), 5.06 (1H, d, H), 3.91 (3H, s, OMe), 2.86 (1H, dd, H), 2.70 (1H, dd, H); ^{13}C NMR spectrum (100MHz, CDCl$_3$), δ_C, ppm: 168.4, 156.3 , 145.8, 143.0, 141.5, 137.5, 132.3, 131.1, 129.3, 129.1, 128.4, 128.1, 126.0, 125.7, 121.4, 120.1, 116.6, 112.8, 97.1, 57.6, 54.2, 50.8, 34.2; MS: m/z

(M$^+$+1): 618.04; Anal. Calcd for C$_{31}$H$_{26}$Br$_2$N$_2$O$_2$: C, 60.21; H, 4.24; N, 4.53. Found: C, 60.05; H, 4.13; N, 4.91.

Spectral data for compound (1d) m.p. 236-238 °C, FTIR (KBr, cm^{-1}) v_{max}: 3356, 2950, 1660, 1593, 1514, 1463, 1347, 1182, 1070; ^{1}H NMR spectrum (DMSO-d6, 400 MHz), δ_H, ppm: 10.23 (1H, s, NH), 8.12 (2H, d, ArH), 8.10 (2H, d, ArH), 7.46 (2H, d, ArH), 7.25 (2H, d, ArH), 7.15-7.11 (3H, m, ArH), 7.07 (1H, ArH), 7.05 (1H, ArH), 6.66 (1H, t, ArH), 6.44 (1H, s, H-2), 6.40-6.35 (4H, m, ArH), 5.23-5.21 (1H, m, H), 3.93 (3H, s, OMe), 2.83 (2H, d, CH$_2$); ^{13}C NMR spectrum (100MHz, CDCl$_3$), δ_C, ppm: 168.1, 155.5, 151.6, 149.2, 147.4, 146.8, 145.6, 137.1, 129.7, 129.2, 127.3, 127.1, 126.8, 125.9, 123.9, 123.3, 118.3, 113.4, 96.4, 57.3, 55.2, 51.4, 34.2; MS: m/z (M$^+$+1): 551.19; Anal. Calcd for C$_{31}$H$_{26}$N$_4$O$_6$: C, 67.63; H, 4.76; N, 10.18. Found: C, 67.50; H, 4.63; N, 10.29.

Spectral data for compound (1f) m.p. 184-186 °C, FTIR (KBr, cm^{-1}) v_{max}: 3259, 3206, 2947, 1654, 1593, 1517, 1452, 1318, 1077; ^{1}H NMR spectrum (DMSO-d6, 400 MHz), δ_H, ppm: 10.28 (1H, s, NH), 7.22 (2H, d, ArH), 7.12 (2H, d, ArH), 7.09 (1H, t, ArH), 7.08 (2H, d, ArH), 7.07 (2H, d, ArH), 6.83 (4H, d, ArH), 6.62 (1H, t, ArH), 6.54 (2H, d, ArH), 6.40-6.36 (3H, m, ArH), 5.09 (1H, d, H), 3.94 (3H, s, OMe), 3.81 (3H, s, OMe), 3.80 (3H, s, OMe), 2.87 (1H, dd, H), 2.77 (1H, dd, H); ^{13}C NMR spectrum (100MHz, CDCl$_3$), δ_C, ppm: 168.6, 158.6, 158.0, 156.3, 147.2, 138.5, 136.1, 134.8, 129.0, 127.8, 127.6, 125.8, 125.6, 115.9, 114.1, 113.5, 113.1, 98.0, 57.7, 55.2, 54.5, 50.8, 34.1; MS: m/z (M$^+$+1): 522.24; Anal. Calcd for C$_{33}$H$_{32}$N$_2$O$_4$: C, 76.13; H, 6.20; N, 5.38. Found: C, 76.03; H, 6.09; N, 5.45.

RESULTS AND DISCUSSION

Firstly, we compared the results of functionalized piperidines synthesis from aromatic aldehyde, aniline and methyl acetoacetate using nano-structured ZnO, nano-sulfated zirconia, nano-γ-alumina and nano-ZSM-5 zeolites as the catalyst (Table 1).

We further investigated the reaction of various aromatic aldehydes having substituents, such as Me, OMe, Cl, Br and NO$_2$ with aniline and methyl acetoacetate under the same reaction conditions (Table 1, entries 2-6). To find the generality and scope of this MCR, various amines were also examined. A wide variety of anilines tethered with substituents such as Me, OMe, Cl and NO$_2$ were treated with benzaldehyde and methyl acetoacetate under similar reaction conditions. All reactions occurred smoothly to provide the corresponding
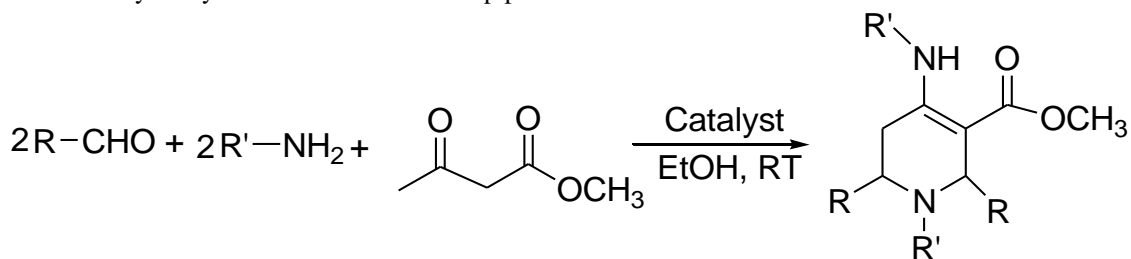
piperidine derivative **1g-j**, in moderate to good yields (Table 1, entries 7-10). Some interesting observations were made during these studies: *p*-methyl and *p*-methoxy aniline reacted faster than aniline, and reactions were completed within 5 h rather than 7 h. *p*-Nitroaniline and 4-chloroaniline reacted very slowly, which is undoubtedly due to the reduced nucleophilicity of these anilines compared to *p*-methyl and *p*-methoxy aniline and aniline. The results showed that nano-crystalline sulfated zirconia (SZ) promoted the reaction more effectively than nano-structured ZnO, nano-γ-alumina and nano-ZSM-5 zeolites, as far as the amount of catalyst and reaction time are concerned. (Table 1)

In a systematic study (Table 2), benzaldehyde was added to a solution of aniline, methyl acetoacetate and catalyst in ethanol and the reaction mixture was stirred under reflux conditions. In an initial endeavor, a blank reaction was carried out using 2.0 equivalents of benzaldehyde, 2.0 equivalents of aniline and 1.0 equivalent of methyl acetoacetate in the presence of a catalyst. The reaction mixture was stirred in ethanol; even after 8 h, 10% of the expected product was obtained in the absence of catalyst. To further improve the yield and to optimize the reaction conditions, the same reaction was carried out in presence of 10 mol % of a catalyst under similar conditions. A tremendous improvement was observed and the product yield

increased up to 87% after stirring the mixture for 6h.

To minimize the formation of byproducts and to achieve good yield of the desired product, the reaction was optimized by varying the amount of catalyst (5, 10 and 15 mg). An increase in the amount of nano SZ from 5 to 15 mg increased the yield of the desired product to a great extent (80–87%, Table 2, entries 2-4). The percentage yield of the product with 5, 10 and 15 mol% of nano-ZnO as a catalyst are 72%, 74% and 70%, respectively (Table 2, entries 5-7). For nano-γ-alumina and nano-ZMS-5 as the catalyst, the increase in the catalyst amount to 15 mg, lead to a decrease in the product yield to 74% (Table 2, entry 10) and 68% (Table 2, entry 13), respectively. Therefore, it was considered that the use of 10 mol % of the catalyst was sufficient to promote the reaction, and greater amounts of the catalyst did not improve the yields. Table 3 compares the efficiency of the present method with that of other methods in the synthesis of piperidine derivatives. As can be seen, SZ shows better efficiency than other catalysts and only $ZrOCl_2.8H_2O$ is slightly better than the sulfated zirconia catalyst. The effect of different solvents on the reaction rate and the yields of products was also investigated and the results are summarized in Table 4. Ethanol, methanol and acetonitrile provided excellent yields and proved to be the solvents of choice, whereas THF, water and dichloromethane afforded lower yields.

Table 1: Acid-catalyzed synthesis of functionalized piperidines [a].

Entry/ Product	R	R'	Time (h)/Yield (%)[b]				MP [O]C (lit.) [Ref.]
			nano-ZnO	nano-γ-alumina	nano-ZMS-5	nano-crystalline SZ	
1 (**1a**)	Ph	Ph	6/74	6/76	6/70	6/87	180-182 (178-180) [14]
2 (**1b**)	$4-ClC_6H_5$	Ph	6/80	6/80	6/81	6/84	210-212 (202-203) [14]
3 (**1c**)	$4-BrC_6H_5$	Ph	6/70	6/75	6/76	6/81	242-244 (245-247) [13]
4 (**1d**)	$4-NO_2C_6H_5$	Ph	7/60	7/64	7/63	7/65	236-238 (239-241) [13]
5 (**1e**)	$4-CH_3C_6H_5$	Ph	6/71	6/73	6/74	6/76	214-216 (212-214) [14]
6 (**1f**)	$4-OCH_3C_6H_5$	Ph	6/68	6/74	6/73	6/74	184-186 (186-188) [13]
7 (**1g**)	Ph	$4-ClC_6H_5$	7/75	7/76	7/78	7/81	200-202
8 (**1h**)	Ph	$4-NO_2C_6H_5$	7/77	7/80	7/83	7/85	243-244
9 (**1i**)	Ph	$4-CH_3C_6H_5$	5/74	5/77	5/81	5/82	216-218 (220-222) [17]
10 (**1j**)	Ph	$4-OCH_3C_6H_5$	5/72	5/74	5/73	5/75	170-172

[a] The products were characterized by IR, ^{1}H-NMR, ^{13}C-NMR, and mass spectroscopy.
[b] Isolated yields

Table 2: Reaction of methyl acetoacetate with aniline and benzaldehydes in etanol catalyzed by different catalysts

Entry	Catalyst	Catalyst (mol%)	Time (h)	Yield (%)[a]
1	None	-	6	10
2	nano-SZ	5 (mg)	6	80
3	nano-SZ	10 (mg)	6	87
4	nano-SZ	15 (mg)	6	83
5	nano-ZnO	5 (mol%)	6	72
6	nano-ZnO	10 (mol%)	6	74
7	nano-ZnO	15 (mol%)	6	70
8	nano-γ-alumina	5 (mg)	6	72
9	nano-γ-alumina	10 (mg)	6	76
10	nano-γ-alumina	15 (mg)	6	74
11	nano-ZMS-5	5 (mg)	6	66
12	nano-ZMS-5	10 (mg)	6	70
13	nano-ZMS-5	15 (mg)	6	68

[a] Yields after isolation of products

Table 3: Comparison of the efficiency of nano-crystalline SZ with other reported catalysts in the synthesis of functionalized piperidines [a]

Entry	Catalyst (mol %)	Condition	Time	Yield (%)[a]	References
1	nano-crystalline SZ	EtOH/rt	6 h	87	This work
2	10% I_2	MeOH /rt	8 h	81	13
3	TBATB	EtOH /rt	24 h	74	15
4	$InCl_3$	MeCN/rt	24-48 h	60	16
5	$ZrOCl_2.8H_2O$	EtOH /reflux	4 h	91	17
6	$Bi(NO_3)_3.5H_2O$	EtOH /rt	12 h	81	18

Banzaldehyde, aniline and methyl acetoacetate were taken in 2:2:1 ratio in presence of catalyst.

Table 4: Effect of solvent on the reaction times and yields.

Entry	Solvent[a]	Time (h)[b]	Yield (%)[c]
1	H_2O	8	40
2	EtOH	8	87
3	MeOH	8	65
4	CH_3CN	8	70
5	CH_2Cl_2	8	65
6	THF	8	60

[a] Reaction was performed with benzaldehyde (2 mmol), aniline (2 mmol) and methyl acetoacetate (1 mmol) in the presence of a catalyst in various solvents.
[b] Reaction time monitored by TLC.
c Isolated yield.

The FT-IR spectra of alumina samples calcinated at 550 °C (Figure 1) showed an intense band centered around 3500 cm^{-1} and a broad band at 1650 cm^{-1}, these are assigned to stretching and bending modes of adsorbed water. The Al–O–Al bending stretching vibrations observed at around 1150 cm^{-1} are due to symmetric and asymmetric bending modes, respectively. The OH torsional mode observed at 800 cm^{-1} overlaps with Al–O stretching vibrations. The weak band at 2091 cm^{-1} is assigned to a combination band. The bands observed at 617 and 481 cm^{-1} may be attributed to stretching and bending modes of AlO_6 [33].

The morphology of the as prepared nano-size γ-Al_2O_3 and nano-sized ZnO powders analyzed by SEM is shown in Figs. 3-4. The SEM image clearly demonstrates the formation of spherical ZnO nanoparticles. The γ-Al_2O_3 powders indicated strong agglomeration of particles with various spherical sizes.
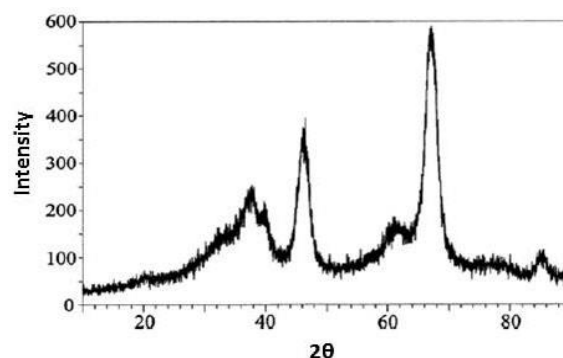
Fig. 1. XRD pattern of nano-γ-alumina catalyst

527
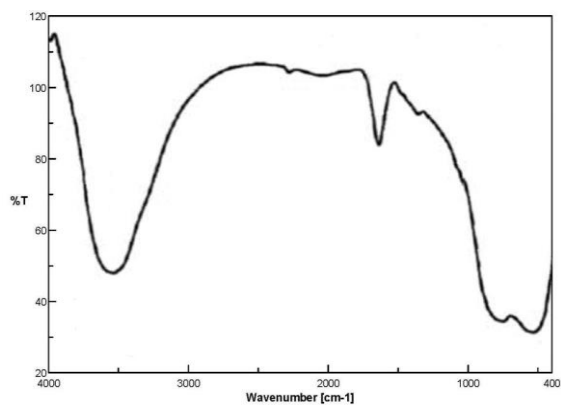
Fig. 2. FT-IR spectra of nano-γ-alumina catalyst
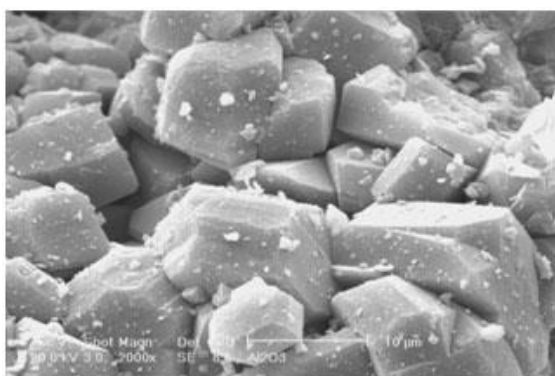
Fig. 3. SEM micrograph of nano-γ-alumina catalyst
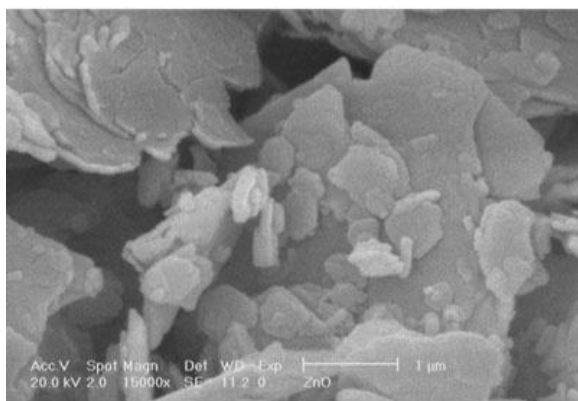
Fig. 4. SEM micrograph of nano-ZnO catalyst

One of the most important advantages of heterogeneous catalysis over homogeneous one is the possibility of reusing the catalyst by simple filtration, without loss of activity. The recovery and reusability of the catalyst in product formation was investigated. After completion of the reaction, the catalyst was separated by filtration, washed 3 times with 5 ml acetone, then several times with redistilled water and dried at 110 ºC. The recovered catalyst was used in the next run. The results of three consecutive runs showed that the catalyst can be reused several times without significant loss of its activity (see figure 5).
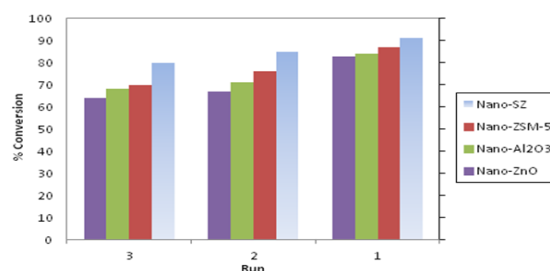
Fig. 5. Results obtained with reused catalyst in the product formation

CONCLUSIONS

In conclusion**,** an efficient one-pot synthesis of functionalized piperidines was developed by reactions of aromatic aldehydes, acetoacetic esters, and amines in the presence of nano-sulfated zirconia, nano-structured ZnO, nano-γ-alumina and nano-ZSM-5 zeolites. The nano-sulfated zirconia demonstrated higher activity. Compared to previously reported methods, the mild reaction conditions, high yields, easy work-up, clean reaction profiles and lower catalyst loading render this approach an interesting alternative to the existing methods.

REFERENCES

1. J.W. Daly, T. F. Spande and H. M. Garraffo, *J. Nat. Prod.* **68**, 1556 (2005).
2. P. S. Watson and B. Jiang, Scott, B. *Org. Lett.* **2**, 3679 (2000).
3. S. Petit, J. P. Nallet, M. Guillard, J. Dreux, R. Chermat, M. Poncelet, C. Bulach, P. Simon, C. Fontaine, M. Barthelmebs and J. L. Imbs, *Eur. J.Med.Chem.* **26**, 19 (1991).
4. Y. Zhou, V. E. Gregor, B. K. Ayida, G. C. Winters, Z. Sun, D. Murphy, G. Haley, D. Bailey, J. M. Froelich, S. Fish, S. E. Webber, T. Hermann and D. Wall, *Bioorg. Med. Chem. Lett.* **17**, 1206 (2007).
5. H. Bin, A. M. Crider and J. P. Stables, *Eur. J. Med. Chem.* **36**, 265 (2001).
6. M. Misra, S. K. Pandey, V. P. Pandey, J. Pandey, R. Tripathi and R. P. Tripathi, *Bioorg. Med. Chem.* **17**, 625 (2009).
7. A. Takemiya and J. F. Hartwig, *J. Am. Chem. Soc.* **128**, 6042 (2006).

8. K. Takasu, N. Shindoh, H. Tokuyama, M. Ihara, *Tetrahedron* **62**, 11900 (2006).
9. M. S. R. Murty, R. Ram and J. S. Yadav, *Tetrahedron Lett.* **49**, 1141 (2008).
10. S. Fustero, D. Jimenez, J. Moscardo, S. Catalan and C. D. Pozo, *Org. Lett.* **9**, 5283 (2007).
11. F. A. Davis, B. Chao and A. Rao, *Org. Lett.* **3**, 3169 (2001).
12. C. J. Chapman and C. G. Frost, *Synthesis.* 1 (2007).
13. A. T. Khan, M. M. Khan and K. K. R. Bannuru, *Tetrahedron.* **66**, 7762 (2010).
14. A. T. Khan, T. Parvin and L. H. Choudhury, *J. Org. Chem.* **73**, 8393 (2008).
15. A. T. Khan, M. Lal and M. M. Khan, *Tetrahedron Lett.* **51**, 4419 (2010).
16. P. A. Clarke, A. V. Zaytzev and A. C. Whitwood, *Synthesis* 3530 (2008).
17. S. Mishra and R. Ghosh, *Tetrahedron Letters.* **52**, 2857 (2011).
18. G. Brahmachari and S. Das, *Tetrahedron Letters.* **53**, 1479 (2012).
19. H. J. Wang, L. P. Mo and Z.-H. Zhang, *ACS Comb. Sci.* **13**, 181 (2011).
20. R. Aeluri, M. Alla, V. R. Bommena, R. Murthy, and N. Jain, *Asian J. Org. Chem.* **1**, 71 (2012).
21. S. Das, and G. Brahmachari *Signpost Open Access J. Org. Biomol. Chem.* **1**, 33 (2013).
22. S. Khameneh Asl, S.K. Sadrnezhaad and M.

23. V. Indovina, D. Pietrogiacomi and M. C. Campa, *Appl. Catal. B* **39**, 115 (2002).
24. H.S. Potdar, Ki-Won Jun, Jong Wook Bae, Seung-Moon Kim and Yun-Jo Lee, *Applied Catalysis A: General.* **321**, 109 (2007).
25. Y. Ni, A. Sun, X. Wu, G. Hai, J. Hu, T. Li and G. Li, *Microporous and Mesoporous Materials.* **143**, 435 (2011).
26. G. Santor, R. Maryi and P. Righi, *Chem. Ber.* **104**, 199 (2004).
27. A. Teimouri and A. Najafi Chermahini, *Journal of Molecular Catalysis A: Chemical.* **346**, 39 (2011).
28. B. Tyagi, M.K. Mishra and R.V. Jasra, *Catal. Commun.* **7**, 52 (2006).
29. K.J. Chen, F.Y. Hung, S.J. Chang, S.J. Young and Z.S. Hu, *Current Applied Physics.* **11**, 124 (2011).
30. M. Firoozi, M. Baghalha and M. Asadi, *Catalysis Communications.* **10**, 1582 (2009).
31. B.D. Cullity, S.R. Stock, *Elements of X-ray Diffraction*, third edition Prentice Hall, Upper Saddle River, NJ, (2001) pp. 388.
32. S.J. Gregg and K.S.W. Sing, *Adsorption, Surface Area and Porosity*, second edition Academic Press, New York, (1982).
33. A.D. Cross, *An Introduction to Practical IR Spectroscopy*, 2nd ed., Butterworth, London, (1964).

Синтеза на функционализирани пиперидини чрез единедноетапна многокомпонентна реакция с използване на нано-кристални киселинни катализатори

А. Теимури [1,*] , А. Н. Чермахини [2], Л. Горбаниан [3]

[1] *Катедра по химия, Университет Паям Нуур, Техеран, Иран*
[2] *Катедра по химия, Технологичен университет в Исфахан,, Исфахан, Иран*
[3] *Катедра по материално инженерство, Технологичен университет в Исфахан, Исфахан, Иран*

(Резюме)

Разработена е една проста и удобена едноетапна многокомпонентна реакция за синтеза на функционализирани пиперидини е. Процедурата включва смесване на 1,3-дикарбонилни съединения, амини и ароматни алдехиди в етанол при стайна температура, използвайки нано-сулфатиран циркониев наноструктуриран ZnO, нано-γ-двуалуминиев триокис и нано-ZSM-5 зеолити, като катализатор. Проучени са оптичните свойства на наноструктурираните органичните молекули. Предимствата на метода са кратки срокове за реакция, меки условия, както и лесно извършване. Катализаторите могат да бъдат рагенерирани за следващите реакции и да се използват отново, без значителна загуба на ефективност.

Study on the production of a new generation of electrospun nanofiber webs

M. Mohammadian[1], A. K. Haghi[2*]

[1]*Department of Textile Engineering, Kashan Branch, Islamic Azad University, Kashan, Iran*
[2]*University of Guilan, Iran*

Electrospun nanofiber web has many potential applications due to its large specific area, very small pore size and high porosity. Despite such potentials, the mechanical properties of nanofiber web are very poor for use in textile application. To remedy this defect, a lamination process could be accomplished in order to protect nanofiber web *versus* mechanical stress. However, nanofiber properties may change during the process. The purpose of this study is to consider the influence of lamination temperature on nanofiber/laminate properties. Hot-press lamination was carried out at five different temperatures and nanofiber web morphology was observed under an optical microscope. Also, air permeability experiments were performed to examine the effect of lamination temperature on the breathability of a multilayer fabric. Optical microscope images showed that the nanofiber web began to damage at lamination temperatures above the melting point of the adhesive layer. Air permeability decreased with increasing the lamination temperature. The adhesive force between layers increased by increasing the lamination temperature.

Keywords: Nanofiber, lamination, protective clothing

INTRODUCTION

Clothing is a person's second skin, since it covers large parts of the body and has a large surface area in contact with the environment. Therefore clothing is a proper interface between environment and the human body, and could act as an ideal tool to enhance personal protection. Over the years, growing concern regarding health and safety of persons in various sectors, such as industries, hospitals, research institutions, battlefields and other hazardous conditions, has led to intensive research and development in the field of personal protective clothing. Today, there are different types of protective clothing, both disposable and non-disposable. The simplest and earliest specimens of this equipment have been made of rubber or plastic that is completely impervious to hazardous substances. Unfortunately, these materials are also impervious to air and water vapor, and thus retain body heat, exposing their wearer to heat stress which can build quite rapidly to a dangerous level. Another approach to protective clothing is to incorporate activated carbon into a multilayer fabric in order to absorb toxic vapors from the environment and prevent penetration to the skin [1]. The use of activated carbon is considered only a short-term solution because it loses its effectiveness upon exposure to sweat and moisture. The use of semi-permeable membranes as a constituent of the protective material is another approach. In this way, reactive chemical decontaminants are encapsulated in microparticles [2] or filled in microporous hollow fibers [3] and coated onto fabric. The microparticle or fiber walls are permeable to toxic vapors, but impermeable to decontaminants, so that the toxic agents diffuse selectively into them and neutralize.

Generally, a negative relationship always exists between thermal comfort and protection performance for currently available protective clothing. Thus there still exists a real demand for improved protective clothing that can offer acceptable levels of impermeability to highly toxic pollutions of low molecular weight, while minimizing wearer discomfort and heat stress.

Electrospinning provides an ultrathin membrane-like web of extremely fine fibers with very small pore size and high porosity, which makes them excellent candidates for use in filtration, membrane, and possibly protective clothing applications. Preliminary investigations have indicated that using of nanofiber web in protective clothing structure could present minimal impedance to air permeability and extreme efficiency in trapping dust and aerosol particles [4-6]. Many researchers have shown an enhancement of aerosol protection by a thin layer of electrospun

---

* To whom all correspondence should be sent:
E-mail: Haghi@Guilan.ac.ir

fibers. They found that the electrospun webs of nylon, polybenzimidazole, polyacrylonitrile, and polyurethane provided good aerosol particle protection, without a considerable change in moisture vapor transport or breathability of the system. While nanofiber webs offer exciting characteristics, it has been reported that they have limited mechanical properties. In order to provide suitable mechanical properties for use as a cloth, nanofiber webs must be laminated using an adhesive into the fabric system [7,8]. This system could protect ultrathin nanofiber web *versus* mechanical stress over an extended period of time.

The adhesives could be in the form of melt adhesive or solvent-based adhesive. When a melt adhesive is used, hot-press lamination is carried out at temperatures above the softening or melting point of the adhesive. If a solvent-based adhesive is used, the lamination process could be performed at room temperature. In addition, the solvent-based adhesive is generally environmentally unfriendly, more expensive and usually flammable, whereas the hot-melt adhesive is environmentally friendly, inexpensive, requires less heat, and is now preferred. Lee *et al.* [9], without disclosure of lamination details, reported that the hot-press method is more suitable for nanofiber web lamination. In this method, lamination temperature is one of the most important parameters. Incorrect selection of this parameter may lead to change or damage of the nanofiber web. Thus, it is necessary to find out a lamination temperature which has the least effect on the nanofiber web.

The purpose of this study was to consider the influence of the lamination temperature on nanofiber/laminate properties. Multilayer fabrics were made by electrospinnig polyacrylonitrile nanofibers onto nonwoven substrate and incorporating into fabric system *via* hot-press method at different temperatures.

EXPERIMENTAL

Electrospining and Laminating process

Polyacrylonitrile (PAN) of 70,000 g/mol molecular weight from Polyacryl Co. (Isfehan, Iran) was used with dimethylformamide (DMF) from Merck, to form a 12% w/w polymer solution after stirring for 5 h and exposing for 24 h at ambient temperature. The yellow ripened solution was inserted into a plastic syringe with a stainless steel nozzle 0.4 mm in inner diameter and then it was placed in a metering pump from WORLD PRECISION INSTRUMENTS (Florida, USA).

Next, this set was installed on a plate which it could traverse to left-right along drum (Fig.1).
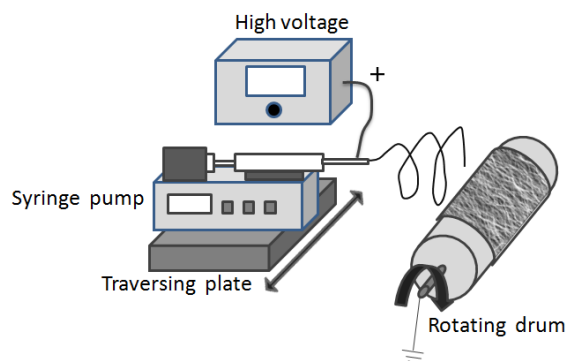
Fig.1. Electrospinning setup

A flow rate of 1 μl/h for the solution was selected and the fibers were collected on an aluminum-covered rotating drum (with speed of 9 m/min) previously covered with a polypropylene spun-bond nonwoven (PPSN) substrate of 28cm×28cm dimensions; 0.19 mm thickness; 25 g/m² weight; 824 cm³/s/cm² air permeability and 140ºC melting point. The distance between the nozzle and the drum was 7 cm and an electric voltage of approximately 11kV was applied between them. The electrospinning process was carried out for 8 h at room temperature to reach an approximate web thickness of 3.82 g/m². Then the nanofiber webs were laminated into cotton weft-warp fabric with a thickness of 0.24 mm and density of 25×25 (warp-weft) per centimeter to form a multilayer fabric (Fig.2).
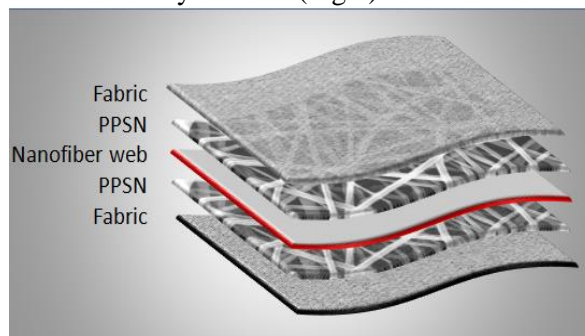
Fig. 2. Multilayer fabric components

Lamination was performed at temperatures of 85,110,120,140 and 150°C for 1 min under a pressure of 9 gf/cm².

Nanofiber Web Morphology

In order to consider nanofiber web morphology after hot-pressing, another lamination was performed by a non-stick sheet made of Teflon (0.25 mm thickness) instead one of the fabrics (fabric /pp web/nanofiber web/pp web/non-stick sheet). Finally, after removing the Teflon sheet, the nanofiber layer side was observed under an optical

microscope (MICROPHOT-FXA, Nikon, Japan) connected to a digital camera.

Measurement of Air permeability

Air permeability of the multilayer fabric after lamination was tested on a TEXTEST FX3300 instrument (Zürich, Switzerland). Five pieces of each sample were tested under air pressure of 125pa at ambient conditions (16ºC, 70% RH).

RESULTS AND DISCUSSION

PPSN was selected as the melt adhesive layer for hot-press lamination (Fig.2). This process was performed at different temperatures in order to find the optimum conditions. Fig. 3 presents the optical

microscope images of the nanofiber web after lamination.

It is obvious that on increasing the lamination temperature to the melting point (samples a-c), the adhesive layer gradually melts and spreads on the web surface. When the melting point was selected as lamination temperature (sample d), the nanofiber web began to damage. In this case, the adhesive layer completely melted, penetrated into the nanofiber web and occupied its pores. This procedure was intensified by increasing the lamination temperature above the melting point. As shown in Fig. 2 (sample e), perfect absorption of the adhesive by the nanofiber web creates a transparent film which leads to appear fabric structure.
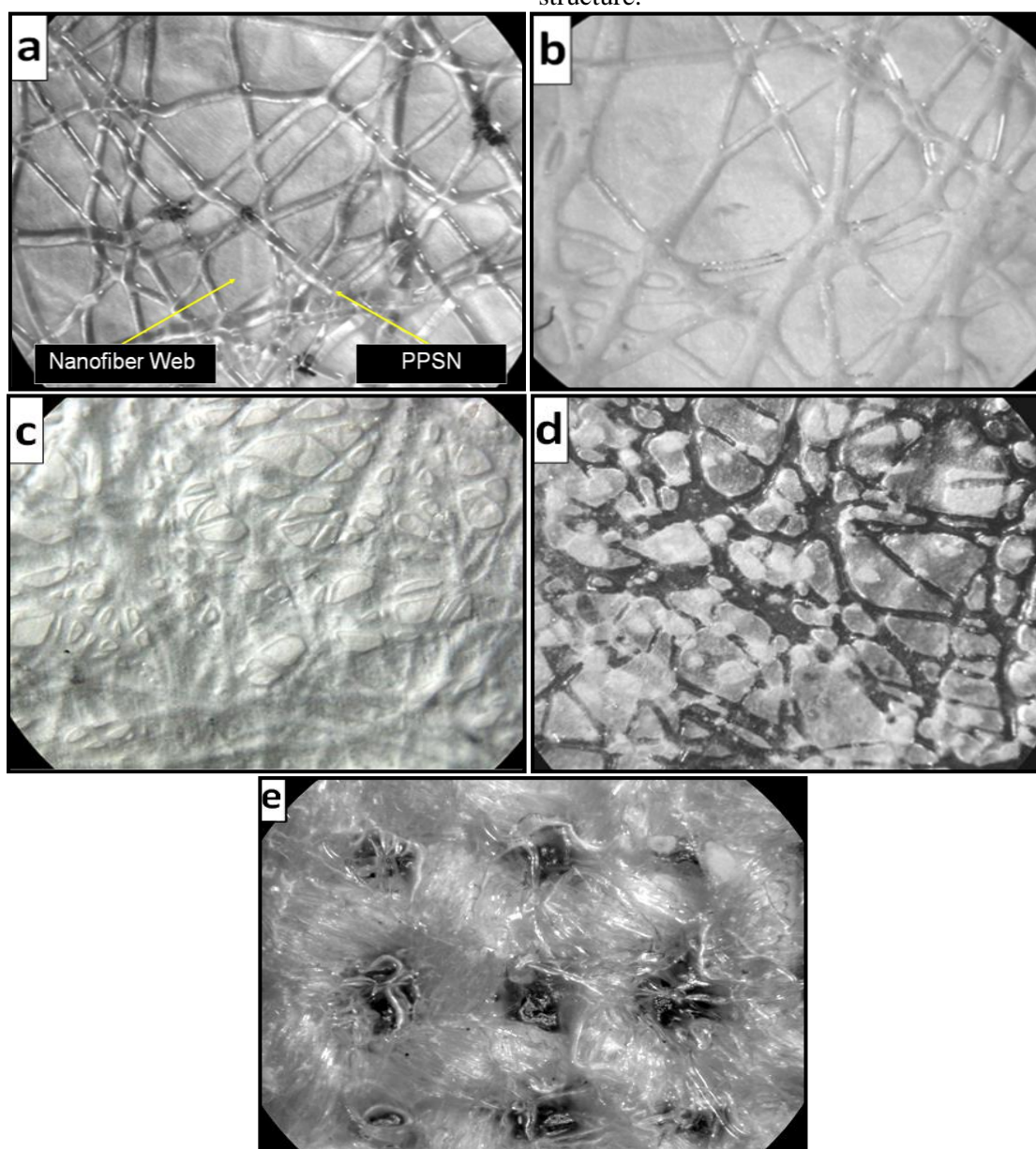
Fig. 3. Optical microscope images of nanofiber web (at 100× magnification) after lamination at (a) 85ºC, (b) 110ºC, (c) 120ºC, (d) 140ºC and (e) >140ºC.

Also, to examine how lamination temperature affects the breathability of a multilayer fabric, air permeability experiment was performed. Fig. 4 illustrates the effect of lamination temperature on air permeability. As might be expected, air permeability decreased with increasing lamination temperature.
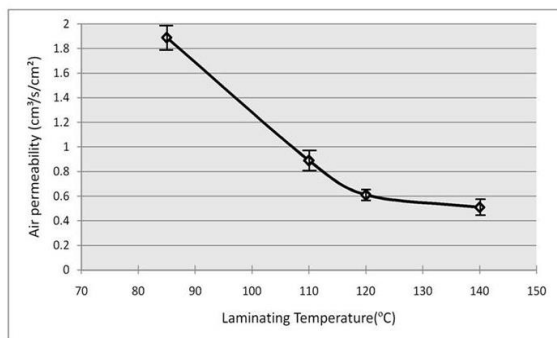
Fig. 4 . Air permeability of a multilayer fabric as a function of lamination temperature.

This behavior was attributed to the melting of the adhesive layer. As mentioned above, prior to the melting point, the adhesive gradually spreads on the web surface. This phenomenon causes that the adhesive layer acts like an impervious barrier to air flow and reduces air permeability of the multilayer fabric. At the melting point and above, the penetration of melt adhesive into the nanofiber/fabric structure fills its pores and finally decreases its air permeability.

Furthermore, we observed that the adhesive force between the layers increased according to the temperature rise. Sample (a) exhibited very poor adhesion between the nanofiber web and the fabric: it could be separated by slight abrasion with the thumb. Adhesion increased by increasing the lamination temperature to the melting point. It should be noted that above the melting point, because of melt PPSN passing across the nanofiber web, adhesion between two layers of fabric will occur.

CONCLUSION

In this study, the effect of lamination temperature on the nanofiber/laminate properties was investigated with a view to the elaboration of a new generation of protective clothing. First, surface images of nanofiber web after lamination were taken using optical microscope in order to consider morphology changes. It was observed that the nanofiber web remains unchanged when the lamination temperature is below the PPSN melting point. In addition, to compare breathability of laminates, air permeability was measured. It was found that by increasing the lamination temperature, air permeability decreased. Furthermore, it was observed that the adhesive force between layers in laminate increased with temperature rise.

These results indicated that lamination temperature is an effective parameter in the lamination of a nanofiber web into fabric structure. Thus, by varying this parameter fabrics with different levels of thermal comfort and protection could be developed depending on need and use.

REFERENCES

1. M. Ziabari, V. Mottaghitalab, A.K.Haghi, Application of direct tracking method for measuring electrospun nanofiber diameter. *Braz. J. Chem. Eng.*, 26, n.1, 53-62, 2009
2. M. Ziabari, V. Mottaghitalab, S. T. McGovern, A. K. Haghi, Measuring Electrospun Nanofibre Diameter: A Novel Approach, *Chin.Phys.Lett*., 25, No. 8, 3071-3074, 2008
3. M. Ziabari, V. Mottaghitalab, S. T. McGovern, A. K. Haghi, A new image analysis based method for measuring electrospun nanofiber diameter, *Nanoscale Research Letters*, 2, 297-600, 2007.
4. M. Ziabari, V. Mottaghitalab, A. K. Haghi, Simulated image of electrospun nonwoven web of PVA and corresponding nanofiber diameter distribution, *Korean Journal of Chemical Engng.*, 25, No. 4, 919-922, 2008.
5. M. Ziabari, V. Mottaghitalab, A. K. Haghi, Evaluation of electrospun nanofiber pore structure parameters, *Korean Journal of Chemical Engng.*, 25, No. 4, 923-932, 2008.
6. M. Ziabari, V. Mottaghitalab, A. K. Haghi, Distance transform algorithm for measuring nanofiber diameter, *Korean Journal of Chemical Engng.*, 25, No. 4, 905-918, 2008.
7. A.K.Haghi and M. Akbari, Trends in electrospinning of natural nanofibers, *Physica Status Solidi*, 204, No. 6 1830–1834, 2007.
8. Lee, S. M., Kimura, D., Yokoyama, A., Lee, K. H., Park, J. C., and Kim, I. S., *Textile Res. J.*, 79 (12),1085, 2009.
9. Lee Sumin, D. Kimura, Keun Hyung Lee, J. C. Park and Ick Soo Kim, *Textile Res. J.*, 80 (2), 99, 2010.

ИЗСЛЕДВАНЕ ВЪРХУ ПОЛУЧАВАНЕТО НА НОВО ПОКОЛЕНИЕ ТЪКАНИ ОТ ЕЛЕКТРОПРЕДЕНИ НАНОВЛАКНА

М. Мохамадиан[1], А.К. Хаги[2*]

[1]DДепартамент по текстилно инженерство, Ислямски университет „Азад“. клон Кашан, Иран

[2]Университет в Гилян, Иран

(Резюме)

Електропредените нановлакна има много потенциални приложения поради голямата си специфична повърхност, малките размери на порите и голямата си порьозност. Въпреки тези възможности механичните им свойства са лоши за приложението им като текстил. За намаляването на този ефект и защитата на тъканите от нановлакна срещу механични напрежения може да се приложи ламинирането. Целта на тази работа е да се изследва влиянието на температурата на ламиниране върху свойствата на нановлакната. Извършено е ламиниране на при горещо пресуване и е наблюдавана морфологията на тъканите под оптичен микроскоп. Освен това са извършени експерименти по въздухопроницаемостта, за да се проучи ефекта на температурата на ламиниране върху проницаемостта на многослойни тъкани. Микроскопските образи показват, че тъканите от нановлакна започват да се повреждат, когато температурите на ламиниране са над точката на топене на адхезивния слой. Въздухопроницаемостта намалява с повишаването на температурата на ламиниране. Освен това бе наблюдавано, че адхезионната сила между слоевете нараства с повишаването на температурата на ламиниране.

Effect of porosity on the flow and heat transfer between two parallel porous plates with the Hall effect and variable properties under constant pressure gradient

H. A. Attia [1], W. Abbas [2], M. A. M. Abdeen [3*], A. El-Din Abdin [4]

[1] *Department of Engineering Mathematics and Physics, Faculty of Engineering, El-Fayoum University, Egypt*

[2] *Basic and Applied Science Department, College of Engineering and Technology, Arab Academy for Science, Technology and Maritime Transport (Cairo branch), Cairo, Egypt*

[3] *Department of Engineering Mathematics and Physics, Faculty of Engineering, Cairo University, Egypt.*

[4] *National Water Research Center, Ministry of Water Resources and Irrigation, Egypt*

The transient hydromagnetic flow through a porous medium between two infinite parallel porous plates is studied with heat transfer considering the Hall effect and the temperature dependent physical properties under constant pressure gradient. An external uniform magnetic field and a uniform suction and injection are applied perpendicular to the horizontal plates. A numerical solution for the governing non-linear coupled set of the momentum equations and the energy equation including the viscous and Joule dissipations is adopted. The effect of the porosity of the medium, the Hall current and the temperature-dependent viscosity and thermal conductivity on both the velocity and temperature distributions is reported.

Keywords: Flow between two parallel plates, temperature-dependent properties, hydromagnetics, porous medium, heat transfer, finite differences.

INTRODUCTION

The flow of an electrically conducting fluid between infinite horizontal parallel plates, known as Hartmann flow, has interesting applications in magnetohydrodynamic (MHD) power generators pumps, etc. Hartmann and Lazarus [1] investigated the effect of a transverse uniform magnetic field on the flow of a viscous incompressible electrically conducting fluid between two infinite parallel plates. Exact solutions for the velocity fields were developed [2-5] under different physical effects. Some exact numerical solutions for the heat transfer problem are derived in [6]. Soundalgekar *et al.* [7,8] examined the effect of Hall current on the steady MHD Couette flow with heat transfer. The temperatures of the two plates were assumed constant [7] or varying along the plates in the direction of the flow [8]. Attia [9] examined the effect of Hall current on the velocity and temperature fields of an unsteady Hartmann flow with uniform suction and injection applied perpendicular to the plates.

In these studies the physical properties are assumed to be constant; however, it is known that some physical properties are functions of temperature and assuming constant properties is a good approximation as long as small differences in temperature are involved. More accurate prediction for the flow and heat transfer can be achieved by considering the variation of the physical properties with temperature [10-13]. Klemp *et al.* [14] studied the effect of temperature-dependent viscosity on the entrance flow in a channel in the hydrodynamic case. Attia and Kotb [15] solved the steady MHD fully developed flow and heat transfer between two parallel plates with temperature dependent viscosity which has been extended to the transient state by Attia [16]. The influence of the dependence of the physical properties on temperature in the MHD Couette flow between parallel plates was studied [14,15].

In this paper, the transient Hartmann flow through a porous medium of a viscous incompressible electrically conducting fluid is investigated with heat transfer under constant pressure gradient. The viscosity and thermal conductivity of the fluid are assumed to vary with temperature while the Hall current is taken into consideration. The fluid is flowing between two electrically insulating porous plates and is acted upon by an axial constant pressure gradient. A uniform suction and injection and an external uniform magnetic field are applied perpendicular to the surface of the plates. The two plates are kept at two constant but different temperatures and the viscous and Joule dissipations are taken into

* To whom all correspondence should be sent:
E-mail: mostafa_a_m_abdeen@hotmail.com

consideration in the energy equation. The flow in the porous medium is described by a differential equation governing the fluid motion based on the Darcy's law which considers the drag exerted by the porous medium [17-21]. The coupled set of the non-linear momentum and energy equations is solved numerically using the method of finite differences to determine the velocity and temperature fields. The effect of porosity of the medium, the Hall current, the suction and injection velocity and the temperature-dependent viscosity and thermal conductivity on both the velocity and temperature distributions is discussed.

FORMULATION OF THE PROBLEM

The fluid flows between two infinite horizontal parallel plates located at the y=±h planes, as shown in Fig. 1. The two plates are porous, insulating and kept at two constant but different temperatures T_1 for the lower plate and T_2 for the upper plate with $T_2>T_1$. A constant pressure gradient is imposed in the axial x-direction and uniform suction from above and injection from below, with velocity vo, are applied impulsively at t=0. A uniform magnetic field Bo, assumed unaltered, is applied perpendicular to the plates in the positive y-direction. The Hall effect is considered and accordingly, a z-component of the velocity is initiated. The viscosity and the thermal conductivity of the fluid depend on temperature exponentially and linearly, respectively, while the viscous and Joule dissipations are not neglected in the energy equation.
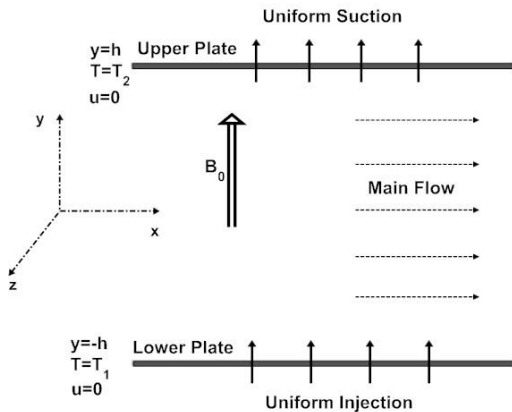
Fig. 1 The geometry of the problem

The flow is through a porous medium where the Darcy model is assumed [19]. The fluid motion starts from rest at t=0, and the no-slip condition at the plates implies that the fluid velocity has neither a z nor an x-component at y=±h. The initial temperature of the fluid is assumed to be equal to T_1 as the temperature of the lower plate. Since the

plates are infinite in the x and z-directions, the physical quantities do not change in these directions, which leads to one-dimensional problem.

The flow of the fluid is governed by the Navier-Stokes equation:

$$\rho \frac{D\vec{v}}{Dt} = -\vec{\nabla}p + \vec{\nabla}.(\mu \vec{\nabla} v) + \vec{J} \wedge \vec{B}_o \quad (1)$$

where, ρ is the density of the fluid, μ is the viscosity of the fluid, $\vec{J}$ is the current density, and $\vec{v}$ is the velocity vector of the fluid, which is given by:

$$\vec{v} = u(y,t)\vec{i} + v_o\vec{j} + w(y,t)\vec{k}$$

If the Hall term is retained, the current density $\vec{J}$ is given by the generalized Ohm's law [4]:

$$\vec{J} = \sigma(\vec{v} \wedge \vec{B}_o - \beta(\vec{J} \wedge \vec{B}_o)). \quad (2)$$

where, σ is the electric conductivity of the fluid and β is the Hall factor [4]. Equation (2) may be solved in $\vec{J}$ to yield:

$$\vec{J} \wedge \vec{B}_o = -\frac{\sigma B_o^2}{1+m^2}((u+mw)\vec{i} + (w-mu)\vec{k}) \quad \dots (3)$$

where, m is the Hall parameter and $m = \sigma \beta B_o$. Thus, the two components of the momentum Eq. (1) read:

$$\rho \frac{\partial u}{\partial t} + \rho v_o \frac{\partial u}{\partial y} = G + \mu \frac{\partial^2 u}{\partial y^2} + \frac{\partial \mu}{\partial y}\frac{\partial u}{\partial y} - \frac{\sigma B_o^2}{1+m^2}(u+mw) - \frac{\mu}{K}u, \quad (4)$$

$$\rho \frac{\partial w}{\partial t} + \rho v_o \frac{\partial w}{\partial y} = \mu \frac{\partial^2 w}{\partial y^2} + \frac{\partial \mu}{\partial y}\frac{\partial w}{\partial y} - \frac{\sigma B_o^2}{1+m^2}(w-mu) - \frac{\mu}{K}w. \quad (5)$$

where, $\overline{K}$ is the Darcy permeability [19] and the last term in the right side of Eqs. (4) and (5) represents the porosity force in the x- and z-directions respectively. It is assumed that the pressure gradient is applied at t=0 and the fluid starts its motion from rest. Thus

$$t = 0: u = w = 0. \quad (6a)$$

For t > 0, the no-slip condition at the plates implies that

$$y = -h: u = w = 0, \quad (6b)$$

$$y = h: u = w = 0. \quad (6c)$$

The energy equation describing the temperature distribution for the fluid is given by [18]:

$$\rho c_p \frac{\partial T}{\partial t} + \rho c_p v_o \frac{\partial T}{\partial y} = \frac{\partial}{\partial y}(k\frac{\partial T}{\partial y}) + \mu((\frac{\partial u}{\partial y})^2 + (\frac{\partial w}{\partial y})^2) + \frac{\sigma B_o^2}{1+m^2}(u^2+w^2). \quad (7)$$

Where, T is the temperature of the fluid, cp is the specific heat at constant pressure of the fluid, and k is the thermal conductivity of the fluid. The last two terms in the right side of Eq. (7) represent the viscous and Joule dissipations, respectively.

The temperature of the fluid must satisfy the initial and boundary conditions,

$$t = 0 : T = T_1, \tag{8a}$$

$$t > 0 : T = T_1, y = -h, \tag{8b}$$

$$t > 0 : T = T_2, y = h. \tag{8c}$$

The viscosity of the fluid is assumed to vary with temperature and is defined as, $\mu = \mu_o f_1(T)$. By assuming the viscosity to vary exponentially with temperature, the function $f_1(T)$ takes the form [7], $f_1(T) = exp(-a_1(T-T_1))$. In some cases a1 may be negative, i.e., the coefficient of viscosity increases with temperature [7,22]. Also the thermal conductivity of the fluid is varying with temperature as $k = k_o f_2(T)$. We assume a linear dependence for the thermal conductivity upon the temperature in the form $k = k_o(1 + b_1(T-T_1))$ [23], where the parameter b1 may be positive or negative [24].

Introducing the following non-dimensional quantities,

$$(\hat{x}, \hat{y}, \hat{z}) = \frac{(x, y, z)}{h}, \hat{t} = \frac{t\mu_o}{\rho h^2}, \hat{G} = \frac{\rho G}{h^2 \mu_o^2}, (\hat{u}, \hat{w}) = \frac{(u, w)\rho h}{\mu_o}, \theta = \frac{T - T_1}{T_2 - T_1},$$

$$\hat{f}_1(\theta) = e^{-a_1(T_2 - T_1)\theta} = e^{-a\theta}$$, a is the viscosity variation parameter,

$$\hat{f}_2(\theta) = 1 + b_1(T_2 - T_1)\theta = 1 + b\theta$$, b is the thermal conductivity variation parameter,

$S = \rho v_o h / \mu_o$ is the suction parameter,

$Ha^2 = \sigma B_o^2 h^2 / \mu_o$, Ha is the Hartmann number,

$M = h^2 / \overline{K}$, is the porosity parameter,

$Pr = \mu_o c_p / k_o$ is the Prandtl number,

$Ec = \mu_o^2 / h^2 c_p \rho^2 (T_2 - T_1)$ is the Eckert number,

$Nu_L = (\partial T / \partial \hat{y}) \hat{y}_{=-1}$ is the Nusselt number at the lower plate,

$Nu_U = (\partial T / \partial \hat{y}) \hat{y}_{=1}$ is the Nusselt number at the upper plate

Equations (4) to (8) read (the hats are dropped for simplicity)

$$\frac{\partial u}{\partial t} + S \frac{\partial u}{\partial y} = G + f_1(\theta) \frac{\partial^2 u}{\partial y^2} + \frac{\partial f_1(\theta)}{\partial y} \frac{\partial u}{\partial y} - \frac{Ha^2}{1 + m^2}(u + mw) - Mu, \tag{9}$$

$$\frac{\partial w}{\partial t} + S \frac{\partial w}{\partial y} = f_1(\theta) \frac{\partial^2 w}{\partial y^2} + \frac{\partial f_1(\theta)}{\partial y} \frac{\partial w}{\partial y} - \frac{Ha^2}{1 + m^2}(w - mu) - Mw. \tag{10}$$

$$t = 0 : u = w = 0, \tag{11a}$$

$$t > 0 : y = -1, \ u = w = 0, \tag{11b}$$

$$t > 0 : y = 1, \ u = w = 0. \tag{11c}$$

$$\frac{\partial \theta}{\partial t} + S \frac{\partial \theta}{\partial y} = \frac{1}{Pr} f_2(\theta) \frac{\partial^2 \theta}{\partial y^2} + \frac{1}{Pr} \frac{\partial f_2(\theta)}{\partial y} \frac{\partial \theta}{\partial y} + Ecf_1(\theta) \left(\left(\frac{\partial u}{\partial y} \right)^2 + \left(\frac{\partial w}{\partial y} \right)^2 \right) + \frac{EcHa^2}{1 + m^2}(u^2 + w^2). \tag{12}$$

$$t = 0 : \theta = 0, \tag{13a}$$

$$t > 0 : \theta = 0, y = -1, \tag{13b}$$

$$t > 0 : \theta = 1, y = 1. \tag{13c}$$

Equations (9), (10), and (12) represent a system of coupled non-linear partial differential equations which are solved numerically under the initial and boundary conditions (11) and (13) using the method of finite differences. A linearization technique is first applied to replace the nonlinear terms at a linear stage, with the corrections incorporated in subsequent iterative steps until convergence is reached. Then the Crank-Nicolson implicit method is used at two successive time levels [25]. An iterative scheme is used to solve the linearized system of difference equations. The solution at a certain time step is chosen as an initial guess for next time step and the iterations are continued till convergence, within a prescribed accuracy. Finally, the resulting block tri-diagonal system is solved using the generalized Thomas-algorithm [25]. Finite difference equations relating the variables are obtained by writing the equations at the mid point of the computational cell and then replacing the different terms by their second order central difference approximations in the y-direction. The diffusion terms are replaced by the average of the central differences at two successive time-levels. The computational domain is divided into meshes each of dimension Δt and Δy in time and space, respectively. We define the variables $A = \partial u / \partial y$, $B = \partial w / \partial y$ and $H = \partial \theta / \partial y$ to reduce the second order differential Eqs. (9), (10) and (12) to first order differential equations, and an iterative scheme is used at every time step to solve the linearized system of difference equations. All calculations are carried out for the non-dimensional variables and parameters given by, $G = 5$, $Pr = 1$, and $Ec = 0.2$ where G is related to the externally applied pressure gradient and where the chosen given values for Pr and Ec are suitable for steam or water vapor. Grid-independence studies show that the computational domain $0 < t < \infty$ and $-1 < y < 1$ is divided into intervals with step sizes $\Delta t = 0.0001$ and $\Delta y = 0.005$ for time and space respectively. Smaller step sizes do not show any significant change in the results. Convergence of the scheme is assumed when all of the unknowns u, w, A, B, θ and H for the last two approximations differ from unity by less than 10^{-6} for all values of y in $-1 < y < 1$ at every time step. Less than 7 approximations are required to satisfy

these convergence criteria for all ranges of the parameters studied here.

RESULTS AND DISCUSSION

Figures 2-4 show the time development of the profiles of the velocity and temperature for various values of the suction parameter S and for Ha =1, m=1, M=1, a=0.5 and b=0.5.
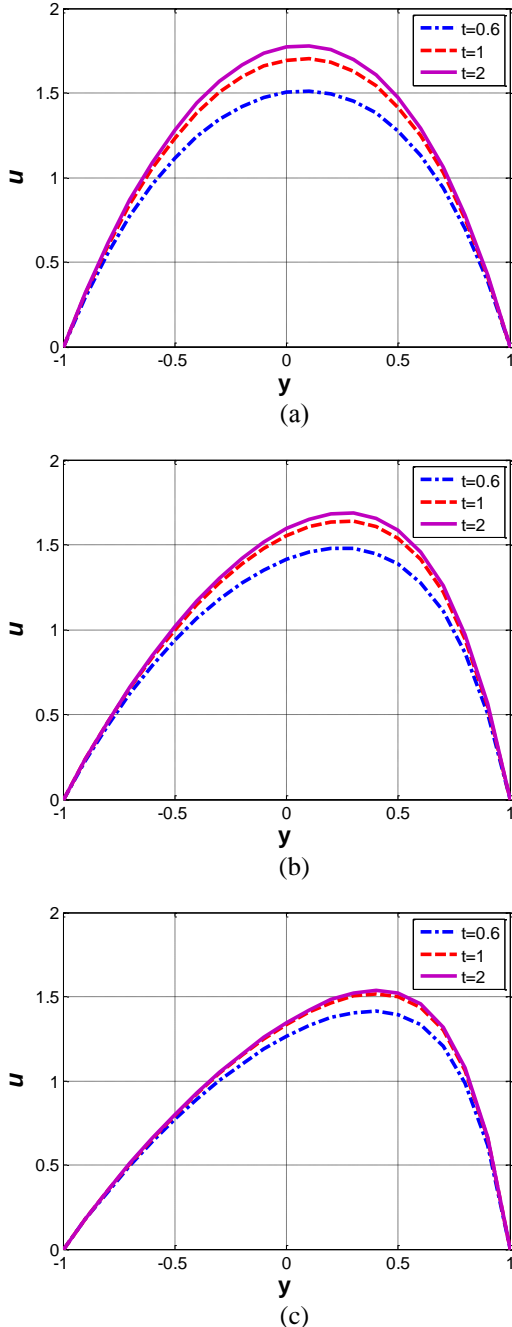

(a)

(b)

(c)

Fig. 2 The evolution of the profile of: u; (a) S=0; (b) S=1; (c) S=2. (Ha=1, m=1, M=1, a=0.5, b=0.5)

(a)

(b)

(c)
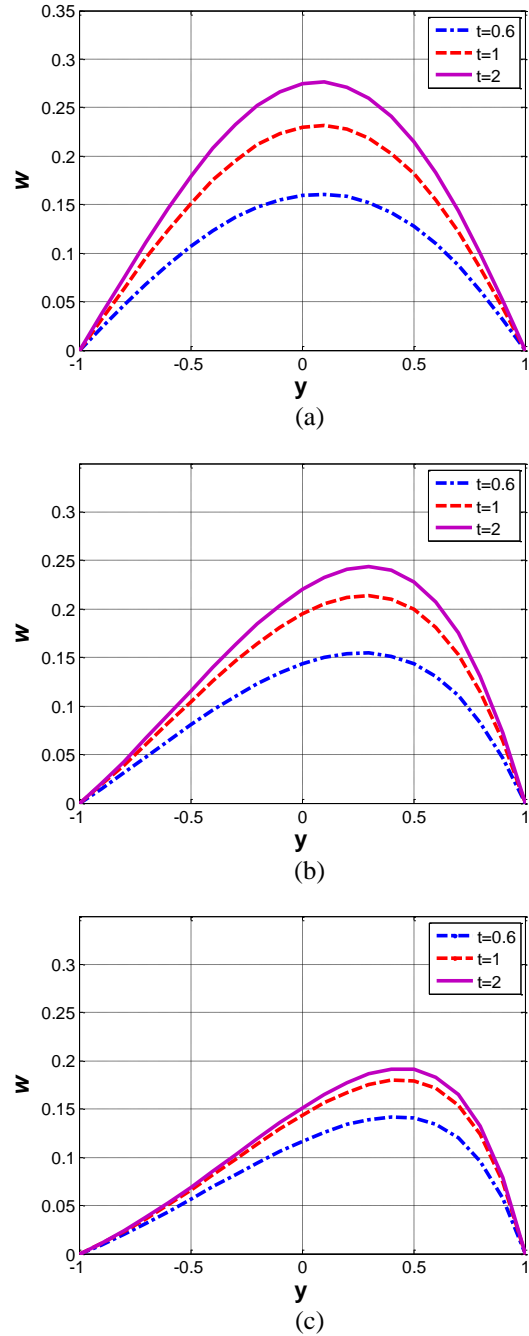
Fig. 3 The evolution of the profile of w; (a) S=0; (b) S=1; (c) S=2. (Ha=1, m=1, M=1, a=0.5, b=0.5)

The velocity and temperature distributions reach their steady state monotonically as shown in the figure. The velocity component u reaches steady state faster than w which, in turn, reaches steady state faster than θ. This is expected, as u is the source of w, while both u and w are sources of θ. It is also clear from Figs. 2-3 that the velocity components are asymmetric about the centre of the channel because of the effect of the suction.
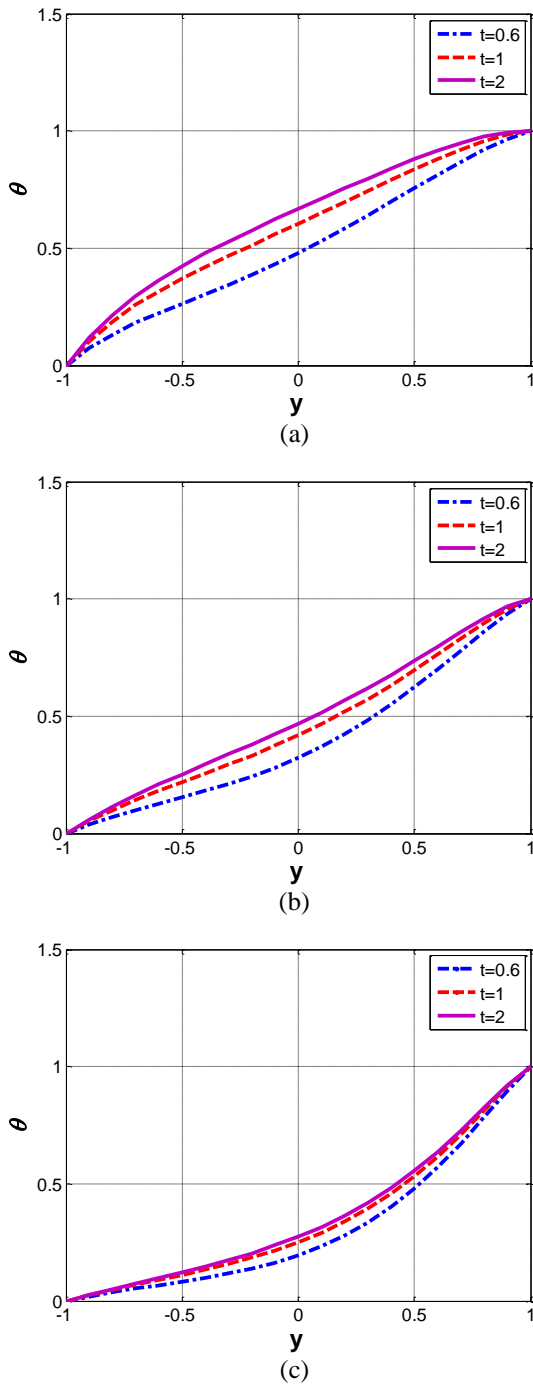
Fig. 4 The evolution of the profile of θ; (a) S=0; (b) S=1; (c) S=2. (*Ha*=1, m=1, *M*=1, a=0.5, b=0.5)

Fig. 5 The evolution of u at y=0 for various values of a and m: (a) m=0; (b) m=1; (c) m=2; . (*Ha=1, M=1,* S=1, b=0)
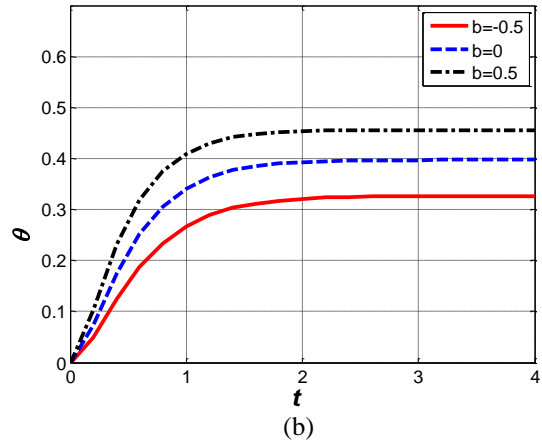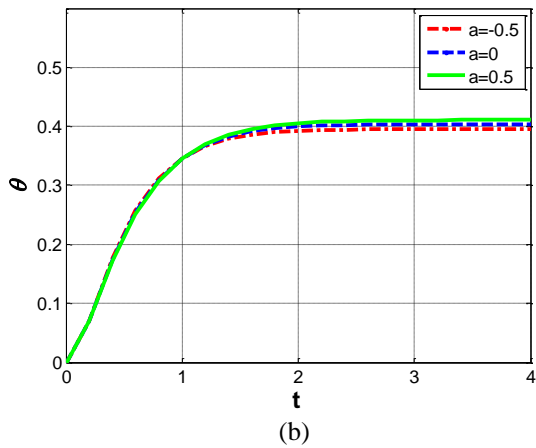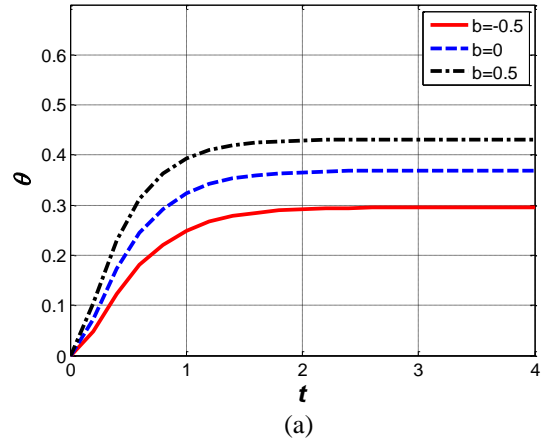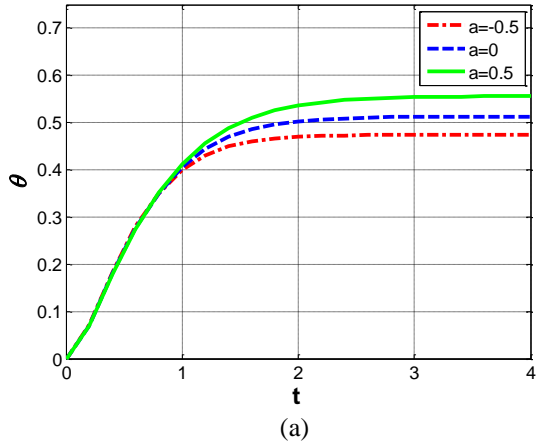
Figures 5-7 present the time progression of the velocity components u and w and the temperature θ at the centre of the channel (y=0) for different values of m and a and for Ha=1, M=1, S=1 and b=0. Increasing the parameter a increases the velocity components u and w and the temperature θ for all values of m as shown in all figures.
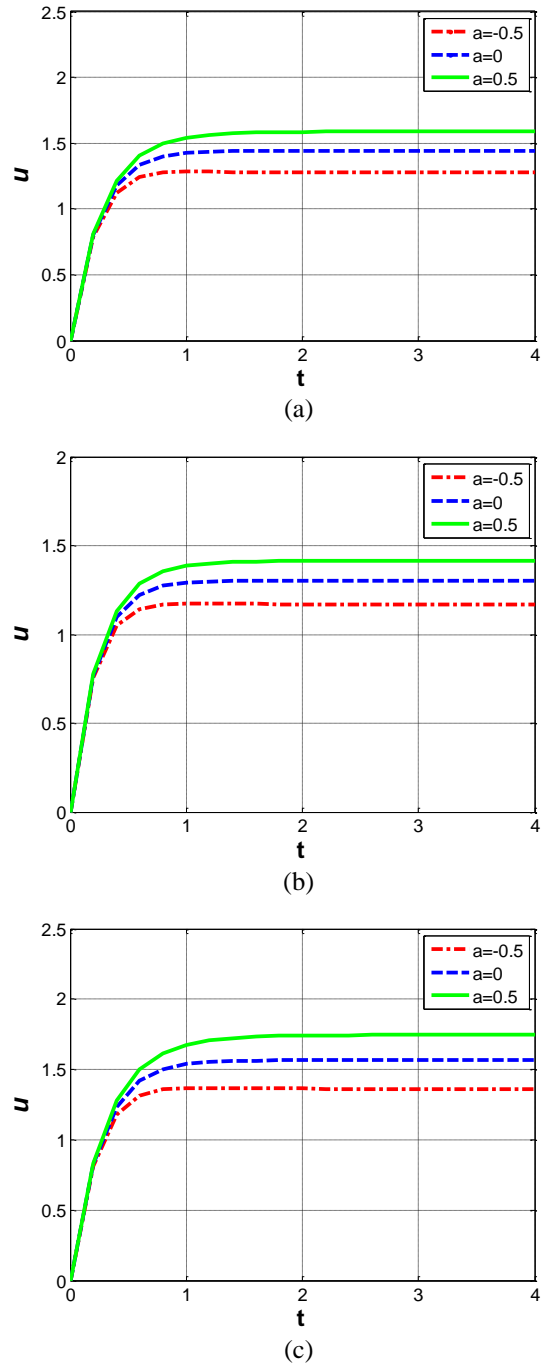
Figure 5 indicates that u increases with increasing m for all values of a, which can be attributed to the fact that an increment in m decreases the resistive force. Figure 6 shows that w decreases with increasing m for all values of a, which can be attributed to the fact that an increment in m increases the resistive force. Figure 7 shows that θ increases with increasing m for all values of a as a result of increasing the dissipations.

Figures 8-10 present the time progression of the velocity components u and w and the temperature θ at the centre of the channel (y=0) for different values of M and *a* and for Ha=1, m=1, S=1 and b=0.

(a)

(b)
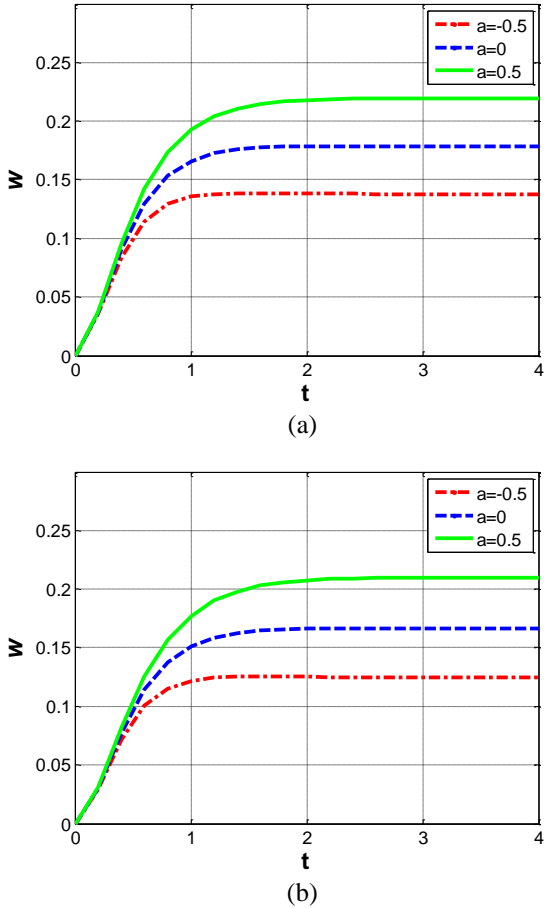
Fig. 6 The evolution of w at y=0 for various values of a and m: (a) m=1; (b) m=2; (Ha=1, M=1, S=1, b=0)

Figures 8-9 indicate that u and w decrease with increasing M for all values of a as a result of the damping effect of the porosity. Figure 10 depicts that the temperature θ decreases with increasing M for all values of a as a result of the damping effect of the porosity which decreases the velocity and velocity gradients and, in turn, deceases the dissipations. Increasing the parameter a increases the velocity components u and w and the temperature θ for all values of *M* as shown in all figures.

(a)

(b)

(c)
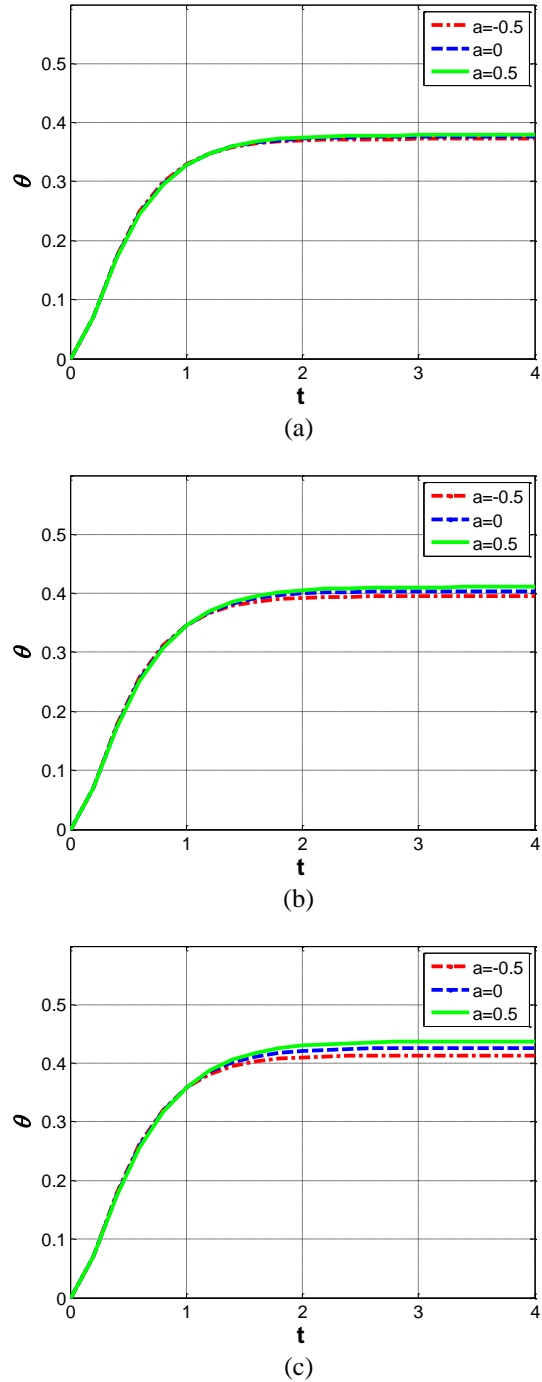
Fig. 7 The evolution of θ at y=0 for various values of a and m: (a) m=0; (b) m=1; (c) m=2 . (Ha=1, M=1, S=1, b=0)

(a)

(b)

(c)
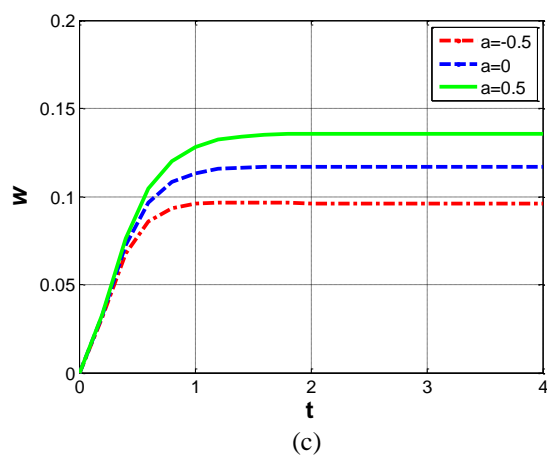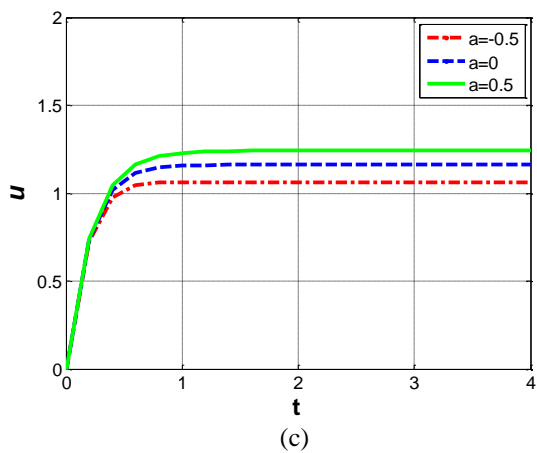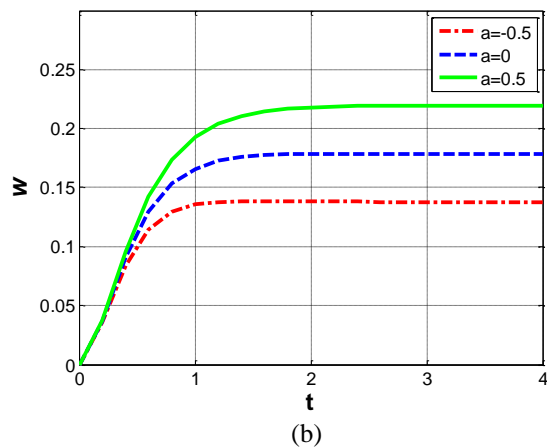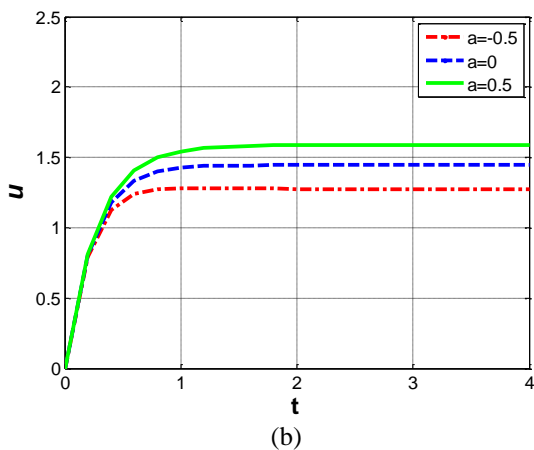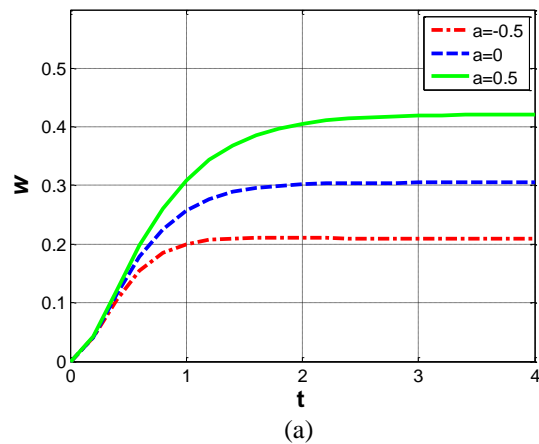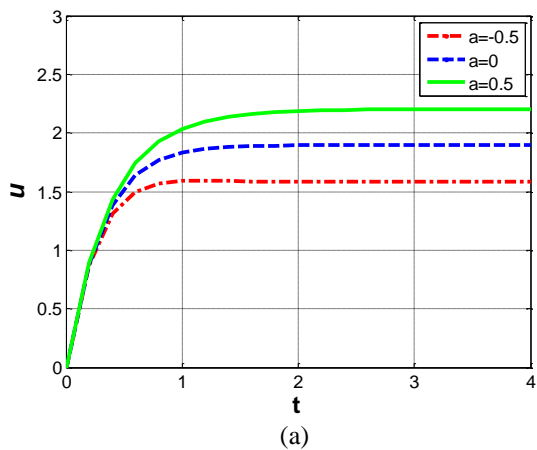
Fig. 8 The evolution of u at y=0 for various values of a and M: (a) M=0; (b) M=1; (c) M=2; . (Ha=1, m=1, S=1, b=0)

Fig. 9 The evolution of w at y=0 for various values of a and M: (a) M=0; (b) M=1; (c) M=2. (Ha=1, m=1, S=1, b=0)

(a)

(b)

(c)
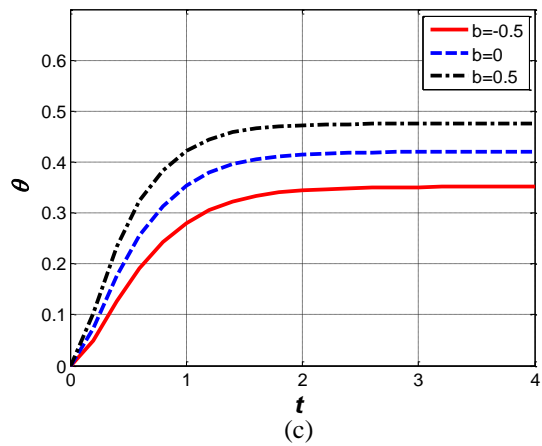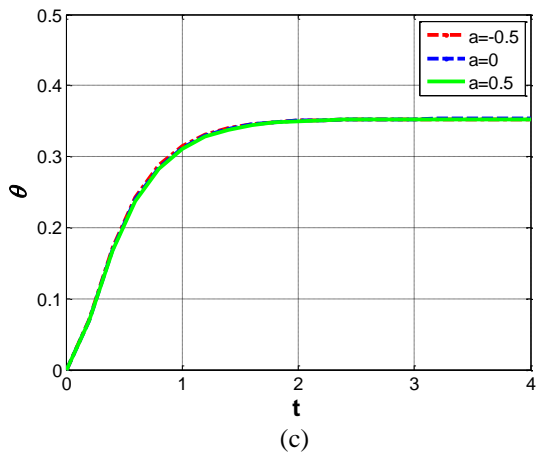
Fig. 10 The evolution of θ at y=0 for various values of a and M: (a) M=0; (b) M=1; (c) M=2;. (Ha=1, m=1, S=1, b=0)

Figure 11 presents the time progression of the temperature θ at the centre of the channel (y=0) for different values of m and b and for *Ha=1, M=1, S=1* and b=0.

(a)

(b)

(c)

Fig. 11 The evolution of θ at y=0 for various values of b and m: (a) m=0; (b) m=1; (c) m=2. (*Ha=1, M=1, S=1, a=0*)

Increasing the parameter b increases the temperature θ for all values of m as shown in all figures. Figure 12 presents the time progression of the temperature θ at the centre of the channel (y=0) for different values of M and b and for Ha=1, M=1, S=1 and a=0.

(a)

(b)

(c)
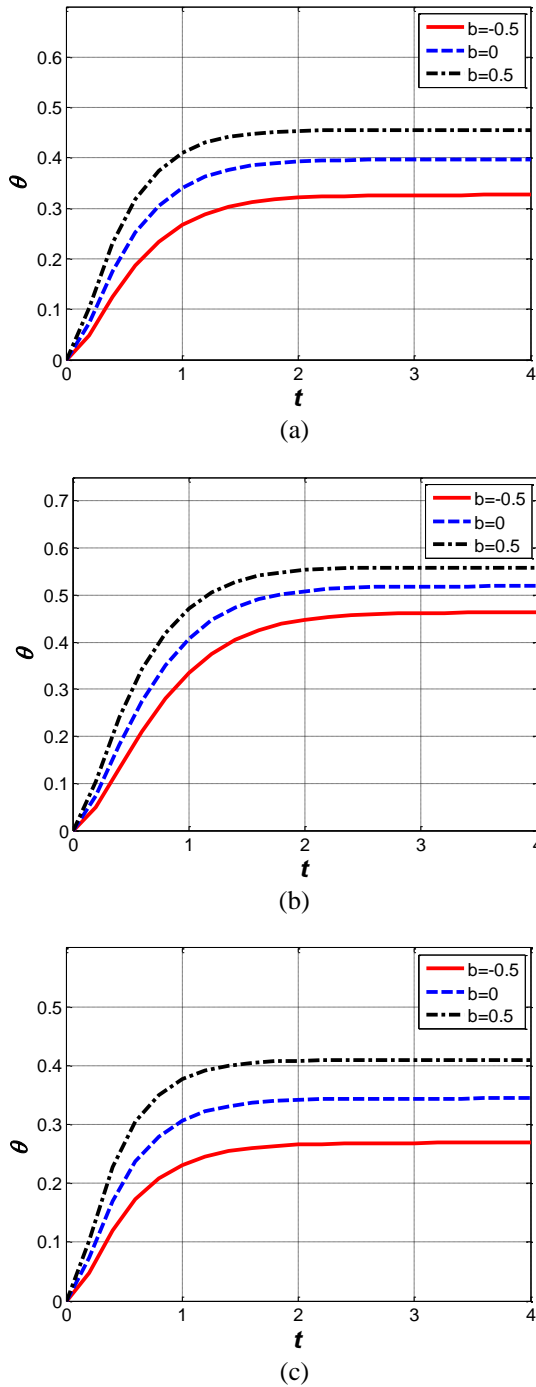
Fig. 12 The evolution of θ at y=0 for various values of b and M: (a) M=0; (b) M=1; (c) M=2. (Ha=1, m=1, S=1, a=0)

Increasing the parameter b increases the temperature θ for all values of M, as shown in all figures. However, the effect of the parameter b on θ becomes more pronounced for higher values of M.

CONCLUSIONS

The time varying MHD flow through a porous medium between two parallel plates was investigated considering the Hall current under the action of a constant pressure gradient. The viscosity and the thermal conductivity of the fluid are assumed to be temperature dependent. The effect of the porosity parameter M, the Hartmann number Ha, the Hall parameter m, the viscosity variation parameter a and the thermal conductivity variation parameter b on the velocity and temperature fields at the centre of the channel are discussed. Introducing the Hall term gives rise to a velocity component w in the z-direction and affects the main velocity u in the x-direction. It is found that the parameter *a* has a marked effect on the velocity components u and w for all values of M. However, the parameter b has no significant effect on u or w. The porosity parameter M has a marked effect on the velocity and temperature distributions, however, its effect on the velocity and its steady state time is more pronounced than that for the temperature.

REFERENCES

1. J. Hartmann, F. Lazarus, Kgl. Danske Videnskab. Selskab, *Mat.-Fys. Medd.*, **15**(6,7), (1937).
2. L.N. Tao, *J. Aerospace Sci.*, **27,**334 (1960).
3. R.A. Alpher, *Int. J. Heat Mass Transfer,* **3,**108 (1961).
4. Sutton, G.W. and Sherman, A., Engineering Magnetohydrodynamics, McGraw-Hill, 1965.
5. K.Cramer, S. Pai, Magnetofluid dynamics for engineers and applied physicists, McGraw-Hill, 1973.
6. S.D. Nigam, S.N. Singh, *Quart. J. Mech. Appl. Math.,* **13**, 85 (1960).
7. V.M. Soundalgekar, N.V. Vighnesam, H.S. Takhar, *IEEE Transactions on Plasma Sciences*, PS-7, No. 3, 1979.
8. V.M. Soundalgekar, A.G. Uplekar, *IEEE Transactions on Plasma Science*, PS-14, No. 5, 1986.
9. H.A. Attia, *Canad. J. Phys.* **76,** 739 (1998).
10. H Herwig, G. Wicken, *Wärme- und Stoffübertragung*, **20**, 47 (1986).
11. A.V. Kuznetsov, D.A. Nield, *Int. J. Heat Mass Transfer*, **53**, 2676 (2010).
12. D.A. Nield, A.V. Kuznetsov, *Int. J. Heat Mass Transfer*, **53**, 2680 (2010).
13. D.A. Nield, A.V. Kuznetsov, A.V., *J. Heat Transfer-Transactions of ASME,* **132**, 074503 (2010).
14. K.Klemp, H. Herwig, M. Selmann, *Proceedings of the ThirdInternational Congress of Fluid Mechanics,* **3**, 1257, 1990.
15. H.A. Attia, N.A. Kotb, *Acta Mechanica*, **117**, 215 (1996).
16. H.A.Attia, *Mech. Res. Commun.,* **26**, 115 (1999).
17. D.D. Joseph, D.A. Nield, G. Papanicolaou, *Water Resources Res.*, **18**, 1049 (1982).
18. D.B. Ingham, I. Pop, Transport phenomena in porous media, Pergamon, Oxford, 2002.
19. A.R.A. Khaled, K. Vafai, *Int. J. Heat Mass Transfer*, **46**, 4989 (2003).
20. H.A. Attia, M.A.M. Abdeen, *J. Theor. Appl. Mech.,* **51**, 53 (2013).

21. M.A.M Abdeen, H.A Attia, W.Abbas, W. Abd El-Meged, *Indian J. Phys.*, **87**, 767 (2013).
22. Z.Joaquín, E. Pablo, G. Enrique, L.M. José, A.B. Osman, *Int. Commun. Heat Mass Transfer*, **37**, 1432 (2010).
23. P. Eguia, J. Zueco, E. Granada, D. Patiño, *Appl. Math. Modelling*, **35**, 303 (2011).
24. M.F. White, Viscous fluid flow, McGraw-Hill, 1991.
25. W.F. Ames, Numerical solutions of partial differential equations, 2nd ed., Academic Press, New York, 1977.

ЕФЕКТ НА ПОРЬОЗНОСТТА ВЪРХУ ТЕЧЕНИЕТО И ТОПЛОПРЕНАСЯНЕТО МЕЖДУ ДВЕ ПОРЬОЗНИ ПЛОЧИ С ЕФЕКТ НА ХОЛ И ПРОМЕНЛИВИ СВОЙСТВА ПРИ ПОСТОЯНЕН ГРАДИЕНТ НА НАЛЯГАНЕТО

Х. А. Атиа [1], У. Абас[2], М. А. М. Абдийн [3], А. Ел-Дин Абдин[4]

[1] *Департамент по инженерна математика и физика, Инженерен факултет, Университет Ел-Фаюм, Египет*
[2] *Департамент по основни и приложни науки, Колеж за инженерство и технология, Арабска академия за наука, технология и морски транспорт (клон Кайро), Кайро, Египет*
[3] *Департамент по инженерна математика и физика, Инженерен факултет, Университет в Кайро, Египет*
[4] *Национален център за водни изследвания, Министерство по водни източници и напояване, Египет*

(Резюме)

Изследвано е преходното хидромагнитно течение през порьозна среда между две безкрайни успоредни порьозни плоскости с топлообмен и с отчитането на ефекта на Хол и температурно зависими свойства при постоянен градиент на налгането. Приложено е външно постоянно магнитно поле с равномерно всмукване и инженктиране перпендикулярно на хоризонталните плочи. Получено е числено решение на нелинейните уравнения на движението и енергията с отчитане на дисипация на енергията от вискозитета и ефекта Джаул. Съобщава се за ефекти на порьозността, тока на Хол, температурата зависимост на вискозитета и топлопроводността върху разпределението на скоростта и температурата.

Systematic parameter study for nano-fiber fabrication *via* electrospinning process

M. Mohammadian[1], A. K. Haghi[2*]

[1]*Department of Textile Engineering, Kashan Branch, Islamic Azad University, Kashan, Iran*
[2]*University of Guilan, P.O.Box 3756, Rasht, Iran*

Elecrospinning is a process that produces continuous polymer fibers with diameter in the submicron range. In the electrospinnig process the electric body force acts on the elements of a charged fluid. Electrospinning has emerged as a specialized processing technique for the formation of sub-micron fibers (typically between 100 nm and 1 μm in diameter), with high specific surface area. The objective of this paper is to establish quantitative relationships between the electrospinning parameters and the mean and standard deviation of fiber diameter, as well as to evaluate the effectiveness of the empirical models with a set of test data.

Keywords: Electrospinning, Nanofibers, Fiber diameter, Processing variables, Response surface methodology

INTRODUCTION

Electrospinning is a novel and efficient method to produce fibers with diameters in the nanometer scale, named nanofibers. In the electrospinning process, a strong electric field is applied on a droplet of polymer solution (or melt) held by its surface tension at the tip of a syringe needle (or a capillary tube) [1-5]. Fig. **1** shows a schematic illustration of an electrospinning setup.
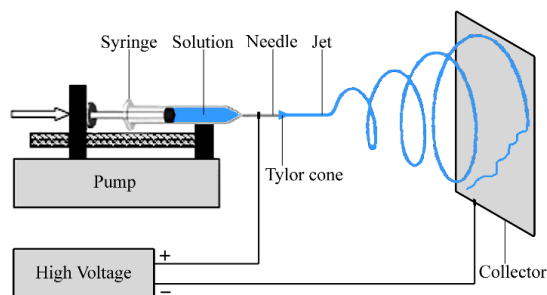
Fig. 1: Electrospinning setup [6]

Featuring various outstanding properties such as very small fiber diameters, large surface area per mass ratio [3], high porosity along with small pore sizes [7], flexibility, and superior mechanical properties [8], electrospun nanofiber mats have found numerous applications in biomedicine (tissue engineering [9]-[11], drug delivery [12], [13], wound dressing [14], [15]), protective clothing [7], filtration [16], reinforcement of composite mats [8], [17], micro-electronics (batteries [18], supercapacitors [19], transistors [20], sensors [21], and display devices [22-24]).

Among the characteristics of the final product such as physical, mechanical and electrical properties, fiber diameter is one of the most important structural features of electrospun nanofiber mats. Podgorski *et al*. [25] indicated that filters made of fibers with smaller diameters have higher filtration efficiency. This was also proved by the work of Qin *et al*. [16]. Ding *et al*. [26] reported that the sensitivity of sensors increases with decreasing the mean fiber diameter due to the higher surface area. In the study on designing polymer batteries consisting of electrospun PVdF fibrous electrolyte by Kim *et al*. [27], it was demonstrated that smaller fiber diameter results in a higher electrolyte uptake and thereby increased ionic conductivity of the mat. Moroni *et al*. [28] found that fiber diameters of electrospun PEOT/PBT scaffolds influence cell seeding, attachment and proliferation. The carbonization and activation conditions, as well as the structure and properties of the ultimate carbon fibers are also affected by the diameters of the precursor PAN nanofibers [29]. Consequently, precise control of the electrospun fiber diameter is very crucial.

Sukigara *et al*. [30] employed response surface methodology (RSM) to model mean fiber diameter of electrospun regenerated Bombyx mori silk with electric field and concentration at two spinning distances.

Gu *et al*. [31] and Gu *et al*. [32] also exploited the RSM for quantitative study of PAN and PDLA.

* To whom all correspondence should be sent:
E-mail: Haghi@Guilan.ac.ir

In the most recent investigation in this field, Yördem *et al.* [33] utilized RSM to correlate the mean and coefficient of variation (CV) of the diameter of electrospun PAN nanofibers to solution concentration and applied voltage at three different spinning distances.

Several patents are reported on the process for production of ultrahigh-tensile strength PVA fibers comparable to Kevlar® [36]-[38]. PVA has found many applications in biomedical uses as well, due to its biocompatibility [39]. For instance, PVA hydrogels were used in regenerating articular cartilages [40], [41], artificial pancreas [42], and drug delivery systems [43], [44]. More recently, PVA nanofibers were electrospun and used as a protein delivery system [45], for retardation of enzyme release [45] and wound dressing [46].

In this paper, response surface methodology (RSM) was employed to quantitatively investigate the simultaneous effects of four of the most important parameters, namely solution concentration (*C*), spinning distance (*d*), applied voltage (*V*) and volume flow rate (*Q*) on the mean fiber diameter (MFD) and the standard deviation of the fiber diameter (StdFD) in electrospinning of polyvinyl alcohol (PVA) nanofibers.

EXPERIMENTAL

Solution preparation and electrospinning

PVA with molecular weight of 72000 g/mol and degree of hydrolysis of >98% was obtained from Merck and was used as received. Distilled water was added as a solvent to a predetermined amount of PVA powder to obtain 20 ml of a solution with desired concentration. The solution was prepared at 80°C and was gently stirred for 30 min to expedite the dissolution. After the PVA had completely dissolved, the solution was transferred to a 5 ml syringe and was ready to electrospin. The experiments were carried out on a horizontal electrospinning setup shown schematically in **Fig.**

1. The syringe containing PVA solution was placed on a syringe pump (New Era NE-100) used to dispense the solution at a controlled rate. A high voltage DC power supply (Gamma High Voltage ES-30) was used to generate the electric field needed for electrospinning. The positive electrode of the high voltage supply was attached to the syringe needle via an alligator clip and the grounding electrode was connected to a flat collector wrapped with aluminum foil where electrospun nanofibers were accumulated to form a nonwoven mat. The electrospinning was carried out at room temperature. Subsequently, the aluminum foil was removed from the collector. A small piece of mat was placed on the sample holder and gold sputter-coated (Bal-Tec). Thereafter, the morphology of the electrospun PVA fibers was observed by an environmental scanning electron microscope (SEM, Phillips XL-30) under magnification of 10000×. For each specimen, fiber diameter distribution was determined from the SEM micrograph based on 100 measurements of random fibers. A typical SEM micrograph of an electrospun nanofiber mat and its corresponding diameter distribution are shown in Fig. *2*.

Choice of parameters and range

In this study, solution concentration (*C*), spinning distance (*d*), applied voltage (*V*), and volume flow rate (*Q*) were selected to be the most influential parameters in electrospinning of PVA nanofibers for the purpose of this study.

The relationship between intrinsic viscosity ([η]) and molecular weight (*M*) is given by the well-known Mark-Houwink-Sakurada equation as follows:

$$[\eta] = KM^a \tag{1}$$

where *K* and *a* are constants for a particular polymer-solvent pair at a given temperature [47]. For the PVA with molecular weight in the range of 69000 *g/mol* <*M*<690000 *g/mol* in water at room
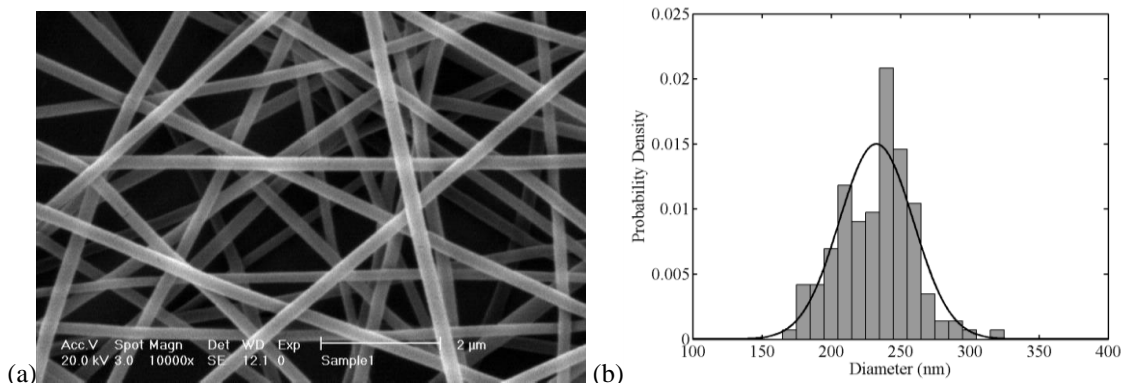

Fig. 2. (a) a typical SEM micrograph of electrospun nanofiber mat, (b) its corresponding diameter distribution

temperature, K=6.51 and a=0.628 were found by Tacx *et al.* [48]. Using these constants in the equation, the intrinsic viscosity of PVA in this study (molecular weight of 72000 *g/mol*) were calculated to be $[\eta]$=0.73.

Polymer chain entanglements in a solution can be expressed in terms of Berry number (B), which is a dimensionless parameter and is defined as the product of intrinsic viscosity and polymer concentration ($B = [\eta]C$) [49]. At each molecular weight, there is a minimum concentration at which the polymer solution cannot be electrospun. Koski *et al.* [50] observed that B>5 is required to form stabilized fibrous structures in electrospinning of PVA. On the other hand, they reported the formation of flat fibers at B>9. Therefore, the appropriate range in this case could be found within the 5<B<9 domain which is equivalent to 6.8%<C<12.3% in terms of concentration of PVA. Furthermore, Koski *et al.* [50] observed that beaded fibers were electrospun at low solution concentration. Hence, it was thought that the domain 8%≤C≤12% would warrant the formation of stabilized bead-free fibers with circular cross-sections. This domain was later justified by some preliminary experiments.

For determining the appropriate range of applied voltage, referring to previous works, it was observed that the changes of voltage lay between 5 *kV* and 25 *kV* depending on experimental conditions; voltages above 25 *kV* were rarely used. Afterwards, a series of experiments was carried out to obtain the desired voltage domain. At V<10 *kV*, the voltage was too low to spin fibers and 10 *kV*≤V<15 *kV* resulted in formation of fibers and droplets; in addition, electrospinning was impeded at high concentrations. In this regard, 15 *kV*≤V≤25 *kV* was selected as the desired domain for the applied voltage.

The use of 5 *cm* – 20 *cm* for spinning distance was reported in the literature. Short distances are suitable for highly evaporative solvents whereas wet conglutinated fibers are obtained with nonvolatile solvents due to insufficient evaporation time. Since water was used as a solvent for PVA in this study, short spinning distances were not expected to be favorable for dry fiber formation. Afterwards, this was proved by experimental observations and 10 *cm*≤d≤20 *cm* was considered as the effective range for the spinning distance.

Few researchers have addressed the effect of volume flow rate. Therefore, in this case, the attention was focused on experimental observations. At Q<0.2 *ml/h*, in most cases,

especially at high polymer concentrations, fiber formation was hindered due to insufficient supply of solution to the tip of the syringe needle, whereas excessive feed of solution at Q>0.4 *ml/h* incurred formation of droplets along with fibers. As a result, 0.2 *ml/h*≤Q≤0.4 *ml/h* was chosen as the favorable range of flow rate in this study.

Experimental design

Three levels were selected for each parameter in this study so that it would be possible to use quadratic models. These levels were chosen equally spaced. A full factorial experimental design with four factors (solution concentration, spinning distance, applied voltage, and flow rate) each at three levels (3^4 design) was employed, resulting in 81 treatment combinations. This design is shown in Fig. 3.
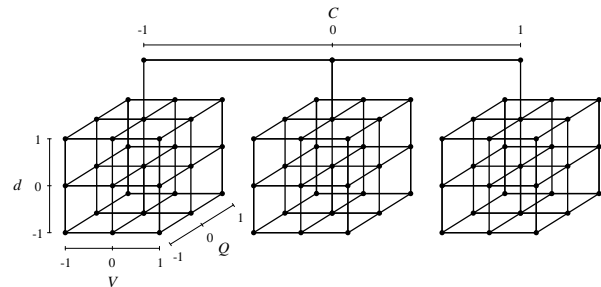

Fig. 3. 3^4 Full factorial experimental design used in this study

-1, 0, and 1 are coded variables corresponding to low, intermediate and high levels of each factor respectively. The coded variables (x_j) were calculated using Equation (2) from natural variables (ξ_i). The indices 1 to 4 represent solution concentration, spinning distance, applied voltage, and flow rate, respectively. In addition to the experimental data, 15 treatments inside the design space were selected as test data and were used for evaluation of the models. The natural and coded variables for experimental data (numbers 1-81) as well as test data (numbers 82-96) are listed in listed in Table 6.

$$x_j = \frac{\xi_j - [\xi_{hj} + \xi_{lj}]/2}{[\xi_{hj} - \xi_{lj}]/2} \qquad (2)$$

Response surface methodology

The relationship between the response (y) and k input variables ($\xi_1, \xi_2, ..., \xi_k$) could be expressed in terms of mathematical notations as follows:

$$y = f(\xi_1, \xi_2, ..., \xi_k) \qquad (3)$$

where the true response function f is unknown. It is often convenient to use coded variables ($x_1, x_2, .., x_k$) instead of natural (input) variables. The response function will then be:

$$y = f(x_1, x_2, ..., x_k) \qquad (4)$$

347

Since the form of true response function f is unknown, it must be approximated. Therefore, the successful use of RSM is critically dependent upon the choice of appropriate function to approximate f. Low-order polynomials are widely used as approximating functions. First-order (linear) models are unable to capture the interaction between parameters which is a form of curvature in the true response function. A second-order (quadratic) model will likely perform well in these circumstances. In general, the quadratic model is in the form of:

$$y = \beta_0 + \sum_{j=1}^{k} \beta_j x_j + \sum_{j=1}^{k} \beta_{jj} x_j^2 + \sum_{i<j} \sum_{j=2}^{k} \beta_{ij} x_i x_j + \varepsilon \quad (5)$$

where ε is the error term in the model. The use of polynomials of higher order is also possible but infrequent. The βs are a set of unknown coefficients needed to be estimated. In order to do that, the first step is to make some observations on the system being studied. The model in Equation (5) may now be written in matrix notations as:

$$\mathbf{y} = \mathbf{X\beta} + \mathbf{\varepsilon} \quad (6)$$

where $\mathbf{y}$ is the vector of observations, $\mathbf{X}$ is the matrix of levels of the variables, $\mathbf{\beta}$ is the vector of unknown coefficients, and $\mathbf{\varepsilon}$ is the vector of random errors. Afterwards, the method of least squares, which minimizes the sum of squares of errors, is employed to find the estimators of the coefficients ($\hat{\mathbf{\beta}}$) through:

$$\hat{\mathbf{\beta}} = (\mathbf{X'X})^{-1}\mathbf{X'y} \quad (7)$$

The fitted model will then be written as:

$$\hat{\mathbf{y}} = \mathbf{X}\hat{\mathbf{\beta}} \quad (8)$$

Finally, response surfaces or contour plots are depicted to help visualize the relationship between

Table **1**, the values of R^2, R_{adj}^2, and R_{pred}^2. R^2 is a measure of the amount of response variation which is explained by the variables and will always increase when a new term is added to the model – regardless of whether the inclusion of the additional term is statistically significant or not. R_{adj}^2 is the R^2 adjusted for the number of terms in the model, therefore it will increase only if the new terms improve the model and decreases if unnecessary terms are added. R_{pred}^2 implies how well the model predicts the response for new observations, whereas R^2 and R_{adj}^2 indicate how well the model fits the experimental data. The R^2 values demonstrate that 95.74% of MFD and 89.92% of StdFD are explained by the variables. The R_{adj}^2 values are 94.84% and 87.78% for MFD and StdFD respectively, which account for the number of

548

the response and the variables and see the influence of the parameters [53].

RESULTS AND DISCUSSION

After the unknown coefficients (βs) were estimated by the least squares method, the quadratic models for the mean fiber diameter (MFD) and standard deviation of fiber diameter (StdFD) in terms of coded variables are written as:

$$\begin{aligned} \text{MFD} = {} & 282.031 + 34.953\,x_1 + 5.622\,x_2 - 2.113\,x_3 + 9.013\,x_4 \\ & - 11.613\,x_1^2 - 4.304\,x_2^2 - 15.500\,x_3^2 \\ & - 0.414\,x_4^2 + 12.517\,x_1 x_2 + 4.020\,x_1 x_3 \\ & - 0.162\,x_1 x_4 + 20.643\,x_2 x_3 + 0.741\,x_2 x_4 + 0.877\,x_3 x_4 \end{aligned} \quad (9)$$

$$\begin{aligned} \text{MFD} = {} & 282.031 + 34.953\,x_1 + 5.622\,x_2 - 2.113\,x_3 + 9.013\,x_4 \\ & - 11.613\,x_1^2 - 4.304\,x_2^2 - 15.500\,x_3^2 \\ & - 0.414\,x_4^2 + 12.517\,x_1 x_2 + 4.020\,x_1 x_3 \\ & - 0.162\,x_1 x_4 + 20.643\,x_2 x_3 + 0.741\,x_2 x_4 + 0.877\,x_3 x_4 \end{aligned} \quad (10)$$

In the next step, a couple of very important hypothesis-testing procedures were carried out to measure the usefulness of the models presented here. First, the test for significance of the model was performed to determine whether there is a subset of variables which contributes significantly in representing the response variations. The appropriate hypotheses are:

$$\begin{aligned} & H_0 : \beta_1 = \beta_2 = \cdots = \beta_k \\ & H_1 : \beta_j \neq 0 \quad \text{for at least one } j \end{aligned} \quad (9)$$

The p-values of the models are very small (almost zero), therefore it is concluded that the null hypothesis is rejected in both cases suggesting that there are some significant terms in each model. There are also included in

terms in the models. Both R^2 and R_{adj}^2 values indicate that the models fit the data very well. The slight difference between the values of R^2 and R_{adj}^2 suggests that there might be some insignificant terms in the models. Since the R_{pred}^2 values are so close to the values of R^2 and R_{adj}^2, the models does not appear to be overfit and have very good predictive ability.

The second testing hypothesis performed in this study was the test on individual coefficients, which would be useful in determining the value of the variables in the models. The hypotheses for testing the significance of any individual coefficient are:

$$\begin{aligned} & H_0 : \beta_j = 0 \\ & H_1 : \beta_j \neq 0 \end{aligned} \quad (10)$$

Table 1. Summary of the results from the statistical analysis of the models

	F	p-value	R^2	R^2_{adj}	R^2_{pred}
MFD	106.02	0.000	95.74%	94.84%	93.48%
StdFD	42.05	0.000	89.92%	87.78%	84.83%

Since the model might be more effective with inclusion or perhaps exclusion of one or more variables, by means of this test, we could evaluate the value of each term in the model and eliminate the statistically insignificant terms, thereby obtain more efficient models. The results of this test for the models of MFD and StdFD are summarized in Table 2 and Table 3, respectively.

Table 2. Test on individual coefficients for the model of mean fiber diameter

Term	Coef.	T	p-value
Constant	282.031	102.565	0.000
C	34.953	31.136	0.000
d	5.622	5.008	0.000
V	-2.113	-1.882	0.064
Q	9.013	8.028	0.000
C^2	-11.613	-5.973	0.000
d^2	-4.304	-2.214	0.030
V^2	-15.500	-7.972	0.000
Q^2	-0.414	-0.213	0.832
Cd	12.517	9.104	0.000
CV	4.020	2.924	0.005
CQ	-0.162	-0.118	0.906
dV	20.643	15.015	0.000
dQ	0.741	0.539	0.592
VQ	0.877	0.638	0.526

Table 3: Test on individual coefficients for the model of standard deviation of fiber diameter

Term	Coef.	T	p-value
Constant	36.1574	39.381	0.000
C	4.5788	12.216	0.000
D	-1.5536	-4.145	0.000
V	6.4012	17.078	0.000
Q	1.1531	3.076	0.003
C^2	-2.2937	-3.533	0.001
d^2	-0.1115	-0.172	0.864
V^2	-1.1891	-1.832	0.072
Q^2	3.0980	4.772	0.000

Table 4. It is obvious that the p-values for the new models are close to zero indicating the Table **1**, the F statistic increased for the new models, indicating the improvement of the models after eliminating the insignificant terms. Despite the slight decrease in R^2, the values of R^2_{adj} and R^2_{pred} increased a great deal for the new models. The new models have the ability to better explain the experimental data. Due to higher R^2_{pred} values obtained, the new models also have higher prediction ability. In other words, eliminating the

Cd	-0.2088	-0.455	0.651
CV	1.0010	2.180	0.033
CQ	2.7978	6.095	0.000
dV	0.1649	0.359	0.721
dQ	-2.4876	-5.419	0.000
VQ	1.5182	3.307	0.002

As depicted, the terms Q^2, CQ, dQ, and VQ in the model of MFD and d^2, Cd, and dV in the model of StdFD have very high p-values, therefore they do not contribute significantly in representing the variation of the corresponding response. Eliminating these terms will enhance the efficiency of the models. Recalculating the unknown coefficients, the new models are then given by:

$$MFD = 281.755 + 34.953\,x_1 + 5.622\,x_2 - 2.113\,x_3 + 9.013\,x_4$$
$$- 11.613\,x_1^2 - 4.304\,x_2^2 - 15.500\,x_3^2 \qquad (13)$$
$$+ 12.517\,x_1 x_2 + 4.020\,x_1 x_3 + 20.643\,x_2 x_3$$

$$StdFD = 36.083 + 4.579\,x_1 - 1.554\,x_2 + 6.401\,x_3 + 1.153\,x_4$$
$$- 2.294\,x_1^2 - 1.189\,x_3^2 + 3.098\,x_4^2 \qquad (14)$$
$$+ 1.001\,x_1 x_3 + 2.798\,x_1 x_4 - 2.488\,x_2 x_4 + 1.518\,x_3 x_4$$

in terms of coded variables and:

$$MFD = 10.3345 + 48.7288\,C - 22.7420\,d + 7.9713\,V + 90.1250\,Q$$
$$- 2.9033\,C^2 - 0.1722\,d^2 - 0.6120\,V^2 \qquad (15)$$
$$+ 1.2517\,Cd + 0.4020\,CV + 0.8257\,dV$$

$$StdFD = -1.8823 + 7.5590\,C + 1.1818\,d + 1.2709\,V - 300.3410\,Q$$
$$- 0.5734\,C^2 - 0.0476\,V^2 + 309.7999\,Q^2 \qquad (16)$$
$$+ 0.1001\,CV + 13.9892\,CQ - 4.9752\,dQ + 3.0364\,VQ$$

in terms of natural (uncoded) variables. The results of test for significance as well as R^2, R^2_{adj}, and R^2_{pred} for the new models are given in

Now that the relationships have been developed, the test data were used to investigate the prediction ability of the models. Root mean square errors (RMSE) between calculated responses (Ci)

existence of some significant terms in each model. Comparing the results of this table with insignificant terms, simpler models were obtained which not only better explain the experimental data, but also are more powerful in predicting new conditions.

Now that the relationships have been developed, the test data were used to investigate the prediction ability of the models. Root mean square errors (RMSE) between calculated responses (C_i)

Table 4. Summary of the results from the statistical analysis of the models after eliminating the insignificant terms

	F	p-value	R^2	R^2_{adj}	R^2_{pred}
MFD	155.56	0.000	95.69%	95.08%	94.18%
StdFD	55.61	0.000	89.86%	88.25%	86.02%

and real responses (R_i) were determined using equation (11) for experimental data as well as test data for the sake of evaluation of both MFD and StdFD models and are listed in Table 5. Hence, the results imply the acceptable prediction ability of the models.

$$RMSE = \sqrt{\frac{\sum_{i=1}^{n}(C_i - R_i)^2}{n}} \qquad (11)$$

Table 5 RMSE values of the models for the experimental and test data

	Experimental data	Test data
MFD	7.489	10.647
StdFD	2.493	2.890

Response surfaces for mean fiber diameter

Solution concentration

Increasing polymer concentration will result in greater polymer chain entanglements. This causes the viscoelastic force to increase enabling the charged jet to withstand a larger electrostatic stretching force leading to a larger diameter of fibers. A monotonous increase in MFD with concentration was observed in this study as shown in Fig. **4** (a), (b), and (c) which concurs with the previous observations [23], [29], [56]-[58]. The concentration effect was more pronounced at longer spinning distances (Fig. **4** (a)). This could be attributed to the twofold effect of distance which will later be discussed in the paper. At low concentrations, there are higher amounts of solvent in the solution and longer distance provides more time not only to stretch the jet in the electric field but also to evaporate the solvent, thereby favoring thinner fiber formation. At higher concentrations, however, there are extensive polymer chain entanglements resulting in higher viscoelastic forces which tend to resist the electrostatic stretching force.

Spinning distance

Increasing the spinning distance, the electric field strength will decrease ($E = \dfrac{V}{d}$) resulting in less acceleration, hence stretching of the jet which leads to thicker fiber formation. The balance between these two effects will determine the final fiber diameter. Increase in fiber diameter [57], [60], [61] as well as decrease in fiber diameter [29] with increasing spinning distance was reported in the

literature. There were also some cases in which spinning distance did not have a significant influence on fiber diameter [56], [62]-[64]. The impact of spinning distance on MFD is illustrated in Fig. **4** (a), (d), and (e). As it is depicted in these figures, the effect of spinning distance is not always the same. Hence, the electrostatic stretching force, which has now become weaker, will be dominated easier by the viscoelastic force. As a result, the increasing effect of spinning distance on fiber diameter will be assisted, rendering higher MFD (Fig. **4** (a)). The effect of spinning distance will alter at different applied voltages (Fig. **4** (d)). The function of spinning distance was observed to be independent from the volume flow rate for MFD (Fig. **4** (e)). The interaction of spinning distance with solution concentration and applied voltage demonstrated in Fig. **4** (a) and (d), proved the existence of terms *Cd* and *dV* in the model of MFD.

Applied voltage

Increasing applied voltage may decrease [66]-[68], increase [56], [57], [61] or may not change [23], [29], [62], [69] the fiber diameter. Fig. **4** (b), (d), and (f) show the effect of applied voltage on MFD. Increasing the voltage, MFD underwent an increase followed by a decrease. The effect of voltage on MFD was influenced by solution concentration to some extent (Fig. **4** (b)). At high concentrations, the increase in fiber diameter with voltage was more pronounced. This could be attributed to the fact that the effect of the mass of solution will be more important for solutions of higher concentration. Spinning distance dramatically influenced the way voltage affects fiber diameter (Fig. **4** (d)). Looking at the figures, it is apparent that there is a huge interaction between applied voltage and spinning distance, a slight interaction between applied voltage and solution concentration and no interaction between applied voltage and volume flow rate which is in agreement with the presence of *CV* and *dV* and absence of *VQ* in the model of MFD.

Volume flow rate

It was suggested that a minimum value for solution flow rate is required to form the drop of polymer at the tip of the needle for the sake of maintaining a stable Taylor cone [70]. In this study, the MFD slightly increased with volume flow rate (Fig. **4** (c), (e), and (f)) which agrees with previous research [29], [70]-[72]. Flow rate was also found to influence MFD independent from solution

concentration, applied voltage, and spinning distance, as suggested earlier by the absence of *CQ*, *dQ*, and *VQ* in the model of MFD.
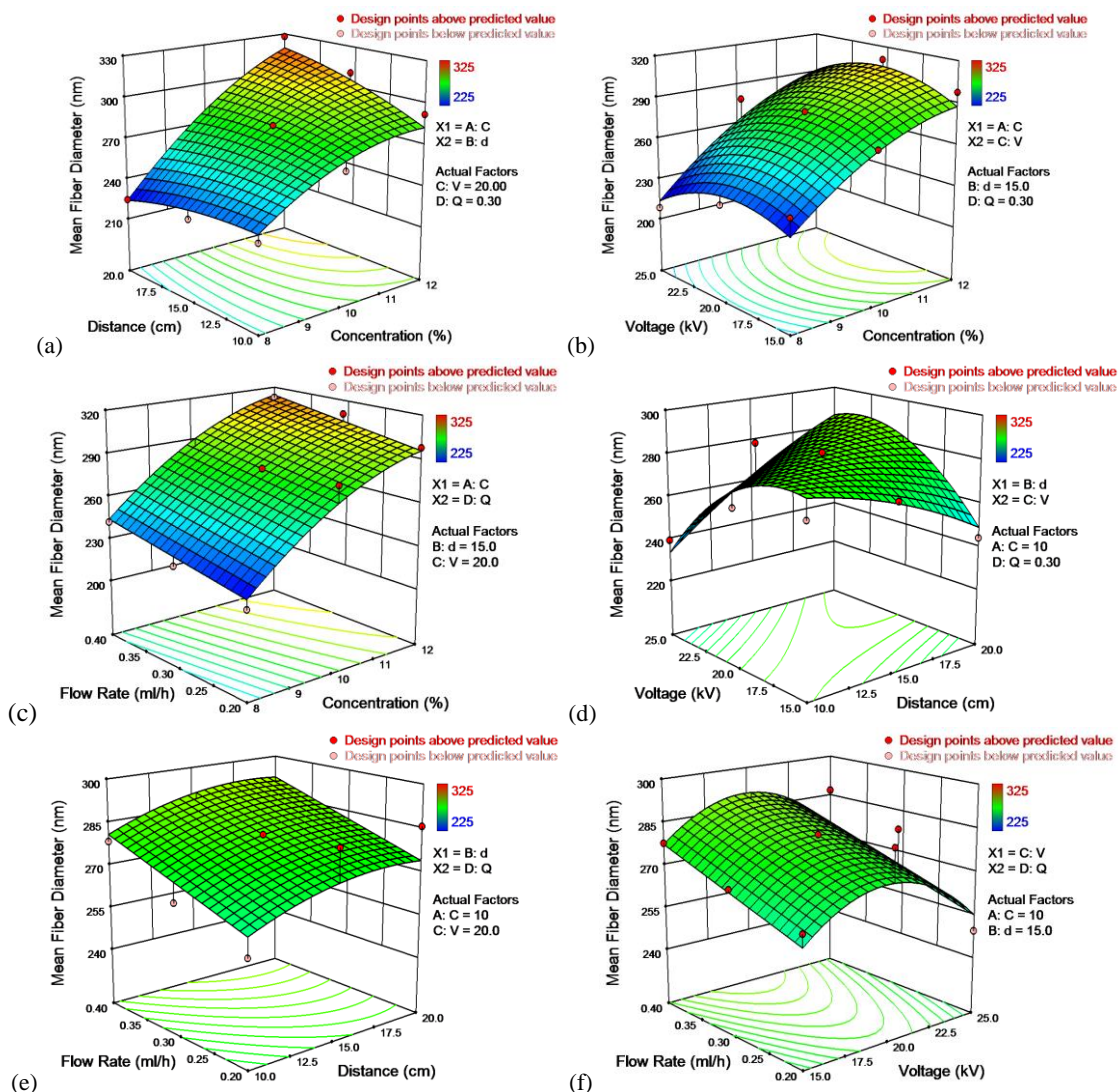

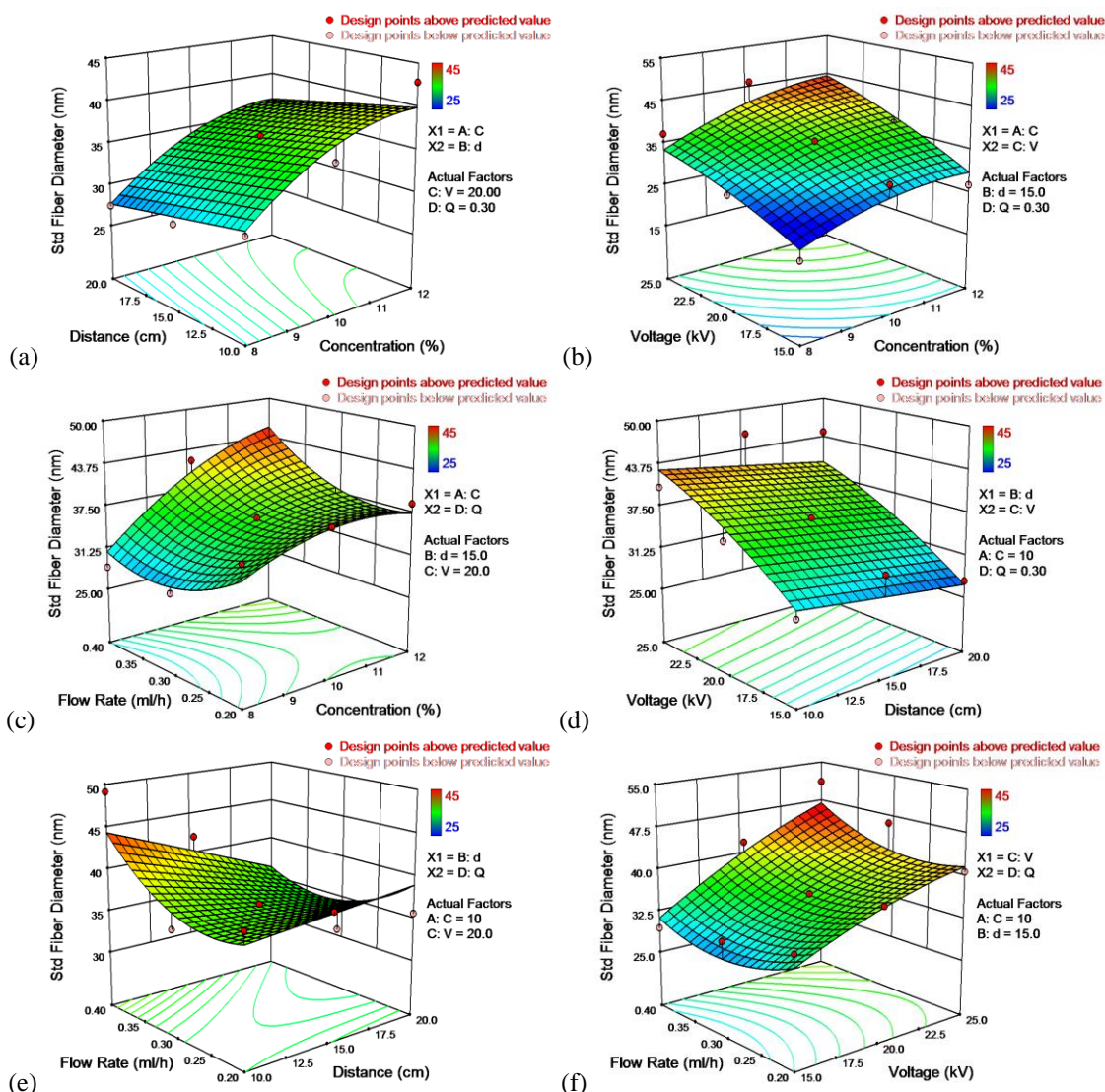**Fig. 4** Response surfaces for mean fiber diameter in terms of: (a) solution concentration and spinning distance, (b) solution concentration and applied voltage, (c) solution concentration and flow rate, (d) spinning distance and applied voltage, (e) spinning distance and flow rate, (f) applied voltage and flow rate

Response surfaces for standard deviation of fiber diameter

Solution concentration

As depicted in Fig. **5** (a), (b), and (c), StdFD increased with concentration which concurs with the previous observations [23], [31], [56], [59], [29], [61], [73], [74]. Concentration affected StdFD regardless of spinning distance (Fig. **5** (a)), suggesting that there was no interaction between these two parameters (absence of *Cd* in the model of StdFd). At low applied voltages, the formation of more uniform fibers upon decreasing the concentration was facilitated. In agreement with the existence of the term *CV* in the model of StdFd, solution concentration was found to have a slight interaction with applied voltage (Fig. **5** (b)). The

curvature of the surface in Fig. **5** (c) suggested that there was a noticeable interaction between concentration and flow rate and this agrees with the presence of the term *CQ* in the model of StdFD.

Spinning distance

More uniform fibers (lower StdFD) were obtained on increasing the spinning distance as shown in Fig. **5** (a), (d), and (e). Our finding is consistent with the trend observed by Zhao *et al.* [74]. Spinning distance influenced StdFD regardless of solution concentration and applied voltage (Fig. **5** (a) and (d)) meaning that no interaction exists between these variables as could be inferred from the model of StdFD.

Fig. 5 Response surfaces for the standard deviation of fiber diameter in terms of: (a) solution concentration and spinning distance, (b) solution concentration and applied voltage, (c) solution concentration and flow rate, (d) spinning distance and applied voltage, (e) spinning distance and flow rate, (f) applied voltage and flow rate

Applied voltage

StdFD was found to increase with applied voltage (Fig. 5 (b), (d), and (f)), as observed in other works [56], [57], [61], [74]. The effect of applied voltage on StdFD was influenced by solution concentration as depicted in Fig. 5 (b), implying the interaction of voltage with concentration.

Volume flow rate

As demonstrated in Fig. **5** (c), (e), and (f), increasing the flow rate, the uniformity of fibers increased (StdFD decreased), reached an optimum value and then decreased (StdFD increased). When the flow rate is low, the amount of solution fed to the tip of the needle is not sufficient, whereas an excess amount of solution is delivered to the tip of the needle at high flow rates. The shorter the distance, the shorter is the time provided to the jet to thin and dry. Therefore, at high flow rates at

which a larger amount of solution is delivered to the tip of the needle, the given time may not suffice, resulting in formation of less uniform fibers. High applied voltage favored the increase in StdFD at fast flow rates as depicted in Fig. **5** (f).

CONCLUSION

For MFD:
1- Increasing solution concentration, MFD increased rigorously. The effect of concentration was more pronounced at a longer spinning distance and at a higher applied voltage.
2- The effect of spinning distance on MFD changed depending on solution concentration and applied voltage. At low applied voltages, MFD decreased as the spinning distance became longer, whereas higher MFD resulted in lengthening the

spinning distance when the applied voltage was high. Increasing the solution concentration tended to assist the formation of thicker fibers at a longer spinning distance.

3- Rising the applied voltage, MFD was observed to first increase and then decrease. High solution concentrations partly and long spinning distances largely favored the increase of MFD with applied voltage.

4- MFD slightly increased with flow rate. The impact of flow rate on MFD was not related to the other variables.

For StdFD:

1- The higher the solution concentration, the less uniform fibers (higher StdFD) were formed. Low applied voltages facilitated the formation of more uniform fibers (lower StdFD) on decreasing the concentration. The increase of StdFD with concentration gained momentum at high flow rates.

2- Longer spinning distance resulted in more uniform fibers (lower StdFD). The effect of spinning distance was more pronounced at higher flow rates.

3- Rising the applied voltage increased StdFD. Low concentrations facilitated the formation of uniform fibers (high StdFD) with decreasing the applied voltage.

4- Flow rate was found to have a significant impact on the uniformity of fibers (StdFD). As the flow rate increased, StdFD decreased and then increased. Higher solution concentration, higher applied voltage, and shorter spinning distance favored the formation of non-uniform fibers (high StdFD) at fast flow rates.

REFERENCES

1. G.I. Taylor, *Proceedings of the Royal Society of London*, **313**, (1515), 453, (1969)
2. J. Doshi and D.H. Reneker, *Journal of Electrostatics*, **35**, 151, (1995)
3. H. Fong and D.H. Reneker, Electrospinning and Formation of Nanofibers, Chapter 6, 225-, In: D. R. Salem, Structure Formation in Polymeric Fibers, Hanser, Cincinnati, 2001.
4. D. Li and Y. Xia, *Advanced Mats*, **16**(14), 1151, (2004)
5. R. Derch, A. Greiner and J.H. Wendorff, Polymer Nanofibers Prepared by Electrospinning, In: J. A. Schwarz, C. I. Contescu and K. Putyera, Dekker Encyclopedia of Nanoscience and Nanotechnology, CRC, New York, 2004.
6. A.K. Haghi and M. Akbari, *Physica Status Solidi* (a), **204**, 1830, (2007)
7. P.W. Gibson, H.L. Schreuder-Gibson and D. Rivin, *AIChE Journal*, **45**,(1), 190, (1999)
8. Z.M. Huang, Y.Z. Zhang, M. Kotaki and S. Ramakrishna, *Composites Science and Technology*, **63**, 2223, (2003)
9. M. Li, M.J. Mondrinos, M.R. Gandhi, F.K. Ko, A.S. Weiss and P.I. Lelkes, *Biomats,* **26**, 5999, (2005)
10. E.D. Boland, B.D. Coleman, C.P. Barnes, D.G. Simpson, G.E. Wnek and G.L. Bowlin, *Acta Biomatia*, **1**, 115, (2005)
11. J. Lannutti, D. Reneker, T. Ma, D. Tomasko and D. Farson, *Mats Science and Engineering* C, **27**, 504, (2007)
12. J. Zeng, L. Yang, Q. Liang, X. Zhang, H. Guan, C. Xu, X. Chen and X. Jing, *Journal of Controlled Release*, **105**, 43, (2005)
13. E.R. Kenawy, G.L. Bowlin, K. Mansfield, J. Layman, D.G. Simpson, E.H. Sanders and G.E. Wnek, *Journal of Controlled Release*, **81**, 57, (2002)
14. M.-S. Khil, D.-I. Cha, H.-Y. Kim, I.-S. Kim and N. Bhattarai, *Journal of Biomedical Mats Research - Part B: Applied Biomats,* **67**, 675, (2003)
15. B.M. Min, G. Lee, S.H. Kim, Y.S. Nam, T.S. Lee and W.H. Park, *Biomats,* **25**, 1289, (2004)
16. X.H. Qin and S.Y. Wang, *Journal of Applied Polymer Science*, **102**, 1285, (2006)
17. J.S. Kim and D.H. Reneker, *Polymer Engineering and Science*, **39**,(5), 849, (1999)
18. S.W. Lee, S.W. Choi, S.M. Jo, B.D. Chin, D.Y. Kim and K.Y. Lee, *Journal of Power Sources*, **163**, 41, (2006)
19. C. Kim, *Journal of Power Sources*, **142**, 382, (2005)
20. N.J. Pinto, A.T. Johnson, A.G. MacDiarmid, C.H. Mueller, N. Theofylaktos, D.C. Robinson and F.A. Miranda, *Applied Physics Letters*, **83**,(20), 4244, (2003)
21. D. Aussawasathien, J.-H. Dong and L. Dai, , *Synthetic Metals*, **54**, 37, (2005)
22. S.-Y. Jang, V. Seshadri, M.-S. Khil, A. Kumar, M. Marquez, P.T. Mather and G.A. Sotzing, *Advanced Mats,* **17**, 2177, (2005)
23. S.-H. Tan, R. Inai, M. Kotaki and R. Ramakrishna, , *Polymer*, **46**, 6128, (2005)
24. A. Ziabicki, Fundamentals of Fiber Formation: The Science of Fiber Spinning and Drawing, Wiley, New York, 1976.
25. A. Podgóski, A. Bałazy and L. Gradoń, *Chemical Engineering Science*, **61**, 6804, (2006)
26. B. Ding, M. Yamazaki and S. Shiratori, *Sensors and Actuators* B, **106**, 477, (2005)
27. J.R. Kim, S.W. Choi, S.M. Jo, W.S. Lee and B.C. Kim, *Electrochimica Acta*, **50**, 69, (2004)
28. L. Moroni, R. Licht, J. de Boer, J.R. de Wijn and C.A. van Blitterswijk, *Biomats*, **27**, 4911, (2006)
29. T. Wang and S. Kumar, *Journal of Applied Polymer Science*, **102**, 1023, (2006)

30. S. Sukigara, M. Gandhi, J. Ayutsede, M. Micklus and F. Ko, *Polymer*, **45**, 3701, (2004)

31. S.Y. Gu, J. Ren and G.J. Vancso, *European Polymer Journal*, **41**, 2559, (2005)

32. S.Y. Gu and J. Ren, *Macromolecular Mats and Engineering*, **290**, 1097, (2005)

33. O.S. Yördem, M. Papila and Y.Z. Menceloğlu, *Mats and Design*, **29**, 34, (2008)

34. I. Sakurada, Polyvinyl Alcohol Fibers, CRC, New York, 1985.

35. F.L. Marten, Vinyl Alcohol Polymers, In: H. F. Mark, Encyclopedia of Polymer Science and Technology, 3rd Eddition, vol. 8, Wiley, 2004.

36. Y.D. Kwon, S. Kavesh and D.C. Prevorsek (Allied Corporation), Method of Preparing High Strength and Modulus Polyvinyl Alcohol Fibers, U. S. Patent, no. 4,440,711, April 3, 1984.

37. S. Kavesh and D.C. Prevorsek (Allied Corporation), Producing High Tenacity, High Modulus Crystalline Article Such as Fiber or Film, U. S. Patent, no. 4,551, 296, November 5, 1985.

38. H. Tanaka, M. Suzuki and F. Uedo (Toray Industries, Inc.), Ultra-High-Tenacity Polyvinyl Alcohol Fibers and Process for Producing Same, U. S. Patent, no. 4,603,083, July 29, 1986.

39. G. Paradossi, F. Cavalieri, E. Chiessim, C. Spagnoli and M.K. Cowman, *Journal of Mats Science: Mats in Medicine*, **14**, 687, (2003)

40. G. Zheng-Qiu, X. Jiu-Mei and Z. Xiang-Hong, *Bio-Medical Mats and Engineering*, **8**, 75, (1998)

41. M. Oka, K. Ushio, P. Kumar, K. Ikeuchi, S.H. Hyon, T. Nakamura and H. Fujita, *Journal of Engineering in Medicine*, **214**, 59, (2000)

42. K. Burczak, E. Gamian and A. Kochman, *Biomats*, **17**, 2351, 1996.

43. J.K. Li, N. Wang and X.S. Wu, *Journal of Controlled Release*, **56**, 117, (1998)

44. A.S. Hoffman, *Advanced Drug Delivery Reviews*, **43**, 3, (2002)

45. J. Zeng, A. Aigner, F. Czubayko, T. Kissel, J.H. Wendorff and A. Greiner, *Biomacromolecules*, **6**, 1484, (2005)

46. K.H. Hong, *Polymer Engineering and Science*, **47**, 43, (2007)

47. L.H. Sperling, Introduction to Physical Polymer Science, 4th Edition, Wiley, New Jersey, 2006.

48. J.C.J.F. Tacx, H.M. Schoffeleers, A.G.M. Brands and L. Teuwen, *Polymer*, **41**, 947, (2000)

49. F.K. Ko, Nanofiber Technology, Chapter 19, In: Y. Gogotsi, Nanomats Handbook, CRC Press, Boca Raton, 2006.

50. A. Koski, K. Yim and S. Shivkumar, *Mats Letters*, **58**, 493, (2004)

51. D.C. Montgomery, Design and Analysis of Experiments, 5th Edition, Wiley, New York, 1997.

52. A. Dean and D. Voss, Design and Analysis of Experiments, Springer, New York, 1999.

53. G.E.P. Box and N.R. Draper, Response Surfaces, Mixtures, and Ridge Analyses, Wiley, New Jersey, 2007.

54. K.M. Carley, N.Y. Kamneva and J. Reminga, Response Surface Methodology, CASOS Technical Report, CMU-ISRI-04-136, 2004.

55. S. Weisberg, Applied Linear Regression, 3rd Edition, Wiley, New Jersey, 2005.

56. C. Zhang, X. Yuan, L. Wu, Y. Han and J. Sheng, *European Polymer Journal,* **41**, 423, (2005)

57. Q. Li, Z. Jia, Y. Yang, L. Wang and Z. Guan, Preparation and Properties of Poly(Vinyl Alcohol) Nanofibers by Electrospinning, Proceedings of IEEE International Conference on Solid Dielectrics, Winchester, U. K., July 8-13, 2007.

58. C. Mit-uppatham, M. Nithitanakul and P. Supaphol, *Macromolecular Chemistry and Physics*, **205**, 2327, (2004)

59. Y.J. Ryu, H.Y. Kim, K.H. Lee, H.C. Park and D.R. Lee, *European Polymer Journal*, **39**, 1883, (2003)

60. T. Jarusuwannapoom, W. Hongrojjanawiwat, S. Jitjaicham, L. Wannatong, M. Nithitanakul, C. Pattamaprom, P. Koombhongse, R. Rangkupan and P. Supaphol, *European Polymer Journal*, **41**, 409, (2005)

61. S.C. Baker, N. Atkin, P.A. Gunning, N. Granville, K. Wilson, D. Wilson and J. Southgate, *Biomats,* **27**, 3136, (2006)

62. S. Sukigara, M. Gandhi, J. Ayutsede, M. Micklus and F. Ko, *Polymer*, **44**, 5721, (2003)

63. X. Yuan, Y. Zhang, C. Dong and J. Sheng, *Polymer International*, **53**, 1704, (2004)

64. C.S. Ki, D.H. Baek, K.D. Gang, K.H. Lee, I.C. Um and Y.H. Park, *Polymer*, **46**, 5094, (2005)

65. J.M. Deitzel, J. Kleinmeyer, D. Harris and N.C. Beck Tan, *Polymer*, **42**, 261, (2001)

66. C.J. Buchko, L.C. Chen, Y. Shen and D.C. Martin, *Polymer*, **40**, 7397, (1999)

67. J.S. Lee, K.H. Choi, H.D. Ghim, S.S. Kim, D.H. Chun, H.Y. Kim and W.S. Lyoo1, *Journal of Applied Polymer Science*, **93**, 1638, (2004)

68. S.F. Fennessey and R.J. Farris, *Polymer*, **45**, 4217, (2004)

69. S. Kidoaki, I. K. Kwon and T. Matsuda, *Biomats*, **26**, 37, (2005)

70. X. Zong, K. Kim, D. Fang, S. Ran, B.S. Hsiao and B. Chu, *Polymer*, **43**, 4403, (2002)

71. D. Li and Y. Xia, *Nano Letters*, **3**,(4), 555, (2003)

72. W.-Z. Jin, H.-W. Duan, Y.-J. Zhang and F.-F. Li, *Proceedings of the 1st IEEE International Conference on Nano/Micro Engineered and Molecular Systems*, 42, Zhuhai, China, January 18-21, 2006.

73. X.M. Mo, C.Y. Xu, M. Kotaki and S. Ramakrishna, *Biomats*, **25**, 1883, (2004)

74. S. Zhao, X. Wu, L. Wang and Y. Huang, *Journal of Applied Polymer Science*, **91**, 242, (2004)

СИСТЕМАТИЧНО ПАРАМЕТРИЧНО ИЗСЛЕДВАНЕ НА ПОЛУЧАВАНЕТО НА НАНОВЛАКНА ЧРЕЗ ЕЛЕКТРОПРЕДЕНЕ

М. Мохамадиан[1], А.К. Хаги[2*]

[1]*Департамент по текстилно инженерство, Ислямски университет „Азад“. клон Кашан, Иран*
[2]*Университет в Гилян, Ращ, Иран*

(Резюме)

Електропреденето е процес при който се получават непрекъснати полимерни влакна с суб-микронни диаметри. При електропреденето електричеката масова сила действа върху елемент от зареден флуид. Електропреденето е специализирана техника за образуването на суб-микронни влакна (с диаметри типично между 100 nm и 1 μm) с висока специфична повърхност. Целта на тази работа е да се установят количествени зависимости между параметрите на електропредене и средните и стандартните отклонения в диаметрите на влакната, както и да се оцени ефективността на намерените емпирични модели.

New morpholine and piperazine derivatives of ketamine: synthesis and anti-nociceptive effects

A. Ahmadi* [1], M. Khalili[2], A. Asadi[1], B. Nahri-Niknafs[1]

[1]Department of Chemistry, Faculty of Science, Islamic Azad University, Karaj, Branch, Iran
[2]Department of Physiology, School of Medicine, Shahed University, Tehran, Iran.

Ketamine has widely been used as ananesthetic and analgesic in human and veterinary medicine. Although it interacts with multiple binding sites in receptors, NMDA receptor antagonism is believed to account for most of its anesthetic and analgesic effects. In this work, two new derivatives of ketamine with a substitution in methylamine group for N-amino-morpholine and N-amino-4-methyl piperazine were synthesized. Their analgesic effects were evaluated in tail immersion and formalin tests with rats and the results were compared to ketamine effects on control groups. Results indicated that the new derivatives could effectively decrease pain in tail immersion and formalin tests and their analgesic effects were more significant in the acute thermal period and in late phase II of chronic chemical pains on rats at 6 mg/kg dosage.

Keywords: Ketamine, Morpholine derivative, Piperazine derivative, Anti-nociceptive effect, Tail immersion test, Formalin test.

INTRODUCTION

Ketamine (2-o-chlorophenyl-2-methylamino-cyclohexane, **I**, Scheme 1) has widely been used as anaesthetic and analgesic in human and veterinary medicine [1]. Its chemical structure, action mechanism, and pharmacological effects are similar to those of phencyclidine (1-[1-phenylcyclohexyl] piperidine, **II**, Scheme 1), but KT is much less potent than PCP [2]. Although ketamine interacts with multiple binding sites (N-methyl-d-aspartate [NMDA], non-NMDA glutamate receptors, nicotinic and muscarinic cholinergic receptors, adrenergic and opioid receptors), it is mostly believed that NMDA receptor antagonism accounts for its anesthetic and analgesic effects. Some of ketamine analgesic effects, however, are mediated through its agonistic effects on opioid receptors within the central nervous system (CNS) and non-opioid mechanisms [3-7]. Ketamine shows anti-nociceptive effects in many analgesic standard tests, such as tail-flick test in rats, acetic acid and phenyl quinone writhing test in mice, latency increase of tail withdrawal from heat stimulus in Rhesus monkeys, formalin test in rats [8] and curing patients with neuropathic pain of various origins, such as postherpetic neuralgia, complex regional pain syndrome (CRPS), cancer pain, orofacial pain, and phantom limb pain [9, 10].
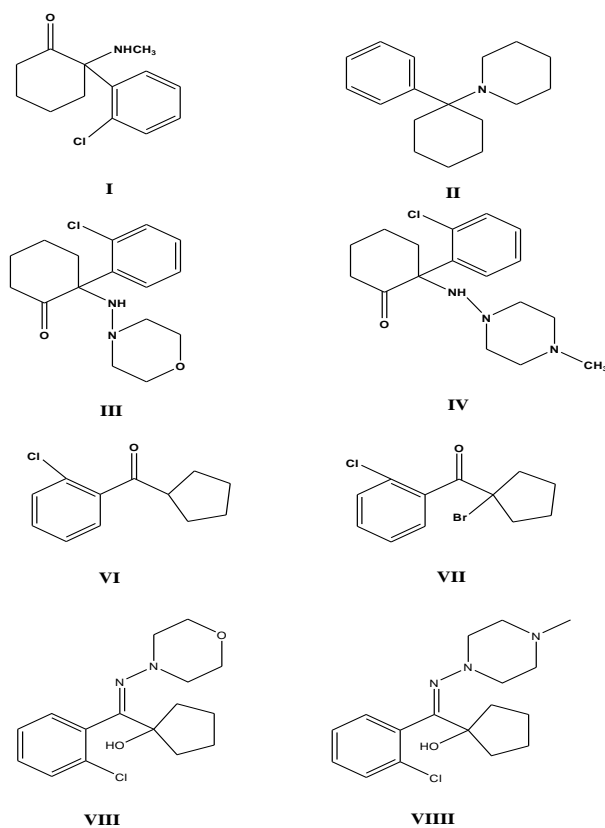
Scheme 1. Structure formulas of ketamine (**i**), phencyclidine (**ii**), ketamino-morpholine (**iii**),ketamino-piperazine (**iv**), (2-chlorophenyl)-cyclopentyl-methanone (**vi**), (1-bromocyclopentyl)-(2-chlorophenyl)-methanone (**vii**), 1-[(2-chloro-phenyl)-(morpholin-4-ylimino)-methyl]-cyclopentanol (**viii**) and 1-[(2-chloro-phenyl)-(4-methyl-piperazin-1-ylimino)-methyl]-cyclopentanol (**ix**).

* To whom all correspondence should be sent:
E-mail: ahmadikiau@yahoo.com

So far, many ketamine derivatives have been synthesized [11-16] and their pharmacological activities, such as anti-nociceptive activity [11, 17-22] have been studied. It may be concluded, therefore, that the potency of this family is directly influenced by substitutions of amine group in the ketamine molecule [11]. In this study, therefore, two new derivatives (**III** and **IV**) of **I** were synthesized with a substitution for amine group (N-amino-4-methylpiperazine and N-amino morphine instead of methylamine) in the ketamine molecule. The analgesic effects of these new compounds were evaluated in tail immersion (as a model of acute thermal pain) and formalin (as a model of acute chemical and chronic pain) tests [23-25] with experimental animals and the results were compared to ketamine (**I**) effects on control (saline) groups.

EXPERIMENTAL

General

All chemicals and reagents were purchased from Merck Chemicals Co. (Darmstadt, Germany). Melting points (uncorrected) were determined with a digital electro thermal melting point apparatus (Model 9100, Electrothermal Engineering Ltd., Essex, UK). ^{1}H and ^{13}C NMR spectra were recorded on a Bruker 300MHz (AMX model, Karlsruhe, Germany) spectrometer (internal reference: TMS). IR spectra were recorded with a Thermo Nicolet FT-IR (Nexus-870 model, Nicolet Instrument Corp, Madison, Wisconsin, U.S.A.) spectrophotometer. Mass spectra were recorded with an Agilent Technologies spectrometer (Wilmington, USA) with 5973 mass selective detector (MSD). Elemental analyses were carried out using a Perkin-Elmer, CHN element analyzer model 2400 and were within ± 0.4% of the theoretical values. Column chromatographic separations were performed over Acros silica gel (No.7631-86-9 particle size 35-70 micrometer, Geel, Belgium).

Preparations (Scheme 2)

Cyclopentyl magnesium bromide, V

This compound was prepared from cyclopentyl bromide and magnesium in diethyl ether as a pale green solution following a published method [26].

(2-Chlorophenyl)-cyclopentyl-methanone, VI

This compound was prepared from cyclopentyl magnesium bromide (**V**) and 2-chloro-benzonitrile as pale brown oil according to a known procedure [16].

(1-Bromocyclopentyl) - (2-chlorophenyl)-methanone, VII

This compound was prepared from **VI** and bromine in carbon tetrachloride at 0 °C as brown oil following a published method [16].

2-(2-Chlorophenyl)-2-(morpholin-4-ylamino)-cyclohexanone, III

A benzene (20 ml) solution of bromoketone (**VII**, 5.4 g, 0.019 mol) was added to a benzene (10 ml) solution of N-aminomorpholine (2 g, 0.019 mol) and the mixture was stirred in room temperature for 7 days. Next, N-pentane was added and the mixture was filtered, evaporated and concentrated under reduced pressure to obtain a brown oily hydroxyimine compound (1-[(2-chloro-phenyl)-(morpholin-4-ylimino)-methyl]-cyclopentanol, **VIII**) that was used in the next step without further purification. A decaline (15 ml) solution of this compound was refluxed for 4.5 hours at 190 °C. The solvent was evaporated under reduced pressure. The mixture was extracted with diethyl ether, re-extracted with 10% HCl, neutralized with 10% NaOH and n-hexane, dried over MgSO$_4$, and evaporated under vacuum to obtain the desired oily residue which was passed through a silica gel column with ethyl acetate-hexane as the eluent to afford 1.18 g of **III** as brown oil (49 % yield). The hydrochloride salt of **III** (m.p.127˚C, red-brownish solid) was prepared with 2-propanol and HCl, and re-crystallized from 2-propanol.

IR (KBr): 3367, 2956, 2869, 1614, 1502, 1434, 1305, 1267, 1108, 761 cm^{-1}. ^{1}H-NMR (CDCl$_3$) (ppm):1.49-4.67 (16H, m), 7.07-7.74 (4H, m). ^{13}C{^{1}H}-NMR (CDCl$_3$) (ppm): 24.4, 25.4, 32.2, 38.1, 57.5, 63.3, 69.3, 128.1, 129.6, 130.9, 133.5, 135.6, 137.4, 212.3. Anal. Calcd. for C$_{16}$H$_{21}$ClN$_2$O$_2$: C, 62.23%; H, 6.85%; N, 9.07%. Found: C, 62.33%; H, 6.91%; N, 9.01%. MS: m/z (Regulatory Intensity):86 (37), 100 (100), 113 (61), 197 (19), 207 (42), 211(31), 222 (20), 257 (13), 273 (26), 292 (18), 309 (14).

2-(2-Chlorophenyl)-2-(4-methylpiperazin-1-ylamino)-cyclohexanone, IV

To a benzene (20 ml) solution of bromoketone (**VII**, 5.4 g, 0.019 mol), a benzene (10 ml) solution of N-amino-4-methylpiperazine (2.2 g, 0.019 mol) was added, then the mixture was stirred at room temperature for 7 days. n-Pentane was added to the mixture which was filtered, evaporated and concentrated under reduced pressure to obtain a brown oily hydroxyimine compound (1-[(2-chloro-phenyl)-(4-methylpiperazin-1-ylimino)-methyl]-cyclopentanol, **IX**) that was used in the next step without further purification. A decaline (20 ml)

solution of the compound was refluxed for 3.5 hours at 190 °C. The solvent was evaporated under reduced pressure and the mixture was extracted with diethyl ether, re-extracted with 10% HCl, neutralized with 10% NaOH and n-hexane, dried over $MgSO_4$ and evaporated under vacuum to obtain the desired oily residue which was passed through a silica gel column using ethylacetate-hexane as the eluent to afford 1.56 g of **IV** as a brown oil (52% yield). The hydrochloride salt of **IV** (m.p.141°C, red-brownish solid) was prepared using 2-propanol and HCl, and re-crystallized from 2-propanol.

IR (KBr): 3411, 2952, 1613, 1503, 1454, 1313, 1041, 763, 746 cm^{-1}. ^{1}H-NMR (CDCl$_3$) (ppm): 1.52-4.67 (19H, m), 7.01-7.95 (4H, m).^{13}C{^{1}H}-NMR (CDCl$_3$) (ppm):21.1, 25.2, 32.1, 37.8, 40.8, 49.1, 52.4, 67.6, 121.7, 124.5, 127.2, 129.8, 133.4, 140.6, 212.4. Anal. Calcd. for $C_{17}H_{24}ClN_3O$: C, 63.44%; H, 7.52%; N, 13.06%. Found: C, 63.39%; H, 7.55%; N, 13.09%. MS: m/z (Regulatory Intensity): 81 (45), 84 (28), 96 (56), 98 (100), 111 (27), 115 (25), 206 (23), 210 (18), 306 (14), 321 (8).
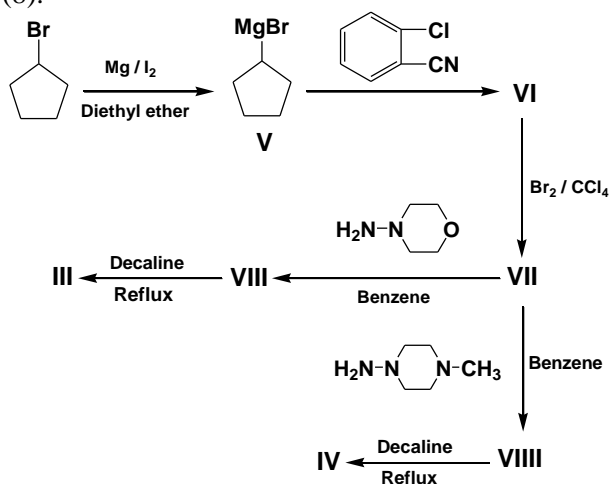
Scheme 2. Synthesis of intermediates (**V**-IX) and final compounds (**III** and **IV**).

Pharmacological Methods

Animals

Sixteen adult female wistar rats (Pasteur's Institute, Tehran, Iran), weighing 100-220 g, were randomly housed in four groups of four per cage in a temperature controlled colony room under light/dark cycles. Rats were given free access to water and standard laboratory rat chow (supplied by Pars Company, Tehran, Iran). All behavioral experiments were carried out from 11 a.m. to 4 p.m. under normal room light and at 25°C temperature. All animals were injected by a researcher, and evaluated by another. This study was carried out according to the Guides for the "Care and Use of Laboratory Animals" (NIH) and those at the "Research Council of Shahed University of Medical Sciences, Tehran, Iran".

Tail Immersion Test

The acute thermal pain was modeled in the tail immersion test [23, 24].Twenty minutes after intra peritoneal injection of drugs in the treatment group (ketamine and its analogues, 6 mg/kg), and an equivalent volume of saline (in the control group), the rats were housed in an animal restrainer. Then, the terminal 5 cm of their tails was first submerged into room temperature water (22~24 °C) to check their aversion to water and then immersed in 52 °C water. The reaction time between immersing the tail and its removal from the heated water was measured and recorded as the pain threshold. Cut-off latency in 15 sec was employed to avoid damaging the tail.

Formalin Test

The formalin test was introduced by Dubuisson and Dennis (1977). In this test, the formaldehyde solution (50 μl, 2.5%) was subcutaneously injected into the plantar surface of the hind paw. Then, the animals were placed in a Plexiglas chamber (30×30×30 cm^3) mirrored at 45° angle underneath for accurate observations. In treatment groups, the drugs (ketamine and its analogues) and in control ones an equivalent volume of saline was intraperitoneally injected 30 min prior to the formaldehyde injection. Before the experiments, all animals were brought to the test chamber five times at five-minute-intervals in order to adapt them to the environment. The behavioral pain reactions after formalin injection were detected and recorded for 1 hour. The scores for pain reaction were as follows: 0, normal weight bearing on the injected paw; 1, limping during locomotion or resting the paw lightly on the floor; 2, elevation of the injected paw; 3, licking or biting of the injected paw, or grooming [25]. Behavioral responses have been observed every 15 seconds. The average pain scores from every 3 minutes block were compared with each other in different groups. The rats were not tested more than once and experiments were carried out between 09:00 and 15:00. The first 15 minutes after formalin injection were labeled as the early (I) or Acute Phase, and the period between 15-60 minutes as the second (II) or Chronic Phase. Chronic Phase was divided into initial (15-40 min) and late (40-60 min) periods.

Experimental psychomotor coordination (PMC) index

This test was done by Rota-rod Treadmill with a shock facility apparatus (Harvard model 865) after

root or new drugs administration. First, animals were trained by their placing on the rolling bar and had been led to walk on it. Then, for 5 times, they were placed in a case with these characteristics: initial speed = 4 rpm, final speed = 30 rpm, initial to final speed time = 4 min, shock intensity = 1.1 mA, shock duration = 0.2-0.8 sec, experimental length time = 5 min, interval between experiments = 2 min. The mean stay time on the rod per trial was taken as a PMC index.

Statistical analysis

Sigmastat 3.5 software was used for statistical analysis. The measured data were presented as means ± S.E.M. Comparisons were carried out as one way analysis of variance (ANOVA) followed by post-hoc Tukey test with a p-value < 0.05 level of significance.

RESULTS
Chemistry

Ketamine (**I**) and its newly synthesized derivatives (**III** and **IV**) were synthesized by reaction of bromoketone (**VII**) with pharmacological amines (methyl amine, N-amino-4-methylpiperazine and N-amino-morpholine).These amines are widely used as intermediates in the synthesis of many drugs [27-30]. The process of this synthesis method involves a thermal rearrangement of the carbon skeleton of cyclopentyl α-hydroxyimines (**VIII** and **IX**) to cyclohexanone amines (**III** and **IV**) in a hydrocarbon solvent (decalin). As it can be seen, this skeletal rearrangement can result in ring expansion of α-hydroxyimines producing larger size of the rings [16].

The known procedures were applied to synthesize the compounds **V**-**VII** [16, 26]. The structures of the newly synthesized compounds (**III** and **IV**) were confirmed on the basis of spectroscopic data IR, ^{1}H-NMR, ^{13}C-NMR, mass spectra and elemental analysis. The purity of each compound was checked by TLC using ethyl acetate-hexane as the eluent.

Pharmacology

General Considerations

Mortality (number of deaths), morbidity (abnormal condition or behavior due to a disorder), irritability (condition of aggressiveness or increased response on handling) and other related abnormal states were observed in the treated animals. The motor coordination index (measured on a Rota-rod apparatus, Harvard, UK) did not indicate any significant differences between control and treated rats.

Anti-nociceptive activity of the compounds in tail immersion test

Intraperitoneal injection of ketamine (**I**) in a dosage of 6 mg/kg generated analgesic affects in the tail immersion test (as a model of acute thermal pain) (Figure 1). However, application of its two newly synthesized derivatives (**III** and **IV**) hydrochlorides at a 6 mg/kg dosage could produce no identical analgesic effects in the tail immersion test. Although, mild prominent analgesia was observed at 30-40 min after new drugs (especially piperazine derivative) administration.
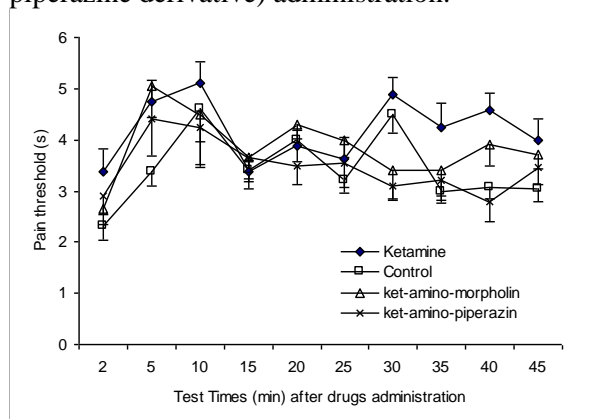
Fig.1. Mean tail immersion latency (s) in animals receiving ketamine (**I**), ketamino-morpholine (**III**) and ketamino-piperazine (**IV**) hydrochloride or saline (control) in doses of 6 mg/kg. The tail immersion test was conducted 20 minutes after the drug injection. Each point represents the mean ± S.E.M. of tail immersion latency (s) in 8 animals. Statistical analysis was done by analysis of variance (ANOVA) test followed by Tukey post-hoc test. p-value < 0.05 was considered as the level of significance.

Anti-nociceptive activity of the compounds in formalin test

The drugs (**I, III** and **IV**) were intraperitoneally injected in a dosage of 6 mg/kg, 30 minutes before formaldehyde injection. Results showed that all compounds significantly decreased the acute and chronic formalin chemical pains (Figure 2) comparing to the control group. However, chronic formalin pain (phase I and II) could significantly attenuate with compounds **III** and **IV** comparing to other groups (**I** and control) in the late second phase.

PMC index in control and treated animals

Figure 3 shows the results of the psychomotor coordination test by Rota-rod treadmill apparatus. The mean PMC indices of experiments for control, ketamine, ketamino-morpholine and ketamino-piperazine animal groups were obtained, 148 ± 20.57, 144 ± 19.29, 163 ± 21.71 and 118 ± 17.56, respectively. However, statistical analysis
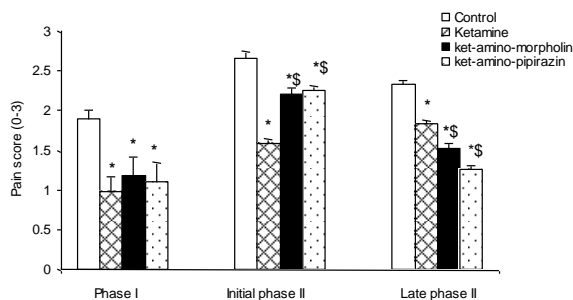
Fig. 2. Comparison between the acute and chronic formalin pains in ketamine (**I**), ketamino-morpholine (**III**), ketamino-piperazine (**IV**) hydrochloride or saline (control) in doses of 6 mg/kg. Data show the mean ± S.E.M of pain score. *n* = 8, * p<0.05, when compared with control and $, p < 0.05 when compared with ketamine group. Analysis of variance (ANOVA) test followed by Tukey post-hoc test and p-value < 0.05 was considered for data analysis.

shows no significant difference between mean of PMC in control and treated animals. Regarding the inflammatory origins for phase II of formalin pain, through release of the local mediators like prostaglandins, kinnins, interleukins, substance p and potassium [31], it can be concluded that these new drugs may have a modulatory effect on the mentioned inflammatory mediators.
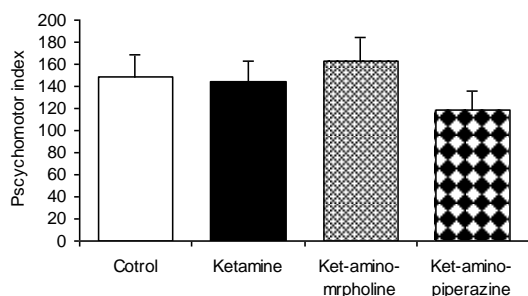
Fig. 3. Comparison effect of motor coordination system between control and treated animals. Bars show the mean ± SEM psychomotor index in the experimental animals. n = 8, each group. Analysis of variance (ANOVA) test followed by post-hoc Tukey test was considered for data analysis. p-value < 0.05 was used for significant comparison.

4. DISCUSSION

Ketamine as an NMDA receptor antagonist in high and low doses, respectively, could yield anesthetic and analgesic properties [32]. The use of ketamine as an analgesic is now generally accepted, however, the evidence base remains poor. Little formal research has been done on the efficacy and safety of ketamine in chronic pain management, especially in long-term oral administration [32]. Because the potency of this family was influenced by substitution on the amine group in the KT molecule [11], two amines with many pharmacological properties (N-amino-4-methylpiperazine and N-amino-morpholine) and intermediates for the synthesis of many drugs [27-30] were substituted on this site of the molecule for obtaining the new ketamine derivatives (**III** and **IV**). Results indicated that these new derivatives (**III** and **IV**) of KT (**I**) could be more effective in decreasing pain, comparing to the control group in formalin chemical pain and especially in the late chronic phase. However, these analgesic effects were not always significant in acute thermal pain (tail immersion test). Nevertheless, the neurological origins especially through the central nervous system were introduced as the main mechanism(s) for acute (thermal or chemical) pain conducting [33]. With respect to the non-significant differences between ketamine and the two new derivatives on acute analgesic potency, it can be concluded that adding morpholine and piperazine to ketamine drug does not change the efficiency of ketamine neurological pain modulation reactions. Unlikely, new drugs' significant chronic anti-nociceptive effects could be resulting from more antagonizing production of inflammatory mediators like kinnins, interleukins, substance p and potassium. Therefore, peripheral inflammatory mediator enhancement following the acute phase is the main mechanism for chronic chemical pain [34]. Although it seems that replacing methylamine (in KT) by N-amino-morpholine (in **III**) and N-amino-4-methylpiperazine (in **IV**) could be as effective as ketamine in producing new analgesic drugs, they could not be more effective than **I** in most cases. However, stronger analgesic effects in acute thermal (in a shorter time) and chronic chemical pains of the morpholine derivative (ketamino-morpholine, **III**) comparing to the piperazine one (ketamino-piperazine, **IV**) were observed due to the stronger pharmacological properties of morpholine [35-37]. These effects were weaker than the ketamine analgesic effects mostly in acute thermal (in tail immersion test) and in acute chemical and initial phase of chronic (in formalin test) pains. From pharmacokinetic point of view, more antagonizing functions displayed by these new drugs (**III** and **IV**) on the NMDA receptor might underlie their more anti-nociceptive activities compared to the control group. Also, a methyl group on the amine moiety of KT had a more effective role in decreasing pain comparing to morpholine and piperazine groups, which might account for a high electron distribution and dipole moments by this group [38]. Moreover, it indicated stronger anti-nociceptive effects produced by some analgesic drugs [39-41] compared to other new amine groups.

5. CONCLUSION

It was concluded that swapping methylamine (in ketamine, **I**) with N-aminomorpholine (in ketamino-morpholine, **III**) and N-amino-4-methylpiperazine (in ketamino-piperazine, **IV**) could generate analgesic effects in tail immersion and formalin tests comparing to the control group (in most of cases) where ketamine was injected in rats at a 6 mg/kg dosage.

REFERENCES

1. E.F. Domino, P. Chodoff, G. Corssen, *Clin. Pharmacol. Ther.*, **6**, 279 (1965)
2. K. Eun-mi, L. Ju-seon, C. Sang-kil, L. Mi-ae, C. Hee-sun, *Forensic Sci. Inter.*, **174**, 197 (2008)
3. S. Kathirvel, S. Balachundhar, A.S. Richard, *Anesth. Analg.*, **99**, 482 (2004)
4. C.J. Murdoch, B.A. Crooks, C.D. Miller, *Anaesthesia*, **57**, 484 (2002)
5. S. Elise, J.T. Luc, O. Cees, N. Diederik, W.D.M. Hans, L.K. Brigitte, D. Albert, *Anesth. Analg.*, **93**,1495 (2001).
6. G. Joó, G. Horvath, W. Klimscha, G. Kekesi, I. Dobos, M. Szikszay, G. Benedek, *Anaesthesiology*, **93**, 231 (2000)
7. I. Kissin, C.A. Bright, E.L.Jr. Bradley, *Anesth. Analg.*, **91**,1483 (2000)
8. I.O. Lee, I.H. Lee, *Acta Anaesthesiol. Sin.*, **39**, 123 (2001)
9. M.I. Blonk, B.G. Koder, V.D. Bemt Pmla, F.J. Huygen, *Eur. J. Pain,* **14**, 466 (2010)
10. M. Shimoyama, N. Shimoyama, A.L. Gorman, K.J. Elliott, C.E. Inturrisi, *Pain*, **81**, 85 (1999)
11. A. Ahmadi, M. Khalili, R. Hajikhani, H. Hosseini, N. Afshin, B. Nahri-Niknafs, *Med Chem.*, **8**, 246 (2012)
12. R. Yokoyama, S. Matsumoto, S. Nomura, *Tetrahedron*, **65**, 5181 (2009)
13. C.Y. Shiue, A.P.S. Vallabhahosula, *Nuc. Med. & Bio.*, **24**, 145 (1997)
14. D.J. Yang, N. Davisson, *J. Med. Chem.*, **28**, 1361 (1985)
15. T. Woolf, A. Trevor, T. Baillie, *J. Org. Chem.*, **49**, 3305 (1984)
16. C.L. Stevens, A. Thuillier, K.G. Taylor, *J. Org. Chem.*, **31**, 2601 (1966)
17. M.K. Boettger, K. Weber, M. Gajda, *Brain Behav. Immun.*, **24**, 474 (2010)
18. M. Yamauchi, M. Asano, *Inter. Anesth. Res. Soc.*, **107**, 1041 (2008)
19. E. Sarton, L.J. Teppema, C. Olievier, *Anesth. Analg.*, **93**, 1495 (2001)
20. L.C. Mathisen, P. Skjelbred, L.A. Skoglund, Pain, **61**, 215 (1995)
21. J.A. Celements, W.S. Nimmo, I.S. *J. Pharmaceutical Sci.*, **71**, 539 (1982)
22. M.S. Sadove, M. Shulman, S. Hatano, *Anesth. Analg.*, **50**, 452 (1971)
23. S.S.V. Padi, S.K. Kulkarni, *Eur. J. Pharmacol.* **601**, 79 (2008)
24. H. Hamura, M. Yoshida, K. Shimizu, *Jpn. J. Pharmacol.* **83**(4), 286 (2000)
25. D. Dubuisson, S.G. Dennis, *Pain*, **4**, 161 (1977)
26. D. Curtinz, S. Schmuklerz, *J. Am. Chem. Soc.,* **77**, 1105 (1955)
27. Sh. R. Pattan, V.P. Rasal, N.V.V. Venkatramana, *In. J. Chem.*, **46B**, 698 (2007)
28. P.M. Kushakova, A.N. Chernobroviy, V.A. Kuznetsov, A.V. Garabadgiu, *Chem. Het. Compounds*, **40**, 1546 (2004)
29. M.G. Vigorita, T. Previtera, C. Zappalà, A. Trovato, M.T. Monforte, R. Barbera, F. Pizzimenti, *Farmaco*, **45**, 223 (1990)
30. V.H. Audia, D.W. McPherson, M. Weitzberg, W. JanuszRzeszotarski, B. Sturm, J.F. Kachur, M. Abreu, C. Kaiser, *J. Med. Chem.,* **33**, 307 (1990)
31. S. Hunskaar, K. Hole, *Pain,* 30, 103 (1987)
32. A. Orser, P.S. Pennefather, J.F. Macdonald, *Anesthesiology,* **86**, 903 (1997)
33. S. Alshahrani, F. Fernandez-Conti, A. Araujo, M. DiFulvio, *J. Vis. Exp.,* **17**, 3785 (2012)
34. Y. Xu, H.Q. Qiu, H. Liu, M. Liu, Z.Y. Huang, J. Yang, Y.P. Su, C.X. Yu,. *Pharmacol. Biochem. Behav.,* **101**, 504 (2012)
35. E. Rekka, S. Retsas, V.J. Demopoulos, P.N. Kourounakis, *Arch. Pharm. (Weinheim),* **323**, 53 (1990)
36. D.M. Chen, K. Chen, H. Wang, *Yao Xue Xue Bao*, **38**, 641 (2003)
37. K. Kaneyoshi, D. Takayuki, Y. Mitsuo, *European Patent*, EP0610793 (1994)
38. P.Y. Johnson, R. Pan, W.J. Quan, C.J. Halfman, *J. Org. Chem.,* **46**, 2049 (1981)
39. A. Ahmadi, M. Khalili, R. Hajikhani, M. Naserbakht, *Arzneimittelforschung,* **61**, 1 (2011)
40. A. Ahmadi, M. Khalili, F. Mihandoust, L. Barghi, *Arzneimittelforschung,* **60**, 30 (2010)
41. A. Ahmadi, M. Khalili, S. Abbassi, M. Javadi, A. Mahmoudi, R. Hajikhani, *Arzneimittelforschung,* **59**, 202 (2009)

Нови производни на кетамина с морфолин и пиперазин: синтези и анти-ноциセптивен ефект

А. Ахмади*[1], М. Халили[2], А. Асади[1], Б. Нахри-Никнафс[1]

[1]*Департамент по химия, Научен факултет, Ислямски университет „Азад", клон Карадж, Иран*
[2]*Департамент по физиология, Училище по медицина, Университет Шахед, Техеран, Иран*

Кетаминът е широко използван като упойка или аналгетик в хуманната и ветеринарна медицина. Въпреки че взаимодейства с множествените свързващи центрове на рецепторите се смята, че NMDA- рецепторен антагонизъм е отговорен за повечето анестетични и аналгетични ефекти. В настоящата работа са синтезирани две нови производни на кетамина чрез заместване в метиламиновата група с N-амино-морфолин или N-амино-4-метил-пиперазин. Оценен е тяхният аналгетичен ефект Their analgesic effects were evaluated върху плъхове и резултатите са сравнени с ефекта на кетамина при контролна група. Резултатите показват, че новите производни могат ефикасно да намалят болката, а техният аналгетичен ефект в доза 6 mg/kg е по-значим в акутния термичен период и в късната фаза II на хронични болки при плъхове.

Multitemperature fitting of isotherms as a simple method of insight into the thermodynamics of water sorption on building materials

S. Furmaniak

Physicochemistry of Carbon Materials Research Group, Department of Chemistry, Nicolaus Copernicus University, Poland

Water sorption on some building materials is studied. Based on three sets of experimental data, the usefulness of the generalised D'Arcy and Watt (GDW) model for simultaneous multitemperature fitting of isotherms is confirmed. The multitemperature data description not only reduces the number of best-fit parameters, but also makes it possible to analyse the thermodynamics of the process in a simple way. The values of the best-fit parameters are used for calculation of the isosteric enthalpy of sorption (representing the energetics of the process) and the entropy of the sorbed phase (which is connected with the degree of order/disorder). In the case of the studied samples of building materials, sorbed water at initial stages has low entropy and high degree of order. It probably forms a solid-like phase. For higher loadings the behavior of sorbed water is close to that of aliquid.

INTRODUCTION

Water sorption and desorption on building materials is still a subject of interest to different researchers [1-9]. Moisture is one of the most deteriorating factors of buildings. Moisture also affects many important properties of materials like thermal conductivity. Most building materials are hygroscopic, which means that they absorb water from the environment or desorb water to the environment until equilibrium conditions are reached [10]. Various mathematical models are used to describe sorption - desorption isotherms of water on building materials [8-12]. Sorption isotherms for different materials are usually described separately for each temperature value even if they are measured at different temperatures. It is also possible to describe isotherms for different temperatures simultaneously. The latter procedure (called multitemperature fitting) is often used in practice (see for example [10,13-16]) because it reduces the number of best-fit parameters. Multitemperature data description needs definition of the temperature dependence of the parameters for the sorption isotherm equation. Therefore, the models with strong thermodynamic bases should be favored [14,17]. However, very often, empirical relations are proposed [10,13,16,18] but this does not guarantee thermodynamic correctness. Researchers applying the multitemperature

isotherms fitting usually do not utilize the additional possibility given by this procedure enabling calculation of the isosteric enthalpy of sorption without the need to generate isosteres [17, 18]. The isosteric enthalpy of sorption is related to the energetic state of a sorbed molecule and may be interpreted as the energy released during the sorption of one mole of water (at constant loading) or the energy required for desorption of one mol of water. So the multitemperature isotherms description may be regarded as a simple method of insight into the energetics and thermodynamics of the water sorption process.

The major aim of this communication is to check the applicability of the generalised D'Arcy and Watt model (GDW) [19] to simultaneous multitemperature description of water sorption isotherms on a few building materials. The obtained values of the best-fit parameters are applied for calculating the isosteric enthalpy of sorption. The differences in entropy between sorbed and bulk water molecules are also calculated, basing on fundamental thermodynamic relations. Finally, the mechanism of water sorption and the thermodynamics of the process are discussed.

MATHEMATICAL MODEL

The GDW model assumes a two-step mechanism of a sorption process [19]. At the first step, water molecules are bound by primary sorption sites. Each of these sites can bind only one molecule. The concentration of these sites depends on the nature of the sorbent surface. Water

---

* To whom all correspondence should be sent:
E-mail: sf@chem.umk.pl

molecules bound on the primary centres become secondary sites and are thus able to sorb subsequent molecules. One molecule sorbed on the primary centre may create one secondary site as it is assumed in the Brunauer-Emmett-Teller (BET) [20] or the Guggenheim-Anderson-de Boer (GAB) model [21-23] but the GDW model is an approach that allows assuming any ratio of sorption on the primary and secondary centres [12]. This gives possibility for a better description of real sorption isotherms. In this case, the ratio of sorption on the secondary and primary sites is usually different from unity [24,25]. The mathematical representation of the GDW model is [26]:

$$M = \frac{m_0 K a_w}{1 + K a_w} \times \frac{1 - k(1 - w)a_w}{1 - k a_w} \qquad (1)$$

where M is the equilibrium moisture content, a_w is the water activity (i.e. the ratio of the equilibrium vapor pressure to the saturated vapor pressure at a given temperature), m_0 is the concentration of the primary sorption sites (this parameter may be also interpreted as the monolayer capacity), K and k are the kinetic constants connected with sorption on the primary and secondary centres, and w is the parameter determining the ratio of molecules bound to the primary centres and converted into secondary ones.

It is worth noting that the GDW model was previously successfully used for fitting water sorption isotherms on different sorbents [16,26-31], including building materials [9,12].

As mentioned above, the multitemperature fitting of sorption isotherms needs definition of the temperature dependence of the model parameters. In the case of the GDW model, the monolayer capacity (m_0) and the w parameter are temperature independent [17]. The kinetic parameters (K and k) depend on temperature according to the basic thermodynamic formulas [17]:

$$K = K_0 \exp\left[\frac{Q}{RT}\right] \qquad (2)$$

$$k = k_0 \exp\left[\frac{q}{RT}\right] \qquad (3)$$

where K_0 and k_0 are almost temperature independent pre-exponential factors, Q and q are the enthalpies of sorption on primary and secondary sites, respectively, and R is the universal gas constant.

The isosteric enthalpy of sorption connected with the GDW model is defined by the equation [32]:

$$q^{st} - L = \frac{\dfrac{K}{(1+Ka_w)^2} \times \left(1 + \dfrac{wka_w}{1 - ka_w}\right) \times Q + \dfrac{Ka_w}{1+Ka_w} \times \dfrac{wk}{(1-ka_w)^2} \times q}{\dfrac{K}{(1+Ka_w)^2} \times \left(1 + \dfrac{wka_w}{1 - ka_w}\right) + \dfrac{Ka_w}{1+Ka_w} \times \dfrac{wk}{(1-ka_w)^2}}$$

$$(4)$$

where L is the enthalpy of water condensation.

THERMODYNAMICS OF SORPTION

It is well known that the difference in Gibbs free energy between sorbed water and bulk gaseous water is given by the basic thermodynamic equation [33]:

$$\Delta G = RT \ln a_w \qquad (5)$$

On the other hand, there are two factors whose balance determines the changes in free energy: enthalpy (ΔH) and entropy (ΔS):

$$\Delta G = \Delta H - T\Delta S \qquad (6)$$

The difference in enthalpy between sorbed and bulk phases is related to the isosteric enthalpy of sorption/desorption:

$$\Delta H = -q^{st} \qquad (7)$$

The negative sign is a consequence of the signing convention. Combining of Eqns. (5)-(7) allows calculating the difference in entropy between water sorbed in a building material and bulk water:

$$\Delta S = -\frac{q^{st}}{T} - R \ln a_w \qquad (8)$$

EXPERIMENTAL DATA AND THEIR FITTING

Three sets of desorption isotherms (measured at different temperatures) taken from the literature are used. These isotherms are for: (a) concrete (at T = 293, 318, 330.5 and 343 K) taken from [11,34], (b) brick (at T = 288, 298 and 308 K) taken from [10], and (c) plaster (at T = 288, 298 and 308 K) taken from [10].

Experimental data sets were fitted by the GDW model (Eqns. (1)-(3)) using the genetic algorithm proposed by Storn and Price [35], which was previously successfully applied for the description of different experimental data – see for example [19,26]. The applied fitting procedure was described previously [32]. m_0, K_0 (formally log K_0), k_0 (formally log k_0), Q, q, and w are the best-fit parameters. The goodness of fit for isotherms at each temperature is estimated using the determination coefficient defined as:

$$DC_T = 1 - \eta_T \qquad (9)$$

where

$$\eta_T = \frac{\sum_i \left(M_{t,i} - M_{o,i} \right)^2}{\sum_i \left(M_{o,i} - \overline{M}_o \right)^2} \qquad (10)$$

$M_{o,i}$ and $M_{t,i}$ are the observed and the theoretically calculated moisture contents for the i-th experimental point and $\overline{M}_o$ is the average observed moisture content. The global parameter defining the quality of the fit for the bunch of isotherms is defined as:

$$DC = 1 - \sqrt{\frac{\sum_T \eta_T^2}{NT}} \qquad (11)$$

where NT is the number of considered temperatures.

RESULTS AND DISCUSSION

Table 1 collects the values of the best-fit parameters obtained from the multitemperature description of the considered data sets by the GDW model (Eqns. (1)-(3)).

Additionally, Fig. 1 shows the graphical representation of the obtained results. Generally, the fit quality is very good, as proven by the high values of the determination coefficients. This confirms the usefulness of the GDW model for the simultaneous multitemperature description of water sorption on building materials.

The obtained values of the best-fit parameters give some insight into the mechanism of the sorption process. The obtained monolayer capacities (m_0) correspond to the values which may be estimated directly from the isotherms plots. One can also see that the values of enthalpy connected with sorption on the primary sites (Q) are high, while those connected with the secondary sites (q) are close to zero. The high values of Q confirm the hydrophilic character of the considered materials, i.e. the high energy of interaction between water

molecules and their surface. On the other hand, if water molecules are sorbed on the second and higher layers, the H_2O–H_2O interactions are of major importance. Thus, the values of q are close to zero (formally, enthalpies in Eqns. (2) and (3) are not absolute values, but they are reduced by the enthalpy of water condensation). It is also interesting that the values of the w parameter for all studied samples are lower than 1. This means that not all water molecules sorbed on the primary centres convert into secondary ones. The reason may be steric effects (see Fig. 2 in [17]). Fig. 2 presents the plots of isosteric enthalpy of sorption and of the differences in entropy between sorbed and bulk water. They were calculated on the basis of the obtained values of the best-fit parameters (Table 1) and Eqns. (4) and (8). One can see that the shape of the plots is qualitatively similar for all the samples. The behavior of the isosteric enthalpy of sorption reflects the differences in energetics of sorption on the primary and secondary sites. The q^{st} has high values for small loadings ($M < m_0$) and it decreases as the monolayer is filled, reaching values close to the enthalpy of condensation for the multilayer sorption ($M > m_0$). The highest enthalpy of sorption on the primary centres is observed for the plaster. This is connected with the most pronounced temperature dependence of isotherms for this material (one can wrongly conclude that the influence of temperature is higher for concrete, but the observed changes are caused by the higher differences in temperature).

On the other hand, the shapes of the entropic plots reflect the changes in the degree of order of the sorbed phase. The decrease in entropy of sorbed water in comparison to the gas phase is the highest for small loadings (below monolayer filling). For higher loadings (multilayer sorption) the entropy increases and reaches similar values for all samples

Table 1 Values of the best-fit parameters obtained from the fitting of the studied experimental data by the GDW model (Eqns. (1)-(3)).

Sample	m_0 [%]	K_0	k_0	Q [kJ/mol]	q [kJ/mol]	w	DC_T [*]	DC
Concrete	2.32	2.73×10^{-6}	0.696	37.2	~0	0.536	0.973 0.986 0.973 0.976	0.977
Brick	0.366	1.17×10^{-6}	0.463	36.9	1.84	0.464	0.995 0.996 0.997	0.996
Plaster	1.01	6.97×10^{-14}	0.223	81.1	3.37	0.484	0.980 0.984 0.975	0.979

[*] – the values are arranged according to the rise in temperature

($\Delta S \approx -150$ J/mol/K). The difference in standard entropy between liquid water and water vapour is equal to -119 J/mol/K [36]. Thus, the obtained results suggest that water sorbed in the multilayer has a slightly higher degree of order than liquid water. In the case of water bound in the monolayer, its entropy is lower. This suggests a high order of the initially sorbed molecules. The high energy of interaction with the surface and the loss of degrees

of freedom may suggest formation of quasi-solid state of water sorbed in the monolayer.

the sorbed phase. The decrease in entropy of sorbed water in comparison to the gas phase is the highest for small loadings (below monolayer filling). For higher loadings (multilayer sorption) the entropy increases and reaches similar values for all samples ($\Delta S \approx -150$ J/mol/K). The difference in standard entropy between liquid water and water vapour is equal to -119 J/mol/K [36]. Thus, the obtained results suggest that water sorbed in the multilayer has a slightly higher degree of order than liquid water. In the case of water bound in the monolayer, its entropy is lower. This suggests a high order of the initially sorbed molecules. The high energy of interaction with the surface and the loss of degrees of freedom may suggest formation of quasi-solid state of water sorbed in the monolayer.

CONCLUSIONS

The presented results confirm the usefulness of the GDW model for simultaneous multitemperature description of water sorption isotherms on building materials. The multitemperature fitting not only reduces the number of best-fit parameters, but it also makes it possible to analyse the thermodynamics of the process in a simple way. The obtained values of the best-fit parameters allow calculating the isosteric enthalpy of sorption (representing the energetics of the process) and the entropy of the sorbed phase (connected with a degree of order). In the case of the considered samples of building materials, similar qualitative behavior is observed. Sorption of water at low activities takes place on high-energetic surface sites and the enthalpy is high. Initially bound H_2O molecules exhibit a high, even solid-like degree of order. In the next stages, molecules are mainly sorbed due to H_2O–H_2O interactions. Thus, the enthalpy of sorption reaches values close to the enthalpy of water condensation. Entropy of H_2O bound in the multilayer is close to the entropy of liquid water, so the packing of these molecules is similar to that of the liquid phase.
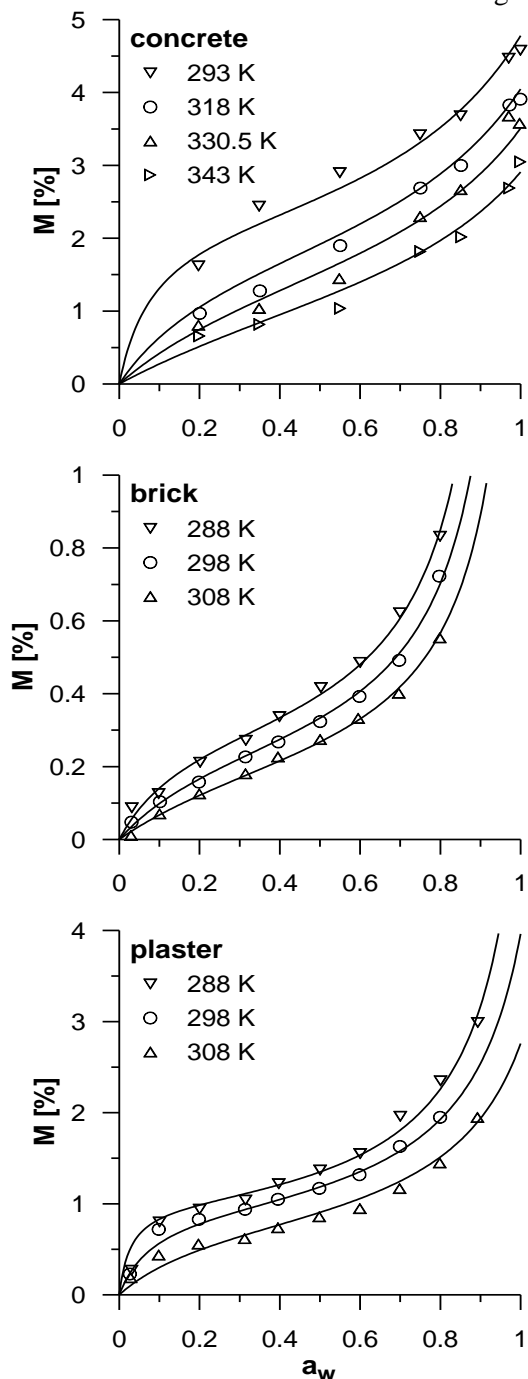
Fig. 1. Results of the simultaneous mutlitemperature fitting of desorption isotherms by the GDW model (Eqns. (1)-(3)) for all the studied experimental data sets.
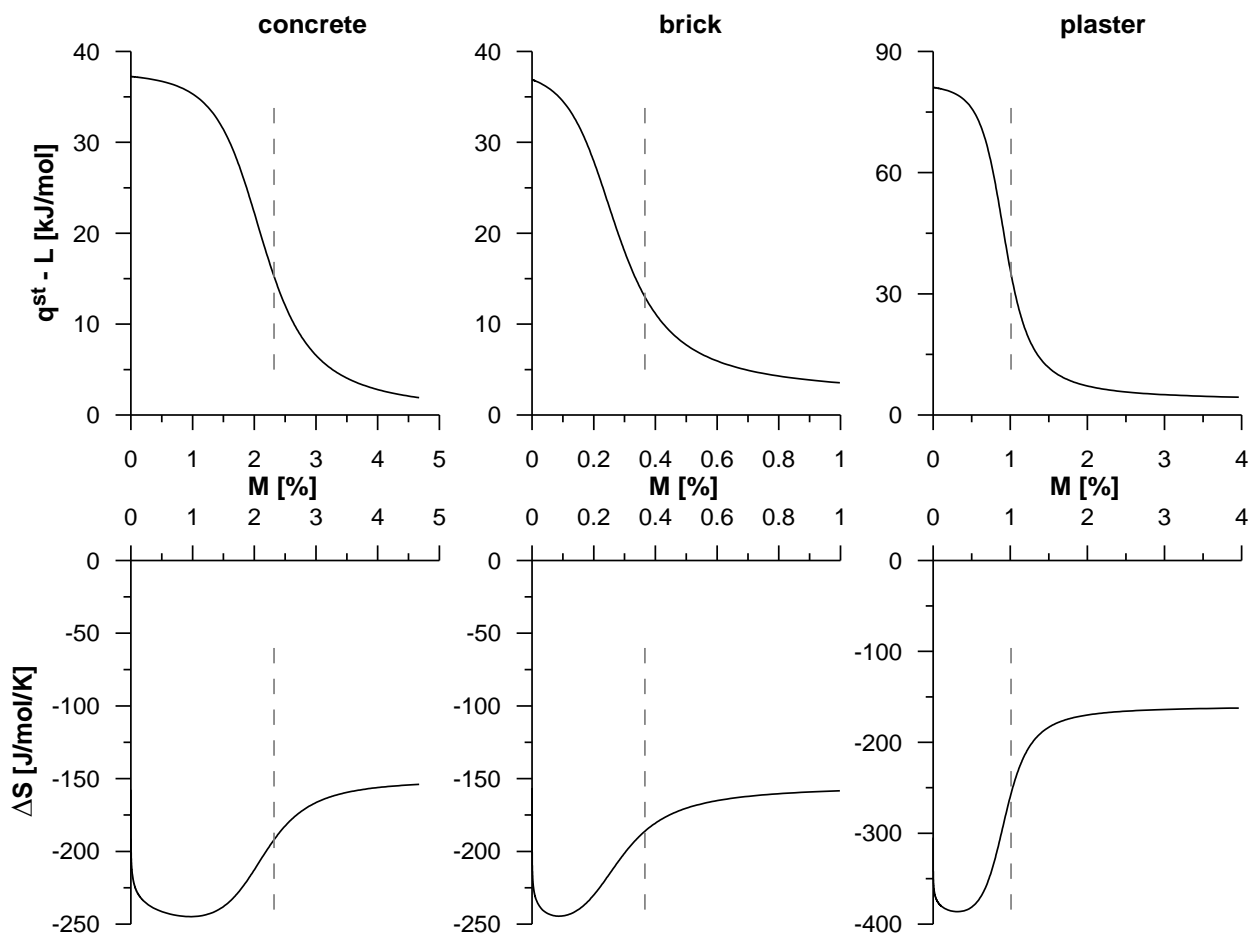
Fig. 2. Plots of isosteric sorption enthalpy and related difference in entropy for water desorption on the studied materials. The data are generated for T = 298 K by Eqns. (4) and (8). The dashed lines represent the monolayer capacities (see Table 1).

REFERENCES

1. J.-Ph. Carlier, Th. Rougelot, N. Burlion, *Constr. Build. Mater.*, **37**, 58 (2012).
2. F. Collet, F. Achchaq, K. Djellab, L. Marmoret, H. Beji, *Constr. Build. Mater.*, **25**, 1079 (2011).
3. M. Jerman, R. Černý, *Energ. Build.*, **53**, 39 (2012).
4. O. Koronthalyova, *Constr. Build. Mater.*, **25**, 879 (2011).
5. L. Kuishan, Z. Xu, G. Jun, *J. Build. Phys.*, **32**, 355 (2009).
6. A. Moropoulou, M. Karoglou, A. Giakoumaki, M. K. Krokida, Z. B. Maroulis, G. D. Saravacos, *Braz. J. Chem. Eng.*, **22**, 203 (2005).
7. M. Karoglou, A. Moropoulou, Z. B. Maroulis, M. K. Krokida, *Drying Technol.*, **23**, 305 (2005).
8. Z. Pavlík, J. Žumár, I. Medved, R. Černý, *Transp. Porous Media*, **91**, 939 (2012).
9. A. Trabelsi, R. Belarbi, P. Turcry, A. Aït-Mokhtar, *Mag. Concr. Res.*, **63**, 333 (2011).
10. M. Karoglou, A. Moropoulou, Z. B. Maroulis, M. K. Krokida, *Drying Technol.*, **23**, 289 (2005).
11. S. Poyet, *Cem. Concr. Res.*, **39**, 1052 (2009).
12. S. Furmaniak, *Transp. Porous Media*, **92**, 21 (2012).
13. S. Basu, U. S. Shivhare, A. S. Mujumdar, *Drying Technol.*, **24**, 917 (2006).
14. R. M. Myhara, S. S. Sablani, S. M. Al-Alawi, M. S. Taylor, *Lebensm.-Wiss. Technol.*, **31**, 699 (1998).
15. Z. Pakowski, R. Adamski, M. Kokocińska, S. Kwapisz, *Fuel*, **90**, 3330 (2011).
16. H. L. Liu, Z. Y. Jin, X. M. Xu, Z. J. Xie, B. H. Pan, J. G. Li, *Appl. Eng. Agr.*, **27**, 115 (2011).
17. S. Furmaniak, A. P. Terzyk, P. A. Gauden, *J. Food Eng.*, **82**, 528 (2007).
18. Ch. Chen, *J. Food Eng.*, **74**, 178 (2006).
19. S. Furmaniak, P. A. Gauden, A. P. Terzyk, G. Rychlicki, *Adv. Colloid Interface Sci.*, **137**, 82 (2008).
20. S. Brunauer, P. H. Emmett, E. Teller, *J. Am. Chem. Soc.*, **60**, 309 (1938).
21. E. A. Guggenheim, Application of Statistical Mechanics, Clarendon Press, Oxford, 1966.
22. R. B. Anderson, *J. Am. Chem. Soc.*, **68**, 686 (1946).
23. J. M. de Boer, The Dynamic Character of Adsorption, Clarendon Press, Oxford, 1953.
24. J. Blahovec, S. Yanniotis, *J. Food Eng.*, **91**, 72 (2009).
25. S. Yanniotis, J. Blahovec, *LWT - Food Sci. Technol.*, **42**, 1688 (2009).

26. S. Furmaniak, A. P. Terzyk, R. Gołembiewski, P. A. Gauden, L. Czepirski, *Food Res. Int.*, **42**, 1203 (2009).
27. G. S. da Rosa, F. C. de Godoi, A. Marsaioli Jr., S. C. Dos Santos Rocha, *Chem. Eng. Trans.*, **24**, 661 (2011).
28. S. Furmaniak, A. P. Terzyk, P. A. Gauden, *Drewno*, **51**, 15 (2008).
29. J. Roja, S. Moren, A. Lopez, *J. Pharm. Sci. Res.*, **3**, 1302 (2011).
30. M. G. A. Vieira, S. C. S. Rocha, *Braz. J. Chem. Eng.*, **25**, 299 (2008).

31. W. Olek, J. Majka, Ł. Czajkowski, *Holzforschung*, **67**, 183 (2013).
32. S. Furmaniak, A. P. Terzyk, P. A. Gauden, *Drying Technol.*, **29**, 984 (2011).
33. S. Ross, J. P. Olivier, On Physical Adsorption, John Wiley & Sons Inc., New York, 1964.
34. S. Poyet, S. Charles, *Cem. Concr. Res.*, **39**, 1060 (2009).
35. R. Storn, K. Price, *J. Glob. Optim.*, **11**, 341 (1997).
36. A. P. Terzyk, G. Rychlicki, M. S. Ćwiertnia, P. A. Gauden, P. Kowalczyk, *Langmuir*, **21**, 12257 (2005)

МНОГО-ТЕМПЕРАТУРНО НАПАСВАНЕ НА ИЗОТЕРМИ КАТО ПРОСТ МЕТОД ЗА ИЗУЧАВАНЕ НА ТЕРМОДИНАМИКАТА НА СОРБЦИЯТА НА ВОДА В СТРОИТЕЛНИ МАТЕРИАЛИ

С. Фурманяк

Група по физикохимия на въглеродни материали, Департамент по химия, Университет „Николай Коперник", Торун, Полша

(Резюме)

Изследвана е сорбцията на вода в някои строителни материали. Потвърден е обобщен модел на D'Arcy и Watt (GDW) за едновременното напасване на изотермите на базата на три групи от експериментални данни. Много-температурното описание на опитните данни не само намалява броя на търсените параметри, но и позволява простия анализ на термодинамиката на процеса. Стойностите на най-добрите параметри са използвани за пресмятане на изостеричната енталпия на сорбция (представляваща енергетиката на процеса) и на ентропията на сорбираната фаза (свързана със степента ред/безпорядък). При изследваните проби от строителни материали сорбираната вода в началото има ниска ентропия и висока степен на порядък, вероятно заради формирането на твърдо-подобна фаза. При високи натоварвания сорбираната вода се отнася повече като течна.

Sorption of Cs+ by nano-sized microporous titanium silicates with pharmacosiderite structure

N. Lihareva, V. Kostov-Kytin*

Institute of Mineralogy and Crystallography, Bulgarian Academy of Sciences, Sofia, Bulgaria

The uptake of Cs^+ on as-synthesized pure sodium and potassium nano-sized end-members of a titanosilicate framework with pharmacosiderite structure is investigated. Batch sorption studies are carried out in order to find the optimal conditions for Cs^+ uptake and to study the kinetics and equilibrium of the process. Kinetic sorption data are analyzed using pseudo-first and pseudo-second order rate models. The adsorption isotherms are described by means of the Langmuir and Freundlich isotherm models. It is found that a simple pseudo-second order rate model and Langmuir isotherm model provide a good accordance with the experimental data of the Cs^+ uptake. The maximum adsorption capacity of Cs^+ is 3.877 and 1.870 meq/g for the Na- and the K-form, respectively. The pseudo-second order rate constants k_2 calculated at different initial Cs^+ concentrations are presented. The experimental results are indicative that the sorption mechanism is an equivalent ion exchange of Cs^+ for K^+ and Na^+, respectively.

Keywords: titanosilicate framework, ion exchange, Cs^+ uptake

INTRODUCTION

Microporous titanosilicates and their analogues have attracted attention for more than two decades, because of their structural and functional similarities to the framework of aluminosilicate-based zeolites. Numerous data have been published on radioactive wastewaters purification using titanosilicate materials [1] and the references therein. In this regard, Clearfield [2] paid attention to two compounds with tunnel structures and great affinity for Cs^+ and Sr^{2+}. The first one is a tetragonal titanosilicate of the general formula, $Na_2Ti_2SiO_7.2H_2O$ [3]. It is a synthetic analogue of the mineral sitinakite. The other one was firstly synthesized by Chapman and Roe in 1990 [4] under the name GTS. It has the general formula $M_3H(TiO)_4(SiO_4)_3.4H_2O$ (M is alkali metal cation) and structure identical to that of the mineral pharmacosiderite.

We were able to hydrothermally synthesize nano-sized pure sodium and potassium end-members of the GTS material, as well as intermediate members of the (Na, K) series [5,6]. In the course of the preliminary characterization excess of Si *vs.* deficiency of Ti in the structures of all run-products was established, being more pronounced for the potassium-rich forms [7]. Based on the 29Si MAS-NMR spectroscopy data a structural model was proposed illustrating the

deficiency of Ti in the framework of all phases being located towards the crystallites periphery [7]. Similarly to the pore size and degree of crystallinity, the controlled surface Ti deficiency appears to be a key-factor for the acid-base properties of such materials and may have a considerable impact on the mechanisms for uptake of radioactive pollutants. The previous investigations on the sorption capability of the GTS materials have mainly been focused on the structural characterization and the crystal-chemical aspects of the process.

In this study nano-sized synthetic pure sodium and potassium end-members of the GTS material were selected and their sorption capacity towards Cs^+ was investigated. The effects of experimental conditions, kinetics and equilibrium were examined in details and to our knowledge, for the first time different models describing the sorption of Cs^+ by this material were tested and determined.

EXPERIMENTAL

Adsorption studies

Materials and methods

Cesium stock solution of 0.1N concentration was prepared from CsCl (Merck). The working solutions were prepared by dilution. The cesium uptake was studied using batch experiments with 0.05 g of titanosilicate and 10 ml of cesium solutions. The initial pH was adjusted by addition of dilute HCl or NaOH. The suspension was shaken on a horizontal shaker and was separated by

* To whom all correspondence should be sent:
E-mail: vkytin@abv.bg

centrifugation at 4000 rpm. The cesium concentration in the recovered solutions was measured by atomic absorption spectrometry (Perkin-Elmer 30-30 apparatus). The cesium concentration in the solid phase was calculated using the mass-balance equation:

$$q_e = [(C_0 - C_e) \, V]/m, \qquad (1)$$

where q_e (mg/g) is the concentration of cesium in the solid phase, C_0 and C_e (mg/L) are the initial and the equilibrium concentrations in the sample solution, respectively, V (L) is the volume, and m (g) is the adsorbent mass.

The sorption effectiveness (E %) was calculated using Eq. 2

$$E\% = 100 m_s/(V C_0), \qquad (2)$$

where C_0 (mg/L) is the initial concentration of Cs^+, m_s (mg) is the mass of sorbed metal, V (L) is the volume.

Effect of the experimental conditions on the Cs^+ uptake

The effect of pH on cesium adsorption was investigated as described above using solutions with initial concentration of 500 mg Cs /L in the pH range from 1.18 to 5.8, shaken for 360 min. Each adsorption experiment was carried out twice. The effect of contact time was determined by the batch sorption experiments described above at pH_{inital} =5.6 and Cs^+ concentrations of 100, 500, and 2500 mg/L for the Na-form, and 500 and 2500 mg/L for the K-form. The contact time for both titanosilicates varied between 15 and 480 min.

The relation between initial concentration and sorbed amount was studied by equilibrium isothermal experiments (optimal pH=5.6, contact time 360 min) by varying the Cs^+ concentrations in the range from 0 to 2500 mg/L.

The distribution coefficient K_d (ml/g) was determined from the equilibrium experiments with 1×10^{-3} M Cs^+ (132.91 mg/L) by the equation:

$$K_d = 1000 \, q_e/C_e \qquad (3)$$

where C_e (mg/L) and q_e (mg/g) are the concentrations of Cs^+ in the solution and in the solid, respectively.

The interference of sodium – the major macro component present in radioactive wastes, on Cs^+ uptake was studied in two types of model solutions. The first type contained $NaNO_3$ with concentrations of 0, 0.25, 0.5, 1.0, and 4.5 M at pH_{inital}=6. The second type solutions contained 3.5 or 5 M Na^+ ($NaNO_3$+NaOH) with pH =13.5.

Modeling of sorption kinetics and equilibrium data

The kinetics of Cs^+ uptake was studied applying the pseudo-first- and the pseudo-second- order kinetic models expressed in terms of Eqs. (4) and (5), respectively [8-10].

$$\log (q_e - q_t) = \log q_e - (k_1/2.303) \, t, \qquad (4)$$
$$t/q_t = 1/(k_2 q_e^2) + (1/q_e) \, t, \qquad (5)$$

where k_1 (min^{-1}) and k_2 (g/(meq min) are the apparent pseudo-first and pseudo-second order rate constants, q_t and q_e are the contents of sorbed cesium (meq/g), at time t and at equilibrium.

The apparent rate constants are complex quantities determined by the processes underlying uptake mechanisms. In general, it is assumed that k_1 is a linear function of the initial ion concentration, whereas k_2 is a complex function of this parameter. However, it should be noted that the actual mechanism of a sorption process also depends on other factors such as sorbent inhomogeneity, transport phenomena (surface and intraparticle diffusion), chemical phenomena (hydrolysis, precipitation), sorbed ion species. Nevertheless, both simple kinetic models are widely used as a base for estimation and comparison of the ion uptake efficiency of sorbents and for prediction of process performance [11].

Adsorption isotherms describe the equilibrium between the ion concentration in solution and the sorbed amount for different initial concentrations. The Langmuir isotherm model (Eq. 6) is based on the assumption that the adsorption for all sites is constant and does not depend on the degree of surface coverage.

$$C_e/q_e = 1/q_m b + C_e/q_m, \qquad (6)$$

where C_e (meq/L) and q_e (meq/g) are the equilibrium cesium concentrations in the liquid and in the solid phase, respectively. The Langmuir parameter q_m (meq/g), represents the maximum sorption capacity and b (L/meq) is the site energy factor describing the equilibrium constant.

The Freundlich isotherm is expressed by equation (8):

$$\log q_e = \log K_F + 1/n \log C_e, \qquad (7)$$

where K_F (meq/g)/(meq/L)$^{1/n}$ and n (dimensionless) are Freundlich parameters.

This model is an empirical equation based on the assumption that sorption is a function of the degree of surface coverage. The surface sites have different energy and are not equally available. This model supposes formation of multi-layers of sorbed ions.

The kinetic and equilibrium data were fitted by regression analysis to the kinetic and isotherm models.

RESULTS AND DISCUSSION

Effect of pH

The pH of a suspension is an important parameter that determines the sorbed ions forms and their behavior and affects the sorbent surface sites. On the other hand, the final pH is a result of the processes of ion uptake and gives information about the nature and mechanisms of reactions.

Fig. 1 shows the change in Cs^+ uptake at different initial pH values. It is indicative that unlike other sorbents, the Na- and K- end-members of the GTS titanosilicates are effective even in highly acidic solution (pH = 1.2), with the efficiency of Cs^+ removal of 67 and 42%, respectively. The adsorption capacity of both materials significantly increases upon pH increase up to 2.0, then changes very slowly up to pH 2.5 and stays stable at higher pH values.
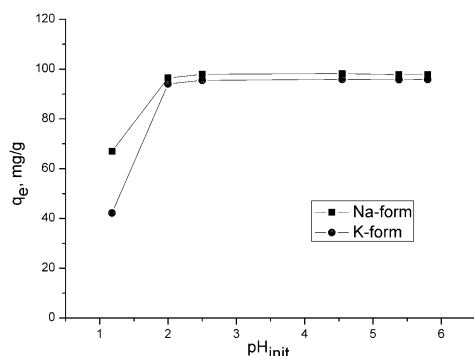
Fig. 1. Changes in the sorbed amount of Cs^+ as a function of pH.

The final pH values of the solutions after 360 min of shaking are shown in Fig. 3.
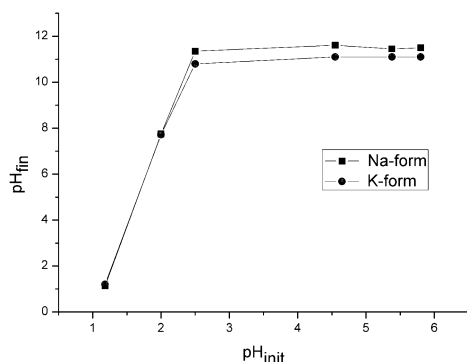
Fig. 2. Changes of pH after the experiments.

From Figs. 1 and 2 it is evident that at pH > 2.5 the q_e, as well as the pH final values remain relatively constant. This is indicative that at pH > 2.5 optimal conditions for Cs^+ uptake are achieved. This is the reason to choose an initial pH = 5.6 for the subsequent kinetic and isothermal

investigations. The elevated final pH values (~11.5) are due to hydrolysis of the sorbents and exchange of Cs^+ for Na^+ and K^+, as described earlier [12, 13].

Kinetic studies

The rate and degree of sorption of Cs^+ from solutions by both titanosilicates are shown in Figs. 3 and 4.
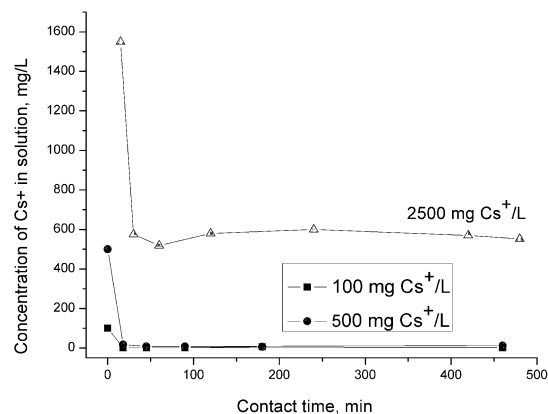
Fig. 3. Cesium uptake kinetics for Na-titanosilicate at three different initial cesium concentrations.
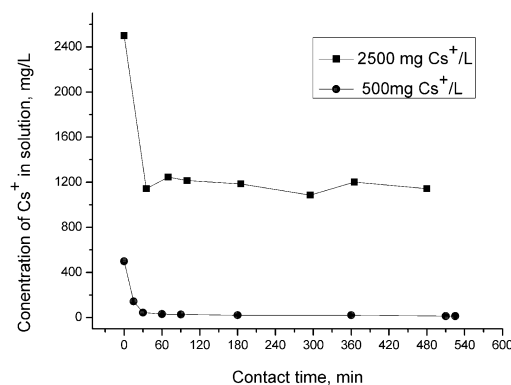
Fig. 4. Cesium uptake kinetics for K-titanosilicate at two different initial cesium concentrations.

Both figures show that the effect of contact time on the uptake of cesium has three different stages. Regarding Na-titanosilicate at 100 mg/L Cs^+ the first stage is almost instantaneous and the effectiveness of removal E is about 99 % within the first 15 min. For the 500 mg/L concentration the effectiveness is >96 % within the first 15 min of treatment, then continues to increase slowly and reaches a value of 99 % after 45 min, after that remaining constant. For the higher initial concentration of 2500 mg/L the effectiveness is 38% after 15 min, 77 % after 30 min, reaching about 80% at the equilibrium measured after 360 min. The pH_{final} increases and falls within the range of 11.0 - 11.3 and 11.0 - 11.5 for the 100 and 500

Table 1. Kinetic data for the uptake of Cs$^+$ by Na and K titanosilicates - pseudo-second order model

Sample	Equation	R^2	k_2 (g meq^{-1}.)	$q_{e,calc}$	$q_{e,exp}$ (meq/g))
– 100 mg/L	$t/q_t = 1.339t + 0.3318$	0.9999	5.410	0.747	0.747 ± 0.005
- 500 mg/L	$t/q_t = 1.3493t + 0.4275$	0.9999	4.258	0.741	0.736 ± 0.004
- 2500 mg/L	$t/q_t = 0.3467 + 0.0.0703$	0.9998	1.710	2.884	2.89 ± 0.05
K-titanosilicate					
500 mg/L	$t/q_t = 1.3648t + 5.6655$	0.9999	0.3287	0.732	0.714 ± 0.013
2500 mg/L	$t/q_t = 0.5153t + 1.1651$	0.9974	0.2297	1.940	1.926 ± 0.070

mg Cs$^+$/L, respectively, the lowest values being measured for the first contact time point.

The K-titanosilicate demonstrates a similar sorption behavior. During the first, very fast stage of 15 min the uptake efficiency is 71 % (for 500 mg/L Cs$^+$). During the second stage the Cs$^+$ uptake slowly increases with contact time up to >90% after 30 min, and as the equilibrium state approaches, the removal efficiency reaches 97 %. The final pH increases, reaching values in the range of 11.0 - 11.2. The uptake profile for a concentration of 2500 mg/L has a similar run. The effectiveness reaches >50 % after the first 30 min, and approaches about 54 % at equilibrium.

Figs. 3 and 4 show that whatever the character of the phenomena governing the interactions between the sorbent and the sorbed ions the uptake is so rapid that almost maximal effectiveness of removal is achieved within the first 15 to 30 minutes of contact time. No doubt, particle size and structural imperfections play a certain role in shortening the diffusion path to the active sites of the sorbent.

Contact time of 360 min was found to be sufficient to reach equilibrium for the batch experiments and thus it was chosen for the subsequent studies.

The data were fitted by regression analysis to the kinetic models. For the pseudo-first order model the values of the correlation coefficient R^2 were low (0.5002 $<R^2<$0.9243) indicating that this model is less appropriate.

Strong correlation with the experimental data was obtained for the pseudo-second order rate model (Table 1) indicated by high R^2 values and good agreement between theoretical values of q$_e$ and the experimentally obtained data (difference < 2.5 %.).

Adsorption isotherms

The isotherms of the adsorbed amount of Cs$^+$ as a function of equilibrium concentration (initial ion concentrations were varied in the range from 0 to 2500 mg/L) are plotted in Fig. 5. The profiles of the curves indicate that both titanosilicates have high affinity for Cs$^+$ ions. In order to study the mechanism of the adsorption process the equilibrium isotherm data were fitted by least square regression analysis to the Langmuir and the Freundlich models (see Section 2.2.). The experimental data correlate well with the Langmuir isotherm model, whereas the Freundlich model is comparatively less applicable (Table 2.). This means that the sorption sites are homogenous and the adsorption is monolayer.
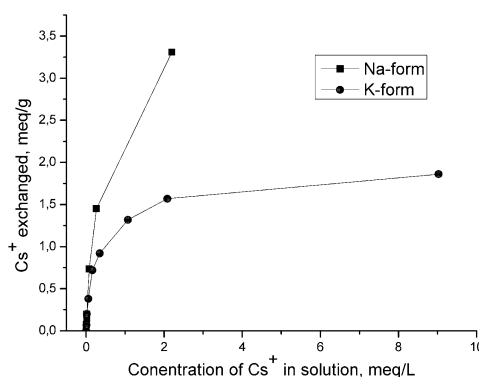
Fig. 5. Cs-exchange isotherm for both pharmacosiderite titanosilcates.

Under the selected experimental conditions, the values of maximum uptake capacity (q_m), calculated from the Langmuir model, are 3.877 and 1.870 meq/g for Na- and K-titanosilicate, respectively. These results are indicative for the higher selectivity of the Na-form for Cs$^+$, as compared to that of the K-form. The sorption capacity of the as-synthesized Na-form is somewhat greater than the reported value of 3.12 meq Cs$^+$/g for the Na-exchanged titanosilicate [12].

No data for the sorption capacity of K-titanosilicate were reported in the same work.

Table 2. Freundlich and Langmuir isotherm parameters for sorption of Cs$^+$ by the Na and K forms of pharmacosiderite titanosilicate

Sample/model	Equation	R^2	b (L/meq)	q_m (meq/g)	q_m (mg/g)
Langmuir					
Na-titanosilicate	$C_e/q_e = 0.2579C_e + 0.0951$	0.9971	2.712	3.877	515.35
K-titanosilicate	$C_e/q_e = 0.5246C_e + 0.1549$	0.9979	3.451	1.870	248.62

Sample/Model	Equation	R^2	K_F	$1/n$	n
Freundlich					
Na-titanosilicate	$\log q_e = 0.6695 \log C_e + 0.4366$	0.9629	2.732	0.6695	1.493
K-titanosilicate	$\log q_e = 0.4317 \log C_e + 0.0504$	0.9259	0.123	0.4317	2.316

The distribution coefficients K_d (ml/g) of Na- and K- titanosilicate for Cs$^+$ determined under the above described conditions and 0.001M Cs$^+$ are 11 300 ± 1700 and 12 700 ± 980, respectively (errors are ± one standard deviation). These results differ from those reported previously for the same concentration distribution coefficients - 15 360 ml/g for the Na-form and 3500 ml/g for the K-titanosilicate, respectively [12].

Adsorption studies for Cs$^+$ in model solutions

The effectiveness of Cs$^+$ uptake in NaNO$_3$ solutions with different molarity is presented in Fig. 6. At low concentrations (up to 0.5M), the effectiveness of Cs$^+$ uptake for the Na-titanosilicate is >90% whereas in 4.5 M NaNO$_3$ the effectiveness drops to about 40 %. These values are even lower for the effectiveness of Cs$^+$ uptake by the K-titanosilicate, which is less than 80% in 0.25 M NaNO$_3$. It is also important to note that in 4.5 M NaNO$_3$ the effectiveness of both samples is almost the same.

At high alkalinity both the K_d values and the effectiveness of Cs$^+$ uptake drop substantially, as compared to those obtained in solutions containing only NaNO$_3$ (Table 3). The detrimental effect of high alkalinity on cesium uptake by similar materials was previously reported by Möller *et al.* [14].
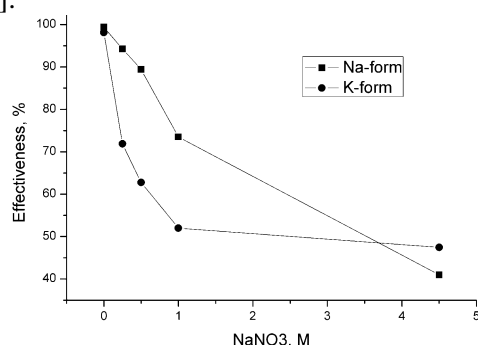
Fig. 6. Effectiveness of Cs$^+$ removal as a function of NaNO$_3$ concentration.

Table 3. Cs+ distribution coefficient and effectiveness in NaNO3 solutions with pH 13.5

Sample	K_d (ml/g)	E, %
Na- titanosilicate		
3.5 M Na$^+$	86	30.2
5M Na$^+$	49	19.6
K- titanosilicate		
3.5 M Na$^+$	58	23.1
5M Na$^+$	37	14.5

Mechanism of the Cs$^+$ uptake

In order to elucidate the mechanism of Cs$^+$ uptake, for each Cs$^+$ concentration on the isotherm curves we measured the concentrations of Na$^+$ and K$^+$ (meq/L) released during the sorption, then we subtracted from these values the concentrations of Na and K released from each titanosilicate in distilled water. The obtained data were compared with the sorbed Cs$^+$ (meq/L) by regression analysis. The experimental data correlate well with the linear regression equations with slopes 0.97 (R^2=0.9764) for the K- and 1.15 (R^2=0.9970) for the Na-form. The obtained results show that cesium uptake by both titanosilicates is due to equivalent cation exchange over the studied concentration range from 0 to 2500 mg Cs$^+$/L. The deviation from the ideal value of 1 could be due to errors of measurement.

Another confirmation of this result came from processing of the Cs$^+$ uptake data for the Na-form in the high Na$^+$ concentration experiments the way Möller *et al.* did [14]. According to these authors the mechanism of uptake in a binary ion system can be estimated from the relation of K_d of the tracer ion (Cs$^+$) and the solution concentration of Na$^+$. Plotting $\log K_d$ for Cs$^+$ as a function of $\log [Na^+]$ (meq/L) gives a straight line with slope $-z_{Cs}/z_{Na}$, (z_{Cs} and z_{Na} being the respective ion charges). When the

573

sorption mechanism is an equivalent ion exchange of Cs^+ for Na^+ the theoretical value $-(z_{Cs}/z_{Na})$ is -1. In our case the regression analysis of the relation $\log K_d$ for Cs^+ as a function of $\log [Na^+]$ for the Na-form gives a value of -1.11 (R^2=0.9882) which shows that the Cs^+ uptake is an equivalent ion exchange for Na^+ (Fig. 7). In contrast, Möller *et al.* [14] showed for their Na-exchanged titanosilicate samples TSi1 and TAM1 slope values of -1.69 and -1.32, respectively, which were indicative that the situation was no longer of ideal binary $^{134}Cs/Na^+$ exchange and other chemical phenomena affected the ideal situation.
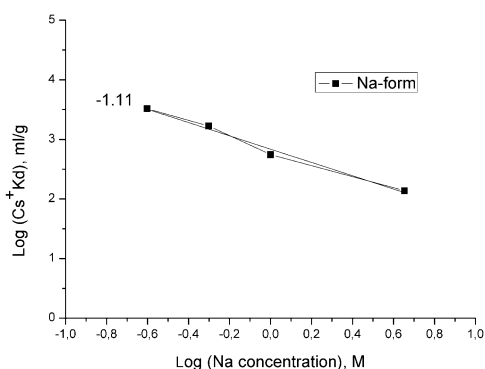
Fig. 7. Effect of the macro component Na^+ on the distribution coefficients of $Cs^+ K_d$, (ml/g) for Na-titanosilicate.

CONCLUSION

Pure sodium and potassium nano-sized end-members of the titanosilicate framework with pharmacosiderite structure – GTS, were hydrothermally synthesized at 100 and 200 ˚C, respectively. They were tested as potential sorbents in the nuclear wastes treatment. The removal of Cs^+ ions was investigated under various conditions and it was found that the maximum uptake is reached between pH 2.5 and 5.8 with contact time of 360 min. The samples were effective in the Cs^+ uptake in slightly acidic (even in acidic liquors at pH about 1) and neutral solutions. Kinetic experiments have shown that both titanosilicates display rapid kinetics, as particle size and compositional imperfections were found to be important factors in shortening the diffusion path to the active sites of the sorbents. The data from batch adsorption kinetic experiments are well described by the pseudo-second order kinetic model. The Langmuir isotherm model adequately represents the adsorption process and the maximum uptake capacities of the sodium and potassium forms were estimated to be 3.87 and 1.87 meq Cs^+/g, respectively. Additionally, the sorption of Cs^+ ions from model solutions with high content of $NaNO_3$ was examined. It is concluded that the strong interference from the competing Na^+ cations substantially lowers the Cs^+ removal effectiveness within the studied pH range. The experimental results are indicative that the sorption mechanism is an equivalent ion exchange of Cs^+ for K^+ and Na^+.

REFERENCES

1. K. Popa, C. C. Pavel, *Desalination*, **293**, 78-86, (2012).
2. 15. A. Clearfield, *Solid State Sci.*, **3**, 103 (2001).
3. D.M. Poojary, R.A. Cahill, A. Clearfield, *Chem. Mater.*, **6**, 2364 (1994).
4. D.M. Chapman, A.L. Roe, *Zeolites*, **10**, 730 (1990).
5. S Ferdov, C. Lengauer, O. Petrov, V. Kostov-Kytin, *J. Mater Sci Lett.*, **39**, 4343 (2004).
6. V. Kostov-Kytin, S Ferdov, B. Mihailova, O. Petrov, *7th International Conference on the Occurrence, Properties, and Utilization of Natural Zeolites, 16–21 July, Socorro, New Mexico, USA, Micropor. Mesopor. Matter.*, 105, 232 (2007).
7. V. Kostov-Kytin, R. Nikolova, N. Nakayama, S. Simova, and P. Tzvetkova. *Compt. Rend. Bulg. Acad. Sci.*, **64, 5** Pages: 683, (2011).
8. F.G. Wu, R.L. Tseng, R.S. Juang, *Water Res.*, **35**, 613 (2001).
9. Z. Reddad, C. Gerente, Y. Andres, P. Le Clirec, *Environ. Sci. Technol.*, **36**, 2067(2002).
10. N. J. Coleman, D.S. Brassington, A. Raza, A.P. Mendham, *Waste Manag.*, **26**, 260 (2006).
11. Y.S. Ho, G. McKay, *Process Biochem.*, **34**, 451 (1999).
12. E.A. Behrens, A. Clearfield, *Micropor. Mater.*, **11,** 65 (1997).
13. A. Dyer, M. Pillinger, S. Amin, *J. Mater. Chem.*, **9**, 2481 (1999).
14. T. Möller, R Harjula, J. Lehto, *Sep. Puriff. Technol.*, **28**, 13 (2002).

Сорбция на Cs$^+$ от наноразмерни микропорьозни титанови силикати със структура на фармакосидерит

Н. Лихарева, В. Костов-Китин *

Институт по минералогия и кристалография, Българска академия на науките, София

(Резюме)

Изследвано е задържането на Cs$^+$ на титаносиликати със структура на фармакосидерит със синтезирани чисти наноразмерни частици, съдържащи калий и натрий. Изследванията са проведени за намиране на оптималните условия за задържането на Cs$^+$ и изучаването на кинетиката и равновесието на процеса. Кинетичните данни са анализирани с помощта на кинетика от псевдо-първи и псевдо-втори порядък. Равновесието се описва от адсорбционните изотерми на Langmuir и Freundlich. Установено е, че простият кинетичен модел на реакция от псевдо-втори порядък и изотермата на Langmuir дават добро съгласие с опитните данни. Максималният адсорбционният капацитет по Cs$^+$ е съответно 3.877 и 1.870 meq/g за натриевата и калиевата форма. Представени са скоростните константи k$_2$, изчислени за различни начални концентрации на Cs$^+$. Опитните резултати са показателни за това, че сорбционният механизъм е еквивалентен на йонообмен на Cs+ съответно с K$^+$ и Na$^+$.

Adsorption of toxic gases by an open nanocone coupled with an iron atom

M. H. Hadizadeh*, M. Hamadanian

Department of Physical Chemistry, Faculty of Chemistry, University of Kashan, Kashan, I. R. Iran

Density functional theory (DFT) calculations were used in order to study the adsorption of some toxic gases in the air by an open nanocone coupled with an iron atom (FeCNC). The BSSE (basis set superposition error) counterpoise correction (CP) was included during the geometry optimization for all systems. The results indicated that the effect of inclusion of BSSE-CP correction during the optimization is very important in the adsorption of some toxic gases by FeCNC.

Keywords: Nanocone; Toxic gases; BSSE-CP

INTRODUCTION

Carbon nanotubes (CNTs) have attracted considerable interest since their discovery by Iijima [1]. These nanomaterials have quickly developed into some of the most fundamental structures in nanotechnology and nanoscience due to their specific structures and unique properties. Many promising applications, including energy storage, nanoelectronic devices, chemical probes, biosensors, gas sensors, etc., have been reported in the literature [2-4]. In recent years, the investigation of the adsorption of different gases on CNTs has been found to be one of the most momentous subjects, and a number of researches have been performed on these systems [5,6]. For example, the physisorption of He, Ne, Ar, Kr, Xe and CH_4 in cylindrical pores, single-walled carbon nanotubes (SWNTs) and SWNT bundles has been inspected both experimentally and theoretically [7-17]. In addition to carbon nanotubes, a new form of carbon nanostructure, namely, carbon nanocone (CNC) has been discovered wherein a single pentagonal ring or community of nearly pentagonal rings defines a conical apex [18-21], i.e., a single walled carbon nanocone (SWNC) consists of a single layer of graphene sheet twisted into a cone. The cones can be classified by their disclination angle, which is defined as the angle of the sector removed from the flat sheet to form a cone [22]. CNCs with a disclination angle of 19°, 39°, 60°, 85° and 113° have been detected in the carbon samples in the pyrolysis of hydrocarbons [23]. Both SWNTs and SWNCs are tube-like made of single graphene sheets with hollow spaces inside. The SWNCs have larger internal pore space and surface area than SWNTs, and therefore gas storage on CNCs has some advantages compared with that in CNTs [24]. These materials are useful for many practical applications, such as gas storage and adsorption processes [21].

Within this work, density functional theory (DFT) calculations are performed to investigate the electronic and structural properties of a representative model of FeCNC. To this aim, the structural models of FeCNC with toxic gases were optimized to reach the minimum energy levels (Fig.1). The subsequent adsorption energy between FeCNC and the toxic gases was investigated. The adsorption energy was calculated at the same level with and without correction for the basis set superposition error (BSSE) using the Boys-Bernardi counterpoise (CP) technique [25].

COMPUTATIONAL DETAILS

The main model of this work is a conical structure with 39° disclination angle, in which the apex tips are saturated by iron atoms. A number of toxic gases in the air (carbon monoxide, carbon dioxide, chlorine, carbonyl chloride, hydrogen sulfide, sulfur dioxide, cyanogen) each one separately, were adsorbed

---

* To whom all correspondence should be sent:
E-mail: Hadizadeh.mh@gmail.com

on the structure of an open nanocone coupled with the iron atom (Fig. 1).
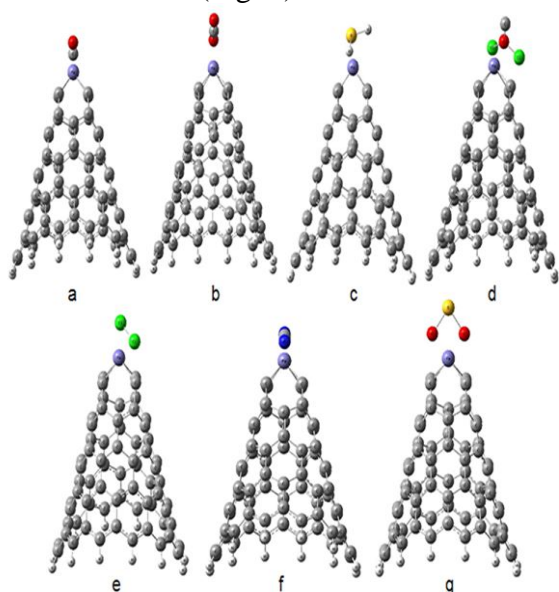
Fig. 1. Optimized absorptive structures of FeCNC with: (a) CO (b) CO_2 (c) H_2S (d) $COCl_2$ (e) Cl_2 (f) C_2N_2 (g) SO_2

All calculations were performed using the Gaussian 98 plan package [26]. GaussView 3.07 [27] was utilized to build molecular structures, display molecular geometry convergence and generate molecular graphics of all related species. The full geometry optimizations of all complexes were carried out

using density functional theory (DFT) with the Beck's three parameter hybrid functional (B3) with the Lee-Yang-Parr correlation functional (LYP) called as B3LYP [28,29] with the basis set LANL2DZ [30]. For comparison, the two-layered ONIOM hybrid method [31] of calculations was also attempted.

The two-layered ONIOM(B3LYP/6-311++G(d,p):B3LYP/LANL2DZ) approach applied on the structure of FeCNC with toxic gases, two sections of CNC/toxic gas and iron atom were treated as the high and low levels of theory, respectively. The following relations were used in order to investigate the adsorption energy of toxic gases in the air by FeCNC :

$$E_{abs}^{(1)}=E_{FeCNC\text{-}gas}-E_{CNC}-E_{Fe}-E_{gas} \qquad (1)$$

$$E_{abs}^{(2)}=E_{FeCNC\text{-}gas}-E_{FeCNC}-E_{gas} \qquad (2)$$

RESULTS AND DISCUSSION

Based on the results calculated from Eqs.(1) and (2), it can be concluded that the amount of adsorbed sulfur dioxide is higher than that of other gases, but there is an important difference between the quantities of $E_{abs}^{(1)}$ and $E_{abs}^{(2)}$ in spite of the fact that the two systems are not very different (Table 1).

Table 1. The distance between FeCNC and toxic gases (D), bond length of toxic gas solely (L), bond length of adsorbed toxic gase (L'), uncorrected adsorption energy ($E^{(1)},E^{(2)}$) and corrected adsorption energy ($E^{*(1)},E^{*(2)}$) .

System	D	L	L'	$E_{abs}^{(1)}$	$E_{abs}^{(2)}$	$E_{abs}^{*(1)}$	$E_{abs}^{*(2)}$
FeCNC-CO	2.065	1.187	1.212	-0.3295	-0.0419	-0.2141	-0.0087
FeCNC-CO_2	1.989	1.227	1.235	-0.3322	-0.0446	-0.2303	-0.0075
FeCNC-Cl2	2.247	2.294	4.442	-0.4373	-0.1497	-0.3545	-0.1317
FeCNC-$COCl_2$	2.095	1.965	3.018	-0.4098	-0.1222	-0.2772	-0.0544
FeCNC-H_2S	2.631	1.447	1.441	-0.3036	-0.016	-0.2342	-0.0114
FeCNC-SO_2	1.821	1.735	1.830	-0.4451	-0.1575	-0.3016	-0.0788
FeCNC-C_2N_2	1.903	1.160	1.264	-0.3400	-0.0524	-0.2365	-0.0137

This shows that in the hybrid systems, there is an important effect of the basis set of a molecule on the basis set of another molecule.

So at a closer look it can be said that such an interpretation of adsorption may not be true because the interaction energy between an open nanocone with an iron atom and the toxic gas molecules is ignored. Therefore, in order to assess the basis set superposition error (BSSE) correction and its impact on the amount of energy changes during adsorption, the Boys-

Bernardi counterpoise (CP) technique [25] was used. The quantities of absorbed energy with respect to interaction energy, named corrected adsorption energy, are listed in Table 1. In addition, the difference between corrected adsorption energy $E^{*(1)}$ and $E^{*(2)}$ is less than the difference between uncorrected adsorption energy $E^{(1)}$ and $E^{(2)}$ for each of the systems. So, based on the interaction energy between open nanocone, iron atom and toxic gases, the chlorine molecule has maximum adsorption (Fig. 2).
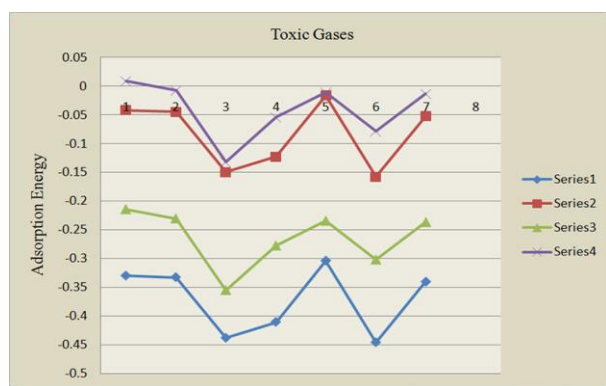
Fig. 2. Uncorrected adsorption energy $E^{(1)}$ (series 1), $E^{(2)}$ (series 2) and corrected adsorption energy $E^{*(1)}$ (series 3), $E^{*(2)}$ (series 4): *(1) FeCNC-CO (2) FeCNC-CO₂ (3) FeCNC-Cl₂ (4) FeCNC-COCl₂ (5) FeCNC-H₂S (6) FeCNC-SO₂ (7) FeCNC-C₂N₂*

After adsorption by FeCNC, bond lengths of toxic gas molecules were also changed, as indicated in Table 1. Unlike other toxic gases it was observed that the bond length of hydrogen sulfide was reduced in consequence of its adsorption by FeCNC, which was consistent with the calculated results.

CONCLUSIONS

In this study the structure of open nanocone coupled with an iron atom was investigated and its impact on the adsorption of some of the toxic gases in the air was assessed. The values of the uncorrected and corrected adsorption energy of the molecules of the toxic gases and the FeCNC were compared. Results showed that in the hybrid systems, there is an important effect of the basis set of a molecule on the basis set of another molecule. It was found that the adsorption of chlorine gas by FeCNC is better than that of other toxic gases while carbon monoxide has the lowest adsorption among other gases.

REFERENCES

1. Iijima, S: Helical microtubules of graphitic carbon. *Nature* **354**, 56−58 (1991).
2. Reich, S, Thomsen, C, Maultzsch, J: Carbon Nanotubes Basic Concepts and Physical Properties, Wiley-VCH Verlag GmbH and Co., KGaA, Weinheim, 2004.
3. Dresselhaus, MS, G, Dresselhaus, Eklund, PC: *Science* of Fullerenes and Carbon Nanotubes; Academic Press: New York (1996).
4. Jalili, S, Majidi, R: The Effect of Gas Adsorption on Carbon Nanotubes Properties: *J. Comput. Theor. Nanosci.* **3**, 664–669 (2006).
5. T. Baei, M, Ahmadi Peyghan, A, Bagheri, Z, Bigdeli Tabar,M: B-doping makes the carbon nanocones sensitive towards NO molecules. *Phys. Lett.* A **377**, 107-111(2012).
6. Bagheri, Z, Ahmadi Peyghan, A: DFT study of NO2 adsorption on the AlN nanocones. *Comput. Theor. Chem.* **1008**, 20-26(2013).
7. Kuznetsova, A, Yates Jr, JT, Liu, J, Smalley, RE: Physical adsorption of xenon in open single walled carbon nanotubes: Observation of a quasi-one-dimensional confined Xe phase. *J. Chem. Phys.* **112**, 9590-9598 (2000).
8. Babaa, MR, Stepanek, I, Masenelli-Varlot, K, Dupont-Pavlovsky, N, McRae, E, Bernier, P: Opening of single-walled carbon nanotubes: evidence given by krypton and xenon adsorption. *Surf. Sci.* **531**, 86-92 (2003).
9. Simonyan, VV, Johnson, JK, Kuznetsova, A, Yates Jr, JT: Molecular simulation of xenon adsorption on single-walled carbon nanotubes, *J. Chem. Phys.* **114**, 4180-4185 (2001).
10. Talapatra, S, Zambrano, AZ, Weber, SE, Migone, AD: Gases do not adsorb in the interstitial channels of SWNT bundles. *Phys. Rev. Lett.* **85**, 138-145 (2000).
11. Jalili, S, Majidi, R: Study of Xe and Kr adsorption on open single-walled carbon nanotubes using molecular dynamics simulations. *Physica E* **39**, 166-170 (2007).
12. Gordillo, MC, Brualla, L, Fantoni, S: Neon Adsorbed in Carbon Nanotube Bundles. *Phys. Rev. B* **70**, 245420-245427 (2004).
13. Rols, S, Johnson, MR, Zeppenfeld, D, Bienfait, M, Vilches, OE, Schneble, J: Argon adsorption in open-ended single-wall carbon nanotubes. *Phys. Rev. B* **71**,155411-155419 (2005).
14. Teizer, W, Hallock, RB, Dujardin, E, Ebbesen, TW: He Desorption from Singel Wall Carbon Nanotubes Bundles: A 1-dimensional Adsorbate, *Phys. Rev. Lett.* **82**, 5305-8 (1999)
15. Teizer, W, Hallock, RB, Dujardin, E, Ebbesen, TW: He Desorption from Single Wall Carbon Nanotube Bundles: A One-Dimensional Adsorbate, *Phys. Rev. Lett.* **84**,1844–1845 (2000)
16. Maddox, MW, Gubbins,KE: A molecular simulation study of freezing/melting phenomena for Lennard-Jones methane in cylindrical nanoscale pores, *J. Chem. Phys.* **107**, 9659-9668 (1997).
17. Cao, D, Zhang, X, Chen, J, Wang, W, Yun, J: Optimization of single-walled carbon nanotube arrays for methane storage at room temperature, *J. Phys. Chem. B* **107**, 13286-13292 (2003).
18. Iijima, S, Ichihashi, T, Ando, Y: Pentagons, heptagons and negative curvature in graphite microtubule growth, *Nature* **356**, 776-778 (1992).
19. Iijima, S, Ichihashi, T: Single-shell carbon nanotubes of 1-nm diameter, *Nature* **363**, 603- 605 (1993) .
20. Ge, M, Sattler, K: Observation of Fullerene Cones, Chem. Phys. Lett. **220**, 192-196 (1994).

21. Yudasaka, M, Iijima, S, Crespi, VH: Single-wall carbon nanohorns and nanocones, *Appl. Phys.* **111**, 605-629 (2008).
22. Bourgeois, L, Band, Y, Han, WQ, Sato, T: Structure of boron nitride nanoscale cones: ordered stacking of 240° and 300° disclinations, *Phys. Rev. B* **61**, 7686-7691 (2000).
23. Krishnan, A, Dujardin, E, Treacy, MMJ, Hugdahl, J, Lynum, S, Ebbesen, TW: Graphitic cones and the nucleation of curved carbon surfaces, *Nature* **388**, 451-454 (1997).
24. Dillon, AC, Jones, KM, Bekkedahl, TA, Kiang, CH, Bethune, DS, Heben, MJ: Storage of hydrogen in single-walled carbon nanotubes, *Nature* **386**, 377-379 (1997).
25. Boys, SB, Bernardi, F: The calculation of small molecular interactions by the differences of separate total energies. Some procedures with reduced error , *Mol. Phys.* **19**, 553-566 (1970).
26. Frisch, MJ, Trucks, GW, Schlegel, HB, Scuseria, GE, Robb, MA, Cheeseman, JR, Montgomery Jr, JA, Stratmann, RE, Burant, JC, Dapprich, S, Millam, JM, Daniels, AD, Kudin, KN, Strain, MC, Farkas, O, Tomasi, J, Barone, V, Cossi, M, Cammi, R, Mennucci, B, Pomelli, C, Adamo, C, Clifford, SO, Chterski, J, Petersson, GA, Ayala, PY, Cui, Q, Morokuma, K, Malick, DK, Rabuck, AD, et al.: Gaussian 98. Gaussian Inc., Pittsburgh, PA (1998)
27. GaussView 03, Revision 3.07, Gaussian, Inc., Wallingford, CT (2006).
28. Becke, AD: Density-Functional Thermochemistry. III. The Role of Exact Exchange. *J. Chem. Phys.* **98**, 5648–5652 (1993).
29. Lee, C, Yang, W, Parr, RG: Development of the Colle-Salvetti conelation energy formula into a functional of the electron density. *Phys. Rev. B* **37**, 785–789 (1988).
30. Hay, PJ, Wadt, WR: Ab initio effective core potentials for molecular calculations. Potentials for K to Au including the outermost core orbitals. *J. Chem. Phys.* **82**, 299–310 (1985).
31. Svensson, M, Humbel, S, Froese, RDJ, Matsubara, T, Sieber, S, Morokuma, K: The IMOMO method: integration of different levels of molecular orbital, *J. Phys. Chem.* **100**, 19357–19363 (1996).

АДСОРБЦИЯ НА ТОКСИЧНИ ГАЗОВЕ С ОТВОРЕН НАНОКОНУС СВЪРЗАН С ЖЕЛЕЗЕН АТОМ

М.Х. Хадизаде*, М. Хамаданиан

Департамент по физикохимия, Химически факултет, Университет в Кашан, Кашан, Иран

(Резюме)

Използвани са изчисления по теорията плътностния функционал (DFT) за изследването на адсорбцията на някои токсични газове от въздуха в отворен наноконус с включен железен атом (FeCNC). BSSE (множеството от суперпозиционните грешки) е включено при оптимизацията на геометрията за всички системи. Резултатите показват, че ефектът на включване на противовесна корекция при оптимизацията е много важен при адсорбцията на токсични газове в FeCNC.

Inhibition of glycolysis and respiration of sarcoma-180 cells by cyclophosphamide

G. Muralikrishna[1], S.K. Pillai[1], S. Kaleem[2], F. Shakeel[3*]

[1]*International Institute of Biotechnology and Toxicology, Paddapai, Kancheepuram district, Chennai, India*
[2]*Department of Pharmacology, Faculty of Pharmacy, Integral University, Lucknow, Uttar Pradesh, India*
[3]*Center of Excellence in Biotechnology Research, King Saud University, P.O. Box 2460, Riyadh 11451, Saudi Arabia*

The malignant cells in tumor are known to exhibit high rate of glycolytic activity leading to high production of lactic acid. The anticancer drug cyclophosphamide has been reported to have a highly promising anticancer activity against fibrosarcoma bearing rats. In the present investigation, the effect of the energy metabolism of sarcoma-180 (S-180) on the mode of action of cyclophosphamide, as well as the effect of cyclophosphamide on the mitochondrial and cellular respiration of S-180 cells was studied. The effects of glucose utilization, pyruvate utilization and lactate formation were studied on whole S-180 cells and S-180 cell-free homogenate. The levels of glycolytic enzymes such as hexokinase and lactate dehydrogenate (LDH) were estimated. The utilization of glucose and pyruvate was found to decrease which resulted in decreased formation of lactic acid. The mitochondrial respiration was also found to decrease significantly after treatment with cyclophosphamide treated cells. The activity of glycolytic enzymes and mitochondrial respiration were also found to decrease. In conclusion, cyclophosphamide affects both cellular and mitochondrial respiration, leading to reduction of cellular energy pool and thereby resulting in a loss of viability of S-180 cells.

Keywords: Cyclophosphamide, Sarcoma-180 cells, Malignant tumor, Hexokinase, Lactate dehydrogenase.

INTRODUCTION

The rate of glucose transport, alterations in the cellular levels and regulatory properties of key glycolytic enzymes are believed to be responsible for the abnormal metabolic properties of malignant tumors [1-3]. The significant increase in the rate of sugar uptake has been consistently observed in cells transformed by sarcoma viruses. In transformed-chick embryo cells, the rate of glycolysis is increased 2 to 4 fold even under conditions of rigorously controlled growth rate and cell densing [4, 5]. The rate of aerobic glycolysis in tumor cells might indicate that the key enzymes are less sensitive to normal feed back control. It has been reported that in a number of systems, stimulation of glycolytic enzymes leads to cell proliferation and deoxyribonucleic acid (DNA) synthesis [6-8]. The tumor promoter 12-O-tetradecanoyl-phorbol-13-acetate (TPA) has been shown to activate glucose metabolism to provide the necessary precursors for cell proliferation in target tissues [9]. Several anticancer drugs have been reported to inhibit the aerobic glycolysis seen in various types of cancers [10, 11]. Cyclophosphamide has been reported to show significant anticancer effects both *in vitro* and *in vivo* [12]. Therefore, the objective of the present study was to investigate the effects of glycolysis and respiration in sarcoma-180 cells caused by cyclophosphamide.

EXPERIMENTAL

Sarcoma-180 cell lines were obtained from the National Facility for Animal Tissue and Cell Culture, Pune, India. Healthy male Swiss albino mice (20-25 g) were used as experimental animal models. The experimental mice were maintained in controlled environmental conditions of temperature and humidity. The experimental mice were maintained in an animal house with food and water given *ad libitum* (Gold Mohar M/s. Hindustan Lever Ltd., Mumbai, India). This research work on Swiss albino mice was sanctioned and approved by the Institutional Animal Ethics Committee, International Institute of Biotechnology and Toxicology, Chennai, India.

Sarcoma-180 cells were grown in the abdominal cavity of Swiss albino mice, 1×10^7 cells were inoculated into the peritoneal cavity at the recipient mice. The cells were harvested between 8 to 10 days and washed with sterile saline. The cells were finally suspended in phosphate buffer saline (PBS) of pH 7.4.

After the exposure of S-180 cells to cyclophosphamide for various time intervals, the

---

* To whom all correspondence should be sent:
E-mail: faiyazs@fastmail.fm

cell viability was determined by the trypan blue exclusion test [13].

Mitochondria from S-180 cells were prepared by the digitonin permeabilization method [14].

The respiratory mechanism for mitochondria of S-180 cells contained in a total volume of 2.2 ml, 0.75 ml of PBS, 125 mg of sucrose, 50 mg of KCl, 2 mg of KH_2PO_4, 1 mg of $MgCl_2$ and respiratory substrate (5 mg of glutamate plus 5 mg of malate) and mitochondria containing approximately 200 mg of protein of S-180 cells was studied. After an indicated period of time, ADP (0.4 mg) was added to start phosphorylating respiration [10].

2×10^8 of S-180 cells in 2.2 ml of PBS were sonicated for 40 seconds (in four 10-S burs) by keeping the cell suspension on ice. After sonication, the cells were centrifuged at 1500 g for 5 min and the cell pellet was discarded and the supernatant was used as S-180 cell-free homogenate.

S-180 cells were incubated with 5 mg of glucose (5 mg of pyruvate instead of glucose for pyruvate utilization study). After 1 h of incubation with cyclophosphamide at different concentrations at 37°C in a metabolic shaker, the reaction was terminated with 70% perchloric acid and the respective metabolites such as glucose [15], pyruvate [16] and lactate [17] were estimated. The results were expressed as micromoles of metabolite cells in 60 min.

S-180 cells (approximately 8×10^7 cells) were suspended in PBS and incubated with or without cyclophosphamide in a total volume of 2 ml. After 1 h of incubation, the cells were washed twice with PBS and cell-free homogenate was prepared as described above, the activities of enzymes such as lactate dehydrogenase [18] and total hexokinase [19] were determined. The hexokinase was also separated into cytosolic and particulate forms and assayed. To separate hexokinase into soluble and particulate forms, S-180 cell-free homogenate was centrifuged at 50000 g for 10 min. The supernatant was used for the assay of cytosolic hexokinase. The pellet was suspended in PBS and again centrifuged as described above. The supernatant was discarded and the pellet was suspended in a minimum volume of PBS and used for the assay of particulate hexokinase.

RESULTS AND DISCUSSION

Table 1 shows the inhibitory effect of cyclophosphamide on glucose utilization and L-lactic acid formation from glucose by S-180 cells. Table 2 shows the effect of cyclophosphamide on pyruvate utilization and L-lactic acid formation by S-180 cells.

Table 3 shows the inhibitory effect of cyclophosphamide on glucose utilization and L – lactic acid formation from glucose by S-180 cell-free homogenate.

Table 4 shows the inhibitory effect of cyclophophamide on pyruvate utilization and L-lactic acid formation by S–180 cell-free homogenate.

Table 5 shows the inhibitory effect of cyclophosphamide on glycolytic enzymatic enzymes of S–180 cells after incubating white blood cells (WBC) with cyclophosphamide.

Table 1 Effect of cyclophosphamide on glucose utilization and L-lactic acid formation by S-180 cells: The results are expressed per 10^8 cells in 1 h (each value is a mean ± SD of 6 experiments)

Groups	Glucose utilized (μmol)	L-Lactic acid formed (μmol)
Control (Cyclophosphamide)	5.51± 0.46	3.85 ± 0.26
(1 mg)	4.98 ± 0.37	3.41 ± 0.22*
(2 mg)	4.75 ± 0.35*	3.10 ± 0.19#
(3 mg)	4.47 ± 0.33#	4.95 ± 0.17#
(5 mg)	4.11 ± 0.29#	4.71 ± 0.14#

*(p<0.05), # (p<0.001)

Table 2 Effect of cyclophosphamide on pyruvate utilization and L-lactic acid formation by S-180 cells: The results are expressed per 10^8 cells in 1 h (each value is a mean ± SD of 6 experiments)

Groups	Pyruvate utilized (μmol)	L-Lactic acid formed (μmol)
Control (Cyclophosphamide)	4.76 ± 0.36	3.18 ± 0.21
Cy (1 mg)	4.37 ± 0.32	2.85 ± 0.18*
Cy(2 mg)	4.45 ± 0.28*	2.61 ± 0.15#
Cy(3 mg)	4.65 ± 0.24#	2.46 ± 0.13#
Cy(5 mg)	4.48 ± 0.22#	2.37 ± 0.12#

*(p<0.05), # (p<0.001)

Table 3 Effect of cyclophosphamide on glucose utilization and L-lactic acid formation by S-180 cell-free homogenates (each value is a mean ± SD of 6 experiments)

Groups	Glucose utilized / mg protein / h, μmol	L-Lactic acid formed / mg ptm / h, μmol
Control	0.89 ± 0.06	0.35 ± 0.02
Cy (5 mg)	0.55 ± 0.04	0.24 ± 0.001#

 # (p<0.001)

Table 4 Effect of cyclophosphamide on pyruvate utilization and L-lactic acid formation by S-180 cell-free homogenates (each value is a mean ± SD of 6 experiments)

Groups	Pyruvate utilized / mg protein / h, μmol	L-Lactic acid formed / mg / protein / h, μmol
Control	0.75 ± 0.04	0.28 ± 0.02
Cy (5 mm)	0.45 ± 0.03#	0.20 ± 0.01#

(p<0.001)

Table 5 Effect of cyclophosphamide on glycolytic enzymatic enzymes of S-180 cells after incubating white blood cells with cyclophosphamide (each value is an average ± SD of 6 experiments)

Enzyme	Enzyme activity, units / mg		
	Control	Cyclophosphamide treated (3 mm)	Cyclophosphamide treated (5 mm)
Hexokinase Total	0.44 ± 0.04	0.29 ± 0.2#	0.18 ± 0.01#
Particulate	0.30 ± 0.02	0.22 ± 0.01#	0.091 ± 0.006#
Cytosolic	0.20 ± 0.01	0.12 ± 0.01	0.09 ± 0.01
LDH	1.68 ± 0.18	1.18 ± 0.13#	1.18 ± 1.12#

(p<0.001)

Figure 1 shows the percent viability of S-180 cells after incubating for various periods of time. From figure 1 it is evident that cyclophosphamide has a profound impact on the viability of S-180 cells.
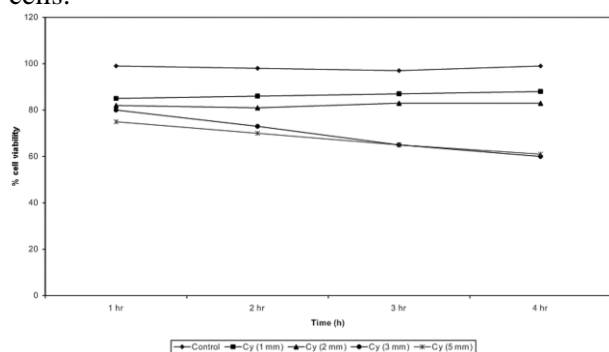
Fig. 1 Effect of cyclophosphamide on the percent viability of S-180 cells after incubating for various time intervals

Figures 2 and 3 show that cyclophosphamide inhibited both the mitochondrial and cellular respiration of S-180 cells.
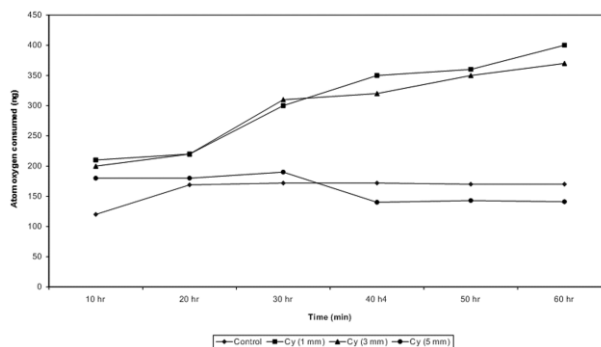
Fig. 2 Effect of cyclophosphamide on the respiration of mitochondria from control and cyclophosphamide (1, 3, 5 mm) treated S-180 cells
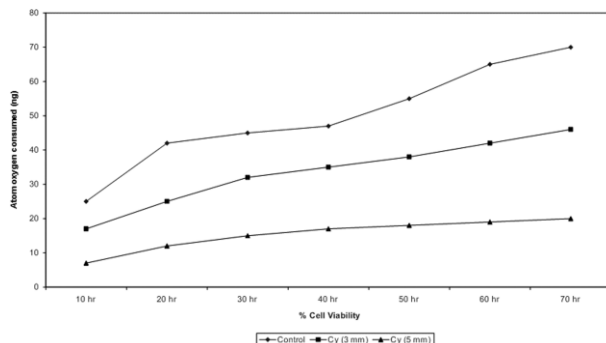
Fig. 3 Effect of cyclophosphamide on the respiration of control and cyclophosphamide (3, 5 mm) treated S-180 cells

Figure 4 shows the inhibitory effects of cyclophosphamide on the biosynthesis of DNA, RNA and protein in S-180 cells.
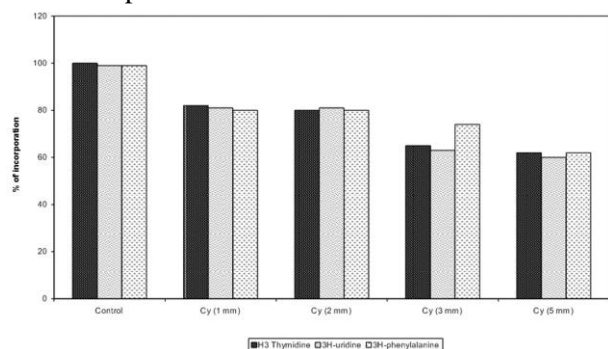
Fig. 4 Effect of cyclophosphamide on % incorporation of 3H-thymidine, 3H-uridine and 3H-phenylalanine in S-180 cells after 1 h of exposure

When incubated with cyclophosphamide, the viability of S-180 cells was found to decrease after 24 h of exposure. The decrease in the viability of S-180 cells after treatment with cyclophosphamide showed that this effect may be due to the inhibition of glycolysis and mitochondrial respiration. The enzyme hexokinase has attracted considerable attention both because it commits glucose to catabolism and it has been shown to be markedly elevated in tumors exhibiting a high glucose catabolic rate [20, 21]. The concentration of hexokinase tumor cells is higher and bound to mitochondria [22, 23]. The mitochondrial bound hexokinase has direct access to ATP generated from oxidative phosphorylation and able to phosphorylate glucose with an enhanced efficiency. Since transformed cells and tumor cells contain large amounts of bound hexokinase [24, 25] and catalyse high rates of glycolysis, the levels of total cytosolic and particulate hexokinase were determined after treatment with cyclophosphamide. The results clearly showed that the levels of both total and particulate hexokinase decreased after treatment with cyclophosphamide with no significant decrease in the cytosolic form, thereby suggesting that cyclophosphamide, even in high concentrations, inhibits glycolysis by blocking only the particulate hexokinase enzyme. Glucose–6–phosphate, a product of hexokinase catalysed reaction, is a critical precursor not only for glycolysis, which in highly glycolytic tumors, provides as much as 60% of cells ATP supply and biosynthesis of nucleic acids [26]. The decreased synthesis of DNA might have resulted in the inhibition of cell division and membrane biosynthesis, thereby restricting the cell growth.

The inhibition of glycolysis by cyclophosphamide was measured both in terms of lactate and pyruvate formation and glucose consumption. In the present study the utilization of glucose and pyruvate was found to decrease resulting in decreased formation of lactic acid. The decreased lactate levels, as observed during pyruvate utilization study, might be due to the inhibition of LDH. LDH is an important rate limiting enzyme of glycolysis. Its activity has been found to decrease significantly after treatment with cyclophosphamide. Hence, the decreased activity, as noted in the present study, is consistent with the decreased rate of glycolysis in cyclophosphamide and suggests that the LDH activity is elevated in tumors [3, 27].

The mitochondrial respiration was also found to decrease significantly after treatment with cyclophosphamide treated cells. The inactivation of these important glycolytic enzymes and mitochondrial respiration of S-180 cells by cyclophosphamide strongly suggested that this compounds act upon specific target sites, which are probably altered in tumor cells. The results of 3H-thymidine, 3H-uridine and 3H-phenylalanine clearly indicated that cyclophosphamide, apart from inhibiting glycolysis and respiration, is also able to inhibit macromolecular biosynthesis of DNA in S-180 cells. Previously this drug was shown to inhibit DNA biosynthesis in the fibrosarcoma cell line [14]. The inhibitory effects of anticancer drugs on macromolecular biosynthesis are also confirmed with Ehrlich ascites carcinoma cell line [28-31].

In the present investigation it was found that the tumor cells lost their ability to respire within minutes after addition of cyclophosphamide. Cyclophosphamide may interfere with tumor cell glycolysis and could induce cell death. As a consequence, the respiration of the malignant cells is inhibited. Thus it is more likely that the cytotoxic effects of cyclophosphamide may be probably mediated through interference with the oxidative process and energy metabolism of the tumor cell. It follows from these observations that cyclophosphamide independently and simultaneously affects both glycolysis and mitochondrial respiration, leading to reduction of the cellular energy pool, thereby reducing the viability of the S-180 cells.

CONCLUSION

The results of the present study showed that cyclophosphamide has great impact on both cellular and mitochondrial respiration of S-180 cells. These impacts cause reduction in cellular energy pool which ultimately results in the loss of viability of S-180 cells. Finally, these results indicated the strong

inhibitory effects of cyclophosphamide on glycolysis and respiration of S-180 cells.

REFERENCES

1. J.S. Flier, M.M. Mucckler, P. Usher, et al, *Science* **235,** 1492, (1987)
2. M.J. Birubaum, H.C. Haspel, O.M. Rosen, *Science* **235,** 1495, (1987)
3. Y.S. Ahn, G.Y. Chemeris, V.S. Turusoy, et al, *Toxicol. Pathol.* **22,** 415, (1994)
4. M. Singh, V.N. Singh, J.T. August, et al, *Arch. Biochem. Biophys.* **165,** 240, (1974)
5. P.L. Pederson, *Prog. Exp. Tumor Res.* **22,** 190, (1978)
6. I. Diamond, A. Legg, J.A. Schneider, et al, *J. Biol. Chem.* **253,** 866, (1978)
7. J.A. Schneider, I. Diamond, E. Rozengurt, *J. Biol. Chem.* **253,** 872, (1978)
8. G. Webben, *New Eng. J. Med.* **296,** 541, (1977)
9. T.G. O'Brien, D. Saladik, L. Diamond, *Biochem. Biophys. Res. Commun.* **88,** 103, (1979)
10. J. Halder, M. Ray, S. Ray, *Int. J. Cancer* **54,** 443, (1993)
11. R. Parimala, P. Sachdanandam, *Mol. Cell. Biochem.* **125,** 59, (1993)
12. G. Bonadonna, P. Valagussa, *J. Clin. Oncol.* **3,** 259, (1985)
13. P. Moldeus, J. Hogberg, S. Orrhenivns, Isolation and use of liver cells, in Fleischer S, Packer L (eds): Methods in Enzymology New York Academic press, 1978, vol 52, pp: 60-71.
14. Moreadith RW, Fiskum G. Isolation of mitochondria from ascites tumor cells permeabilized with digitonin. *Anal. Biochem.*, **137,** 360, (1984);.
15. T. Susaki, S. Matsui, *Rinsho Kugaku* **1,** 346, (1972)
16. T.E. Friedmann, G.E. Hangen, *J. Biol. Chem.* **147,** 415, (1943)
17. S.B. Barker, W.M. Summerson, *J. Biol. Chem.* **138,** 535, (1941)
18. J. King, Assay of alkaline phosphatase, in practical clinical enzymology, London Van Nostrand, 1965, pp: 106-111.
19. N. Brandstrup, J.E. Kirk, C. Bruni, *J. Gerentol.* **12,** 166, (1957)
20. V.N. Singh, M. Singh, J.T. August, et al, *Proc. Nat. Acad. Sci.* **71,** 4129, (1974)
21. M.J. Weber, P.K. Evan, M.A. Tohnson, et al, *Fed. Proc.* **43,** 107, (1984)
22. B.D. Nelson, F. Kabir, *Biochim. Biophys. Acta,* **841,** 195, (1985)
23. R.A. Nakashima, M.G. Paggi, L.J. Scott, et al, *Cancer Res.,* **48,** 913, (1988)
24. E. Bustamante, H.P. Motris, P.L. Pederson, *J. Biol. Chem.,* **256,** 8699, (1981)
25. D.M. Parry, P.L. Pederson, *J. Biol. Chem.* **258,** 10904, (1983)
26. R.A. Nakashima, M.G. Paggi, P.L. Pederson, *Cancer Res.,* **44,** 5702, (1984)
27. G. Bacci, M. Avella, D. McDonald, et al, *Tumor,* **74,** 644, (1988)
28. V. Saraswathi, N. Ramamoorthi, I.V. Mathuram, et al, *Med. Sci. Res.,* **25,** 167, (1977)
29. A. Pain, S. Samanta, S. Dutta, et al, *Acta Pol. Pharm.,* **60,** 285, (2003)
30. A. Pain, S. Samanta, S. Dutta, et al, *J. Exp. Clin. Res.,* **22,** 411, (2003)
31. S. Kanno, A. Tomizawa, T. Hiura, et al, *Biol. Pharm. Bull.,***28**5,27,**,** (2005)

ИНХИБИРАНЕ НА ГЛИКОЛИЗАТА И ДИШАНЕТО НА КЛЕТКИ НА САРКОМА-180 ЧРЕЗ ЦИКЛОФОСФАМИД

Г. Мулаликришна[1], С.К. Пилаи[1], С. Калеем[2], Ф. Шакеел[3*]

[1]Международен институт по биотехнология и токсикология, Паддапаи, Ченаи, Индия

[2]Департамент по фармакология, Факултет по фармация, Интегрален университ, Лукноу, Утар Прадеш, Индия

[3]Център за компетентност по биотехнологични изследвания,Университет „Крал Сауд", Рияд 11451, Саудитска Арабия

(Резюме)

Известно е, че злокачествените туморни клетки проявяват висока гликолизна активност, водеща до високо производство на млечна киселина. Съобщава се, че противораковото лекарство циклофосфамид има многообещаващо противораково действие срещу фибросаркома при опитни плъхове. В настоящата работа е изследван ефектът на енергиен метаболизъм при клетки саркома-180 (S-180) при въздействието на циклофосфамид върху митохондриалното и клетъчното дишане на клетките S-180. Ефектът на използване на глюкоза, пирувати и образуването на лактати е изследван върху цели клетки S-180 cells и тяхно безклетъчни хомогеати. Оценено е нивото на гликолитичнте ензими като хексокиназа и лактат-дехидрогеназа (LDH). В настоящата работа се забелязва намаляване на утилизацията на глюкоза и пируват, което води до образуване на млечна киселина. Освен това е намерен, че митохондриалното дишане намалява значително след третиране на клетките с циклофосфамид циклофосфамид. Активността на гликолитичните ензими и митоондриалното дшане. В заключение, циклофосфамидът влияе върху клетъчното и митохондриалното дишане, водещи до намаляване клетъчния енергиен резервоар и с това до загубата на жизненост на клетките S-180.

Synthesis, characterization and properties of ZnO/TiO₂ powders obtained by combustion gel method

A. D. Bachvarova-Nedelcheva[1*], R. D. Gegova[1], A. M. Stoyanova[2], R. S. Iordanova[1],V. E. Copcia[3], N. K. Ivanova[2], I. Sandu[3]

[1]*Institute of General and Inorganic Chemistry, Bulgarian Academy of Sciences, Sofia, Bulgaria*
[2]*Medical University, Pleven, Bulgaria*
[3]*Arheoinvest interdisciplinary platform, Laboratory of the Scientific Investigation, Iasi*

Submicron ZnO/TiO2 powders were obtained via combustion gel method. The structure, morphology and elemental composition of the obtained samples were characterized by XRD, IR spectroscopy and SEM with EDX analysis. The photocatalytic activities of the samples were evaluated by the degradation of Malachite Green and Reactive Black5 in aqueous solutions under ultraviolet light irradiation. The antibacterial properties of samples obtained via combustion sol-gel method were studied in solid media (agar plates) against Gram-negative Escherichia coli ATCC 25922 and Gram-positive Staphylococcus aureus ATCC 25923. The inhibition diameter was measured for all investigated samples. No clear zone of inhibition was seen around of blank experiments. Thus, all samples exhibited strong bactericidal action toward both selected bacterial cells.

Keywords: composite powders, sol-gel chemistry.

INTRODUCTION

Recently, the combustion synthesis (CS) became more popular and has emerged as an important technique for the synthesis and processing of oxide and non-oxide advanced materials [1]. This method has many potential advantages, such as low-processing cost, energy efficiency, and high production rate. Several books [2 - 4] and review articles [5 - 12] have been published on this subject in recent years. By combustion synthesis, TiO₂, nanoparticles sized from 100 nm to 1000 nm were very quickly obtained through gasification, nucleation, and crystal growth [13, 14]. Zinc oxide (ZnO) powders with different types of morphology were synthesized by a combustion synthesis method using zinc nitrate, metallic zinc and glycine as precursors [15]. Nanosized ZnO powder was synthesized by solution combustion method. The obtained powder showed three times higher photocatalytic efficiency than any other commercial photocatalysts [16]. Zn doped TiO₂ and N-doped TiO₂/ZnO composite powders were obtained by combustion method with better photocatalytic activity compared to pure TiO₂ [17]. Their photocatalytic properties were studied towards methyl orange dye. The authors reported that the

enhanced photocatalytic activity of the composites is related to the good crystallization, the presence of anatase phase, and the particle size reduction.

It is well known that ZnO and TiO₂ oxides are close to being two of the ideal photocatalysts in several respects. In recent years, they become more attractive and important since it has a great potential for contribution to environmental problems. Several authors [18-19] found that the coupling of TiO₂ with ZnO is useful to achieving higher photocatalytic reaction rate. The results showed that the photocatalytic activity of ZnO/TiO₂ coupled photocatalysts was higher than that of the single phase. Although ZnO and TiO₂ in general have been proved to be very active in the photocatalytic oxidation of different pollutants, the problem concerning the influence of particles size and morphology on their performance efficiency is very crucial and not yet clarified. Both TiO₂ and ZnO were extensively studied as antimicrobial agents mainly under UV light irradiation [20-26]. It was found that TiO₂ is very effective in killing *Escherichia coli* (*E. coli*) [20], while ZnO is most effective in disinfection of *Staphylococcus aureus* (*S. aureus*) [24].

The present study is a continuation of our previous investigations in the ZnO-TiO₂ system. By applying different sol-gel methods we proved that the type of precursor and the order of adding the components influence on the microstructure of the

* To whom all correspondence should be sent:
E-mail: albenadb@svr.igic.bas.bg

final product. We also found that the selection of an appropriate scheme for synthesis is very important point [27]. Synthesis and antibacterial properties of nanosized powders obtained by aqueous and non-aqueous sol-gel methods in this system were studied recently by our team [28, 29]. Regardless of the large number of investigations in this system, studies of photocatalytic and antibacterial properties of ZnO/TiO₂ composite powders obtained via combustion method are very scarce.

The aim of the present study is to synthesize, characterize as well as to evaluate the photocatalytic and antibacterial properties of selected powder samples obtained by combustion gel method. The photocatalytic activity of obtained powders was verified toward Malachite Green

(MG) and Reactive Black 5 (RB 5). The antibacterial activity was performed in solid media (agar nutritive) against the cells of *E. coli* and *S. aureus*.

EXPERIMENTAL

Samples preparation

Based on the results of our previous studies in this system [27, 30-32], samples with different nominal compositions 90ZnO.10TiO₂ (sample A), 10ZnO.90TiO₂ (sample B) and 5ZnO.95TiO₂ (sample C) were selected for investigation (Table 1).

Table 1. Samples obtained by combustion gel method

samples N	Nominal composition	Precursors	Final product according to X-ray diffraction
A	90ZnO.10TiO₂.	Ti etoxide (sol A) + Zn nitrate (sol B)	ZnO
B	10ZnO.90TiO₂.	Ti etoxide (sol A) + Zn nitrate (sol B)	TiO₂ (rutile, anatase) + ZnTiO₃
C	5ZnO.95TiO₂.	Ti butoxide (sol A) + Zn nitrate (sol B)	TiO₂ (anatase)

The starting materials were: zinc nitrate – $Zn(NO_3)_2.6H_2O$ (Merck), titanium (IV) ethoxide (Fluka AG) - $Ti(OC_2H_5)_4$, titanium (IV) butoxide (Sigma-Aldrich) - $Ti(OC_4H_9)_4$ and ethylene glycol $(C_2H_6O_2)$ (Table 1). The main scheme for the synthesis is presented in Fig. 1.
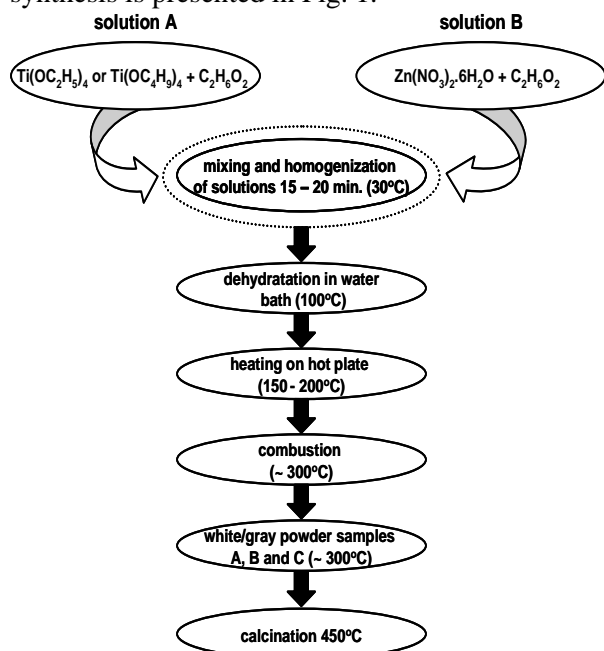
Fig. 1. Scheme for combustion gel synthesis of ZnO/TiO₂ powders

All solutions were prepared via dissolving of the precursors in ethylene glycol and absolute alcohol by means of vigorous magnetic stirring. A white xerogel was obtained by drying at 110ºC for 5h.

Subsequently, the as-obtained xerogel was subjected to evaporation in a water bath. During the heating on a hot plate up to 200-300ºC, combustion process takes place and as a result gray-white powders were obtained. According to the classification for the combustion synthesis made by [1], our method could be classified as a gel combustion method. The last step of synthesis consists of calcinations of the powders at 400-450ºC for 2 hours in air, until obtaining white powders (samples A, B and C). The calcinations temperature was selected on the basis of our previous investigations: from one side because there is almost no presence of organic constituents above 400⁰C and from another - to keep the small size of the obtained crystals. All samples were prepared by addition of Ti precursor solutions to the zinc nitrate. During the experiments the measured pH varied from 5 to 7 depending on compositions.

Samples characterization

The phase formation and morphology of the obtained powders were established by X-ray diffraction (Bruker D8 Advance X-ray apparatus) and SEM (JEOL Superprobe 733). Scanning electron micrographs were obtained from a VEGA 11 LSH scanning electron microscope (TESCAN, Czech Republic). Samples were deposited on a sample holder with an adhesive carbon foil. The energy dispersive X-ray spectra-EDX patterns were carried out using a Quantax QX2 system (Bruker/Roentec, Germany). The main short range

orders of the obtained powders were determined by IR spectroscopy using the KBr pellets method (Nicolet-320, FTIR spectrometer with a resolution of $\pm 1 cm^{-1}$, by collecting 64 scans in the range 4000–400 cm^{-1}).

Photocatalytic activity experiments

The photocatalytic activities of the synthesized powders were evaluated by UV-light induced photobleaching of two model pollutants - Malachite Green (MG) and Reactive Black 5 (RB5) aqueous solutions. The initial concentrations of MG and RB5 solutions were 5 ppm and 11 ppm, respectively. The composite sample (100 mg) was added to 150 ml dye solution to form slurry. After that, the suspension was magnetically stirred in the dark for 30 min to ensure the establishment of an adsorption-desorption equilibrium. The irradiation source was a black light blue UV-lamp (Sylvania BLB 50 Hz 8W T5) with the major fraction of irradiation occurring at 365 nm. The lamp was fixed 10 cm above the solution surface. All photocatalytic tests were performed at constant stirring (400 rpm) and room temperature of 25°C. At regular time intervals of illumination, aliquot samples of mixtures (3 mL) were collected and centrifuged in order to remove the solid particles. The discoloration was monitoring by measuring the absorbance of clear aliquots using Jenway 6505 UV-Vis spectrophotometer at maximum absorption wavelengths - 618 nm for MG and 600 nm for RB5.

Antibacterial measurements

Procedure for qualitative determination of inhibition zone

The strains of microorganisms - *E. coli* ATCC 25922 and *S. aureus* ATCC 25923, were cultured aerobically at 37°C for 18 h in 10mL nutrient broth. 20 ± 2mL of sterilized nutrient agar (solid media) was dispersed into each standard flat bottom Petri dish to obtain firmly solid agar before inoculating. 2 mL of inoculum from the ten times diluted inoculum cultured was transferred on the surface of the sterile agar area of a Petri dish. After that the tested samples were gently pressed to contact intimately the agar surface and the inoculum. The obtained mixtures were incubated at 37°C for 24 hours. The antibacterial activity is evident when a clear zone of inhibition of bacterial growth around the tested samples becomes visible.

RESULTS AND DISCUSSION

The X-ray diffraction patterns of obtained ZnO/TiO$_2$ white coloured powders are shown in Figure 2.
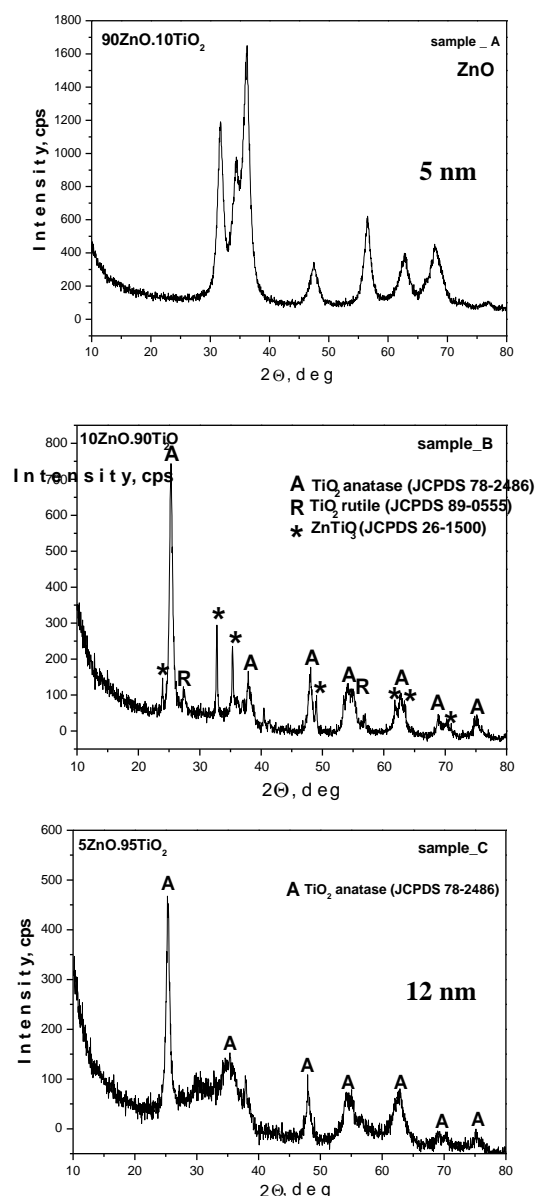
Fig. 2. XRD patterns of the investigated samples A, B and C

As can be seen different products were obtained. The characteristic peaks for zinc oxide (ZnO - JCPDS 36-1451) were identified in sample A. A mixture of TiO$_2$ polymorphous modifications (anatase - JCPDS 78-2486 and rutile - JCPDS 89-0555) as well as ZnTiO$_3$ (JCPDS 26-1500) were found is sample B, while anatase only, was separated in sample C. The average crystallite size of samples A and C calculated from the broadening of the diffraction line using Sherrer's equation are 5 and 12 nm, respectively. Our XRD results are compatible with the our previous data [33] as well as to the data reported for ZnO obtained by solution combustion method, where the size of the powders was found to be about 30 nm [16]. The SEM images and EDX spectra of obtained samples are presented in Fig. 3a, b, c.
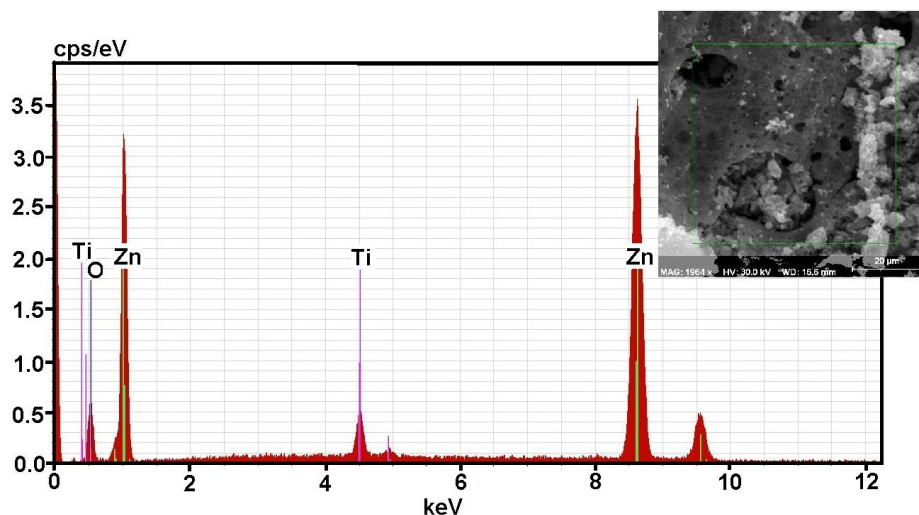
Fig. 3a. SEM micrograph and EDX spectrum of sample A
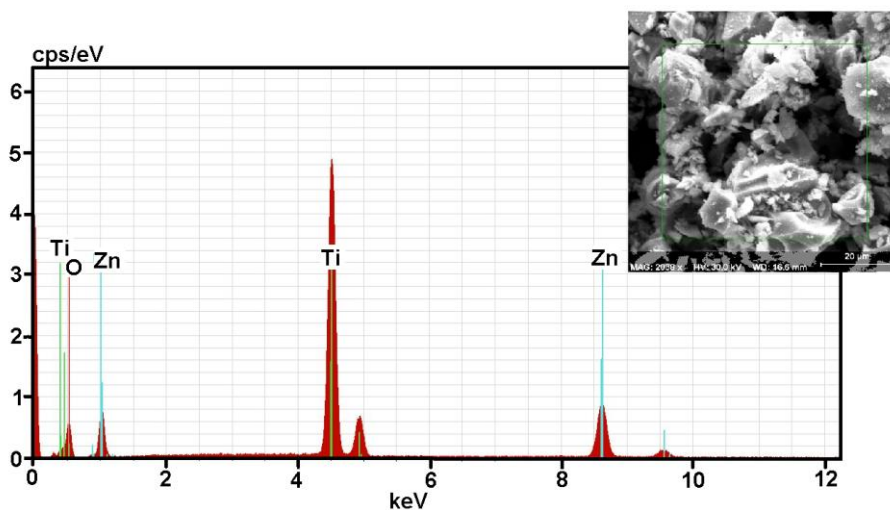
Fig. 3b. SEM micrograph and EDX spectrum of sample B
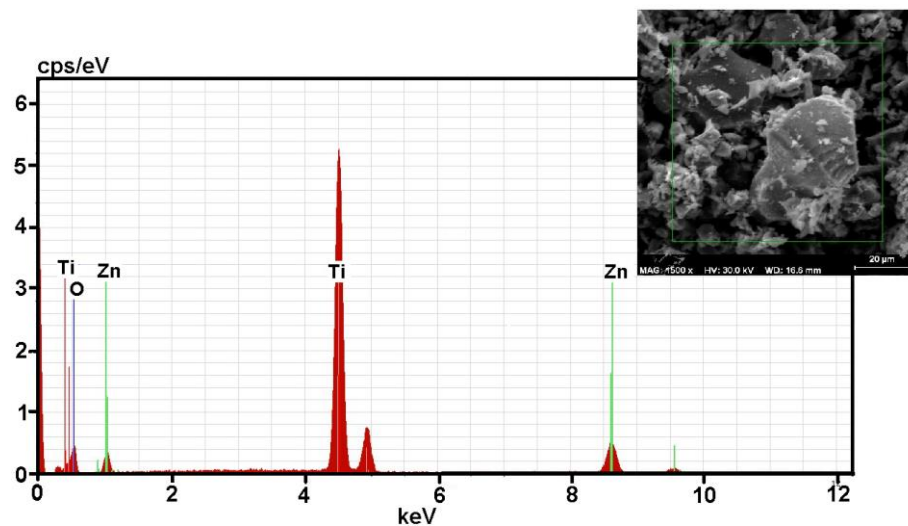
Fig. 3c. SEM micrograph and EDX spectrum of sample C

Irrespective that all samples are obtained by combustion method, the crystal morphology is different and sample A showed a porous agglomerate structure compared to the other two samples. The reason for that is may be due to the higher amount of zinc nitrate used as a precursor for ZnO at obtaining of this sample. This fact did not confirmed the previous suggestions of other

588
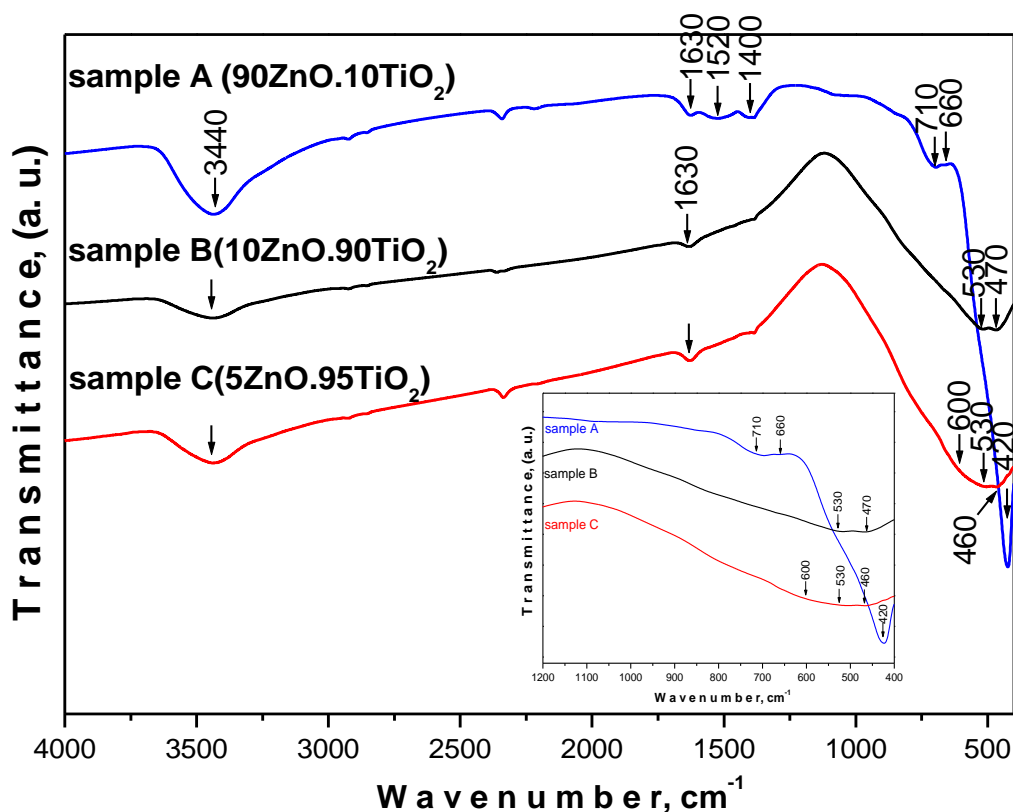
Fig. 4. IR spectra of the samples A, B and C in the range 4000 - 400 cm-1. The inset shows the IR spectra in the range 1200 - 400 cm-1.

authors, who claimed that Zn acetate leads to obtaining of more porous samples [18].

According to SEM observations (Figure 3a, b, c), during the calcinations, samples B and C are characterized by a strong tendency to agglomeration with the average particle size of the aggregates about 20-25 nm. The EDX results shows that the Ti, Zn and O are the principal components of investigated samples.

The IR spectroscopy was used in order to obtain an additional information for the phase formation in the investigated system. IR spectra of the powders calcinated at 450^0C are shown in Figure 4 and vibrations of the inorganic building units, only were recognized.In the spectrum of sample A ($90ZnO.10TiO_2$), dominant bands at 420 cm^{-1} along with weak shoulders at 700 and 660 cm^{-1} are observed. It is well known that bands in the absorption range 440-420 cm^{-1} could be related to the vibrations of ZnO_4 polyhedra [31, 34, 35]. The IR spectra of other two samples (B - $10ZnO.90TiO_2$ and C - $5ZnO.95TiO_2$) exhibited broad absorption region from 600 to 400 cm^{-1} in which follow the characteristic vibrations of ZnO and TiO_2 (anatase

and rutile) [36, 37, 38]. The XRD patterns of the samples did not detected the presence of TiO_2 and ZnO, when they are in low content (5, 10 mol %). Despite that fact, their presence was registered by IR (weak bands at 700, 660 cm^{-1} and bands in the range 600-400 cm^{-1}) due to the higher sensibility of this method [37]. The observed at 3440 and 1630 cm^{-1} bands in all IR spectra may be assigned to the absorbed water molecule [37].

Photocatalytic activity

The changes in MG and RB5 dyes concentration C/C_o (C_o initial concentration and C reaction concentration of the dye) by the synthesized composite samples with the time of radiation are shown in Figure 5 a, b.

The kinetics of photocatalytic degradation of many organic compounds has often been modeled by the Langmuir-Hinshelwood treatment of heterogeneous catalytic systems [39-41], expressed by Eq. (1):

$$r = -\frac{dC}{dt} = \frac{k_r KC}{1 + KC} \tag{1}$$
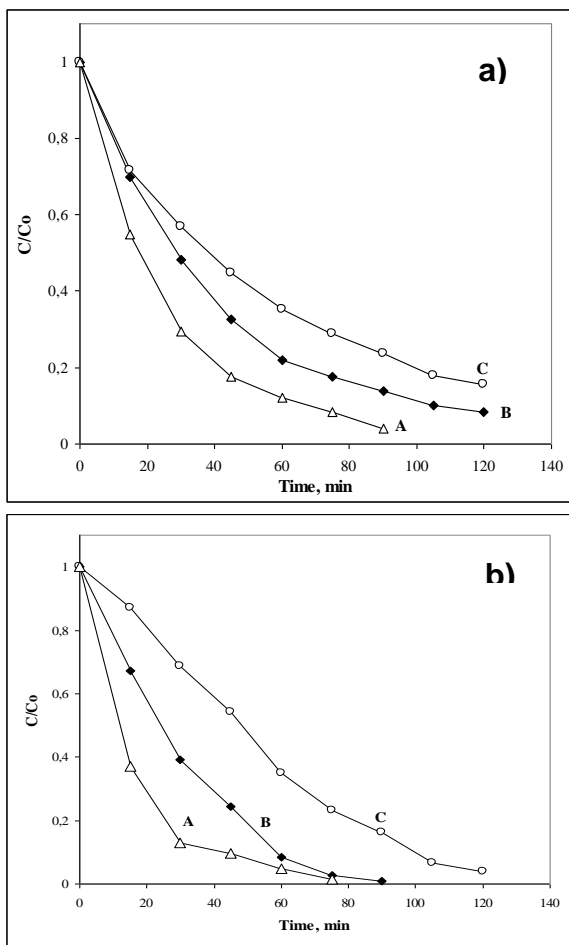
Fig. 5. Photocatalytic activity of samples A, B and C toward: a) MG and b) RB5.

where r represents the initial rate of photodegradation, i.e. dC/dt is the rate of disappearance of the pollutant, C is its concentration, k_r is the Langmuir-Hinshelwood reaction rate constant, and K is the Langmuir adsorption equilibrium constant. At a dilute concentration of pollutants ($C<10^{-3}$ M, i.e., $KC<<1$), pseudo-first-order kinetics model can be assumed as shown in Eq. (2):

$$-\frac{dC}{dt} = k_r K C \qquad (2)$$

Equation (2) can be integrated to expression (3):

$$ln\frac{C_o}{C} = k_r K t = k' t \qquad (3)$$

where C_o and C are, respectively, the initial concentration and the reaction concentration of the pollutant at time t, and k' – the apparent pseudo-first order rate constant. Under the same conditions, the initial degradation rate could be written in a form conforming to the apparent first order rate law:

$$r = k' C$$

The reaction kinetics for the initial 45 min of dyes degradation was studied by applying the pseudo-first order model expressed by equation (3). Figure 6 shows the plots of $ln(C_o/C)$ versus time for the studied samples. A good correlation to the pseudo-first order kinetics (R>0.99) was found from these results (Figure 6 a, b).
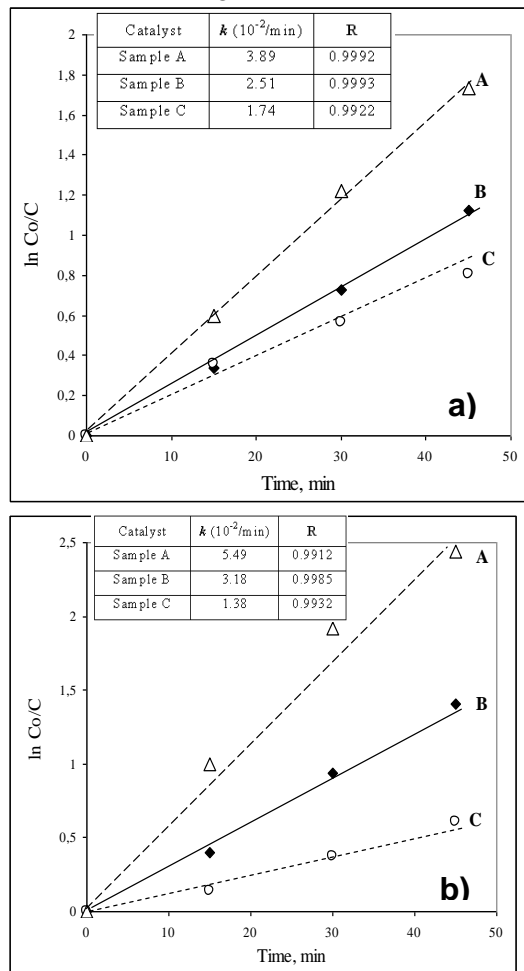
Fig. 6. Photocatalytic reaction kinetics of: a) MG decoloration and b) RB5 decoloration, both under UV irradiation.

The resulting first order rate constants were used for a comparison of the efficiency of photocatalytic process. The values of apparent rate constants show the highest photocatalytic activity of sample A on decoloration of both MG and RB5 dyes.

On one hand, the comparison between our present and previous results showed that as obtained ZnO/TiO$_2$ composite powders exhibited lower photocatalytic activity to that of pure ZnO and pure TiO$_2$ ($\sim$ 30 min toward MG and RB 5) under UV irradiation. On the other hand, the obtained results are better than those reported for TiO$_2$/ZnO composite powders obtained by combustion method, for which decolouration of azo dyes completed in 3 h under UV irradiation [42].

Antibacterial activity

The antibacterial activity was investigated by exposing studied microorganisms in nutritive media to the action of samples A, B and C. Each of the circular specimens with 5 mm diameter (filter paper with 0.005 g sample) was gently pressed on the *E. coli* and *S. aureus* inoculated agar surface before incubation. After incubation at 37°C for 24 h bacteria inhibition took place and a zone of inhibition appeared around the samples. No clear zone of inhibition was seen around the blank sample. The inhibition diameter was measured for all tested samples. The antibacterial activities of the samples against *E. coli* and *S. aureus* are presented in Fig. 7a and Fig. 7b, respectively.
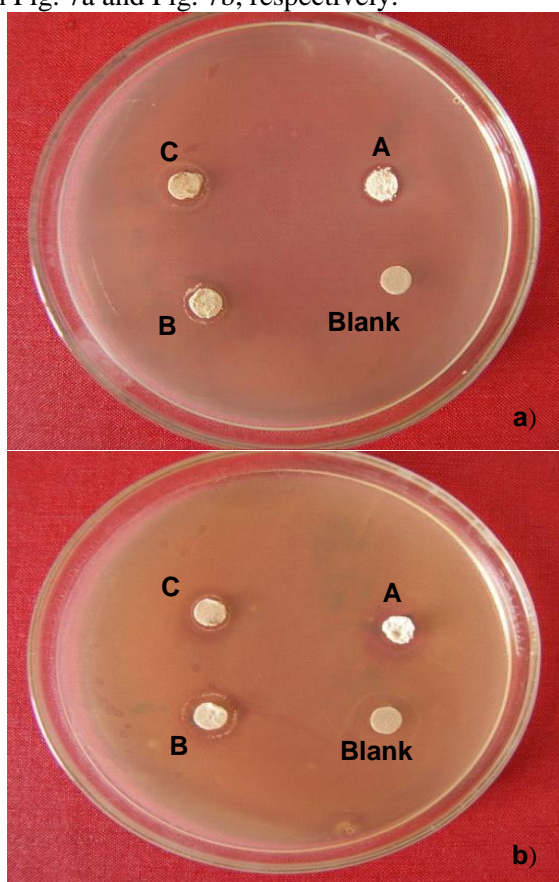
Fig. 7. Growth inhibition of the investigated samples for *E. coli* (a) and *S. Aureus* (b)

The antibacterial activity assessment of the powders is presented graphically in Figure 8. The synthesized ZnO/TiO$_2$ powders were found to have inhibition activity against both *E. coli* and *S. aureus*. The results for inhibition diameters are

Fig. 8. Antibacterial activity assessment of the investigated samples for E. coli and S. Aureus

shown in Table 2. As can be seen, sample A exhibited the best antibacterial activity in disinfection of *S. aureus*, while sample C exhibited best results for *E. coli* disinfection. This can be explained probably by the sample composition. The results obtained are in accordance with our previous findings [27, 43] and to the results obtained by other authors. ZnO has been found to be more effective toward Gram- negative than to gram-positive bacteria and to exhibit a sustainable antibacterial activity even in the dark conditions [44 - 46]. As is shown in Table 2, sample A contains mainly ZnO, in sample B a mixture of anatase, rutile and ZnTiO$_3$ was found while sample C contains only anatase. It is known that the photocatalytic activity of pure rutile phase is lower than that of pure anatase phase [47, 48]. Probably, the reason for the reduced antibacterial efficiency of sample B is the presence of small amount of rutile in its composition.

CONCLUSIONS

Nanosized (5-12 nm) ZnO/TiO$_2$ powders were obtained via combustion gel method. The as-prepared powders exhibited good photocatalytic activity towards two organic dyes Malachite green and Reactive Black5 under UV light. The synthesized powders showed antibacterial activity against *E. coli* and *S. Aureus* without induction of irradiation. The antibacterial effect of sample rich in ZnO was more pronounced for the culture of *S. aureus* while the antibacterial effect of sample rich in TiO$_2$ (anatase) was stronger for the culture of *E coli*. The obtained powders could be a candidate for environmental and biomedical application after further investigations on their antimicrobial activity.

Table 2. Antibacterial activity of investigated samples

Samples	Inhibition diameter (E. coli)	Inhibition diameter (S. aureus)
A (ZnO)	9 mm	19 mm
B (A, R, ZnTiO$_3$)	8 mm	12 mm
C (TiO$_2$ - A)	11 mm	14 mm

REFERENCES

1. K. C. Patil, S. T. Aruna, S. Ekambaram, *Curr. Opin. Solid State Mater. Sci.*, **2**, 158 (1997).

2. A. G. Merzhanov, A. S. Mukasyan, *Combustion of solid flame*, Moscow: Torus Press; 336 (2007).

3. A. S. Mukasyan, K. Martirosyan, editors, *Combustion of heterogeneous systems: fundamentals and applications for material synthesis*. Kerala, India: Transworld Research Network, 234 (2007).

4. A. A. Borisov, L. De Luca, A. G. Merzhanov, editors, *Self-propagating high temperature synthesis of materials*, New York: Taylor and Francis, p. 337 (2002).

5. A. M. Segadaes, *Eur. Ceram. News Lett.*, **9**, 1 (2006).

6. A. Varma, V. Diakov, E. Shafirovich, *AIChE J*, **51**, 2876 (2005).

7. A. S. Mukasyan, P. Epstein, P. Dinka, *Proceedings of the Combustion Institute*, **31**, 1789 (2007).

8. A. G. Merzhanov, I. P. Borovinskaya, A. E. Sytchev, SHS of nano-powders. In: Baumard J-F, editor. *Lessons in nanotechnology from traditional materials to advanced ceramics.* Dijon, France: Techna Group Srl, p. 1-27 (2005).

9. A. S. Mukasyan, A. S. Rogachev, *Prog. Energ. Comb. Sci.*, **34**, 377 (2008).

10. I. A. Filimonov, N. I. Kidin, *Comb. Explos. Shock Waves*, **41**, 639 (2005).

11. S. Ekambaram, K. C. Patil, M. Maaza, *J. Alloys Compd.*, **393**, 81 (2005).

12. K. C. Patil, S. T. Aruna, T. Mimami, "Combustion synthesis: an update", *Current Opinion in Solid State and Materials Science*, **6**, 507 (2002).

13. Y. Kitamura, N. Okinaka, T. Shibayama et al., *Powder Technology*, **176**, 93 (2007).

14. A. Sedghi, S. Baghshahi et al., *Digest J. Nanomater. Biostr.*, **6** (4), 1457 (2011).

15. Lin Cheng-Shiung, Hwang Chyi-Ching et al., *Mater. Sci. and Engineering B,* **140** 31 (2007).

16. S. Park, J. C. Lee, W. Lee et al., *J. Mater. Sci.*, **38**, 4493 (2003).

17. J. Tian, J. Wang, J. Dai, et al., *Surface & Coatings Technology*, **204**, 723 (2009).

18. G. Marci et al., V. Augugliaro, M. Lopez-Munoz et al., *J. Phys. Chem. B.*, **105**, 1026 (2001).

19. C. Shifu, Z. Wei, L. Wei et al., *Applied Surface Science*, **255**, 2478 (2008).

20. M. Cho, H. Chung et al., *Water Res.*, **38**, 1069 (2004).

21. K. Kuhn, I. Chaberny et al., *Chemosphere*, **58**, 71 (2003).

22. K. Sunada, Y. Kikuchi et al., *Environ. Sci. Technol.*, **32**, 726-728 (1998).

23. I. Ivanova, S. Kambarev, R. Popova, et al., *Biotechnology & biotechnol. eq. – special edition*, Second Balkan Confer. on Biology, 21-23 May 2010, Plovdiv; 567-570 (2010).

24. J. Sawai, T. Yoshikawa, *J. Appl. Microbiology*, **96**, 803 (2004).

25. N. Jones, B. Ray et al., *Microbiology Lett.*, **279**, 71 (2008).

26. N. Padmavathy and R. Vijayaraghavan, *Sci. Techol. Adv. Mater.*, **9**, 035004 (2008).

27. A. Shalaby, Y. Dimitriev, R. Iordanova, A. Bachvarova-Nedelcheva, Tz. Iliev, *J. Univ. Chem. Techn. Metall.*, **46** (2), 137 (2011).

28. A. Stoyanova, H. Hitkova, A. Bachvarova-Nedelcheva, R. Iordanova, N. Ivanova, M. Sredkova, *J. Univ. Chem. Techn. Metall.*, **48**, 154-161 (2013).

29. A. Stoyanova, A. Bachvarova-Nedelcheva, R. Iordanova, N. Ivanova, H. Hitkova, M. Sredkova, *Digest J. Nanomat. Biostr.*, **7**, 777 (2012).

30. A. Stoyanova, M. Sredkova, A. Bachvarova-Nedelcheva, R. Iordanova, Y. Dimitriev, H. Hitkova, Tz. Iliev, *Opt. Adv. Mater.-RC*, **4**, 2059 (2010).

31. Y. Dimitriev, Y. Ivanova, A. Staneva, L. Alexandrov, M. Mancheva, et al., *J. Univ. Chem. Techn. Metall.*, **44**, 235 (2009).

32. A. Bachvarova-Nedelcheva, R. Iordanova, A. Stoyanova, R. Gegova, Y. Dimitriev, A. Loukanov, *Central Eur. J. Chem.*, **11**, 364 (2013).

33. R. Gegova, A. Bachvarova-Nedelcheva, R. Iordanova, Y. Dimitriev, *J. Univ. Chem. Techn. Metall.*, **48**, 147-153 (2013).

34. M. Mancheva, R. Iordanova, Y. Dimitriev, *J. Alloys Compd.*, **509**, 15 (2011).

35. M. Andres-Verges, M. Martinez-Gailego, *J. Mater. Sci.*, **27**, 3756 (1992).

36. E. Yurchenko, G. Kustova, S. Bacanov, „*Vibratioanl spectroscopy of inorganic compounds*", Nauka, 1981 (in Russian).

37. A. I. Boldyrev, "*Infrared spectroscopy of minerals*", Nedra, 1976 (in Russian).

38. A. Murashkevich, A. Lavitkaya, T. Barannikova et al., *J. Appl. Spectr.*, **75**, 730 (2008).

39. B. Stefanov, N. Kaneva, G. Puma, C. Dushkin, *Colloids and Surfaces A: Physicochemical and Engineering Aspects*, **382**, 219 (2011).

40. K. Kumar, K. Porkodi, F. Rocha, *Cat. Comm.*, **9**, 82 (2008).

41. A. Bojinova, R. Kralchevska, I. Poulios, C. Dushkin, *Mater. Chem. Phys.*, **106**, 187 (2007).

42. X. Xu, J. Wang, J. Tian, et al., *Ceram. Intern.*, **37**, 2201 (2011).

43. A. Stoyanova, H. Hitkova, A. Bachvarova-Nedelcheva, R. Iordanova, N. Ivanova and M. Sredkova, *NanoScience and Nanotechnology*, **12**, 23 (2012).

44. Z. Emami-Karvani and P. Chehrazi, *African J. Microbiol. Res.*, **5**, 1368 (2011).

45. R. Rajendran, C. Balakumar, Hasabo A. Mohammed Ahammed, S. Jayakumar, et al., *Int. J. Eng. Sci. Techn.*, **2**, 202 (2010).

46. K. Hirota, M. Sugimoto, M. Kato, K. Tsukagoshi, T. Tanigawa, H. Sugimoto, *Ceramics International*, **36**, 497 (2010).

47. S.M. Gupta, M. Tripathi, *Chinese Science Bulletin*, **56**, 1639 (2011).

48. H. Hitkova, A. Stoyanova, N. Ivanova, M. Sredkova, R. Iordanova, A. Bachvarova-Nedelcheva, *J. Optoel. Biomed. Materials*, **4**, 9 (2012).

СИНТЕЗА, ХАРАКТЕРИЗИРАНЕ И СВОЙСТВА НА ПРАХОВЕ ОТ ZNO/TIO$_2$, ПОЛУЧЕНИ ПО МЕТОДА НА ИЗГАРЯНЕ В ГЕЛ

А.Д. Бъчварова-Неделчева[1*], Р.Д. Гегова[1], А.М. Стоянова[2], Р.С. Йорданова[1],В.Е. Копциа[3], Н.К. Иванова[2], И. Санду[3]

[1]Институт по обща и неорганична химия, Българска академия на науките, София
[2] Медицински университет, Плевен
[3] Инердисциплинарна платформа „Археоинвест“, Лаборатория за научни изследвания, Яш, Румъния

(Резюме)

Получени са прахове от ZnO/TiO$_2$ със субмикронни размери по метода на изгаряне в гел. Охарактеризирани са структурата, морфологията и елементния състав чрез XRD, IR-спектроскопия, сканираща електронна микроскопия с SEM с EDX-анализ. Фотокаталитичната активност на пробите е оценена чрез разпадането на малахитово зелено и реактивно черно 5 във водни разтвори при облъчване с ултравиолетва светлина. Антибактериалните отнасяния на получените проби са изследвани в твърда среда (върху агар) спрямо Грам-негативните бактерии *Escherichia coli* АТСС 25922 и Грам- положителните *Staphylococcus aureus* АТСС 25923. Диаметърът на инхибиране е измерван за всички проби. Не са забелязани зони на инхибиране при контролните експерименти. Всички проби проявяват силна бактерицидна активност срещу двата избрани бактериални клетки.

Full factorial design of experiments for boron removal from Colemanite mine wastewater using Purolite S 108 resin

M. Korkmaz*,[1], B. A. Fil[1,2], C. Özmetin[1] , Y. Yaşar[1]

[1]*Balıkesir University, Engineering & Architecture Faculty, Environmental Engineering Department, Çağış Campus Balıkesir, Turkey*
[2]*Atatürk University, Engineering Faculty, Environmental Engineering Department, Erzurum Turkey*

Boron pollution has a vital importance in Bigadiç boron mine in Turkey because the wastewaters of the mine are stored in a soil dam that threats the underground water quality. In this study the optimization of boron removal from the boron mine wastewater using Purolite S 108 resin was investigated by means of a 2^3 full factorial experimental design. Experiments were carried out in batch mode as a function of pH, temperature and resin-to-solution ratio. The low (1) and high (2) levels of the parameters for pH, temperature and resin-to-solution ratio were 2.5 and 10, 12 ºC and 40 ºC and 1 g/50mL and 2 g/50mL respectively. Boron adsorption capacity of the resin increased with low temperature, low resin-to-solution ratio and high pH. When the probability constants ($p<0.05$) at 95% confidence level were taken into consideration, only pH was found as statistically important parameter. The optimization of the parameters to obtain optimum conditions was done by interpretation of cube plots, Pareto chart and contour plots. A time span of 48 hours was enough to reach the equilibrium. Adsorption data were analyzed with the Langmuir and Freundlich isotherms. Data fitted to the Langmuir isotherm with a coefficient of determination value of 0.988. Maximum adsorption capacity was calculated as 12.87 mg g^{-1}. The fixed bed kinetics of boron adsorption onto resin could be explained by the Thomas and Yoon-Nelson models with a coefficient of determination value of 0.938. The fixed bed capacity of the resin was calculated as 12.71 mg g^{-1}.

Keywords: Boron Removal; Ion Exchange; Purolite S 108; Full Factorial Design; Isotherm; Fixed Bed

INTRODUCTION

The borate minerals identified in nature have 230 different crystal structures and it is thought that new borates may be found in nature [1]. At nature borates found in oxide forms together with the structural metal cations such as potassium, calcium, magnesium, aluminum, etc. [1,2]. Only several borates have commercially important deposit viz., colemanite (Ca2B6O11.5H2O), ulexide (NaCaB5O9.8H2O), pandermit (Ca4B10O19.7H2O), kernit (Na2B4O7.4H2O) and tinkal (Na2O.2B2O3.10H2O) [1,2]. Boron is widely used in a variety of applications including the nuclear, fuel, military, glass, electronic and computer, energy devices, photography, medicine, cosmetic, construction, communication, paper, rubber, plastic, chemistry, surface protecting material, machinery, metallurgy, explosive, automotive, ceramic, agriculture, textile, space and aviation industries [3]. Turkey has about 61% of the World boron reserves [4]. The known borate reserves in Turkey are located in four main districts, namely Emet, Bigadiç, Kırka and Mustafa Kemal Paşa [5]. One of the richest colemanite deposits of Turkey is located in Bigadiç region. After colemanite is mined in Bigadiç deposit, it is subjected to washing to remove attached clay minerals. Eventually, colemanite is dissolved with water and washing waster is polluted with boron. Therefore, washing waters are stored in a soil wastewater dam that causes a great concern due to contamination risk of underground water with boron. Boron containing wastewaters are not appropriate for irrigation because boron accumulates very fast in soils as it adsorbs onto clays [6]. Although boron is a required trace element for plants, animals and humans, there is a narrow concentration range between its detrimental and toxic effects [7]. Boron also forms complexes with heavy metals in the soil which are more toxic than boron and heavy metals [6]. Therefore, washing waters of Bigadiç colemanite mine should be refined from boron with a suitable method.

In the last two decades, several physico-chemical methods have been reported for removal of boron viz., adsorption[5], ion exchange [6], electrocoagulation [8], reverse osmosis [9], electrodialysis [10], solvent extraction after

* To whom all correspondence should be sent:
E-mail: korkmazm@balikesir.edu.tr

complexation [11] and chemical coagulation [12]. Although boron resins are expensive, ion exchange method is still one of the effective methods for boron removal from wastewaters especially if the boron should be recovered. In the literature, several boron selective or strong base resins were reported to remove boron from solution [6]. But the Purolite S 108 resin is lack of any reported study showing its exact capacity under different experimental conditions. The cheap, easy and short-winded way of adsorption capacity determination of adsorbents is to design of experiments by the full factorial, response surface or taguchi approaches. Of these approaches, the full factorial design of experiments requires the most few experiments [13]. Therefore, in this study, the experiments were designed by the full factorial approach using Minitab 16.0 programme.
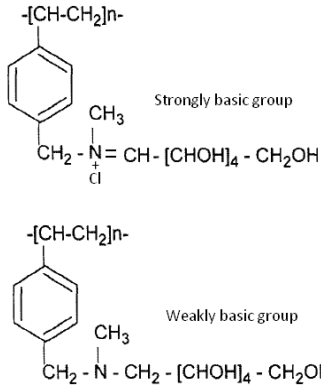
In this study, boron removal from Bigadiç mine wastewater by ion exchange method using Purolite S 108 resin was investigated by means of 23 full factorial experimental design. In the experiment the effects of pH, temperature and solid-to-solution ratio were optimized. The equilibrium data were applied the Langmuir and Freundlich models. The fixed bed kinetics of the resin were also investigated.

MATERIAL AND METHOD

Material

In this study, Purolite S 108 was used as boron resin. The characteristics of Purolite S 108 resin are given in Table 1.

Table 1: Typical chemical and physical characteristics of Purolite S 108

Property	Description
Polymer structure	Macroporous polystyrene cross-linked with divinylbenzene
Optical appearance	Spherical beads
Functional groups	Complex amino
Ionic form, as shipped	Cl
Total capacity (Cl_ form) (eq L^{-1})	0.6 (min)
Total boron capacity (Cl_ form) (eq L^{-1})	0.35
Selective boron capacity (Cl_ form) (eq L^{-1})	0.20 (min)
Moisture retention (Cl_ form) (%)	45–55
Reversible swelling FB→Cl (%)	10 (max)
Specific gravity (Cl_ form)	1.1
Temperature limit (Cl_ form) (ºC) 60	60
pH limits (operating)	1–13
Structure	

The resin was in the chlorine form when purchased. The real capacity of the resin was calculated as 0.538 meq g-1 by an ion exchange reaction between OH- and exchangeable Cl- in the resin [14]. The theoretical capacity of the resin was reported as 0.545 meq g-1 [14].

Experimental Method

Batch boron removal experiments were carried out in a temperature controlled incubator shaker at 150 rpm agitation speed. The used wastewater in the experiments was supplied from Bigadiç colemanite mine and had a 382 mg L^{-1} boron concentration. The pHs of the solutions were adjusted by appropriate addition of diluted HCl and NaOH solutions. The high and low levels of the parameters used in the experimental design are given in Table 2.

Table 2: The high and low levels of the parameters used in the experimental design

Parameter	Abbreviation	Low Level (1)	High Level (2)
pH	pH	2.5	10
Temperature (ºC)	T	12	40
Resin-to-solution ratio (g/50mL)	M	1	2

Boron analysis was done by the titrimetric method in which mannitol was used as a complexing agent because boric acid is a weak acid. The procedure of the boron analysis was as follow: 5 mL boron solution was pipetted into 100 mL beaker and 50 mL distilled was added. Then solution pH was adjusted to 7.6 and 5 g mannitol was added while the solution being stirred, thereafter the solution was titrated with 0.02 N KOH up to solution pH became again 7.6. 1 mL 0.02 N KOH is equal to 0.6964 mg B_2O_3 [8]. The boron analyses were duplicated and arithmetic average of the results was put into analysis. The capacity of the resin was calculated using the following equation:

$$q_e = \frac{(C_0 - C_e) \times V}{M} \qquad (1)$$

Where C_0 (mg L^{-1}) and C_e (mg L^{-1}) are the boron concentration at initial and after equilibrium respectively. V is the volume of the solution (L) and M is the mass (g) of the resin.

The adsorption isotherm experiments were carried out by synthetic boric acid solutions of which concentrations changed from 100 to 700 mg L^{-1} (Merck Product). For this purpose, the pHs of the solutions were adjusted to 7 and 1 g resin was added to the solutions and thereafter solutions were treated with the resin during 48 hours at 30 ºC. The fixed bed experiments were carried out in a jacketed glass column reactor that had 2 cm inner diameter and 30 cm length. 10 grams of the resin were immersed in deionized water during 30 min and then filled to the reactor. The wastewater was transferred to the reactor at 2.038 mL min^{-1} speed. Temperature and pH of the wastewater was 12 ºC and 10 respectively. The optimum conditions obtained from 2^3 full factorial design were applied to fixed bed experiment. Resin capacity was calculated by the following equation.

$$q_0 = \int_0^{V_t} \frac{(C_0 - C)dV}{m} \qquad (2)$$

Where, q_0 resin capacity (mg g^{-1}), V_t solution volume passing from the fixed bed at time t, C and C_0 are the concentration of an outward solution and its initial concentration, respectively, m is resin amount in fixed bed (g).

RESULTS AND DISCUSSION

Statistical Design of Experiments

The application of statistical design to the adsorption process provides the overall process control to reach the desired response and also requires less experimental time and cost. Statistical design of experiment reduces the total number of experiments when compared with the classical single parameter experiments. The design determines separately the importance degrees of each factor and their interactions on the response [13]. In this study, the parameters such as pH, temperature and resin-to-solution ratio were optimized by 2^3 full factorial design using statistical software MINITAB (Version 16) of Minitab, Inc., USA. The low (1) and high (2) levels of the parameters were 2.5 and 10 for pH, 12 and 40 ºC for temperature and 1 and 2 g/50 mL for solid-to-solution ratio respectively. The response used in the statistical analysis was the adsorption capacity (Q_e) of the resin. The experimental matrix for boron removal from the wastewater is given in Table 3. The number of experiments in the experimental matrix was calculated by the equation of $a^k = 2^3 = 8$ where a is the number of levels and k is the number of factors [13]. Boron analysis was carried out in duplicate and the arithmetic average of the results was used in the statistical analysis. In the statistical analysis, the effect degrees of the parameters and their interaction effect on the response were investigated by taking into consideration the regression model coefficients. The significance of model coefficients was determined by the Student's t test. The P values (probability constants) were used as control parameter to check the reliability of the developed statistical model, individual and interaction effects of the parameters. In general, the larger the magnitude of t and the smaller the value of P, the more significant is the corresponding coefficient term [13]. Main factor, interaction effect, coefficients of the model, standard deviation of each coefficient, and probability for the full 2^3 factorial design are presented in Table 4.

Table 3: Experimental matrix for boron removal from wastewater

Trial	T	pH	M	Adsorption Capacity (Q_e, mg g^{-1})		
				(1)	(2)	Average
1	2	2	2	9.32171	9.32171	9.32171
2	2	2	1	12.2514	12.2514	12.2514
3	2	1	2	7.78078	7.78078	7.78078
4	2	1	1	8.14227	8.14227	8.14227
5	1	2	2	9.43586	9.37879	9.40732
6	1	2	1	13.0504	12.7080	12.8792
7	1	1	2	8.00907	7.89493	7.95200
8	1	1	1	8.14227	8.14227	8.14227

Table 4: Full factorial fit for the boron adsorption.

Term	Effect	Coefficient	t-value	p
Constant		9.4846	106.36	0.006
T	-0.2212	-0.1106	-1.24	0.432
pH	2.9606	1.4803	16.60	0.038
M	-1.7383	-0.8692	-9.75	0.065
T pH	-0.1355	-0.0678	-0.76	0.586
T M	0.0927	0.0464	0.52	0.695
pH M	-1.4625	-0.7312	-8.20	0.077
[a]pH·M·T	—	—	—	—

S.E. of coefficient = 0.251023 R^2 = 99.76%, t-value: Student's test value, p: probability.
[a]When the trial effect (pH·m·T) was added to the analysis, the programme gave error and therefore its statistical results were not shown.

The analysis of variance for the full 2^3 factorial design is presented in Table 5.

Table 5: Analysis of variance for boron adsorption.

Source	Degree of freedom (d.f.)	Sum of squares (seq. SS)	Adjusted Sum of squares (adj. SS)	Adjusted Mean square (adj. MS)	F-value	p-value
Main Effects	3	23.6716	23.6716	7.8905	124.03	0.066
2-Way Interactions	3	4.3315	4.3315	1.4438	22.70	0.153
Residual Error	1	0.0636	0.0636	0.0636		
Total	7	28.0667				

As can be seen in Table 4, only solution pH effect was found as statistically important at 95% confidence level (p<0.05) and the other parameters were unimportant. The developed statistical model was as follows.

Boron adsorption;

(Q_e) = 9.4846-0.1106T+1.4803pH-0.8692m-0.0678TpH+0.0464Tm-0.7312pHm (3)

This function describes how the experimental variables and their interactions influence the boron adsorption (the response). As can be seen both in equation (3) and Table 4, the increasing solution temperature and resin-to-solution ratio had negative effect on the response; however, solution pH had positive effect. Furthermore, while the increasing TpH and pHm interactions had negative effect on the response, Tm interaction had positive effect on response. The reason of positive effect of Tm interaction is the swelling of resin with increasing temperature. The solution pH had the greatest effect on response and followed by resin amount (m), pH-

resin-to-solution ratio interaction (pHm), temperature (T), temperature-pH interaction (TpH), temperature-resin-to-solution ratio interaction (Tm). When the trial effect (pH·m·T) was added to the analysis, the programme gave error, therefore its statistical results were not shown. We thought that this error occurred due to extremely distortion of statistical importance of p value of trial effect (pH·m·T) from 95% confidence level.

Cube Plots, Pareto Chart and Contour Plots

Figure 1 (Cube plot) illustrates the change of the resin capacity based on low and high levels of temperature, initial pH, and resin-to-solution ratio. As can be seen in Figure 1, the resin-to-solution ratio and temperature decreased the adsorption capacity with increase of the low level (1) of factors to high (2) level; however, pH increased the capacity when low (1) level of the factor increased to high (2) level. The relative importance of the main effects and their interactions was also observed on the Pareto chart (Figure 2).
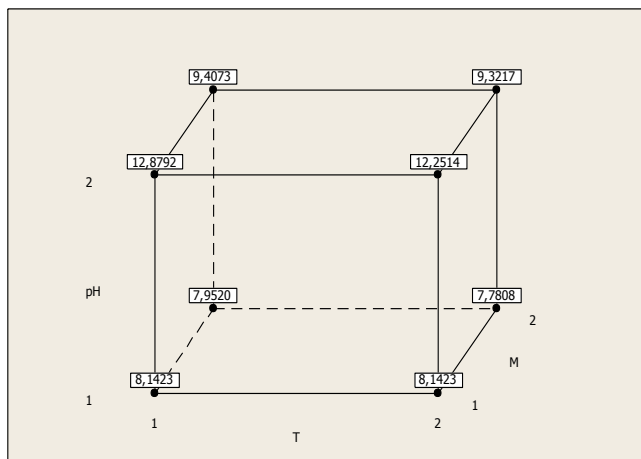
Fig. 1. Cube plots for adsorption capacity (Q_e).

Fig. 2. Pareto chart of the standardized effects

A limit value for statistically comparison of importance of the factors was calculated by t-test as 12.71 (Pareto chart). According to Figure 2, as right side of reference line (12.71) indicates statistically importance of the factors, only pH effect was determined as statistically important and the other factors were statistically unimportant. Contours of the estimated response surface are given in Figure 3.

Contour plots enable to estimate the response Q_e values and the height of the surface represents the value of Q_e in Figure 3. In principle as the contour plots represent the interaction effect of factors, the lines are inclined shaped [15].

Effect of Parameters

In this study the effects of pH, temperature and solid-to-solution ratio on response (Q_e) were optimized using 2^3 full factorial experimental design.

Effect of temperature

Solution temperature significantly effects the boron removal by ion exchange method because boron anion type changes in liquid phase based on

Fig. 3. Contours of the estimated response surface for Qe.

temperature. In general, lower the solution temperature and higher the concentration, the more high is the molar fraction of polyborate ions in solution [16]. According to Figure 1, the decreasing temperature increased the polyborate anion number and thus much more boron adsorption occurred on the resin [14, 16]. The increasing effect of lower temperature on the capacity showed that the process had exothermic nature.

Effect of pH

Solution pH effects boron anion type in liquid phase and resin exchangeable anion type. Purolite S 108 resin used in this study was in the chloride form at box form but it started to convert to the (OH-) form at high pHs. Korkmaz (2011) reported that when 16 grams Purolite S 108 were treated with 100 mL 2 M NaOH solution during 24 hours, the resin gave approximatelly 0.3 grams chlorine to the solution [14]. This showed the ion exchange reaction between chlorine and hydroxyl ions [14]. OH binded to the protonated amine [17]. As can be seen in Figure 1, borate anions increased at high pHs and this resulted in adsorption capacity increase [14, 16]. Furthermore complexation reaction number at the resin phase increased with conversion of the resin to OH form [14, 16]. The reaction mechanism between boric acid and resin is given in Figure 4.
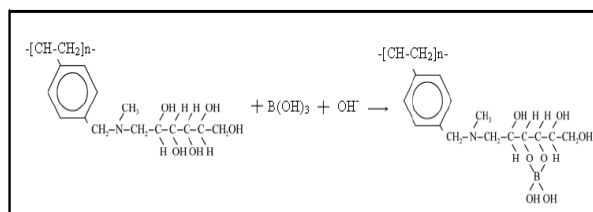
Fig. 4. The reaction mechanism between boric acid and Purolite S 108 resin

Effect of resin-to-solution ratio

Increasing resin-to-solution ratio decreased the driving force of borate anions on per unit resin particle and therefore boron adsorption capacity of the resin decreased at high resin-to-solution ratios [14, 18].

Adsorption Isotherms and Fixed Bed Kinetics

Adsorption isotherms are useful functions in design of batch adsorbers and their fitness to the equilibrium data is an important criterion. For this purposes, the most applied procedures to the isotherm data are linear regression and non-linear regression analyses. While linear-regression analysis occurs possible with the direct linearization of isotherm model, the non-linear analysis of the isotherm models occurs possible with minimization of standard normalized errors of different error functions [19]. The Langmuir and Freundlich isotherm models were applied to the isotherm data by the linear regression analysis. The Langmuir isotherm is given as follows [19].

$$q_e = q_m k_a C_e / (1 + k_a C_e) \qquad (4)$$

The above equation can be rearranged to the following linear form,

$$C_e / q_e = 1 / q_m k_a + C_e / q_m \qquad (5)$$

Where, Ce is the equilibrium concentration in liquid phase (mg/L). qe is the maximum amount of the boron adsorbed (mg/g). qm is qe for a complete monolayer (mg/g). ka is a sorption equilibrium constant (L/mg).

Freundlich isotherm is given as follow [19]:

$$q_e = k_F C_e^{1/n} \qquad (6)$$

The equation is frequently used in the linear form by taking the logarithm of the both sides of the above equation.

$$\ln q_e = \ln k_F + \frac{1}{n} \ln C_e \qquad (7)$$

Where, Ce is the equilibrium concentration in liquid phase (mg/L). qe is the maximum amount of boron adsorbed (mg/g). k_F is the Freundlich adsorption capacity $(mg/g)(L/mg)^{1/n}$. 1/n is sorption equilibrium constant (unitless).

The fitness of isotherms to the data is given in Table 6. According to Table 6, the data fitted to the Langmuir isotherm and this showed the homogeneously distribution of active sites throughout the resin particles [19]. According to Figure 5, boron capacity of the resin at high concentrations decreased.
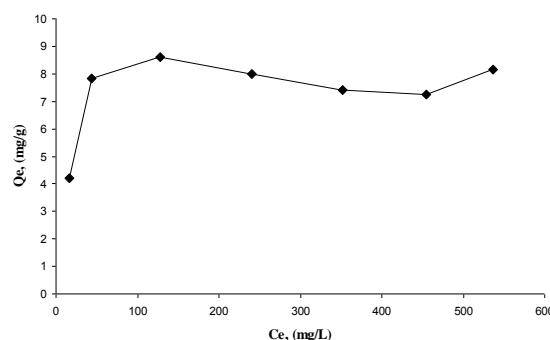
Fig. 5. Adsorption isotherm plot for boron adsorption (pH 7, temperature 30 oC, solid-to-solution ratio 1g/50 mL, agitation speed 150 rpm)

This attributed to product film outer surface of the resin [14]. The resin performance in a fixed bed is given in Figure 6.
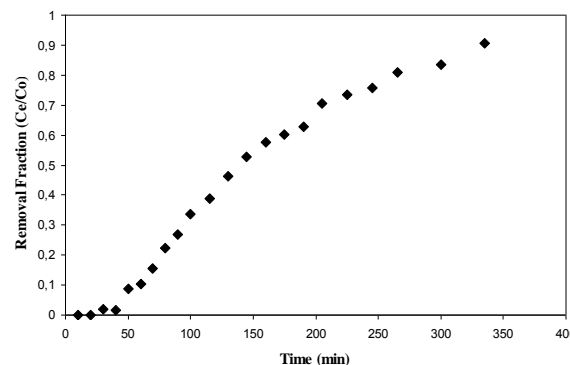
Fig. 6. Boron removal in the fixed bed reactor

The fixed bed kinetics of the resin were analyzed with the Thomas and Yoon-Nelson models. The linear model equation for Thomas model is given as follows [20].

$$\ln\left(\frac{C_0}{C} - 1\right) = \frac{K_T q_0 m}{Q} - \frac{K_T C_0}{Q} V \qquad (8)$$

Table 6: The coefficient of determination values and isotherm parameters

Isotherm		Value
	R^2	0.991
Langmuir Isotherm	k_a (L/mg)	3.302
	q_m (mg/g)	7.776
	R^2	0.498
Freundlich Isotherm	k_F $(mg/g)(L/mg)^{1/n}$	21.712
	n (unitless)	7.898

Table 7: The coefficient of determination values and model constants for kinetic models.

	Model	Value
	R^2	0.938
Thomas	K_T (mL/(min mg))	-39×10^{-6}
	q_0 (mg/g)	12.71
	R^2	0.938
Yoon-Nelson	K_{YN} (min^{-1})	0.015
	τ (min)	163.41

Where K_T is the Thomas rate constant (mL min^{-1} mg^{-1}) and Q is the volumetric flow rate (mL min^{-1}). C and C_0 are the concentration of an outward solution and its initial concentration (mg L^{-1}), respectively. m is the weight of ion-exchange resin (g), q_0 is the maximum concentration of boron ion-exchanged, and V is the volume of solution (L). The main advantages of this model are its simplicity and reasonable accuracy in predicting the breakthrough curves under various operating conditions [21].

The linear model equation for Yoon-Nelson model is given as follows [20].

$$\ln\left(\frac{C}{C_0 - C}\right) = K_{YN}t - \tau K_{YN} \qquad (9)$$

Where K_{YN} is the rate constant (min^{-1}); τ, the time required for 50% adsorbate breakthrough (min). C and C_0 are the concentration of an outward solution and its initial concentration (mg L^{-1}), respectively. t is time (min). The Yoon-Nelson model is not only less complicated than other models, but also requires no detailed data concerning the characteristics of the sorbate, the type of the sorbent, and the physical properties of the sorption bed [20]. The coefficient of determination values and model constant for Thomas and Yoon-Nelson models are given in Table 7. The coefficient of determination values for both the models are the same (0.938). The fitness of the kinetic models to data was given in Figure 7 and 8.
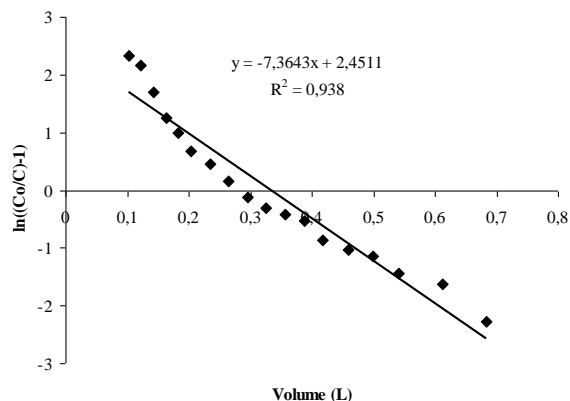
Fig. 7. The fitness of fixed bed kinetic data to the Thomas model
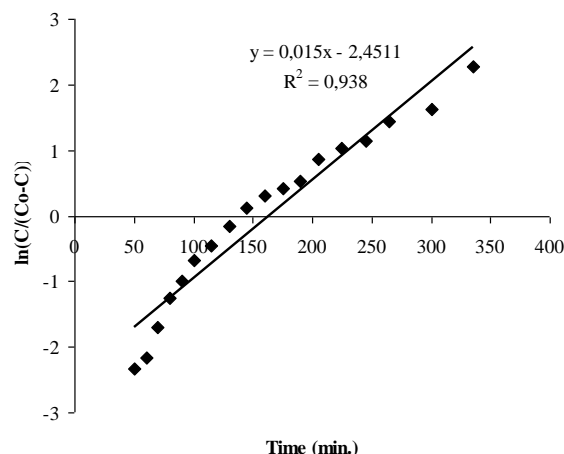
Fig. 8. The fitness of fixed bed kinetic data to the Yoon-Nelson model

CONCLUSION

The optimization of boron removal from colemanite mine wastewater using Purolite S 108 resin was performed by means of 2^3 full factorial experimental design. For this purpose, the optimization of the factors to obtain optimum conditions was done by interpretation of cube plots, Pareto chart and contour plots. Results showed that the resin-to-solution ratio and temperature decreased the adsorption capacity with increase of the low level (1) of factors to high (2) level; however, pH increased the capacity when low (1) level of the factor increased to high (2) level (Cube Plots Figure 1). The solution pH had the greatest effect on response and followed by resin amount (m), pH-resin-to-solution ratio interaction (pHm), temperature (T), temperature-pH interaction (TpH), temperature-resin-to-solution ratio interaction (Tm) (Pareto Chart Figure 2). Solution pH was found as statistically important based on the probability parameter ($p < 0.05$) at 95% confidence level. The isotherm data fitted to the Langmuir model. Maximum capacity of the resin in batch mode was calculated as 12.87 mg g^{-1}. Boron removal kinetic of the resin was fitted both to Thomas and Yoon-Nelson models. The fixed bed capacity of the resin was calculated as 12.71 mg g^{-1}. Due to high boron capacity Purolite S 108 resin is an effective resin for boron removal from waters.

REFERENCES

1. D. E. Garrett, *Borates:Handbook of Deposits, Processing, Properties, and Use*: Academic Press, 1998.
2. A. E. Yilmaz, R. Boncukcuoglu, M. T. Yilmaz, M. M. Kocakerim, *J. Hazard. Mater.,* **117**, 221 (2005).
3. S. Ayaz, "Beneficiation of fine tailings of Emet Hisarcık Boron Plant waste dam by flotation," Master Thesis, Institute of Science, Department of Mining Engineering, Dumlupınar University, Kütahya, 2007.
4. A. Demirbas, H. Yuksek, I. Cakmak, M. M. Kucuk, M. Cengiz, M. Alkan, *Resources, Conservation & Recycling,* **28**, 135 (2000).
5. N. Öztürk, D. Kavak, *J. Hazard. Mater.,* **127**, 81 (2005).
6. R. Boncukcuoğlu, A. E. Yılmaz, M. Muhtar Kocakerim, M. Çopur, *Desalination,* **160**, 159 (2004).
7. C. Özmetin, Ö. Aydın, M. M. Kocakerim, M. Korkmaz, E. Özmetin, *Chem. Eng. J.,* **148**, 420 (2009).
8. A. E. Yılmaz, R. Boncukcuoğlu, M. M. Kocakerim, E. Kocadağistan, *Desalination,* **230**, 288 (2008).
9. P. Dydo, M. Turek, J. Ciba, J. Trojanowska, J. Kluczka, *Desalination,* **185**, 131 (2005).
10. Z. Yazicigil, Y. Oztekin, *Desalination,* **190**, 71 (2006).
11. M. Matsumoto, K. Kondo, M. Hirata, S. Kokubu, T. Hano, T. Takada, *Sep. Sci. Technol.,* **32**, 983 (1997).
12. A. E. Yilmaz, R. Boncukcuoğlu, M. M. Kocakerim, *J. Hazard. Mater.,* **149**, 475 (2007).
13. D. Kavak, *Environ. Progress & Sustainable Energy,* **30**, 527 (2011).
14. M. Korkmaz, "Boron Removal from waters using Purolite S 108 resin," Master Thesis, Institute of Science, Department of Environmental Engineering, Balikesir University, Balikesir, 2011.
15. D. Bingol, N. Tekin, M. Alkan, *Applied Clay Science,* **50**, 315 (2010).
16. J.W. Na, K. J. Lee, *Ann. Nucl. Energy,* **20**, 455 (1993).
17. R. Boncukcuoğlu, A. E. Yilmaz, M. M. Kocakerim, M. Copur, *Desalination* **160** 159 (2004)
18. M. Korkmaz, C. Özmetin, B.A. Fil, E. Özmetin, Y. Yaşar, *Fresenius Environ. Bull.,* **22**, 1524 (2013).
19. A. Gunay, *J. Hazard. Mater.,* **148**, 708 (2007).
20. T. E. Köse, N. Öztürk, *J. Hazard. Mater.,* **152**, 744 (2008).
21. S. H. Lin, C. D. Kiang, *Chem. Eng. J.,* **92**, 193 (2003).

ПЪЛЕН ФАКТОРЕН ЕКСПЕРИМЕНТ ЗА ОТСТРАНЯВАНЕТО НА БОР ОТ ОТПАДЪЧНИТЕ ВОДИ ОТ МИНАТА КОЛЕМАНИТ С ЙОНООБМЕННАТА СМОЛА PUROLITE S 108

М. Коркмаз*,[1], Б.А. Фил[1,2], Дж. Йозметин[1], И. Яшар[1]

[1]*Департамент по екологично инженерство, Факултет по инженерство и архитектура, Университет Балъкешир, клон Чаъш, Балъкешир, Турция*
[2]*Департамент по екологично инженерство, Факултет по инженерство, Университет „Ататюрк", Ерзурум, Турция*

Замърсяването с бор има жизнено важно значение в мината Бигадич в Турция, тъй като отпадъчните води от мината се съхраняват в бент с пръстено дъно, което застрашава чистотата на подпочвените води. В настоящата работа се оптимизира отстраняването на бор от бородобивната мина с помощта на йонообменна смола чрез 2^3 пълен факторен експеримент. Изследванията са по периодичен способ при различни pH, температура и съотношения смола/разтвор. Ниските (1) и високите (2) нива и параметри за pH, температурата и съотношенията смола/разтвор са съответно 2.5 и 10, 12 °C и 40 °C и 1 g/50mL и 2 g/50mL. Адсорбционният капацитет на смолата по бор нараства при ниска температура, ниско съотношение смола/разтвор и високо pH. Когато се отчита вероятността $p<0.05$ при доверителни граници 95% се оказва, че само pH е статистически значим параметър. Оптимизацията на параметрите за постигане на оптимални условия е извършена чрез интерпретацията на кубични и контурни диаграми и таблици на Pareto. Времето от 48 часа е достатъчно за постигане на равновесие. Данните за адсорбция са анализирани по изотермите на Langmuir и Freundlich. Данните се описват по-доре с изотермата на Langmuir с коефициент на корелация 0.988. Максималният адсорбционен капацитет е определен на 12.87 mg g^{-1}. Кинетиката на адсорбция на бор в неподвижен слой може да се обясни с моделите на Thomas и Yoon-Nelson с коефициент на корелация 0.938. Капацитетът в този случай бе изчислен на 12.71 mg g^{-1}.

BULGARIAN CHEMICAL COMMUNICATIONS

Instructions about Preparation of Manuscripts

General remarks: Manuscripts are submitted in English by e-mail or by mail (in duplicate). The text must be typed double-spaced, on A4 format paper using Times New Roman font size 12, normal character spacing. The manuscript should not exceed 15 pages (about 3500 words), including photographs, tables, drawings, formulae, etc. Authors are requested to use margins of 3 cm on all sides. For mail submission hard copies, made by a clearly legible duplication process, are requested. Manuscripts should be subdivided into labelled sections, e.g. **Introduction, Experimental, Results and Discussion**, *etc*.

The title page comprises headline, author's names and affiliations, abstract and key words.

Attention is drawn to the following:

a) **The title** of the manuscript should reflect concisely the purpose and findings of the work. Abbreviations, symbols, chemical formulas, references and footnotes should be avoided. If indispensable, abbreviations and formulas should be given in parentheses immediately after the respective full form.

b) **The author**'s first and middle name initials, and family name in full should be given, followed by the address (or addresses) of the contributing laboratory (laboratories). **The affiliation** of the author(s) should be listed in detail (no abbreviations!). The author to whom correspondence and/or inquiries should be sent should be indicated by asterisk (*).

The abstract should be self-explanatory and intelligible without any references to the text and containing not more than 250 words. It should be followed by key words (not more than six).

References should be numbered sequentially in the order, in which they are cited in the text. The numbers in the text should be enclosed in brackets [2], [5, 6], [9–12], etc., set on the text line. References, typed with double spacing, are to be listed in numerical order on a separate sheet. All references are to be given in Latin letters. The names of the authors are given without inversion. Titles of journals must be abbreviated according to Chemical Abstracts and given in italics, the volume is typed in bold, the initial page is given and the year in parentheses. Attention is drawn to the following conventions:

a) The names of all authors of a certain publications should be given. The use of "*et al.*" in the list of references is not acceptable.

b) Only the initials of the first and middle names should be given.

In the manuscripts, the reference to author(s) of cited works should be made without giving initials, e.g. "Bush and Smith [7] pioneered...". If the reference carries the names of three or more authors it should be quoted as "Bush *et al*. [7]", if Bush is the first author, or as "Bush and co-workers [7]", if Bush is the senior author.

Footnotes should be reduced to a minimum. Each footnote should be typed double-spaced at the bottom of the page, on which its subject is first mentioned.

Tables are numbered with Arabic numerals on the left-hand top. Each table should be referred to in the text. Column headings should be as short as possible but they must define units unambiguously. The units are to be separated from the preceding symbols by a comma or brackets.

Note: The following format should be used when figures, equations, *etc*. are referred to the text (followed by the respective numbers): Fig., Eqns., Table, Scheme.

Schemes and figures. Each manuscript (hard copy) should contain or be accompanied by the respective illustrative material as well as by the respective figure captions in a separate file (sheet). As far as presentation of units is concerned, SI units are to be used. However, some non-SI units are also acceptable, such as °C, ml, l, etc.

The author(s) name(s), the title of the manuscript, the number of drawings, photographs, diagrams, etc., should be written in black pencil on the back of the illustrative material (hard copies) in accordance with the list enclosed. Avoid using more than 6 (12 for reviews, respectively) figures in the manuscript. Since most of the illustrative materials are to be presented as 8-cm wide pictures, attention should be paid that all axis titles, numerals, legend(s) and texts are legible.

The authors are asked to submit **the final text** (after the manuscript has been accepted for publication) in electronic form either by e-mail or mail on a 3.5'' diskette (CD) using a PC Word-processor. The main text, list of references, tables and figure captions should be saved in separate files (as *.rtf or *.doc) with clearly identifiable file names. It is essential that the name and version of

the word-processing program and the format of the text files is clearly indicated. It is recommended that the pictures are presented in *.tif, *.jpg, *.cdr or *.bmp format, the equations are written using "Equation Editor" and chemical reaction schemes are written using ISIS Draw or ChemDraw programme.

The authors are required to submit the final text with a list of three individuals and their e-mail addresses that can be considered by the Editors as potential reviewers. Please, note that the reviewers should be outside the authors' own institution or organization. The Editorial Board of the journal is not obliged to accept these proposals.

EXAMPLES FOR PRESENTATION OF REFERENCES

REFERENCES

1. D. S. Newsome, *Catal. Rev.–Sci. Eng.*, **21**, 275 (1980).
2. C.-H. Lin, C.-Y. Hsu, *J. Chem. Soc. Chem. Commun.*, 1479 (1992).
3. R. G. Parr, W. Yang, Density Functional Theory of Atoms and Molecules, Oxford Univ. Press, New York, 1989.
4. V. Ponec, G. C. Bond, Catalysis by Metals and Alloys (Stud. Surf. Sci. Catal., vol. 95), Elsevier, Amsterdam, 1995.
5. G. Kadinov, S. Todorova, A. Palazov, in: New Frontiers in Catalysis (Proc. 10th Int. Congr. Catal., Budapest, 1992), L. Guczi, F. Solymosi, P. Tetenyi (eds.), Akademiai Kiado, Budapest, 1993, Part C, p. 2817.
6. G. L. C. Maire, F. Garin, in: Catalysis. Science and Technology, J. R. Anderson, M. Boudart (eds), vol. 6, Springer-Verlag, Berlin, 1984, p. 161.
7. D. Pocknell, *GB Patent* 2 207 355 (1949).
8. G. Angelov, PhD Thesis, UCTM, Sofia, 2001.
9. JCPDS International Center for Diffraction Data, Power Diffraction File, Swarthmore, PA, 1991.
10. CA **127**, 184 762q (1998).
11. P. Hou, H. Wise, *J. Catal.*, in press.
12. M. Sinev, private communication.
13. http://www.chemweb.com/alchem/articles/1051611477211.html.

CONTENTS

СЪДЪРЖАНИЕ